

Final Report to CNSC-CCSN for Project:

R444.2

**Development of Analytical Tools for
Soil-Structure Analysis**

Contract No. 87055-10-0266

by:

Dr. Boris Jeremić

Consulting Engineer

1309 Lake Blvd., Davis, CA

Phones: 530.867.3434 ; 530.756.2682

jeremic@omsoft.com

DISCLAIMER

The Canadian Nuclear Safety Commission is not responsible for the accuracy of the statements made or opinions expressed in this publication and does not assume liability with respect to any damage or loss incurred as a result of the use made of the information contained in this publication.

Contents

1	Introduction	5
2	Motivation	6
2.1	Work Premise	7
3	Task 4.1: Seismic Input into NPP FEM Models	9
3.1	Summary of Findings for Task 4.1	9
3.2	Methodology	11
3.2.1	3D, Inclined, Body and Surface Wave Input into SSI	11
3.3	Work Performed, Subtasks	18
3.3.1	Analytic Modeling Body and Surface Incoming Seismic Waves	18
3.3.2	Properties of the DRM Layer	19
3.3.3	Damping of Outgoing Waves	20
3.3.4	Caughey Damping 2 nd Order (aka Rayleigh Damping)	21
3.3.5	Caughey Damping 3 rd Order	22
3.3.6	Caughey Damping 4 th Order	23
3.3.7	Proper Propagation of Torsional, Rolling and Rocking Motions	24
3.3.8	Propagation of Rotational Waves through a Structure	24
3.3.9	Simplified Representative 3D Model	25
3.3.10	Structure-Soil-Structure Interaction	26
3.3.11	Propagation of High Frequencies of Input Motions	30
3.3.12	Mesh Size Effects for Linear (8 Node Brick) and Quadratic (27 Node Brick) Finite Elements on Wave Propagation	32
4	Task 4.2: Spatially Variable Ground Motions	40
4.1	Summary of Findings for Task 4.2	40
4.2	Methodology	42
4.2.1	Incoherence, Sources	42
4.2.2	Introduction to Modeling	43
4.2.3	Incorporate of Incoherence (Lack of Correlation) into Simulated Motions	45
4.2.4	Description of Selected Incoherence Models	46
4.2.5	Range of Incoherence Model Applicability	47
4.3	Work Performed, Subtasks	48
4.3.1	Empirical SVGM models only for surface motions.	48
4.3.2	Spatially Variable Ground Motions Development	49

4.3.3	Multi axial SVGM models.	56
4.3.4	SVG M models and ergodic assumption.	57
4.3.5	SVG M models and multiple NPPs on a same soil.	58
4.3.6	SVG M models and multiple NPPs on a different soil.	58
5	Task 4.3: Material Nonlinear Response of Soil/Rock, Calibrated from Available Data	61
5.1	Summary of Findings for Task 4.3	61
5.2	Methodology	62
5.2.1	Assessment of Soil/Rock Nonlinearities in a Zone Adjacent to NPP Foundation.	62
5.2.2	Assessment of Material Models that can be Calibrated from Available Data.	63
5.2.3	Assessment of Contributions to Safety of this type of Nonlinearity.	64
5.3	Work Performed, Subtasks	64
5.3.1	Spatial Variability of Soil/Rock Domain.	64
5.3.2	Lack of Volume Change Data for Soil.	76
5.3.3	Extrapolation from 1D Data to full 3D Data, Pisano Material Model	77
5.3.4	Energy Dissipation of Soil/Rock (Viscous and Frictional).	106
5.3.5	Calibration of Material Model from Available G/G_{max} and Damping Curves.	107
5.4	NPP Model with Inelastic Soil	107
6	Task 4.4: Modeling Slipping and Gaping	109
6.1	Summary of Findings for Task 4.4	109
6.2	Methodology	110
6.2.1	Formulation	111
6.3	Work Performed, Subtasks	116
6.4	NPP Model with Nonlinear Contact, Illustrative Results	117
6.4.1	Slipping behavior of SSI models by considering 3D wave propagation	122
6.4.2	Example Nonlinear Model for Gaping and Slipping, Following Design Provisions and Standards	124
7	Task 4.5: Energy Dissipation	136
7.1	Summary of Findings for Task 4.5	136
7.2	Methodology	137
7.2.1	<i>Seismic energy input into SFS system</i>	137
7.2.2	<i>Seismic energy dissipation in SFS system</i>	138
7.3	Work Performed, Subtasks	140
7.4	Illustrative Example	143
7.4.1	Example #1	143
7.4.2	Example #2	144
8	Task 4.6: Buoyancy Modeling	146
8.1	Summary of Findings for Task 4.6	146
8.2	Methodology	147
8.3	Work Performed, Subtasks	147

8.3.1	Background	147
8.3.2	Modeling Approach	149
8.4	Illustrative Example	151
8.5	Fully Coupled Formulation for Porous Solid – Pore Fluid	152
8.5.1	u-p-U Formulation	152
8.5.2	Modified Governing Equations.	157
8.5.3	Numerical Solution of the u-p-U Governing Equations	159
8.5.4	Buoyant Forces: Surface Loads for Solid Bricks	162
9	Task 4.7: Piled Foundations	165
9.1	Summary of Findings for Task 4.7	165
9.2	Methodology	166
9.2.1	Modelling approach	166
9.2.2	Modeling Details	168
10	Task 4.8: Recommendations Regarding Safety Importance of Phenomena 4.1 – 4.7, and Methods to Take Them Into Account	192
10.1	Task 4.1: Full 3D, Inclined, Body and Surface Seismic Input	195
10.1.1	Safety Importance	195
10.1.2	Methods to Take into Account	195
10.2	Task 4.2: Incoherence Modeling	196
10.2.1	Safety Importance	196
10.2.2	Methods to Take into Account	197
10.3	Task 4.3: Soil/Rock Nonlinearities	199
10.3.1	Safety Importance	199
10.3.2	Methods to Take into Account	199
10.4	Task 4.4: Contact Problem, Slipping and Gaping	201
10.4.1	Safety Importance	201
10.4.2	Methods to Take into Account	201
10.5	Task 4.5: Timing and Location of Energy Dissipation	203
10.5.1	Safety Importance	203
10.5.2	Methods to Take into Account	204
10.6	Task 4.6: Buoyancy Effects	205
10.6.1	Safety Importance	205
10.6.2	Methods to Take into Account	205
10.7	Task 4.7: Piles and Pile Groups	207
10.7.1	Safety Importance	207
10.7.2	Methods to Take into Account	207
11	Task 4.9: Verification and Validation	208
11.1	Summary of Findings for Task 4.9	208
11.2	Introduction to Verification and Validation	210
11.2.1	Detailed Look at Verification and Validation	212
11.2.2	Prediction	214
11.2.3	Forward Toward Verification and Validation	215

11.3	Source Code Verification	215
11.4	Verification and Validation for Constitutive Problems	216
11.4.1	Verification of Constitutive Integration	216
11.4.2	Validation of Constitutive Model Predictions	219
11.5	Verification and Validation for Static and Dynamic Finite Element Level Solution Advancement Algorithms	223
11.5.1	Verification for Dynamic Solution Advancement	223
11.6	Verification and Validation for Static and Dynamic Behavior of Single Phase Solid Elements	229
11.6.1	Verification of Static, Single Phase Solid Modeling and Simulation	229
11.7	Verification and Validation for Static and Dynamic Behavior of Structural Elements	242
11.7.1	Verification of Shell (Felippa-ANDES) Finite Element Modeling and Sim- ulation	242
11.8	Verification and Validation for Static and Dynamic Behavior of Special Elements	255
11.8.1	Verification of Static and Dynamic Contact Element Modeling and Sim- ulation	255
11.8.2	Verification of Static and Dynamic Coupled (Saturated) Contact Element Modeling and Simulation	265
11.9	Verification and Validation for Coupled, Porous Solid – Pore Fluid Problems	267
11.10	Verification and Validation for Seismic Wave Propagation Problems	268
11.10.1	Verification of the Seismic Input (Domain Reduction Method) for 3D, Inclined Seismic Wave Fields	269
11.10.2	Validation: Lotung Large Scale Seismic Test (LLSST) Earthquake 07	277
12	Summary	281
13	References	282
A	Real ESSI Program and Computer	298
B	Program Command Manual	299
B.1	Introduction	299
B.2	Domain Specific Language (DSL), English Language Binding	300
B.2.1	Running the Program	300
B.2.2	Variables, basic units and flow control	302
B.2.3	Modeling	306
B.2.4	Simulation	394
B.2.5	Checking the Mesh	404

Chapter 1

Introduction

This report presents work performed for a project **R444.2 Development of Analytical Tools for Soil-Structure Analysis**. Project period was from February 2013 until March 2016. A number of developments resulting from this project are described in this report. In addition, links¹ are made to documents that are referenced and used in this report. Moreover, this report relies in part on section of Lecture Notes (Jeremić et al., 1989-2016), that are constantly updated using current developments within the computational geomechanics group at UC Davis.

I am respectfully submitting this report for review by the CNSC.

¹Live links, to web sites that are regularly updated and maintained.

Chapter 2

Motivation

The principal motivation for presented work is development of analysis methodology that will be used to improve seismic design of soil structure systems. It is postulated that Earthquake Soil Structure Interaction (ESSI) in time and space, plays a major role in successes and failures of seismic behavior of structure soil systems, including nuclear power plants and other nuclear facilities. It is also postulated that accurate following (and, if possible directing) the flow of seismic energy in ESSI system can be used to optimize safety and economy. Development of high fidelity numerical modeling and simulation tools to analyze realistic ESSI behavior¹ is used toward that goal.

High fidelity predictive capabilities, comprise prediction under uncertainty. That is, computational models are used to predict the state of soil structure system under conditions for which the computational model has not been validated (Oberkampf et al., 2002). Successful, reliable, dependable numerical prediction rely on detailed, in depth verification and validation procedures (V&V). Verification provides evidence that the model is solved correctly, and it is really a mathematics issue. Validation, on the other hand, provides evidence that the correct model is solved, and it is essentially a physics issue.

The main goal of numerical predictions (modeling and simulations) is predict and inform rather than (force) fit.

¹Epitomized in the Real ESSI simulator, a high fidelity numerical models and simulation system for analysis of ESSI behavior.

2.1 Work Premise

Presented work is premised on following observations and facts:

- **3D (6D) Earthquake Motions:** All the observed earthquake motions are three dimensional, with three translations and three rotations (body and surface waves). It follows that modeling of ESSI has to be utilize those full 3D (6D) motions. This is particularly important as most of the earthquake energy propagates as surface waves, and therefor both translations and rotations are important.
- **Inelastic/Nonlinear Material and Geometric Behavior:** Realistic materials (soil, rock, concrete, metals, etc.) are inelastic for any significant stress level, while soils are inelastic at any stress level. In addition, soil volume change has a first order effect on soil behavior for any constrained (really for all) deformation. Moreover, contact between concrete and soil/rock is highly nonlinear, with gap opening and closing and shear slip. Further, water in contact zone gives rise to coupled (nonlinear), soil/water behavior and dynamic (nonlinear) buoyant forces.
- **Modeling Uncertainty:** Simplified modeling is always performed, which implies that some features (possibly important features) are neglected. For example, simplified modeling of seismic motions as 1D vertically propagating waves as opposed to what is really observed, a full 3D (6D: 3 translations and 3 rotations) wave fields. In addition, usually inelastic/nonlinear material can be simply modeled as linear elastic (or so called equivalent elastic) material, thus neglecting potentially important inelastic effects, that are always present. Modeling uncertainty is introduced in results when unrealistic and unnecessary modeling simplifications are made. Such modeling simplifications can only be justified if one or two level higher sophistication model shows that features being simplified out are not important.
- **Uncertain Material and Loads:** Material behavior (modeling, material parameters) is always uncertain, due to spatial variability, measuring errors and transformation errors. In addition to that, loads (earthquake, etc.) are also always uncertain. It is therefor important to be able to propagate uncertainties in material and load results for proper decision making.

- Verification and Validation (V&V) for Prediction: V&V procedures and activities represent primary means of assessing accuracy in modeling and computational simulations. They are used to build confidence and credibility in numerical predictions. Verification is a process of determining that a model implementation accurately represents the developer's conceptual description and specification. It is a mathematics issue and it provides evidence that the model is solved correctly. Validation is a process of determining the degree to which a model is accurate representation of the real world from the perspective of the intended uses of the model. It is a physics issue, and it provides evidence that the correct model is solved.

Work performed for this project is premised on the above observations and facts. In what follows, Tasks worked on during this project are described in detail.

Chapter 3

Task 4.1: Seismic Input into NPP FEM Models

3.1 Summary of Findings for Task 4.1

This section presents a summary of findings related to the Task 4.1: "Develop methodologies and analytical tools for inputting 3D, inclined, body and surface waves into Soil-Structure Interaction models with resolution of issues related to the influence of surface waves that feature significant torsional, rolling and rocking motions. Develop a simplified but representative 3D model of the nuclear island to capture 3D effects of Soil-Structure Interaction." Summarized are findings, while more details are given in sections below.

The main findings are:

- Seismic input for finite element models has to be done using a method that can model all significant seismic waves fields, including body waves (Primary waves (P, aka compressional waves), Secondary (SV, aka secondary or shear waves polarized in vertical plane); SH, aka secondary or shear waves polarized in horizontal plane), and surface waves (Rayleigh, Love, and any other type of surface waves). Method used has also to be able to accurately model input of seismic energy as well as dissipation of seismic waves to the outside domain (radiation damping). In addition to that, method has to allow for seismic energy dissipation within the domain of interest (soil/rock – structure model). One such method is the

Domain Reduction Method (DRM), described in some detail here. The PI is not aware of any other currently available method that can achieve these goals for a time domain, nonlinear finite element analysis of soil/rock-structure-interaction (SSI) problems. The DRM has a number of specific requirements that need to be satisfied in order to achieve high accuracy of SSI modeling (material properties and size of the DRM layer, damping outside DRM layer, etc). Those requirements are given in some detail in the main text below. Proper verification needs to be provided to prove that used seismic input method can indeed model all required components of seismic motions (body and surface waves).

- Propagation of all required frequencies of seismic motions through model needs to be modeled using appropriate and finite element sizes (mesh). For solid finite elements, representative finite element size Δh needs to be limited so that seismic waves that are propagated retain all (most) required frequencies. For example for linear interpolation finite elements and for a given wave length λ that is modeled, it is required to have at least 10 linear interpolation finite elements (8 node bricks in 3D, where representative element size is $\Delta h^{LE} \leq \lambda/10 = v/(10 f_{max})$) or at least 2 quadratic interpolation finite elements (27 node bricks in 3D, where representative element size is $\Delta h^{QE} \leq \lambda/2 = v/(2 f_{max})$) for each wave length of importance for modeling. It is important to note that even with an increase in element size, the simulation will produce results, however, accuracy of those results (frequency content, for example) will be diminished as the model element size increase beyond suggested values. Proper verification needs to be provided in order to prove capacity of the model (mesh) to propagate required frequencies of motions.
- Proper propagating rotational motions through structural model can be accomplished provided that two conditions are met:
 - Surface waves (Rayleigh, Love, etc.) need to be present in ground motions. That is, structure, with its center of mass high above base level will rock even if excited by vertically propagating shear waves. However the real seismic waves will consist of both body and surface waves (with potentially significant rolling, rocking and torsional waves) and there will be an additional rotational component to seismic waves that enter (are input to) the foundations of NPP structure.

- Modeling of rotational motions with an NPP structural system relies significantly on in plane (wall) behavior of shells. Finite element models used to model walls (shells) need to be able to model accurately in plane modes of behavior, with an appropriate number of elements (usually fairly small). In addition it is very beneficial if finite elements with drilling degrees of freedom are used, as such elements are much more accurate. Proper verification needs to be provided to prove the accuracy of finite elements used.
- Symmetry and antisymmetry models for modeling Structure-Soil-Structure Interaction (SSSI) should not be used as they assume a vertically propagating shear waves and as such do not take into account surface waves (Rayleigh, Love, etc) that carry significant amount of seismic energy. It is recommended that direct models be used, that is, models that explicitly model both structures, their foundations and the soil/rock beneath with all the geometric and material behavior sophistication that can significantly influence SSSI response

During this project period, work team has spent their time working on issues related to the Task 4.1, and in particular working on sub-tasks as described in the original proposal. A number of developments were made, with a number of examples prepared for the CNSC. In addition to that, the first node of a parallel computer was prepared and will be shipped to the CNSC office in Ottawa. Moreover, an initial version of the program is prepared and placed on the web for download by the CNSC staff. Location will be communicated to CNSC staff via email.

3.2 Methodology

3.2.1 3D, Inclined, Body and Surface Wave Input into SSI

The full seismic wave field is composed of full 3D, inclined waves, consisting of both body (P, SV and SH) and surface (Rayleigh, Love, etc.) waves. The relative influence of any (or all) components of the seismic wave field on dynamics response on NPPs is not known prior to performing the analysis, and thus all above noted wave types need to be properly modeled.

Proper input of all possible wave types into finite element model is performed using the Domain Reduction Method (DRM). The DRM was developed recently Bielak et al. (2003); Yoshimura et al. (2003)). It is a modular, two-step dynamic procedure aimed at reducing the large computational domain to a more manageable size. The method was developed with earthquake ground motions in mind, with the main idea to replace the force couples at the fault with their counterpart acting on a continuous surface surrounding local feature of interest. The local feature can be any geologic or man made object that constitutes a difference from the simplified large domain for which displacements and accelerations are easier to obtain. The DRM is applicable to a much wider range of problems. It is essentially a variant of global–local set of methods and as formulated can be used for any problems where the local feature can be bounded by a continuous surface (that can be closed or not). The local feature in general can represent a soil–foundation–structure system (bridge, building, dam, tunnel...), or it can be a crack in large domain, or some other type of inhomogeneity that is fairly small compared to the size of domain where it is found.

In what follow, the DRM is developed in a somewhat different way than it was done in original papers by Bielak et al. (2003); Yoshimura et al. (2003)). The main features of the DRM are then analyzed and appropriate practical modeling issues addressed.

A large physical domain is to be analyzed for dynamic behavior. The source of disturbance is a known time history of a force field $P_e(t)$. That source of loading is far away from a local feature which is dynamically excited by $P_e(t)$ (see Figure 3.1).

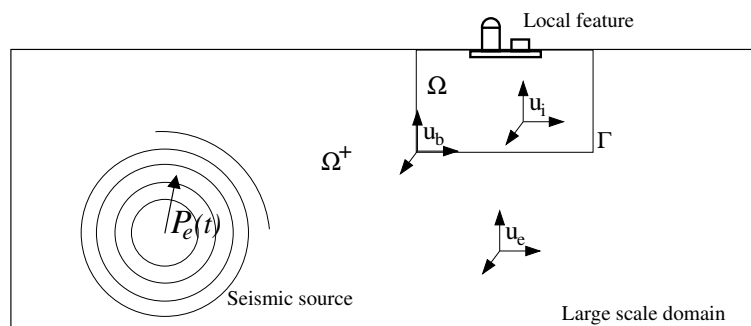


Figure 3.1: Large physical domain with the source of load $P_e(t)$ and the local feature (in this case a soil-structure system).

The system can be quite large, for example earthquake hypocenter can be many kilometers away from the local feature of interest. Similarly, the small local feature in a machine part can be many centimeters away from the source of dynamic loading which influences this local feature. In this sense the term large domain is relative to the size of the local feature and the distance to the dynamic forcing source.

It would be beneficial not to analyze the complete system, as we are only interested in the behavior of the local feature and its immediate surrounding, and can almost neglect the domain outside of some relatively close boundaries. In order to do this, we need to somehow transfer the loading from the source to the immediate vicinity of the local feature. For example we can try to reduce the size of the domain to a much smaller model bounded by surface Γ as shown in Figure 3.1. In doing so we must ensure that the dynamic forces $P_e(t)$ are appropriately propagated to the much smaller model boundaries Γ .

In order to appropriately propagate dynamic forces $P_e(t)$ one actually has to solve the large scale problem which will include the effects of the local feature. Most of the time this is impossible as it involves all the complexities of large scale computations and relatively small local feature. Besides, the main goal of presented developments is to somehow reduce the large scale domain as to be able to analyze in details behavior of the local feature.

In order to propagate consistently the dynamic forces $P_e(t)$ we will make a simplification in that we will replace a local feature with a simpler domain that is much easier to be analyzed. That is, we replace the local feature (bridge, building, tunnel, crack) with a much simpler geometry and material. For example, Figure 3.2 shows a simplified model, without a foundation–building system. The idea is to simplify the model so that it is much easier to consistently propagate the dynamic forces to the boundary Γ . The notion that it is much easier to propagate those dynamic forces is of course relative. This is still a very complex problem, but at least the influence of local feature is temporarily taken out.

It is convenient to name different parts of domain. For example, the domain inside the boundary Γ is named Ω_0 . The rest of the large scale domain, outside boundary Γ , is then named Ω^+ . The outside domain Ω^+ is still the same as in the original model, while the change, simplification, is done on the domain inside boundary Γ . The displacement fields for exterior, boundary and interior of the boundary Γ are u_e , u_b and u_i , on the original domain.

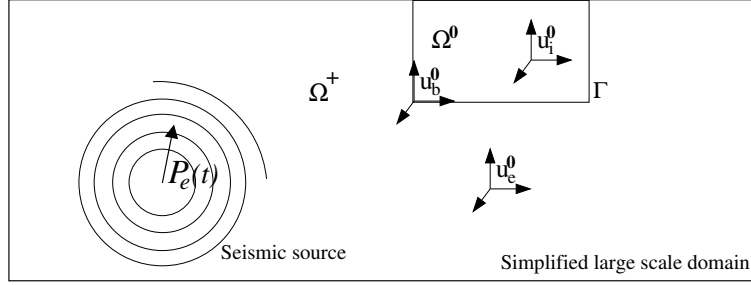


Figure 3.2: Simplified large physical domain with the source of load $P_e(t)$ and **without** the local feature (in this case a soil–foundation–building system. Instead of the local feature, the model is simplified so that it is possible to analyze it and simulate the dynamic response as to consistently propagate the dynamic forces $P_e(t)$.

The equations of motions for the complete system can be written as

$$\left[M \right] \left\{ \ddot{u} \right\} + \left[K \right] \left\{ u \right\} = \left\{ P_e \right\} \quad (3.1)$$

or if written for each domain (interior, boundary and exterior of Γ) separately, the equations obtain the following form:

$$\begin{bmatrix} M_{ii}^{\Omega} & M_{ib}^{\Omega} & 0 \\ M_{bi}^{\Omega} & M_{bb}^{\Omega} + M_{bb}^{\Omega^+} & M_{be}^{\Omega^+} \\ 0 & M_{eb}^{\Omega^+} & M_{ee}^{\Omega^+} \end{bmatrix} \begin{Bmatrix} \ddot{u}_i \\ \ddot{u}_b \\ \ddot{u}_e \end{Bmatrix} + \begin{bmatrix} K_{ii}^{\Omega} & K_{ib}^{\Omega} & 0 \\ K_{bi}^{\Omega} & K_{bb}^{\Omega} + K_{bb}^{\Omega^+} & K_{be}^{\Omega^+} \\ 0 & K_{eb}^{\Omega^+} & K_{ee}^{\Omega^+} \end{bmatrix} \begin{Bmatrix} u_i \\ u_b \\ u_e \end{Bmatrix} = \begin{Bmatrix} 0 \\ 0 \\ P_e \end{Bmatrix} \quad (3.2)$$

In these equations, the matrices \mathbf{M} and \mathbf{K} denote mass and stiffness matrices respectively; the subscripts i , e , and b refer to nodes in either the interior or exterior domain or on their common boundary; and the superscripts Ω and Ω^+ refer to the domains over which the various matrices are defined.

The previous equation can be separated provided that we maintain the compatibility of displacements and equilibrium. The resulting two equations of motion are

$$\begin{bmatrix} M_{ii}^{\Omega} & M_{ib}^{\Omega} \\ M_{bi}^{\Omega} & M_{bb}^{\Omega} \end{bmatrix} \begin{Bmatrix} \ddot{u}_i \\ \ddot{u}_b \end{Bmatrix} + \begin{bmatrix} K_{ii}^{\Omega} & K_{ib}^{\Omega} \\ K_{bi}^{\Omega} & K_{bb}^{\Omega} \end{bmatrix} \begin{Bmatrix} u_i \\ u_b \end{Bmatrix} = \begin{Bmatrix} 0 \\ P_b \end{Bmatrix}, \quad \text{in } \Omega \quad (3.3)$$

and

$$\begin{bmatrix} M_{bb}^{\Omega^+} & M_{be}^{\Omega^+} \\ M_{eb}^{\Omega^+} & M_{ee}^{\Omega^+} \end{bmatrix} \begin{Bmatrix} \ddot{u}_b \\ \ddot{u}_e \end{Bmatrix} + \begin{bmatrix} K_{bb}^{\Omega^+} & K_{be}^{\Omega^+} \\ K_{eb}^{\Omega^+} & K_{ee}^{\Omega^+} \end{bmatrix} \begin{Bmatrix} u_b \\ u_e \end{Bmatrix} = \begin{Bmatrix} -P_b \\ P_e \end{Bmatrix}, \quad \text{in } \Omega^+ \quad (3.4)$$

Compatibility of displacements is maintained automatically since both equations contain boundary displacements u_b (on boundary Γ), while the equilibrium is maintained through action–reaction forces P_b .

In order to simplify the problem, the local feature is removed from the interior domain. Thus, the interior domain is significantly simplified. In other words, the exterior region and the material therein are identical to those of the original problem as the dynamic force source. On the other hand, the interior domain (denoted as Ω_0), is simplified, the localized features is removed (as seen in figure 3.2).

For this simplified model, the displacement field (interior, boundary and exterior, respectively) and action–reaction forces are denoted by u_i^0 , u_b^0 , u_e^0 and P_b^0 . The entire simplified domain Ω_0 and Ω^+ is now easier to analyze.

The equations of motion in Ω^+ for the auxiliary problem can now be written as:

$$\begin{bmatrix} M_{bb}^{\Omega^+} & M_{be}^{\Omega^+} \\ M_{eb}^{\Omega^+} & M_{ee}^{\Omega^+} \end{bmatrix} \begin{Bmatrix} \ddot{u}_b^0 \\ \ddot{u}_e^0 \end{Bmatrix} + \begin{bmatrix} K_{bb}^{\Omega^+} & K_{be}^{\Omega^+} \\ K_{eb}^{\Omega^+} & K_{ee}^{\Omega^+} \end{bmatrix} \begin{Bmatrix} u_b^0 \\ u_e^0 \end{Bmatrix} = \begin{Bmatrix} -P_b^0 \\ P_e \end{Bmatrix} \quad (3.5)$$

Since there was no change to the exterior domain Ω^+ (material, geometry and the dynamic source are still the same) the mass and stiffness matrices and the nodal force P_e are the same as in Equations (3.3) and (3.4).

Second part of previous equation (3.5) can be used to obtain the dynamic force P_e as

$$P_e = M_{eb}^{\Omega^+} \ddot{u}_b^0 + M_{ee}^{\Omega^+} \ddot{u}_e^0 + K_{eb}^{\Omega^+} u_b^0 + K_{ee}^{\Omega^+} u_e^0 \quad (3.6)$$

The total displacement, u_e , can be expressed as the sum of the free field u_e^0 (from the background, simplified model) and the residual field w_e (coming from the local feature) as following:

$$u_e = u_e^0 + w_e \quad (3.7)$$

It is important to note that this is just a change of variables and not an application of the principle of superposition. The residual displacement field, w_e is measured relative to the reference free field u_e^0 .

By substituting Equation (3.7) in Equation (3.2) one obtains:

$$\begin{bmatrix} M_{ii}^{\Omega} & M_{ib}^{\Omega} & 0 \\ M_{bi}^{\Omega} & M_{bb}^{\Omega} + M_{bb}^{\Omega+} & M_{be}^{\Omega+} \\ 0 & M_{eb}^{\Omega+} & M_{ee}^{\Omega+} \end{bmatrix} \begin{Bmatrix} \ddot{u}_i \\ \ddot{u}_b \\ \ddot{u}_e^0 + \ddot{w}_e \end{Bmatrix} + \begin{bmatrix} K_{ii}^{\Omega} & K_{ib}^{\Omega} & 0 \\ K_{bi}^{\Omega} & K_{bb}^{\Omega} + K_{bb}^{\Omega+} & K_{be}^{\Omega+} \\ 0 & K_{eb}^{\Omega+} & K_{ee}^{\Omega+} \end{bmatrix} \begin{Bmatrix} u_i \\ u_b \\ u_e^0 + w_e \end{Bmatrix} = \begin{Bmatrix} 0 \\ 0 \\ P_e \end{Bmatrix} \quad (3.8)$$

which, after moving the free field motions u_e^0 to the right hand side, becomes

$$\begin{bmatrix} M_{ii}^{\Omega} & M_{ib}^{\Omega} & 0 \\ M_{bi}^{\Omega} & M_{bb}^{\Omega} + M_{bb}^{\Omega+} & M_{be}^{\Omega+} \\ 0 & M_{eb}^{\Omega+} & M_{ee}^{\Omega+} \end{bmatrix} \begin{Bmatrix} \ddot{u}_i \\ \ddot{u}_b \\ \ddot{u}_e \end{Bmatrix} + \begin{bmatrix} K_{ii}^{\Omega} & K_{ib}^{\Omega} & 0 \\ K_{bi}^{\Omega} & K_{bb}^{\Omega} + K_{bb}^{\Omega+} & K_{be}^{\Omega+} \\ 0 & K_{eb}^{\Omega+} & K_{ee}^{\Omega+} \end{bmatrix} \begin{Bmatrix} u_i \\ u_b \\ w_e \end{Bmatrix} = \begin{Bmatrix} 0 \\ -M_{be}^{\Omega+} \ddot{u}_e^0 - K_{be}^{\Omega+} u_e^0 \\ -M_{ee}^{\Omega+} \ddot{u}_e^0 - K_{ee}^{\Omega+} u_e^0 + P_e \end{Bmatrix} \quad (3.9)$$

By substituting Equation (3.6) in previous Equation (3.9), the right hand side can now be written as

$$\begin{bmatrix} M_{ii}^{\Omega} & M_{ib}^{\Omega} & 0 \\ M_{bi}^{\Omega} & M_{bb}^{\Omega} + M_{bb}^{\Omega+} & M_{be}^{\Omega+} \\ 0 & M_{eb}^{\Omega+} & M_{ee}^{\Omega+} \end{bmatrix} \begin{Bmatrix} \ddot{u}_i \\ \ddot{u}_b \\ \ddot{u}_e \end{Bmatrix} + \begin{bmatrix} K_{ii}^{\Omega} & K_{ib}^{\Omega} & 0 \\ K_{bi}^{\Omega} & K_{bb}^{\Omega} + K_{bb}^{\Omega+} & K_{be}^{\Omega+} \\ 0 & K_{eb}^{\Omega+} & K_{ee}^{\Omega+} \end{bmatrix} \begin{Bmatrix} u_i \\ u_b \\ w_e \end{Bmatrix} = \begin{Bmatrix} 0 \\ -M_{be}^{\Omega+} \ddot{u}_e^0 - K_{be}^{\Omega+} u_e^0 \\ M_{eb}^{\Omega+} \ddot{u}_b^0 + K_{eb}^{\Omega+} u_b^0 \end{Bmatrix} \quad (3.10)$$

The right hand side of equation (3.10) is the dynamically consistent replacement force (so called effective force, P^{eff} for the dynamic source forces P_e . In other words, the dynamic force P_e was consistently replaced by the effective force P^{eff} :

$$P^{eff} = \begin{Bmatrix} P_i^{eff} \\ P_b^{eff} \\ P_e^{eff} \end{Bmatrix} = \begin{Bmatrix} 0 \\ -M_{be}^{\Omega+} \ddot{u}_e^0 - K_{be}^{\Omega+} u_e^0 \\ M_{eb}^{\Omega+} \ddot{u}_b^0 + K_{eb}^{\Omega+} u_b^0 \end{Bmatrix} \quad (3.11)$$

DRM features a number of beneficial features:

- **Single Layer of Elements used for P^{eff} .** The Equation (3.11) shows that the effective nodal forces P^{eff} involve only the sub-matrices M_{be} , K_{be} , M_{eb} , K_{eb} . These matrices vanish everywhere except the single layer of finite elements in domain Ω^+ adjacent to Γ . The significance of this is that the only wave-field (displacements and accelerations) needed to determine effective forces P^{eff} is that obtained from the simplified (auxiliary) problem at the nodes that lie on and between boundaries Γ and Γ_e , as shown in Figure 3.3.

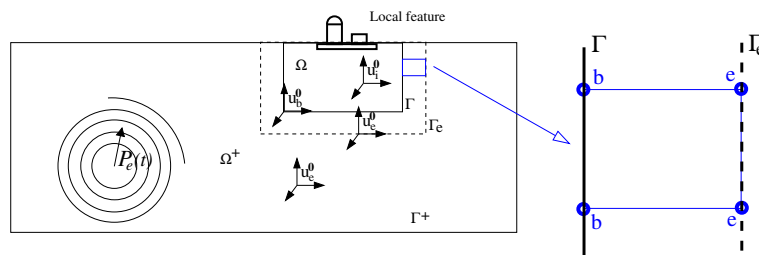


Figure 3.3: DRM: Single layer of elements between Γ and Γ_e is used to create P^{eff} .

- **Only residual waves outgoing.** Another interesting observation is that the solution to problem described in Equation (3.10) comprises full unknowns (displacements and accelerations) inside and on the boundary Γ (\mathbf{u}_i and \mathbf{u}_b respectively). On the other hand, the solution for the domain outside single layer of finite elements (outside Γ_e) is obtained for the residual unknown (displacement and accelerations) field, w_e only. This residual unknown field is measured relative to the reference free field of unknowns (see comments on page 15). That effectively means that the solution to the equation Equation (3.10) outside the boundary Γ_e will only contain additional waves field resulting from the presence of a local feature. This in turn means that if the interest is in behavior of local feature and the surrounding media (all within boundary Γ) one can neglect the behavior of the full model (outside Γ_e in Ω^+) and provide appropriate supports (including fixity and damping) at some distance from the boundary Γ_e into region Ω^+ . This is significant for a number of reasons:

- large models can be reduced in size to encompass just a few layers of elements outside boundary Γ_e (significant reduction for, say earthquake problems where the size of a local feature is orders of magnitudes smaller than the distance to the dynamic source force P_e (earthquake hypocenter)).
 - the residual unknown field can be monitored and analyzed for information about the dynamic characteristics of the local feature. Since the residual wave field is w_e is measured relative to the reference free field u_0^e , the solution for w_e has all the characteristics of the additional wave field stemming from the local feature.
- **Inside domain Ω can be inelastic.** In all the derivations of the DRM no restriction was made on the type of material inside the plastic bowl (inside Γ_e). That is, the assumption that the material inside is linear elastic is not necessary as the DRM is not relying on principle of superposition. The Equation 3.7 was only describing the change of variables, and clearly there was no use of the principle of superposition, which is only valid for linear elastic solids and structures. It is therefore possible to assume that the derivations will still be valid with any type of material (linear or nonlinear, elastic or inelastic) inside Γ_e . With this in mind, the DRM becomes a very powerful method for analysis of soil–foundation–structure systems.
 - **All types of realistic seismic waves are modeled.** Since the effective forcing P^{eff} consistently replaces the effects of the seismic source, all appropriate (real) seismic waves are properly (analytically) modeled, including body (SV, SH, P) and surface (Rayleigh, Love, etc...) waves.

3.3 Work Performed, Subtasks

3.3.1 Analytic Modeling Body and Surface Incoming Seismic Waves

Input of seismic motions that are comprised of all mechanical wave fields (body waves (P, SV, SH) and surface waves (Rayleigh, Love, etc) is done using the Domain Reduction Method. Presence of all mechanical wave fields (as noted above) is proven by doing a verification. A set

of verification examples is shown in chapter 11 on page 208.

3.3.2 Properties of the DRM Layer

The DRM layers (a single layer of finite element where effective DRM forces P_{eff} are applied) needs to be carefully modeled. A number of conditions regarding the DRM layer need to be placed:

- The finite elements within the DRM layer need be linear elastic.
- Material model for the finite elements within the DRM layer needs to be linear elastic, of same (or similar) material properties as the material outside the DRM layer, and of the same of similar properties (the linear elastic part of properties) as the material inside the DRM layer. Although material inside the DRM layer can be elastic-plastic, it is beneficial if the linear elastic portion of material properties (at zero strain, for nonlinear elastic material) for the DRM layer, is similar to the ones used inside the DRM layer. All of the used elastic material properties need to be same as elastic material properties used for free field analysis.
- Material outside the DRM layer needs to be linear elastic, with possible inclusion of damping (Rayleigh or Caughey) for damping outgoing waves (radiation damping).
- Dimensions of the DRM layer finite elements (thickness of the DRM layer) need to follow the same rule for element size (depending on chosen stiffness) so that there is no artificial (mesh dependent) filtering above certain frequencies. That means that 10 linear interpolation finite elements (8 node bricks) or 2 quadratic interpolation elements (27 node bricks) are needed per wave length (Bathe and Wilson, 1976; Hughes, 1987; Argyris and Mlejnek, 1991). For example if maximum modeling frequency is $f_{max} = 20$ Hz, and wave length is given as $\lambda_{min} = v/f_{max}$, where v is the wave velocity, maximum grid spacing (element size) for linear interpolation elements Δh^{LE} should not exceed

$$\Delta h^{LE} \leq \frac{\lambda}{10} = \frac{v}{10 f_{max}} = \frac{v}{10 \times 20 \text{ Hz}} = \frac{v}{200 \text{ Hz}}$$

while for quadratic interpolation elements such grid spacing (element size) Δh^{QE} is limited to

$$\Delta h^{QE} \leq \frac{\lambda}{2} = \frac{v}{2 f_{max}} = \frac{v}{2 \times 20 \text{ Hz}} = \frac{v}{40 \text{ Hz}}$$

The wave velocity v is the lowest wave velocity that is of interest in the simulation, usually the shear wave velocity.

3.3.3 Damping of Outgoing Waves

The formulation of DRM postulates that the only waves that are radiating from the finite element model of soil/rock – structure interaction are the waves that are originating from the vibrations of the additional feature, that is the structure. Those radiating waves do have much less mechanical energy than incoming seismic waves and are thus easier to damp out. In addition, those waves that radiate from the structure will consist of a smaller number of frequencies, due to their origin in structural vibrations (which have a certain number of predominant modes).

The outgoing waves are damped out using layers of finite elements with high viscous damping that are positioned outside of the DRM layer. In general any type of viscous damping can be used outside, but the most common method (and the most efficient) is to use Caughey damping of 2nd, 3rd and 4th order. Caughey damping of 2nd order is also known as Rayleigh damping.

A number of examples were created to illustrate seismic wave damping using Rayleigh and Caughey damping finite elements.

The main conclusions about damping seismic waves that radiate from the model are:

- Based on the DRM formulation, there should be at least one layer of finite elements outside of the DRM layer. It is recommended that a number of layers outside the DRM layer be increased to at least two, and possibly more, in order to use those additional layers for damping outgoing (radiation) waves.
- Damping layers, outside of DRM layers, should be developed in such a way as to damp out multiple frequencies of outgoing waves. Caughey damping can damp efficiently a number of frequencies. For example Caughey damping of 2nd order (also called Rayleigh damping) can damp efficiently two distinct frequencies. If Rayleigh damping is used, then one or more

layers of damping elements are to be used. If more than one layer is used, layers should have variable damping coefficients, so that they damp out different pairs of frequencies.

- Damping ratios of damping layers outside should be evaluated based on dynamic characteristics of the soil/rock profile as well as based on the dynamic characteristic of the oscillating structure.

In addition to relying on features of the DRM, what remains of a wave field that results from oscillations of the NPP, is damped out in out of DRM layers, as noted above.

Presented here are commonly used (viscous) damping methods for time domain analysis of solids and structures. These methods (Rayleigh and Caughey damping) are modeling viscous damping of the solids and structures by generating the damping matrix C from mass and stiffness matrices.

These synthetic viscous damping approaches should be distinguished from a natural viscous damping that is created during interaction of fluid and soil. For example, a natural viscous damping occurs when pore fluid and porous solid have differential displacements (see for example Zienkiewicz and Shiomi (1984); Jeremić et al. (1989-2016)).

Viscous damping described here is used to damp out wave fields that radiate from the structure (wave field w_e in DRM parlance), and is applied to the outside of DRM layer finite elements.

Caughey damping formulation can in general be expressed as

$$C = [M] \sum_{j=0}^{m-1} a_j ([M]^{-1} [K])^j \quad (3.12)$$

3.3.4 Caughey Damping 2^{nd} Order (aka Rayleigh Damping)

The second order Caughey damping is actually Rayleigh damping, where $j = 1$ in Equation (3.12). From dynamic parameters and formulation of the system following equations can be written:

$$\xi_n = \frac{C_n}{2M_n\omega_n} \quad (3.13)$$

$$K_n = \omega_n^2 M_n \quad (3.14)$$

Considering the first two terms in Caughey damping formulation, if the damping matrix formulation is written separately for each term:

$$C = a_0 M \quad (3.15)$$

and based on Equation (3.13), parameter a_0 can be written as:

$$a_0 = 2\xi\omega \quad (3.16)$$

Writing the damping matrix based on the second coefficient:

$$C = a_1 K = a_1 \omega^2 M \quad (3.17)$$

Then a_1 can be obtained as:

$$a_1 = \frac{2\xi}{\omega} \quad (3.18)$$

So the damping ratio of the n^{th} mode of the system is:

$$\xi_n = \frac{a_0}{2} \frac{1}{\omega_n} + \frac{a_1}{2} \omega_n \quad (3.19)$$

Presenting Equation (3.19) for first two modes in matrix form leads to:

$$\frac{1}{2} \begin{bmatrix} \frac{1}{\omega_i} & \omega_i \\ \frac{1}{\omega_j} & \omega_j \end{bmatrix} \begin{bmatrix} a_0 \\ a_1 \end{bmatrix} = \begin{bmatrix} \xi_i \\ \xi_j \end{bmatrix} \quad (3.20)$$

3.3.5 Caughey Damping 3rd Order

Following the same logic as the 2nd order, the last coefficient of the 3rd order Caughey damping formulation can be written as following:

$$C = a_2 K M^{-1} K = a_2 \omega^4 M \quad (3.21)$$

So a_2 can be obtained as:

$$a_2 = \frac{2\xi}{\omega^3} \quad (3.22)$$

Considering the last coefficient in the formulation, the damping ratio of the system can now be shown as:

$$\xi_n = \frac{a_0}{2} \frac{1}{\omega_n} + \frac{a_1}{2} \omega_n + \frac{a_2}{2} \omega_n^3 \quad (3.23)$$

By solving the following set of equations, 3rd order Caughey damping coefficients can be found:

$$\frac{1}{2} \begin{bmatrix} \frac{1}{\omega_i} & \omega_i & \omega_i^3 \\ \frac{1}{\omega_j} & \omega_j & \omega_j^3 \\ \frac{1}{\omega_k} & \omega_k & \omega_k^3 \end{bmatrix} \begin{bmatrix} a_0 \\ a_1 \\ a_2 \end{bmatrix} = \begin{bmatrix} \xi_i \\ \xi_j \\ \xi_k \end{bmatrix} \quad (3.24)$$

3.3.6 Caughey Damping 4th Order

The 4th coefficient of the Caughey damping formulation can be obtained as:

$$C = a_3 K M^{-1} K M^{-1} K = a_3 \omega^6 M \quad (3.25)$$

$$a_3 = \frac{2\xi}{\omega^5} \quad (3.26)$$

$$\xi_n = \frac{a_0}{2} \frac{1}{\omega_n} + \frac{a_1}{2} \omega_n + \frac{a_2}{2} \omega_n^3 + \frac{a_3}{2} \omega_n^5 \quad (3.27)$$

So the damping coefficients can be obtained by solving the following set of equations:

$$\frac{1}{2} \begin{bmatrix} \frac{1}{\omega_i} & \omega_i & \omega_i^3 & \omega_i^5 \\ \frac{1}{\omega_j} & \omega_j & \omega_j^3 & \omega_j^5 \\ \frac{1}{\omega_k} & \omega_k & \omega_k^3 & \omega_k^5 \\ \frac{1}{\omega_l} & \omega_l & \omega_l^3 & \omega_l^5 \end{bmatrix} \begin{bmatrix} a_0 \\ a_1 \\ a_2 \\ a_3 \end{bmatrix} = \begin{bmatrix} \xi_i \\ \xi_j \\ \xi_k \\ \xi_l \end{bmatrix} \quad (3.28)$$

3.3.7 Proper Propagation of Torsional, Rolling and Rocking Motions

Torsional, rolling and rocking motions are propagated through the finite element models using DRM for input. The ability of DRM to successfully propagate all seismic waves from surrounding soil/rock into the finite element model, including body (P, SV, SH) and surface (Rayleigh, Love, etc.) waves allows for all the above noted waves to be very accurately represented within a finite element model.

Current effort to merge work done by Profs. Trifunac and Lee will allow for even wider range of seismic motions (realistic earthquakes) to be used and input into the finite element models.

3.3.8 Propagation of Rotational Waves through a Structure

Rotational motions (torsional, rolling and rocking) that propagate through soil/rock, will be transferred to the structural system through the foundation. Such motions will be amplified by rocking, rolling and torsional modes of the structure itself (rocking and rolling since the center of mass for the structure is at some elevation, while additional torsional modes will be caused by the non-symmetry of the structural system).

Rotational motions through the structure will be modeled appropriately using the ANDES shell finite element (Bergan and Felippa, 1985; Alvin et al., 1992; Felippa and Militello, 1992; Felippa and Alexander, 1992; Militello and Felippa, 1991; Stošić, 1984-2013)). This shell finite element is very accurate and features six degrees of freedom per node (three translations, two bending modes and one drilling mode). Verification of modeling and simulation for this element is given in Chapter 11 on page 208. Verification results show that this element, that is used for modeling of structural shell, plate and wall components, has excellent capabilities and that it

can model bending and in plane behavior with high accuracy using only very few elements. This accurate modeling capabilities will allow proper, accurate modeling of propagation of rotational waves through the structure as well as development of translational and rotational floor spectra for any location within NPP structure.

3.3.9 Simplified Representative 3D Model

Representative model of an NPP containment structures was developed in collaboration with the CNSC staff. Figure 3.3.9 shows a general disposition of the representative 3D NPP model.

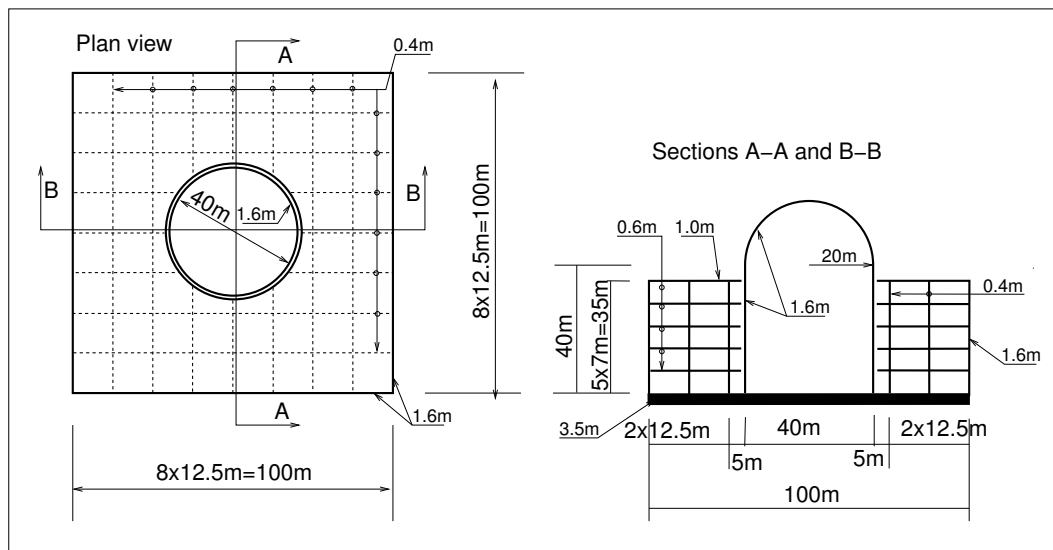


Figure 3.4: General disposition of a representative 3D NPP model.

The model was developed as a cylindrical containment with dome top, while the auxiliary building surrounds the containment. There is no contact between containment and the auxiliary building and current model has a gap of 0.2m while a new model (currently under development) will reduce this gap space, while still maintaining independence of two structural systems.

Finite element mesh for both structures (containment and auxiliary) is show in Figure 3.3.9.

Both structures (containment and auxiliary building) were placed on a slab foundation and then placed on a soil/rock base. Model is flexible enough that soil/rock properties and geology can be varied. The sub-base model also includes a layer of elements for the DRM motion input,

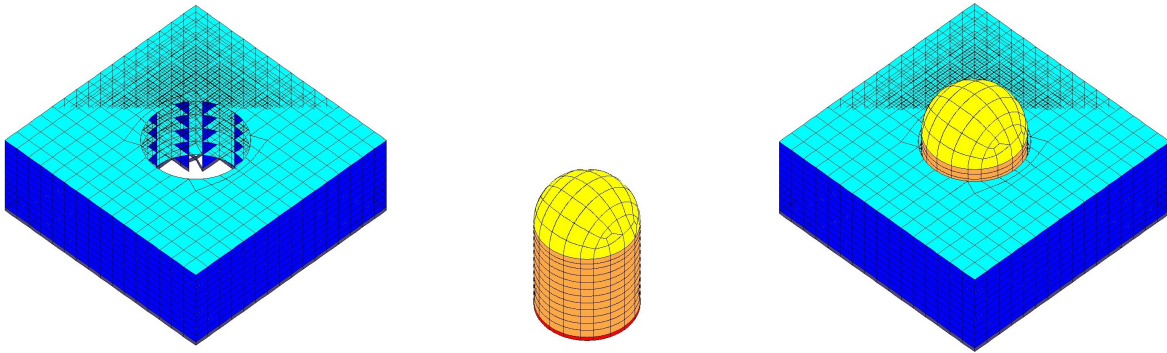


Figure 3.5: Different views of the representative 3D NPP mode. The model consists of a containment and auxiliary building structures. Both structures are connected through the foundation slab (not shown in these plots). Both structures are modeled using shell finite elements with 6 DOFs per node (three translations, two bending and one drilling model).

as well as two layers of elements outside the DRM layer for damping any outgoing waves. Models with a single NPP (Figure 3.3.9) and two NPPs (Figure 3.3.9) are developed and used in analysis.

Both models are based on the same containment and auxiliary buildings on a same foundation mat. Basic statistics for both models are presented in a table 3.1 below.

Table 3.1: Basic statistics of a single and a double NPP finite element models.

	single NPP model	double NPP model
number of (27 nodes) bricks	9576	19152
number of (ANDES) Shell Elements	4386	8772
number of DOFs	269217	534729

3.3.10 Structure-Soil-Structure Interaction

Structure-Soil-Structure Interaction (SSSI) need to be taken into account sometimes, as it might contribute to higher levels of seismic shaking for NPPs. It seems that in the case of making an assumption of elastic soil and rock beneath the NPP foundation, the SSSI will have a larger

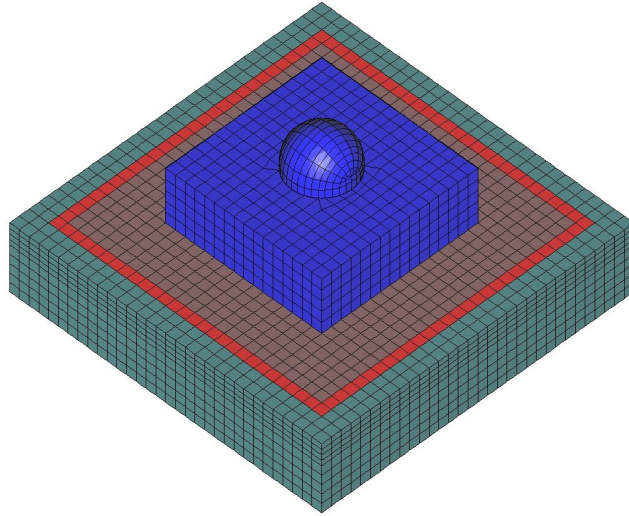


Figure 3.6: Finite element model for a single NPP with the containment and auxiliary buildings on a common base mat, as well as the soil/rock sub-base, DRM layer for seismic motions input and the layers outside of DRM for damping out outgoing waves.

effect most of the time, while with the inclusion of elastic-plastic models for soil and rock under the NPP foundation, those SSSI influences will be reduced most of the time. This is illustrated in one of the models that was developed for analyzing SSSI (to be delivered to CNSC online with the rest of the new code). While SSSI for two NPPs (of similar stiffness and mass) conforms to the above observations, it is noted that SSSI influences of smaller structures on larger (NPPs) can be mostly neglected, the SSSI influence of larger structures (NPPs) on smaller structures Probably cannot be neglected.

There are a number of ways to model SSSI.

- Direct Models. The simplest and most accurate is to develop a direct model of both (two or more) structures on subsurface soil and rock, to develop input seismic motions and analyze results. This was done in a model that will be delivered to CNSC online with the rest of the new code and a first node of a parallel computer. While this approach is the most involved, it is also the most accurate, as it allows for proper modeling of all the structure, foundation and soil/rock geometries and material without making any unnecessary simplifying assumptions.

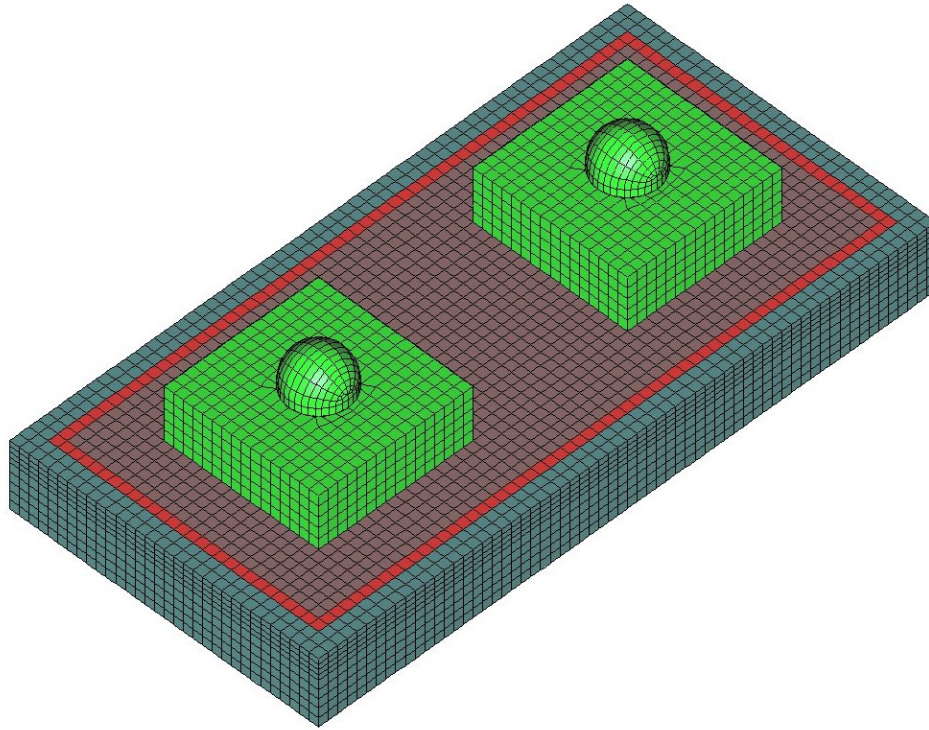


Figure 3.7: Finite element model for two NPPs adjacent to each other, each one with the containment and auxiliary buildings on a common base mat, as well as the soil/rock sub-base, DRM layer for seismic motions input and the layers outside of DRM for damping out outgoing waves.

- Symmetry and Anti-Symmetry Models. These models are sometimes used in order to reduce complexity and sophistication of the direct model (see recent paper by Roy et al. (2013) for example). However, there are a number of concerns regarding simplifying assumptions that need to be made in order for these models to work. These models have to make an assumption of a vertically propagating shear waves and as such do not take into account surface waves (Rayleigh, Love, etc) that carry significant amount of seismic energy. These surface waves will additionally excite NPP for rocking and twisting motions, which will then be transferred to adjacent NPP by means of additional surface waves. If only vertically propagating waves are used for input (as is the case for symmetry and anti-symmetry models) energy of input surface waves is neglected. It is noted that depending

on the surface wave length and the distance between adjacent structures, a simple analysis can be performed to determine if particular surface waves, emitted/radiated from one structure toward the other one (and in the opposite direction) can influence adjacent structures. It is noted that the wave length can be determined using a classical equation $\lambda = v/f$ where λ is the length of the (surface) wave, v is the wave speed¹ and f is the wave frequency of interest. Table 3.2 below gives Rayleigh wave lengths for four different wave frequencies (1, 5, 10, 20 Hz and for three different Rayleigh (very close to shear) wave velocities (300, 1000, 2500 m/s):

Table 3.2: Rayleigh wave length as a function of wave speed [m/s] and wave frequency [Hz].

	1.0Hz	5.0Hz	10.0Hz	20Hz
300m/s	300m	60m	30m	15m
1000m/s	1000m	200m	100m	50m
2500m/s	2500m	500m	250m	125m

It is apparent that for given separation between NPP buildings, different surface wave (frequencies) will be differently transmitted with different effects. For example, for an NPP building that has a basic linear dimension (length along the main rocking direction) of 100m, the surface wave the low frequency waves (1Hz) in soft soil ($v_s \approx 300\text{m/s}$) will be able to encompass a complete building within a single wave length, while for the same soil stiffness, the high frequency (20Hz) will produce waves that are too short to efficiently propagate through such NPP structure. On the other hand, for higher rock stiffness ($v_s \approx 2500\text{m/s}$), waves with frequencies all the way up to approximately 5Hz and maybe even 10Hz, have an extent that can easily be affecting a building with a 100m dimension.

Further comments on symmetric and antisymmetric models:

- Symmetry: motions of two NPPs are out phase and this represents an unrealistic

¹For Rayleigh surface waves, their speed is just slightly below the shear wave speed (within 10%, depending on elastic properties of material), so a shear wave speed can be used for making these Rayleigh wave length estimates.

case, unless the wave length of surface wave created by one NPP (toward the other NPP) is so large that half wave length will encompass both NPPs. This type of motions (symmetry) is illustrated in figure 3.3.10 below

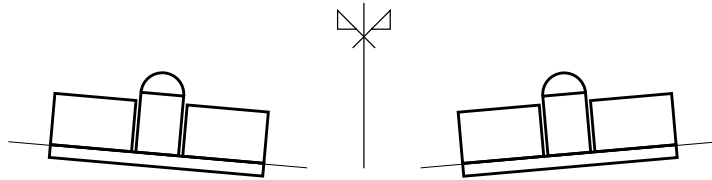


Figure 3.8: Symmetric mode of deformation for two NPPs near each other.

- Antisymmetry: motions of two NPPs are in phase and while that is more realistic than the symmetry case, still requires perfect matching of 1D input motions and the soil/rock conditions beneath, and as such is not realistic. This type of SSSI is illustrated in figure 3.3.10 below

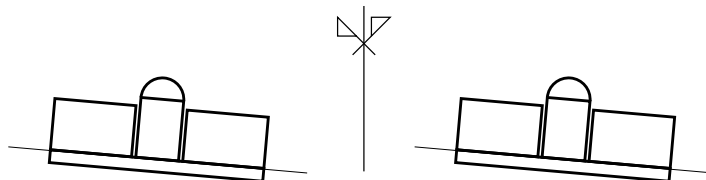


Figure 3.9: Anti-symmetric mode of deformation for two NPPs near each other.

A model of a dual NPP is developed (see Figure 3.3.9 (page 28) is developed with some initial input motions for testing purposes. It is anticipated that with incorporation of seismic motions from a project by Drs. Trifunac and Lee, a more in depth study will be possible of these SSSI effects.

3.3.11 Propagation of High Frequencies of Input Motions

Seismic waves of different frequencies need to be accurately propagated through the mesh. Mesh size can have significant effect on propagating seismic waves due to the influence of the order of displacement interpolation within the mesh. Finite element model (mesh, including nodes and

element interpolation functions) needs to be able to approximate displacement/wave field with accuracy without discarding (filtering out) certain wave components while propagating other wave components. For a given wave length λ that is modeled, it is suggested/required to have at least 10 linear interpolation finite elements (8 node bricks in 3D, where representative element size is $\Delta h^{LE} \leq \lambda/10$) or at least 2 quadratic interpolation finite elements (27 node bricks in 3D, where representative element size is $\Delta h^{QE} \leq \lambda/2$) for each wave length of importance for modeling.

Since wave length λ is directly proportional to the wave velocity v and inversely proportional to the frequency f , $\lambda = v/f$. we can devise a simple rule for appropriate size of finite elements for wave propagation problems:

- Linear interpolation finite elements (1D 2-node truss, 2D 4-node quad, 3D 8-node brick) the representative finite element size needs to satisfy the following condition

$$h^{LE} \leq \frac{v}{10 f_{max}}$$

- Quadratic interpolation finite elements (1D 3-node truss, 2D 9-node quad, 3D 27-node brick) the representative finite element size needs to satisfy the following condition

$$h^{QE} \leq \frac{v}{2 f_{max}}$$

- Structural elements (beams, shells) have at least quadratic interpolation functions (Euler-Bernoulli beam uses cubic Hermite polynomials as interpolation functions) and since material is very stiff, and thus wave propagation speed (shear or compressional) is very high, these elements usually satisfy wave propagation criteria a priori.

It is noted that while the rule for number of elements (or element size Δh) can be used to delineate models with proper and improper meshing, in reality having bigger finite element sizes than required by the above rule will slowly degrade the solution frequency content.

3.3.12 Mesh Size Effects for Linear (8 Node Brick) and Quadratic (27 Node Brick) Finite Elements on Wave Propagation

Presented here are cases of wave propagation modeling through finite element meshes of different sizes. The purpose is to emphasize that wave propagation through a discrete systems (finite element mesh) will always lead to loss of energy (wave magnitude) and that proper choice of mesh size has to be done with respect to accepted loss of energy. In other words, there is no good or bad mesh sizes, some mesh sizes (smaller) will allow for better wave propagation modeling, while some other mesh sizes (large elements) will not allow all required frequencies to be propagated in a required way.

Generally, the results of numerical analysis using finite element method technique for the dynamic problem are affected by size of mesh (grid spacing). According to Argyris and Mlejnek (1991), about 10 nodes per wavelength (for linear interpolating finite elements) are required to simulate accurately for the given frequency and fewer than 10 nodes may induce an artificial damping due to the numerical reason.

In this section, mesh size effect is inspected to address appropriate size of mesh for seismic wave propagation. One dimensional column model is developed, as shown in figure 3.10.

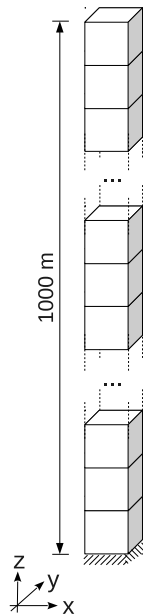


Figure 3.10: One dimensional column test model to address the mesh size effect.

Table 3.3: Analysis cases to determine a mesh size

Case number	V_s (m/s)	Cutoff freq. (Hz)	Element height (m)	Max. propagation freq. (Hz)
1	1000	3	10	10
2	1000	8	10	10
3	1000	15	10	10
4	100	3	10	1
5	100	8	10	1
6	100	15	10	1
7	1000	3	20	5
8	1000	8	20	5
9	1000	15	20	5
10	100	3	20	0.5
11	100	8	20	0.5
12	100	15	20	0.5

Total height of the model is 1000m. Two models are built with element height of 20 m and 50 m, and each model has two different shear wave velocities (100 m/s and 1000 m/s). Density is set to 2000 kg/m³, and Poisson's ratio is set to 0.3, for all test models. Various cases are set and tested as shown in table 3.3. Both 8 node and 27 node brick elements are used for all models. Thus, total 24 parametric study cases are inspected. Linear elastic elements are used for all analyses. All analyses are performed in time domain with Newmark dynamic integrator without any numerical damping ($\gamma = 0.5$, and $\beta = 0.25$, no numerical damping, unconditionally stable).

Ormsby wavelet (Ryan, 1994) is used as an input motion and imposed at the bottom of the model. Ormsby wavelet features a controllable flat frequency content with formulation shown in equation 3.29.

$$\begin{aligned}
 f(t) = & A \left(\frac{\pi f_4^2}{f_4 - f_3} \text{sinc}(\pi f_4(t - t_s))^2 - \frac{\pi f_3^2}{f_4 - f_3} \text{sinc}(\pi f_3(t - t_s))^2 \right) \\
 - & \left(\frac{\pi f_2^2}{f_2 - f_1} \text{sinc}(\pi f_2(t - t_s))^2 - \frac{\pi f_1^2}{f_2 - f_1} \text{sinc}(\pi f_1(t - t_s))^2 \right) \quad (3.29)
 \end{aligned}$$

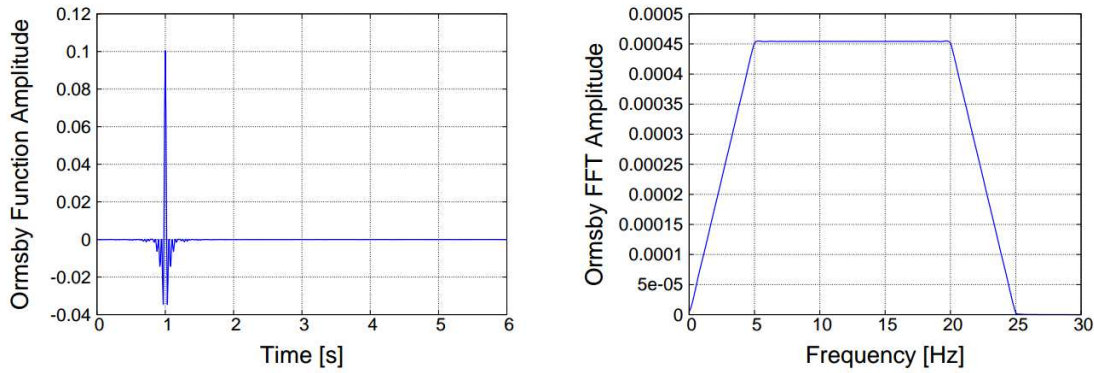


Figure 3.11: Ormsby wavelet in time and frequency domain with flat frequency content from 5 Hz to 20 Hz.

where f_1 and f_2 define the lower range frequency band, f_3 and f_4 define the higher range frequency band, A is the amplitude of the function, and t_s is the time that maximum amplitude is happening, and $sinc(x) = \sin(x)/x$. Figure 3.11 shows an example of Ormsby wavelet with flat frequency content from 5 Hz to 20 Hz.

For this example, cutoff frequencies of Ormsby wavelets are set as 3, 8, and 15 Hz (table 3.3). Figure 3.12 shows number of nodes per wavelength along frequencies and figure 3.13 – 3.15 show comparison of analysis results. As shown in figure 3.13, case 1 and 7 (analysis using Ormsby wavelet with 3 Hz cutoff frequency) predict exactly identical results to the analytic solution in both time and frequency domain. Since, number of nodes per wavelength for both cases are over 10 (see figure 3.12(a) and table 3.3, all cases under 3 Hz shows more than 10 nodes per wavelength), those exact results are expected.

Increasing cutoff frequency from 3 Hz to 8 Hz induces numerical errors as shown in figure 3.14. In frequency domain, both 10 m and 20 m element height model with 27 node brick element predict exactly same results with the analytic one. However, in time domain, asymmetric shape of time history displacements are observed. Observations from top of 8 node brick element models show more numerical error in both time and frequency domain due to the decreasing number of nodes per wavelength (figure 3.12). Figure 3.15 shows analysis results with 15 Hz cutoff frequency. Results from 27 node brick elements are almost same in frequency domain but asymmetric shapes are also observed in time domain. Decreasing amplitudes in frequency domain along increasing frequencies are observed from 8 node brick element cases.

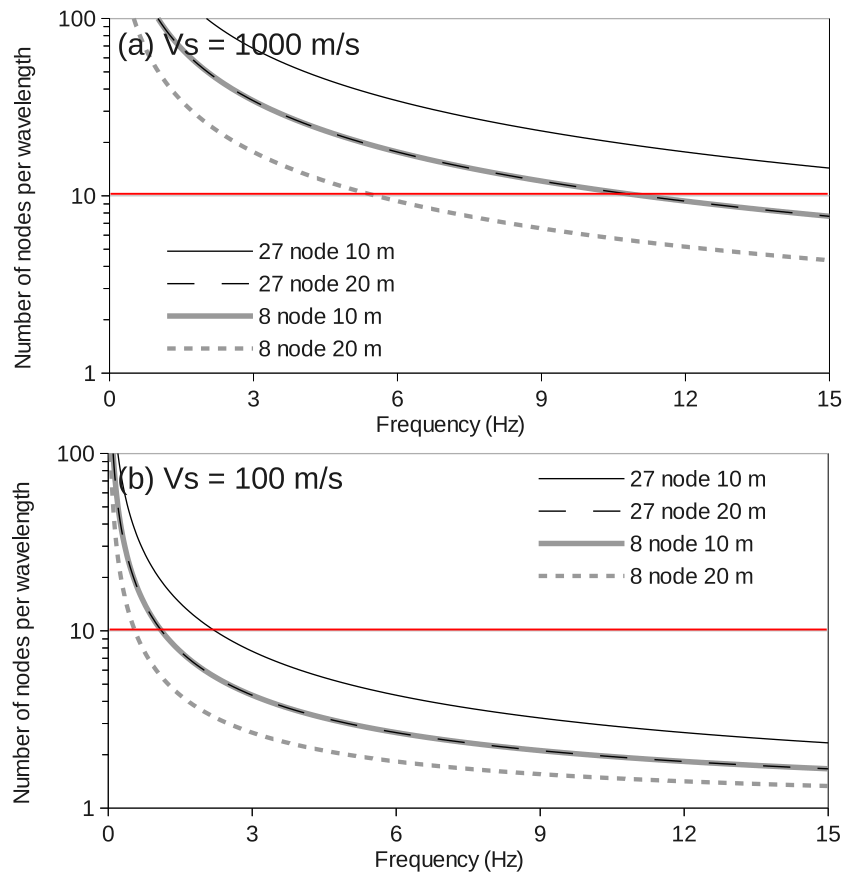


Figure 3.12: Number of nodes per wavelength along frequencies, and element sizes (a) $V_s = 1000$ m/s (b) $V_s = 100$ m/s.

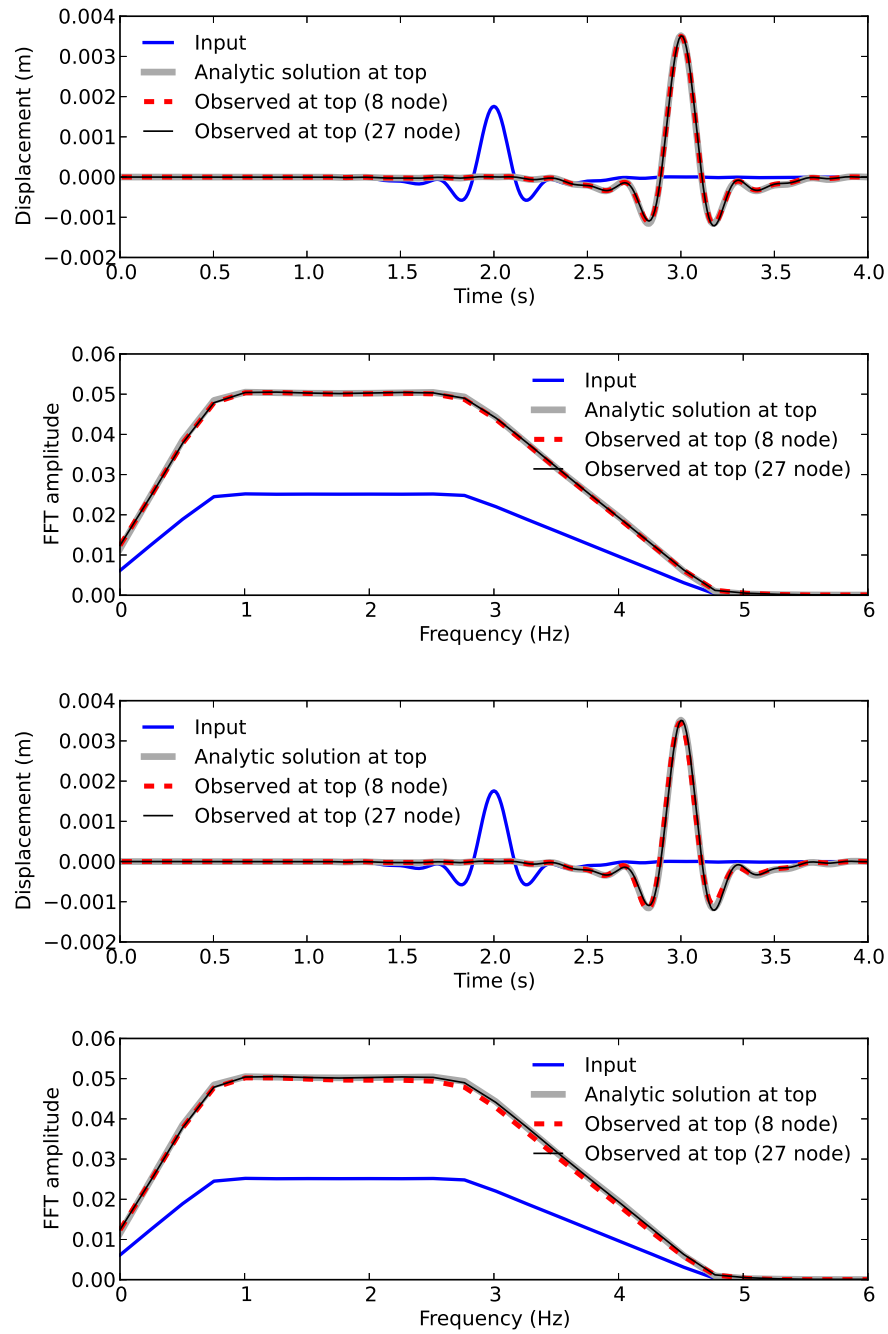


Figure 3.13: Comparison between (a) case 1 (top, $V_s = 1000$ m/s, 3 Hz, element size = 10m) and (b) case 7 (bottom, $V_s = 1000$ m/s, 3 Hz, element size = 20m)

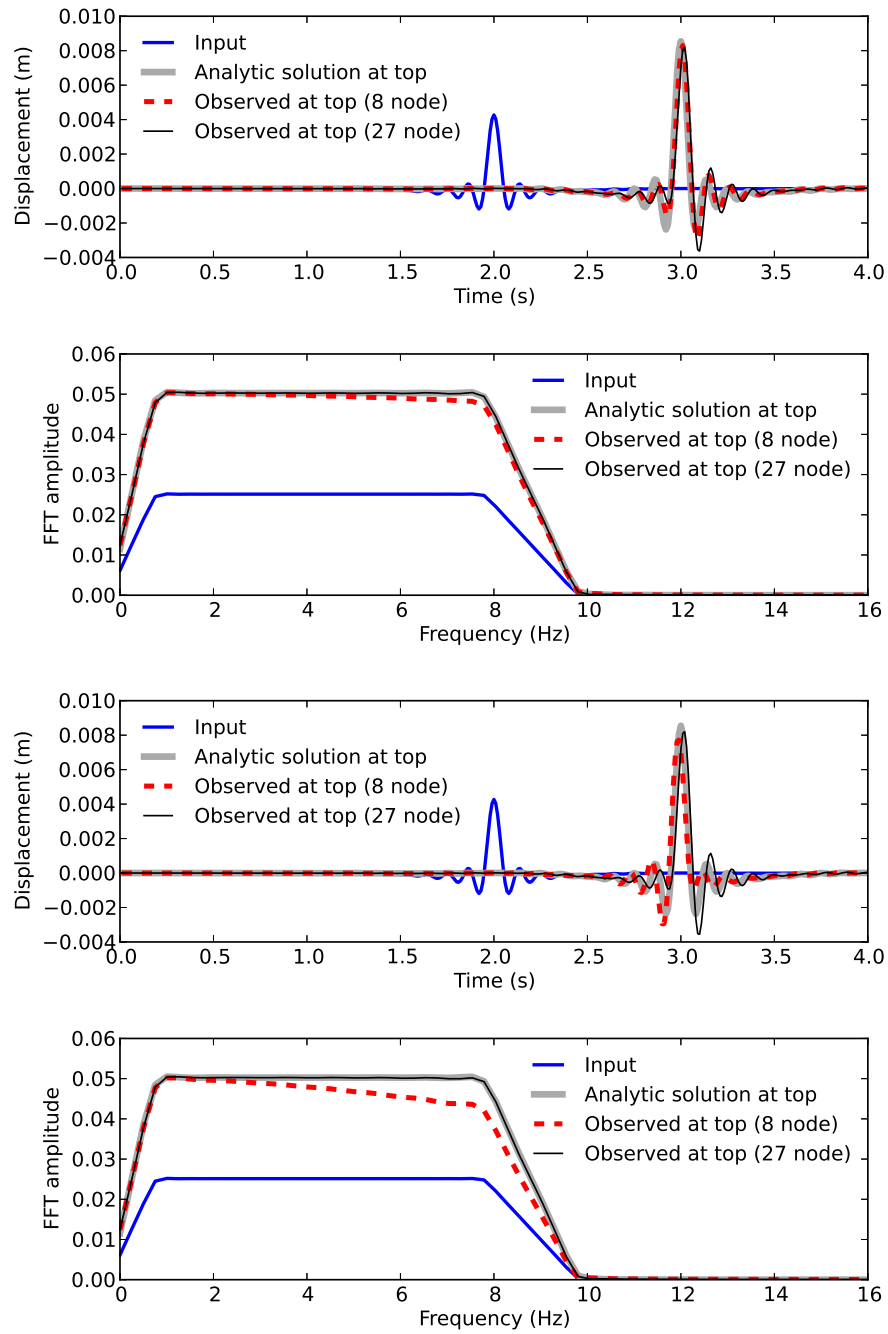


Figure 3.14: Comparison between (a) case 2 (top, $V_s = 1000$ m/s, 8 Hz, element size = 10m) and (b) case 8 (bottom, $V_s = 1000$ m/s, 8 Hz, element size = 20m)

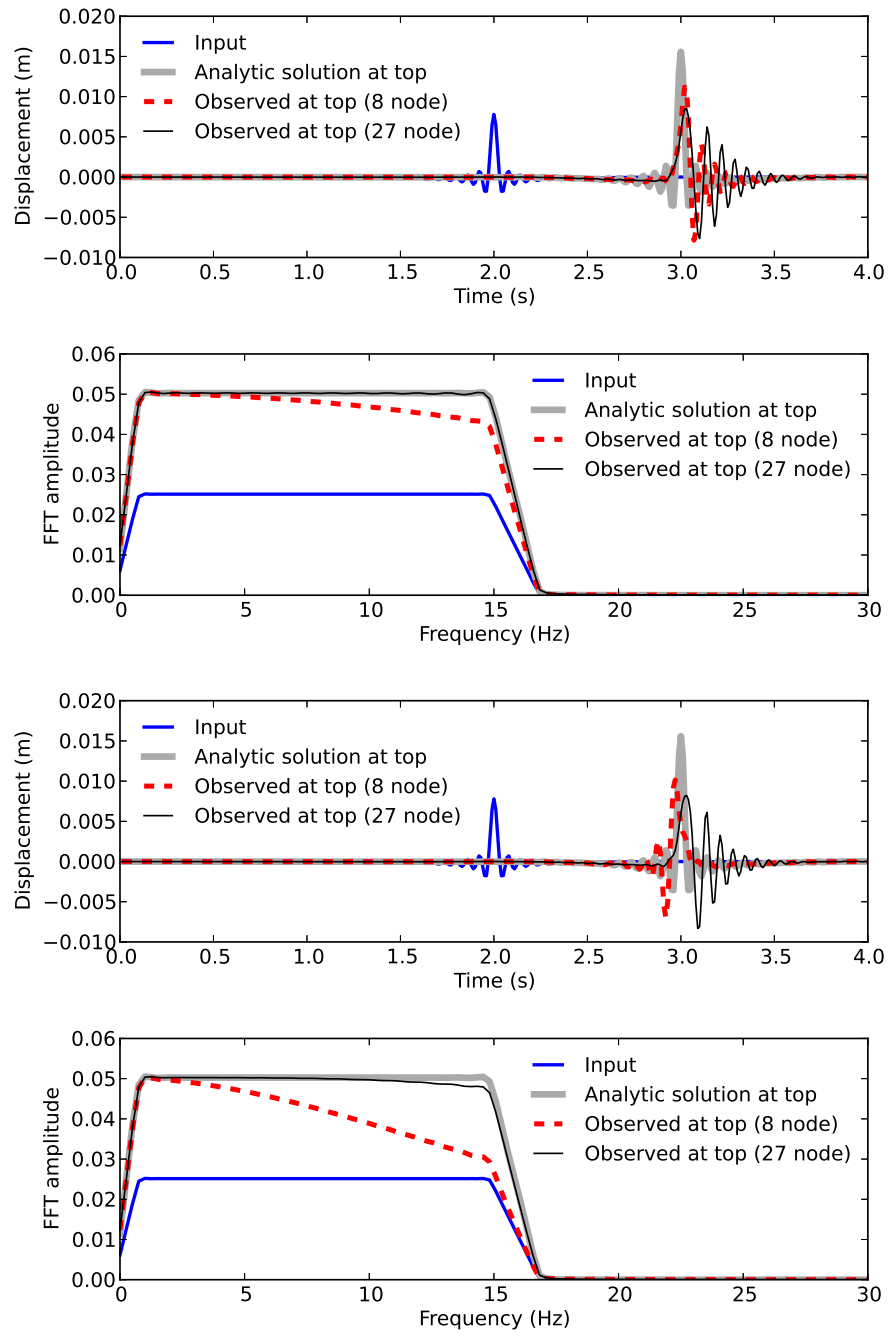


Figure 3.15: Comparison between (a) case 3 (top, $V_s = 1000$ m/s, 15 Hz, element size = 10m) and (b) case 9 (bottom, $V_s = 1000$ m/s, 15 Hz, element size = 20m)

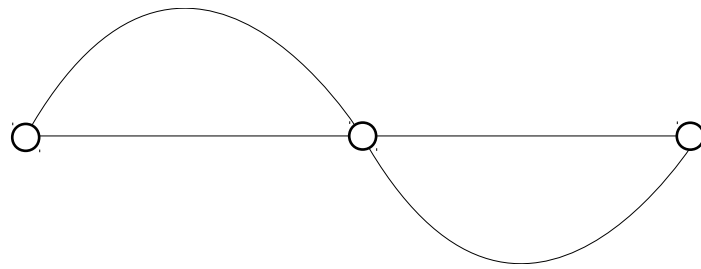


Figure 3.16: Schematic cartoon to show that nodes can behave like frequency contents filter

Chapter 4

Task 4.2: Spatially Variable Ground Motions

4.1 Summary of Findings for Task 4.2

The main findings are:

- Models used for Spatially Variable Ground Motions (SVGM) heavily rely on the ergodic assumption. This assumption states that for a process that is observed and modeled (in our case seismic motions in general and lack of correlation between seismic motions at points at some distance) will feature the same system states if averaged over time and averaged over space. This really means that SVGM models are developed using data from (very few) location (Pinyon Flats, Lotung and perhaps few others) and that those models represent behavior at those specific locations, averaged over time. Those models, developed by considering behavior over time at certain locations, are then used for other spatial locations and at other times. The main problem, of course is that SVGM are to a large extent a function of seismic source(s) mechanisms, path(s) and near field geology of the location where they are measured. Those SVGM are then used at different locations, with probably (very likely) different seismic source mechanisms, different paths and different near field geology.
- In addition to the above argument, it is important to note that SVGM are a results of a

statistical modeling, which means that there are a large number of potential SVGGM that can be produced from each model. It is only right to use a statistically significant number of SVGGMs in any analysis. Results obtained from such (statistically significant number of) analysis would have to be (statistically) processed and understanding of SVGGM effects on SSI (and/or SSSI) behavior understood. Choosing just few SVGGM and analyzing an SSI (or SSSI) system with those does not guaranty that some SVGGMs, that might have detrimental or beneficial effects on SSI, will be accounted for. In fact, since the main goal of any advanced analysis for NPPs is to assess risk of unwanted performance, it might be advisable to choose SVGGMs from (a statistically significant number of) developed SVGGMs those that have detrimental effects on seismic behavior of NPPs,

- For a case of multiple NPPs on same soil/rock in foundations, the SVGGMs need to be applied either to a separate models of those NPPs (if structure-soil-structure interaction (SSSI) is not taken into account) or to a larger, double NPP model. This same rule will apply if two (or more) NPPs are founded on different soils.
- Developed SVGGM methodology and implementation (programs) is flexible and can be used with any input motions (accelerations and displacements defined for nodes of the DRM box) that is obtained using large scale finite element models, analytic solutions, Green's function solutions, etc.
- It is important to note that SVGGM developed motions are applied to nodes of the DRM box and not at the base of the NPP foundation (as is usually done when no SSI is performed or if methods other than DRM are used for inputting seismic motions). The SVGGM applies to the DRM box, and then, any additional sources of SVGGM from within a DRM box will contribute to the SVGGM. There is an important difference in how SVGGM will affect the foundation of an NPP. In a traditional method, the SVGGM are applied at the base of the foundation, and this will lead to averaging of SVGGMs if the foundation concrete is stiffer than sub-base soil/rock. This averaging will reduce effects of SVGGM. If the base is as stiff as foundation concrete (where concrete has a shear wave velocity of $v_s \approx 2200 - 2500\text{m/s}$) than the effects of averaging are not pronounced. In method that we developed, soil/rock structure system is treated as one system and the SVGGMs are applied on the boundary of

that system. As such, there is no averaging of SVGMs, they are fully taken into account for any combination of stiffness of foundation concrete and the sub-base soil/rock.

4.2 Methodology

4.2.1 Incoherence, Sources

This section overviews sources of incoherence.

Seismic motion incoherence (as it is called for frequency domain analysis, for time domain analysis it is called lack of correlation) is a phenomena that results in spatial variability of ground motions over small distances. Significant work has been done in researching seismic motion incoherence over the last few decades (Abrahamson et al., 1991; Roblee et al., 1996; Abrahamson, 1992a, 2005, 1992b; Zerva and Zervas, 2002; Liao and Zerva, 2006; Zerva, 2009)

The main sources of lack of spatial correlation (Zerva, 2009) are

- Attenuation effects, are responsible for change in amplitude and phase of seismic motions due to the distance between observation points and losses (damping, energy dissipation) that seismic wave experiences along that distance. This is a significant source of lack of correlation for long structures (bridges), however for NPPSSS it is not of much significance.
- Wave passage effects, contribute to lack of correlation due to difference in recorded wave field at two location points as the (surface) wave travels, propagates from first to second point.
- Scattering effects, are responsible to lack of correlation by creating a scattered wave field. Scattering is due to (unknown or not known enough) subsurface geologic features that contribute to modification of wave field.
- Extended source effects contribute to lack of correlation by creating a complex wave source field, as the fault ruptures, rupture propagates and generate seismic sources along the fault. Seismic energy is thus emitted from different points (along the rupturing fault) and will have different travel path and timing as it makes it observation points.

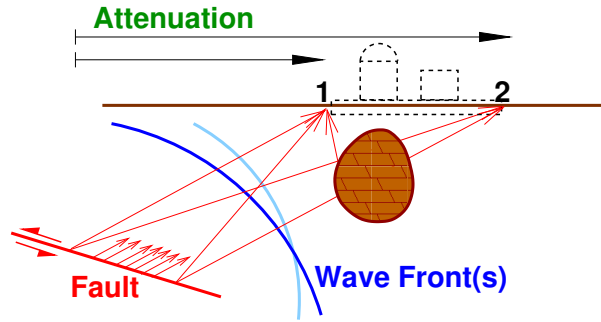


Figure 4.1: Four main sources contributing to the lack of correlation of seismic waves as measured at two observation points.

Figure 4.1 shows an illustration of main sources of lack of correlation.

It is important to note that SVGGM developed in this report does take into account wave passage effects (effectively removing them from SVGGM). This is very important if ground motions (seed ground motions used as a basis for development of SVGGM) are developed as full 3D, inclined seismic motions, as they will be for this effort.

4.2.2 Introduction to Modeling

Early studies concluded that the correlation of motions increases as the separation distance between observation points decreases. In addition to that, correlation increased for decrease in frequency of observed motions. Most theoretical and empirical studies of spatially variable ground motions (SVGGM) have focused on the stochastic and deterministic Fourier phase variability expressed in the form of "lagged coherency" and apparent shear wave propagation velocity, respectively. The mathematical definition of coherency (denoted γ) is given below in equation:

$$\gamma_{jk}(f) = \frac{S_{jk}(f)}{(S_{jj}(f)S_{kk}(f))^{1/2}} \quad (4.1)$$

Coherency is a dimensionless complex-valued number that represents variations in Fourier phase between two signals. Perfectly coherent signals have identical phase angles and a coherency of unity. Lagged coherency, is the amplitude of coherency, and represents the contributions of stochastic processes only (no wave passage). Wave passage effects are typically expressed in the form of an apparent wave propagation velocity.

Lagged coherency does not remove a common wave velocity over all frequencies. Alternatively, plane wave coherency is defined as the real part of complex coherency after removing single plane-wave velocity for all frequencies. Recent simulation methods of SVGM prefer the use of plane-wave coherency as it can be paired with a consistent wave velocity. An additional benefit is that plane-wave coherency captures random variations in the plane-wave while lagged coherency does not. Zerva (2009) has called the variations 'arrival time perturbations'.

Most often, γ is related to the dimensionless ratio of station separation distance ξ to wavelength λ . The functional form most often utilized is exponential (Loh and Yeh, 1988; Oliveira et al., 1991; Harichandran and Vanmarcke, 1986). The second type of functional form relates γ to frequency and ξ independently, without assuming they are related through wavelength. This formulation was motivated by the study of ground motion array data from Lotung, Taiwan (SMART-1 and Large Scale Seismic Test, LSST, arrays), from which Abrahamson (1985, 1992a) found γ at short distances ($\xi < 200\text{m}$) to not be dependent on wavelength. Wavelength-dependence was found at larger distances ($\xi = 400$ to 1000m). Since our study focuses on the SVGM effects over the lateral dimensions of typical structures (e.g., $< 200\text{m}$) we propose the use of non-wavelength dependent models developed by Abrahamson (1992a, 2007); Ancheta (2010).

Moreover, there is a strong probabilistic nature of this phenomena, as significant uncertainty is present in relation to all four sources of lack of correlation, mentioned above. A number of excellent references are available on the subject of incoherent (or lacking correlation) seismic motions (Abrahamson et al., 1991; Roblee et al., 1996; Abrahamson, 1992a, 2005, 1992b; Zerva and Zervas, 2002; Liao and Zerva, 2006; Zerva, 2009)

It is very important to note that all current models for modeling incoherent seismic motions make an ergodic assumption. That is all the models assume that a variability of seismic motions at a single site – source combination will be the same as variability in the ground motions from a data set that was collected over different site and source locations (Walling, 2009). Unfortunately, there does not exist a large enough data set for for example east North American seismic events that can be used to develop incoherence models. Rather, there are models that are used to model possible incoherent behavior for east North American seismic wave propagation.

4.2.3 Incorporate of Incoherence (Lack of Correlation) into Simulated Motions

In addition to (partially) incoherent motions developed using layered half space simulations, an additional (different) set of incoherent motions can be developed in order to test the effects incoherence has on NPP response. In order to introduce appropriate amount of variability over the bandwidth due to incoherence effects, each point may be used as a seed motion to generate a new motion across the grid at a separation distance of 200 meters. In other words point 1 is modified to generate a ground motion at point 2 and vice versa. Alternatively, a grid of ground motions may be generated. The method of introducing incoherence effects is called Frequency Dependent Windowing (FDW) (Ancheta et al., 2012). The method is a non-stationary simulation routine that utilizes a modified short-time Fourier transform (MSTF) for which spectral modifications are made consistent with a selected SVGGM models. The MSTF routine allows the preservation of the non-stationary properties of the motion and incorporation of time-varying non-linear spectral modifications. A simplified outline of the algorithm is summarized below:

1. The seed time series is split into short time segments.
2. A discrete Fourier transform (DFT) is applied to the segments.
3. Fourier amplitudes and phase angles at each frequency within a desired frequency range (dependent on segment length) are modified consistent to a coherency (phase) or standard deviation function (amplitude) for each segment (Ancheta, 2010).
4. The new set of Fourier amplitude and phase angles are combined and transformed into the time domain with an inverse Fourier transform (IFT).
5. The modified short time segments are recombined to form a modified time series.
6. Steps 1-5 are performed multiple times for multiple segment lengths, with each segment length having a specified frequency range over which modifications are made. Hence, multiple modified time series are created. Segment lengths and corresponding frequency limits used are shown in Table 4.1.

7. The multiple modified time series are match-filtered (i.e., band-pass filtered with the limits of the pass-band matching the band of the modification) to combine the modified frequency bands in the frequency domain.
8. The non-overlapping frequency bands are inverted with an IFT to create the final broadband modified time series.

An additional benefit of using the FDW routine is the ability to incorporate Fourier amplitude modifications, as there is a greater control of the leakage effect when performing steps 4 and 5.

Table 4.1: Segment duration (L) and frequency bands (b) used in the FDW routine. T is the duration of the seed series.

Segment duration, L_i [sec]	Frequency limits, b_i [Hz]
1.28	2-Nyquist
2.56	1-2
5.12	0.5-1
10.24	0.25-0.5
20.48	0.12-0.25
T	0-0.12

4.2.4 Description of Selected Incoherence Models

Synthetic models created by analytic solution for layered half space, with different profiles but similar source can be used as seed motions for incoherence motion development.

Separate coherency and random Fourier amplitude models are selected for soil sites. In this case, a plane wave coherency (γ_{pw}) and $\sigma_{\Delta A}$ developed by Abrahamson (2007) from the Pinyon Flat array recordings located in California can be selected. These models are shown in equations 4.2 and 4.3 and Table 4.2.

$$\gamma_{pw}(f, \xi) = \left[1 + \left(\frac{f \tanh(a_3 \xi)}{a_1 f_c(\xi)} \right)^{n1(\xi)} \right]^{-1/2} \left[1 + \left(\frac{f \tanh(a_3 \xi)}{a_2} \right)^{n2} \right]^{-1/2} \quad (4.2)$$

Table 4.2: Plane-wave coherency model coefficients for the horizontal component.

Coefficient name	Horizontal coefficient value
a_1	1.0
a_2	40
a_3	0.4
$n_1(\xi)$	$3.80 - 0.040 \ln(\xi + 1) + 0.0105 [\ln(\xi + 1) - 3.6]^2$
n_2	16.4
$f_c(\xi)$	$27.9 - 4.82 \ln(\xi + 1) + 1.24 [\ln(\xi + 1) - 3.6]^2$

$$\sigma_{\Delta A}(f, \xi) = 0.79(1 - e^{-0.45 - 0.0017\xi}f) \quad (4.3)$$

For soil cases, a plane wave coherency developed by Abrahamson (2005) and $\sigma_{\Delta A}$ developed by Ancheta (2010) from the Lotung LSST (Large Scale Seismic Test) and BVDA (Borrego Valley Differential Array) recordings located in Taiwan and California, respectively, can be selected. The models are shown in equations 4.4 and 4.5.

$$\tanh^{-1} |\gamma(f, \xi)| = (3.79 - 0.499(\ln \xi)) \exp((-0.115 - 0.0084\xi)f) + \frac{1}{3}(\xi)f^{-0.878(\xi)} + 0.35 \quad (4.4)$$

$$\sigma_{\Delta A}(f, \xi) = (1 - e^{-0.1005 - 0.0025\xi}f) \quad (4.5)$$

Currently, no random Fourier amplitude models exist for the vertical component. Therefore, only the Fourier phase will be modified for the vertical component.

4.2.5 Range of Incoherence Model Applicability

Based on a report by Abrahamson (2007) the incoherence models developed from the Pinyon Flat array appears to be applicable to separation distances of 5 to 150 meters and a frequency range of from 5 to 40 Hz. Since the model is developed from Pinyon Flat recordings alone, it is somewhat uncertain how well this model fits similar rock site array recordings or possible future array recordings located in the eastern North America region.

The incoherence models developed by Ancheta (2010) are a slight modification of incoherence models developed by Abrahamson (1992a) and are applicable to separation distances of 6 to 160 meters and frequencies greater than 1 Hz.

Both models have been extrapolated to 200 meters for the process of including incoherence using the FDW routine. It is also important to note that different point separations can be modeled too.

4.3 Work Performed, Subtasks

4.3.1 Empirical SVGM models only for surface motions.

Empirical SVGM models are developed for surface motions only. This is based on a fact that a vast majority of measured motions are surface motions, and that those motions were used for SVGM model developments. This surface origin and availability of SVGM models, creates a difficulty for seismic motion input using Domain Reduction Method (DRM). For DRM, motions are needed at a number of location beneath the surface (at all nodes of the DRM box). Solution developed here creates SVGM for each level of DRM nodes under the surface. With this solution, each level of DRM nodes is treated as a separate SVGM plane. Two approaches were considered in developing these SVGM for each level:

- Un-correlated SVGM between each level where each level of DRM nodes is treated as an independent SVGM plane, and the SVGM are therefor developed using SVGM model but without any correlation to other nearby SVGM levels. This assumption of lack of correlation between DRM nodes in vertical direction is based on lack of vertical SVGM data. In addition, treating each DRM node plane as a separate SVGM plane will introduce higher frequencies into the DRM box, based on a fact that these SVGM might be quite different for a nearby vertically separated nodes. However, those higher frequency motions will naturally be damped out by the nonlinear material within a DRM box, and by the numerical damping of higher frequencies within the model. Such numerical damping of higher frequencies is always necessary as discretization of continuum into a finite element mesh introduces additional (un-physical) higher frequencies into the FEM model. These new frequencies

from difference in motions at SVGM layers will correspond to a discretization introduced higher frequencies and will thus be filtered out.

- Correlated SVGM between each level is a simpler approach whereas each level of DRM nodes receives the same SVGM motions. This approach is based on a fact that, in addition to the lack of data about SVGM in vertical direction, separation distances in vertical direction are smaller compared to the horizontal separation distances. As such, and such smaller distances, the SVGM become more and more correlated and as such are treated as fully correlated (only in vertical direction!).

4.3.2 Spatially Variable Ground Motions Development

This description relies in part on material developed by Jeremić et al. (2011).

Introduction.

Given Time Series. A variable (depending on size of the DRM grid) set of 3-component (H1,H2, and V) synthetic time series are used as seed motions to generate a set of spatially variable ground motions. This set of test locations is used as an example application of the broadband simulation methodology. Since the input format for DRM is used as input to the 'FDW2D.m' routine the format of the initial time series file is described.

Approach. Ground motion simulations (point source or finite fault) can create a 3 dimensional representation of the 3-component wave-field. In our case this is created for the the DRM box with a set of 3-component motions. Additionally, current limitations within the fault source assumptions and the medium that the simulated waves propagate through, only a narrow band of energy (long period/low frequency) can be reliably simulated. A recent attempt by Walling (2009) to reproduce the high frequency energy (dominated by stochastic processes) proposed a randomized medium to induce a scattering effect to match an incoherence function. Abrahamson (1985) proposed and Ancheta et al. (2013) developed a method for generating synthetic broadband strong motion seismograms. The method uses the ground motion simulations as a

starting set of Fourier amplitudes and phases at each location and an energy randomization process called Frequency Dependent Windowing is used to conserve the low frequency (coherent) energy and resample the high frequency (random) energy consistent to a set of SVGGM functions. The SVGGM functions are a sigma amplitude and plane-wave coherency model representing the statistics of the random Fourier amplitudes and phases respectively. A definition of plane-wave coherency and sigma amplitude may be found in Abrahamson (1992a).

A 2 dimensional wave-field can be developed as proposed by Abrahamson (1993) by realizing that all three spatial axes (main, radial horizontal direction, along the principal direction of wave propagation motions, in our case X, transverse horizontal direction, in our case Y, and the vertical direction) do exhibit lack of correlation (incoherence). This existence of three spatial directions of lack of correlation requires existence of data and models for all three directions. Abrahamson (1992a) investigated incoherence of a large set of 3-component motions recorded by the Large Scale Seismic Tests (LSST) array in Taiwan. Abrahamson (1992a) concluded that there was little difference in the radial and transverse lagged coherency computed from the LSST array selected events. Therefore, the horizontal coherency models by Abrahamson (1992a) and subsequent models (Abrahamson, 2005, 2007) assumed the horizontal coherency model may apply to any azimuth. Coherency models using the vertical component of array data are independently developed from the horizontal.

Currently, there are no studies of coherency effects with depth (i.e. shallow site response domain). Therefore, it is proposed here to utilize the simulation method developed by Ancheta et al. (2013) and the incoherence functions for the horizontal and vertical directions developed for a hard rock site by Abrahamson (2005) to create a full 3-D set of incoherent strong motions. We propose to create a 2-D set of incoherent motions at each elevation of the DRM simulated set of motions independently assuming that the coherency functions may apply at any depth within the near surface domain ($j \leq 100$ m). Therefore, by randomizing the energy at each depth full 3-D synthetic broadband strong motion seismograms are created.

FDW methodology. Spatially variable ground motions (SVGGM) were simulated using a code developed by Dr. Ancheta that implemented a simulation method presented by Ancheta et al. (2013). It is an updated version of the methodology proposed by Abrahamson (1992b). In short,

a seed ground motion is modified by adding a random phase and amplitude at each frequency as determined by the input a coherency and sigma amplitude model. Additionally, the set of components are selected for all locations simultaneously where, for example, the coherency between the seed-to-simulation and simulation-to-simulation matches the target coherency function. Additional details of the methodology can be found in Ancheta et al. (2013).

SVGM Functions. Selected SVGM functions are required for the horizontal and vertical components of the Fourier phases and amplitudes. We intend to rely on empirically generated SVGM functions, as the underlying physical processes are not well understood. Additionally, the following limitations are imposed while selecting the desired SVGM functions:

1. The SVGM functions must be derived from either soil or rock arrays but not a mixture.
2. The SVGM functions must be based on a large set of input motions from events with various apparent wave propagation azimuths.
3. The SVGM functions must be applicable to the desired simulation extent.
4. The stochastic Fourier phase model or coherency function must be a plane-wave coherency, γ_{pw} , function to incorporate stochastic phase and arrival time perturbations.
5. The stochastic Fourier amplitude model must be able predict the median sigma of the random amplitude component.
6. The phase and amplitude model must have a complementary horizontal and vertical model. This internal consistency requirement is desirable due to the large possibilities within the data processing procedures used in the model development. Additionally, the phase and amplitude model should come from the similar, if not same, set of ground motion recordings. This internal consistency requirement is more important for rock sites as the variability of incoherence observed at rock arrays is greater than soil arrays.

Given the above limitations we have selected the following SVGM functions for the soil and rock profiles in Tables 4.3 and 4.4. A summary of the entire set of currently available SVGM functions has not been compiled nor reviewed within this project. However, the selected SVGM

functions satisfy the above limitations or are the only available model for the component and soil case. The vertical sigma amplitude model is empty as there are no available functions in the literature.

Table 4.3: Selected SVGM functions for rock sites.

	Plane-wave coherency	Sigma amplitude
Horizontal	Abrahamson (2007)	Abrahamson (2005)
Vertical	Abrahamson (2007)	

Table 4.4: Selected SVGM functions for soil sites.

	Plane-wave coherency	Sigma amplitude
Horizontal	Abrahamson (1993)	Ancheta et al. (2012)
Vertical	Abrahamson (1993)	

The plane-wave coherency model presented by Abrahamson (2007) using the Pinyon Flat array data was selected for rock conditions. A set of 78 events noted from small magnitude events was used to develop the model and the model is applicable for a frequency range of 5 – 40Hz and a separation distance up to 150m. The function was selected, as it is currently the only 'rock' plane-wave coherency model in the literature and there are a significant number of station pairs over the applicable separation distance bins. Two plane-wave coherency models were used for the horizontal and vertical components have the same form (Eq. []) but different coefficients shown below:

$$\gamma_{pw}(f, \xi) = \left[1 + \left(\frac{f \tanh(a_3 \xi)}{a_1 f_c(\xi)} \right)^{n1(\xi)} \right]^{-1/2} \left[1 + \left(\frac{f \tanh(a_3 \xi)}{a_2} \right)^{n2} \right]^{-1/2} \quad (4.6)$$

The model coefficients for the horizontal case is given in Table 4.5. The model for vertical case is similarly given in Table 4.6.

The sigma amplitude model for the Pinyon Flat array data from Abrahamson (2005) was selected for rock conditions. A set of 6 events with a magnitude range of 2.0-3.6 was used

Table 4.5: Plane-wave coherency model coefficients for the horizontal component.

Coefficient name	Horizontal coefficient value
a_1	1.0
a_2	40
a_3	0.4
$n_1(\xi)$	$3.80 - 0.040 \ln(\xi + 1) + 0.0105 [\ln(\xi + 1) - 3.6]^2$
n_2	16.4
$f_c(\xi)$	$27.9 - 4.82 \ln(\xi + 1) + 1.24 [\ln(\xi + 1) - 3.6]^2$

Table 4.6: Plane-wave coherency model coefficients for the vertical component.

Coefficient name	Horizontal coefficient value
a_1	1.0
a_2	200
a_3	0.4
$n_1(\xi)$	$2.03 - 0.40 \ln(\xi + 1) + 0.078 [\ln(\xi + 1) - 3.6]^2$
n_2	16.4
$f_c(\xi)$	$29.2 - 5.2 \ln(\xi + 1) + 1.45 [\ln(\xi + 1) - 3.6]^2$

to develop the model. The applicable for a frequency and separation distance range is not explicitly stated but the maximum separation distance used was 348m and the function tends to asymptotically approach a noise floor at large frequencies ($\approx 50\text{Hz}$). To be consistent with the plane-wave coherency model we suggest that this model be applicable to similar frequency and separation distances as the Abrahamson (2007) model. The function was selected, because it is sigma amplitude model that used similar array data as the selected plane-wave coherency model. Unfortunately, only a horizontal sigma amplitude model is provided as

$$\sigma = A (1 - e^{Bf+Cf}) \quad (4.7)$$

where the model coefficients are $A = 0.79$, $B = -0.45$, and $C = -0.0017$.

The plane-wave coherency model from Abrahamson (1993) developed from LSST (Large Scale Seismic Test) array data was selected soil conditions. A set of events with a large magnitude range was used to develop the model and the model is applicable for appropriate frequency range and a separation distance up to 85 m. The function was selected, because the LSST array has recorded a large number of events with the largest magnitude range and it is the most recently derived plane wave coherency model from the LSST data set from Abrahamson (1992a) and Abrahamson (1993). Two plane-wave coherency models were used for the horizontal and vertical components:

$$\gamma_{pw}(f, \xi) = \tanh \left[\frac{C_3(\xi)}{1 + C_4(\xi)f + C_7(\xi)f^2} + (4.8 - C_3(\xi)) \exp(C_6(\xi)f + 0.35) \right] \left[\frac{1}{1 + \left(\frac{f}{C_8(\xi)}\right)^6} \right] \quad (4.8)$$

where

$$C_3(\xi) = \frac{3.95}{1 + 0.0077\xi + 0.000023\xi^2} + 0.85 \ln -0.00013\xi$$

$$C_4(\xi) = \frac{0.4 \left(1 - \frac{1}{1+(\xi/5)^3}\right)}{(1 + (\xi/190)^8) (1 + (\xi/180)^3)}$$

$$C_6(\xi) = 3(\exp(\xi/20) - 1) - 0.0018\xi$$

$$C_7(\xi) = -0.598 + 0.106 \ln(\xi + 325) - 0.0151 \exp(-0.6\xi)$$

$$C_8(\xi) = \exp(8.54 - 1.07 \ln(\xi + 200)) + 100 \exp(-\xi)$$

Vertical plane-wave coherency model is given as

$$\gamma_{pw}(f, \xi) = \tanh \left[\frac{C_3(\xi)}{1 + C_4(\xi)f + C_7(\xi)f^2} + (4.65 - C_3(\xi)) \exp(C_6(\xi)f + 0.35) \right] \left[\frac{1}{1 + \left(\frac{f}{C_8(\xi)}\right)^6} \right] \quad (4.9)$$

where

$$C_3(\xi) = 3.5 - 0.37 \ln(\xi + 0.04)$$

$$C_4(\xi) = 0.65 \left(1 - \frac{1}{(1 + \xi/4)}\right)$$

$$C_6(\xi) = 3(\exp(-/005\xi) - 1) - 0.0018\xi$$

$$C_7(\xi) = 0$$

$$C_8(\xi) = \exp((5.20 - 0.0634 \ln(\xi + 0.1)))$$

The sigma amplitude model from Ancheta et al. (2012) was selected for soil conditions. A set of 27 events with a magnitude range of 2.5-7.8 was used to develop the model and the model is applicable for a frequency range of 1 – 50Hz and a separation distance up to 160m. The function was selected, because it is sigma amplitude model that used similar array data as the selected plane-wave coherency model. Unfortunately, only a horizontal sigma amplitude model is provided as

$$\sigma = A (1 - e^{Bf+Cf}) \quad (4.10)$$

where the model coefficients are $A = 1$, $B = -0.1005$, and $C = -0.0025$.

Process Assumptions. The assumptions on incoherence with depth, incoherence for the 3-components, and location of the input locations are described and their expected effect on the output are discussed.

Input Parameters. The required and optional input parameters to the program are described in this section along with a description of a script that may be used along with the pre-formatted DRM output.

The required input parameters need for `FDW2D.m` are the set of input time series, the time step, and their relative Cartesian coordinates (x and y). Since the pre-formatted DRM output time series and location files are used as input the formats of the DRM files are used.

The optional input parameters are two flags (`svgm_flag`, `HV_flag`) that will allow the user to select either the soil or rock and horizontal or vertical SVGGM functions. Table 4.7 lists the applicable flag combinations.

Table 4.7: Definition of flag combinations.

	Soil	Rock
Horizontal	<code>svgm_flag = 1, HV_flag = 1</code>	<code>svgm_flag = 2, HV_flag = 1</code>
Vertical	<code>svgm_flag = 1, HV_flag = 2</code>	<code>svgm_flag = 2, HV_flag = 2</code>

Output Formats. The output time series are described along with possible baseline error that may be present. The output time series file is formatted to match the input format and therefore no description is needed. However, the output time series are acceleration at each time step and are not filtered after the Fourier amplitude and phase randomization is complete. Therefore, it may be possible to have output acceleration time series that do not start or end with a near zero displacement. Additionally, the FDW2D.m routine does not de-trend the output and therefore the output time series may not have a mean zero.

4.3.3 Multi axial SVGM models.

Ground motion simulations (point source or finite fault) that will be used in this project (from a project with Drs. Trifunac and Lee) can create a 3D representation of the 3-component wave-field at each location in the soil/rock domain of interest. In our particular case those locations will be within the DRM box. Additionally, current limitations within the fault source assumptions and the medium that the simulated waves propagate through, only a narrow band of energy (long period/low frequency) can be reliably simulated. A recent attempt by Walling (2009) to reproduce the high frequency energy (dominated by stochastic processes) proposed a randomized medium to induce a scattering effect to match an incoherence function. Abrahamson (1985) proposed and Ancheta et al. (2013) developed a method for generating synthetic broadband strong motion seismograms. The method uses the ground motion simulations (that will eventually come from a CNSC project with Drs. Trifunac and Lee) as a starting set of Fourier amplitudes and phases at each location and an energy randomization process called Frequency Dependent Windowing that conserves the low frequency (coherent) energy and re-samples the high frequency (random) energy consistent to a set of SVGM functions. The SVGM functions are a sigma amplitude and plane wave coherency model representing the statistics of the random Fourier amplitudes and phases respectively.

A 2D wave-field can be developed as proposed by Abrahamson (1993) by realizing that all three spatial axes (main, radial horizontal direction, along the principal direction of wave propagation motions, in our case X, transverse horizontal direction, in our case Y, and the vertical direction) do exhibit lack of correlation (incoherence). This existence of three spatial directions

of lack of correlation requires existence of data and models for all three directions. Abrahamson (1992a) investigated incoherence of a large set of 3-component motions recorded by the Large Scale Seismic Tests (LSST) array in Taiwan. Abrahamson (1992a) concluded that there was little difference in the radial and transverse lagged coherency computed from the LSST array selected events. Therefore, the horizontal coherency models by Abrahamson (1992a) and subsequent models Abrahamson (2005) and Abrahamson (2007) assumed the horizontal coherency model may apply to any azimuth. Coherency models using the vertical component of array data are independently developed from the horizontal.

Currently, there are no studies of coherency effects with depth (i.e. shallow site response domain). Therefore, a simulation method developed by Ancheta et al. (2013) is used and the incoherence functions for the horizontal and vertical directions developed for a hard rock site by Abrahamson (2005) to create a full 3D set of incoherent strong motions. A 2D set of incoherent motions is developed at each elevation of the DRM simulated set of motions independently assuming that the coherency functions apply at any depth within the near surface domain (≤ 100 m). Therefore, by randomizing the energy at each depth a full 3D synthetic broadband strong motion seismograms are created. It is worth noting that a recent paper by Konakli et al. (2013) shows that models developed by Abrahamson and the derived models show very good matching (for separations of up to 100m, which is of main interest for our problems) with data from a site from which they were not developed (Parkfield array in California), acting as an independent validation of those models.

Developed methodology is implemented in a separate code that is connected to a analysis system that is being delivered to CNSC in components. This system will be further demonstrated during October 2013 meeting in Ottawa.

4.3.4 SVGM models and ergodic assumption.

As noted in the proposal, the use of SVGM models is based on the ergodic assumption. This assumption allows that statistical data obtained at one (or few) location(s) over a period of time be used for at other locations at certain times. For example, data on SVGM obtained from a Lotung site in Taiwan, over long period of time (dozens of years) is developed into a statistical

model of SVGGM and then used for other locations around the world. This ergodic assumption cannot be proven to be accurate (or to hold) at all, unless more data becomes available. However, ergodic assumption is regularly used for SVGGM models. It is used in our development too.

Very recently, there were a number of smaller and larger earthquakes in the areas with good instrumentation in the form of dense arrays. For example, Parkfield, California measurement experiment has recorder some significant earthquakes in last 10 or so years. It is important that SVGGM models used in our development were developed using data from Lotung and Pinyon Flat measuring stations. Models so developed were recently validated against Parkfield data by Konakli et al. (2013) and showed good matching with our models for nodal separation distances up to 100m. This is one of the first independent validations of family of models developed by Abrahamson and co-workers, that are used in our development as well. This validation gives us new confidence that assumed ergodicity of SVGGM models does hold for all practical purposes of developed SVGGM models.

4.3.5 SVGGM models and multiple NPPs on a same soil.

For multiple NPP models on same soil (for example a model in Figure 3.3.9 on page 28) SVGGM needs to be developed with a new, larger separation distance that covers the new DRM box. This is the only proper method of dealing with SVGGM motions for multiple NPPs (in this case two). Other methodologies, sometimes advocated and used, that are based on considerations of symmetry or anti-symmetry make too many assumptions that reduce the generality and accuracy of obtained results. It is important to note that use of dual NPP models for application of SVGGM, as shown in Figure 3.3.9, is possible if the same type of soil or rock is found in the sub-base of both (or multiple) NPPs. If this is not the case, different approach needs to be used, as discussed below.

4.3.6 SVGGM models and multiple NPPs on a different soil.

For a case of dual (or multiple) NPPs adjacent to each other, but on different soil/rock conditions (say one NPP is founded on soil while the adjacent one is founded on a rock sub-base), a different approach is needed. In this case a model for dual NPP (as shown in Figure 3.3.9) cannot be

used directly as described in the previous paragraph, since this model uses a single set of SVGGM for either soil or rock (soil and rock SVGGM models are different). This issue can be resolved in two ways

- One approach is to still use a dual NPP model, but use different SVGGM functions for two halves of the DRM box. The half of the DRM box that has soil in the foundation get SVGGMs using soil model, while the other half of the DRM box, with rock foundations, will use rock SVGGM motions. This way, both soil and rock SVGGM models will be featured in their appropriate domain of application. The problem with this approach is that near field motions, developed using external programs (for example, one developed by Drs. Trifunac and Lee) are developed for horizontally layered soils/rock profiles, and change of from rock to soil and vice versa can only be in the vertical direction, while in case discussed here this change from rock to soil (or otherwise) is in horizontal direction. Thus the application of this method might be acceptable if differences between stiffness/type of soils and or rock are not too large for adjacent NPPs.
- In the case when differences between soil - rock sub-base material are too large, a different model is advocated. The issue is resolved by modeling dual (or multiple) NPPs using a set of single NPP models (as shown in Figure 3.3.9 on page 27), that are placed adjacent to each other. Each model receives its own set of free field input motions obtained from a auxiliary modeling (for example from a CNSC project with Drs. Trifunac and Lee) and then SVGGM are applied to each of these models separately, given the type of their sub-base conditions (soil or rock). The only issue that needs to be taken into account is the actual influence of one NPP on the other NPP (SSSI). Those influences from one NPP to another NPP (SSSI) can be followed by means of analyzing out of DRM layer motions from both models (portions of those out of DRM motions in the zone facing the other NPP DRM model). It is hypothesized that those inter NPP influences will not be significant (yet they have to be properly analyzed using features of DRM) since NPP models founded on rock will be most likely sending higher frequency motions toward soil founded NPP. This will be similar in the opposite direction, NPP models founded on soil sub-base will be sending low frequency motions toward rock founded NPPs. These inter NPP influences will be small

as motions of non-compatible frequencies will be applied to each domain (high frequency motions from rock sub-base toward soil sub-base, and vice versa, low frequency motions from soil sub-base toward rock sub-base. In both cases, SSSI will be minor if any.

Chapter 5

Task 4.3: Material Nonlinear Response of Soil/Rock, Calibrated from Available Data

5.1 Summary of Findings for Task 4.3

The main findings for task 4.3 are:

- Significant energy dissipation capacity is available in soil and rock adjacent to the foundation, and should be accounted for and used as a mean of reducing seismic energy that goes into the NPP structures, systems and components
- Energy dissipation within soil domain relies on both frictional (displacement proportional) and viscous (velocity proportional) damping mechanisms, with frictional damping (elasto-plasticity) providing the majority of such damping (energy dissipation).
- Soil volume change data, that is often (usually) not available when modulus reduction (G/G_{max}) and damping curves are used, and that affects soil volume changes due to shearing deformation, plays a significant role in seismic wave propagation. Soil volume change due to shearing (for shear wave propagation) will either cause an increase (due to dilatancy) in soil stiffness or a decrease (due to compressibility) in soil stiffness (see

example below).

- Uncertain and spatially variable soil/rock of soil material properties need to be accounted for and at least bounds of behavior established (see data below).
- Elastic-plastic material model that is calibrated from modulus reduction (G/G_{max}) and damping curves, named Pisanò model is developed and can be used within ESSI simulator or modeling soil inelastic response (see detailed description below).

5.2 Methodology

Briefly described here is a methodology developed and used in working on Task 4.3.

5.2.1 Assessment of Soil/Rock Nonlinearities in a Zone Adjacent to NPP Foundation.

It is well known that soils and rock undergo inelastic (nonlinear, elastic-plastic) deformation during loading and unloading cycles. This is particularly true for zones adjacent to NPP foundations. These nonlinearities can be a result of a stiff foundation, with a significant (large, stiff, heavy) structure above it, undergoing a dynamic motions (shear, vertical, rocking, rolling, twisting). It is well known that any material with underlying particulate structure (like soils and rock) will develop nonlinear deformation even under smallest amount of shear (Mindlin and Deresiewicz, 1953). This observation together with a fact that a large, heavy structure (NPP: shield, containment and auxiliary buildings) are undergoing dynamic motions, result in a significant amount of nonlinear deformation developing adjacent to the foundation of an NPP.

While the spatial extent and amounts of such nonlinear behavior will be different on a case by case basis, it is certain that such nonlinear deformation will occur, in soil and in rock. In addition to the fact that soils (always) undergo nonlinear deformations, it is also usually assumed that rock is linear elastic. This is contrary to available evidence (Stavrogin et al., 2001), which shows that rock behaves as nonlinear as any other pressure sensitive material, and that it can produce significant hysteretic loops (energy dissipation).

5.2.2 Assessment of Material Models that can be Calibrated from Available Data.

It is of particular interest to be able to utilize 3D incremental elastic-plastic material models for modeling the nonlinear dynamics of NPPs. This need for utilizing 3D elastic-plastic models comes from a requirement to perform a full 3D elastic-plastic analysis of seismic behavior of NPPs. Developed and used 3D incremental elastic-plastic material models have to be calibrated using data that is usually available at the site during design and construction of an NPP.

For rock modeling, with shear wave velocity available, a linear elastic modeling is usually initially used (Amadei, 1983; Aki and Richards, 2002; Benz and Schwabb, 2008; Jaeger et al., 2007; Zhang, 2005). This is usually a consequence of lack of data on nonlinear behavior of rock at a particular NPP site (although such nonlinearities are known to exist (Stavrogin et al., 2001)). Therefore, as first approximation, a linear elastic model is usually used. Linear elastic model can/should be easily replaced by a nonlinear model, if and when the data about rock nonlinearity becomes available.

The most common soil characterization used in the nuclear power industry is to develop so called G/G_{max} (stiffness degradation) and damping curves for soil and the shear wave velocity profiles for the rock. It is proposed here to use recently developed theory of plasticity with vanishing elastic region and develop full 3D nonlinear dynamic modeling of soil (Pisanò and Jeremić, 2014) from available fields data, given by G/G_{max} and damping curves. It should be noted that development of G/G_{max} and damping curves from fields tests, does introduce an amount of uncertainty in material parameters due to spatial variability, and measuring and transformation error. This uncertainty can be significant, can affect modeling and simulations of soil behavior, and will therefore be addressed in our work using our recently developed methodology (Sett et al., 2011).

Development of elastic-plastic material models from field available data has seen some recent progress, during a short DOE project that Drs. Jeremić and Pisanò were involved with. An initial development, named Pisanò material model (Pisanò and Jeremić, 2014), has been updated, enhanced and improved and is used here. The Pisanò material model is based on incremental elastic-plastic theory. It differs from any other model currently available in that

it features a vanishing (differentially small) elastic region, and a pressure sensitive yield criteria based on Drucker-Prager cone. In addition to that, in conjunction with viscous energy dissipation mechanism, this model can be calibrated, with high fidelity, from available G/G_{max} and damping curves.

It is also very important to note that this material model is a full 3D elastic-plastic material model that uses 1D G/G_{max} and damping curves for calibration, but does produce a full 3D stress-strain relations. This is in contrast to available material models that try to mimic G/G_{max} and damping behavior (in 1D) and that are indeed only defined in 1D, and are then extended to 3D only by using non-rational mechanics tricks that cannot be verified and validated.

5.2.3 Assessment of Contributions to Safety of this type of Nonlinearity.

Nonlinear behavior of soil and rock adjacent to foundations of an NPP can dissipate significant amounts of seismic energy during earthquakes. Energy dissipation capacity of various types of soil and rock will depend on their cyclic (hysteretic) behavior. However, any soil and rock, with its inelastic behavior will contribute to energy dissipation, which will in turn, benefit seismic response. This benefit is simply explained by the fact of an NPP receives a lesser amount of seismic energy as some (most) of that energy is dissipated beneath foundations (Jeremić, 2010). Finite element models that are currently available and running, and that will be available to CNSC, will provide an in depth insight in effects nonlinear behavior of soils has on safety of NPPs.

5.3 Work Performed, Subtasks

5.3.1 Spatial Variability of Soil/Rock Domain.

Variability of material parameters that are used in modeling of soil-structures systems can be significant. This variability needs to be taken into account. A brief overview of documented uncertainties and variability for soil properties is presented below.

Table 5.1 presents tabulated Coefficients of Variation (COV) data for drained friction angle,

ϕ , tangent drained friction angle, $\tan \phi$, undrained shear strength S_u , cohesion, c as well as undrained strength ratio obtained by Jones et al. (2002).

Property (units)	Soil Type	No. of Data Groups	No. of Tests Per Group		Property Value		Property COV (%)		Note
			Range	Mean	Range	Mean	Range	Mean	
$\bar{\phi}$ (°)	Sand	7	29 – 136	62	35 – 41	37.6	5 – 11	9	1
	Clay, silt	12	5 – 51	16	9 – 33	15.3	10 – 56	21	
	Clay, silt	9	*	*	17 – 41	33.3	4 – 12	9	
	*	20	*	*	*	*	*	12.6	4
$\tan \bar{\phi}$	Clay, silt	4	*	*	0.24 – 0.69	0.509	6 – 46	20	1
$\tan \bar{\phi}$	Clay, silt	3	*	*	*	0.615	6 – 46	23	
$\tan \bar{\phi}$	Sand	13	6 – 111	45	0.65 – 0.92	0.744	5 – 14	9	1
	*	7	*	*	*	*	*	11.3	4
$\bar{\phi}$ (°)	Sand	*	*	*	*	*	2 – 5	*	2
ϕ (°)	Gravel	*	*	*	*	*	7	*	3
	Sand	*	*	*	*	*	12	*	
$s_u^{(a)}$ (kPa)	Fine-grained	38	2 – 538	101	6 – 412	100	6 – 56	33	1
$s_u^{(b)}$ (kPa)	Clay, Silt	13	14 – 82	33	15 – 363	276	11 – 49	22	
$s_u^{(c)}$ (kPa)	Clay	10	12 – 86	47	130 – 713	405	18 – 42	32	
$s_u^{(d)}$ (kPa)	Clay	42	24 – 124	48	8 – 638	112	6 – 80	32	
	*	38	*	*	*	*	*	33.8	3
$s_u^{(e)}$ (kPa)	Clay	*	*	*	*	*	5 – 20	*	2
$s_u^{(f)}$ (kPa)	Clay	*	*	*	*	*	10 – 35	*	
$s_u^{(d)}$ (kPa)	Clayey silt	*	*	*	*	*	10 – 30	*	
$c^{(g)}$	*	*	*	*	*	*	40	*	
s_u/σ'_{v0}	Clay	*	*	*	*	*	5 – 15	*	2

Figure 5.1: COV of inherent soil variability for strength parameters as per (Jones et al., 2002) .

Measurement errors are always present during both in-situ and laboratory tests (Baecher and Christian, 2003; Phoon and Kulhawy, 1999a,b). As pointed out by Phoon and Kulhawy (1999a), measurement errors arise from three sources: equipment errors (e.g., inaccuracies of the measuring devices and variations in equipment geometries and systems used for routine testing), procedural-operator errors (e.g., limitations in existing test standards and how these standards are followed by operators), and random testing error (i.e., the remaining scatter in measurements that is not assignable to specific testing parameters and is not caused by inherent variability of soils).

Statistical data on measurements errors is limited in the literature. Table 5.2 provides a summary of total measurement error for different laboratory-measured properties (Phoon and Kulhawy, 1999a).

Table 5.3 presents tabulated data for SPT measured resistance, N , and Table 5.4 presents CPT (tip- and corrected-tip resistance) data (Jones et al., 2002). The reported COVs are larger

Property (units)	Soil Type	No. of Data Groups	No. of Tests Per Group		Property Value		Property COV (%)	
			Range	Mean	Range	Mean	Range	Mean
$s_u^{(a)}$ (kPa)	Clay, silt	11	*	13	7 – 407	125	8 – 38	19
$s_u^{(b)}$ (kPa)	Clay, silt	2	13 – 17	15	108 – 130	119	19 – 20	20
$s_u^{(c)}$ (kPa)	Clay	15	*	*	4 – 123	29	5 – 37	13
$\bar{\phi}^{(a)}$ (°)	Clay, silt	4	9 – 13	10	2 – 27	19.1	7 – 56	24
$\bar{\phi}^{(b)}$ (°)	Clay, silt	5	9 – 13	11	24 – 40	33.3	3 – 29	13
$\bar{\phi}^{(c)}$ (°)	Sand	2	26	26	30 – 35	32.7	13 – 14	14
$\tan \bar{\phi}^{(a)}$ (°)	Clay, silt	6	*	*	*	*	2 – 22	8
$\tan \bar{\phi}^{(b)}$ (°)	Clay	2	*	*	*	*	6 – 22	14
w_n (%)	Fine-grained	3	82 – 88	85	16 – 21	18	6 – 12	8
LL, (%)	Fine-grained	26	41 – 89	64	17 – 113	36	3 – 11	7
PL, (%)	Fine-grained	26	41 – 89	62	12 – 35	21	7 – 18	10
PI, (%)	Fine-grained	10	41 – 89	61	4 – 44	23	5 – 51	24
γ , (kN/m ²)	Fine-grained	3	82 – 88	85	16 – 17	17.0	1 – 2	1

* Not reported.
(a) Triaxial compression test.
(b) Direct shear test.
(c) Laboratory vane shear test.

Figure 5.2: Summary of total measurement error for laboratory-measured properties (Phoon and Kulhawey, 1999a)

in SPT than in CPT tests. In both cases they larger than what is observed for laboratory tests.

Property	Soil Type	No. of Data Groups	No. of Tests Per Group		Property Value		Property COV (%)		Note
			Range	Mean	Range	Mean	Range	Mean	
N	Clay & Sand	*	*	*	10 – 70	*	25 – 50	*	1
N	Sand	22	2 – 300	123	7 – 74	35	19 – 62	54	2
N	Clay Loam	2	2 – 61	32	7 – 63	32	37 – 57	44	
N	*	*	*	*	*	*	26	*	3

Notes:
(1) Phoon and Kulhawey (1996).
(2) Phoon and Kulhawey (1999).
(3) Harr (1987). No comment made on whether measurement variability was included.

Figure 5.3: COV of inherent soil variability for SPT resistance

The measurement of various parameters from a geotechnical test is usually not directly applicable to design. Instead, a transformation model is needed to relate the parameter measurement (for example, SPT N values) to an appropriate design property (for example, a friction angle). Empirical correlations are often obtained from empirical data fitting, and hence they are associated with some uncertainties because of data scatter and inaccuracy of the best fit (e.g., Phoon and Kulhawey (1999b)) Transformation uncertainty arises from a lack of knowledge about the re-

Property (units)	Soil Type	No. of Data Groups	No. of Tests Per Group		Property Value		Property COV (%)		Note
			Range	Mean	Range	Mean	Range	Mean	
q_T (MPa)	Clay	*	*	*	0.5 – 2.5	*	< 20	*	1
	Clay	9	*	*	0.4 – 2.6	1.32	2 – 17	8	2
q_c (MPa)	Clay	*	*	*	0.5 – 2.0	*	20 – 40	*	1
	Sand	*	*	*	0.5 – 30.0	*	20 – 60	*	1
	Sand	57	10 – 2039	115	0.4 – 29.2	4.10	10 – 81	38	2
	Silty Clay	12	30 – 53	43	0.5 – 2.1	1.59	5 – 40	27	2
*	*	*	*	*	*	37	*	3	

* Not reported
Notes:
(1) Phoon and Kulhawy (1996).
(2) Phoon and Kulhawy (1999).
(3) Harr (1987). No comment made on whether measurement variability was included.

Figure 5.4: COV of inherent soil variability for CPT measurements

Test	Coefficient of variation, COV (%)				
	Equipment	Procedure	Random	Total ^a	Range ^b
Standard penetration test (SPT)	5–75 ^c	5–75 ^c	12–15	14–100 ^c	15–45
Mechanical cone penetration test (MCPT)	5	10–15 ^d	10–15 ^d	15–22 ^d	15–25
Electric cone penetration test (ECPT)	3	5	5–10 ^d	7–12 ^d	5–15
Vane shear test (VST)	5	8	10	14	10–20
Dilatometer test (DMT)	5	5	8	11	5–15
Pressuremeter test, prebored (PMT)	5	12	10	16	10–20 ^e
Self-boring pressuremeter test (SBPMT)	8	15	8	19	15–25 ^e

^aCOV(Total) = [COV(Equipment)² + COV(Procedure)² + COV(Random)²]^{0.5}.

^bBecause of limited data and judgment involved in estimating COVs, ranges represent probable magnitudes of field test measurement error.

^cBest to worst case scenarios, respectively, for SPT.

^dTip and side resistances, respectively, for CPT.

^eIt is likely that results may differ for p_o , p_f , and p_L , but the data are insufficient to clarify this issue.

Figure 5.5: Summary of measurement error of common in situ tests

relationship between the measured property and the design property, and it is therefore categorized as epistemic uncertainty and can be reduced as the knowledge about the relationship improves (e.g., Baecher and Christian (2003)).

Phoon and Kulhawy (1999a) provides several correlation equations for soil properties without however quantifying the actual transformation uncertainty to large extent. As an example, according to the above researchers, the transformation uncertainty for undrained shear strength based on triaxial tests lies between 29-35%. A summary of the variability of some design properties as a function of the test measurement, correlation equation, and soil type is presented in Table 5.6.

The COV of S_u varies between 10-60% for different tests, while the COV of ϕ lies in a range of 5-20%.

Design property ^a	Test ^b	Soil type	Point COV (%)	Spatial average COV ^c (%)	Correlation equation
s_u (UC)	Direct (lab)	Clay	20–55	10–40	—
s_u (UU)	Direct (lab)	Clay	10–35	7–25	—
s_u (CIUC)	Direct (lab)	Clay	20–45	10–30	—
s_u (field)	VST	Clay	15–50	15–50	14
s_u (UU)	q_T	Clay	30–40 ^d	30–35 ^d	18
s_u (CIUC)	q_T	Clay	35–50 ^d	35–40 ^d	18
s_u (UU)	N	Clay	40–60	40–55	23
s_u ^e	K_D	Clay	30–55	30–55	29
s_u (field)	PI	Clay	30–55 ^d	—	32
$\bar{\phi}$	Direct (lab)	Clay, sand	7–20	6–20	—
$\bar{\phi}$ (TC)	q_T	Sand	10–15 ^d	10 ^d	38
$\bar{\phi}_{cv}$	PI	Clay	15–20 ^d	15–20 ^d	43
K_o	Direct (SBPMT)	Clay	20–45	15–45	—
K_o	Direct (SBPMT)	Sand	25–55	20–55	—
K_o	K_D	Clay	35–50 ^d	35–50 ^d	49
K_o	N	Clay	40–75 ^d	—	54
E_{PMT}	Direct (PMT)	Sand	20–70	15–70	—
E_D	Direct (DMT)	Sand	15–70	10–70	—
E_{PMT}	N	Clay	85–95	85–95	61
E_D	N	Silt	40–60	35–55	64

^a E_D , dilatometer modulus; E_{PMT} , pressuremeter modulus; K_o , in situ horizontal stress coefficient; s_u , undrained shear strength; s_u (field), corrected s_u from vane shear test; $\bar{\phi}$, effective stress friction angle; $\bar{\phi}_{cv}$, constant-volume $\bar{\phi}$; TC, triaxial compression; UC, unconfined compression test.

^b K_D , dilatometer horizontal stress index; N , standard penetration test blow count; PI, plasticity index; q_T , corrected cone tip resistance.

^cAveraging over 5 m.

^dCOV is a function of the mean; refer to COV equations in the text for details.

^eMixture of s_u from UU, UC, and VST.

Figure 5.6: Approximate guidelines for design soil property variability (Phoon and Kulhawy, 1999a).

Lacasse and Nadim (1996) suggest a pdf of ϕ to be follow the normal distribution for sands and lognormal distribution for S_u in clays. It is suggested here that lognormal distribution (more realistic since it prohibits negative values) is adopted and, utilizing the published COVs of undrained shear strength and angle of friction, provided are visualization of the uncertainty of the above properties for the cases of minimum and maximum reported COVs.

Figures 5.7, 5.8, 5.9, 5.10 correspond to laboratory tests, while Figures 5.11, 5.12, 5.13, 5.14 correspond to field (SPT, CPT) tests. The solid vertical lines form a 68.3% interval of confidence, while the dashed lines form a 95.5% interval of confidence. The circular points represent the geometric mean values of the lognormal distributions.

If the actual test data are available, we can represent the residual values of a material property as shown in the figures below where Sett et al. (2011) provide the residual undrained shear strength based on SPT data. The authors came up with a Pearson VI distribution to best fit the data, as shown in Figures 5.15 and 5.16.

Little data has been published so far on soil stiffness uncertainty. The pressuremeter test

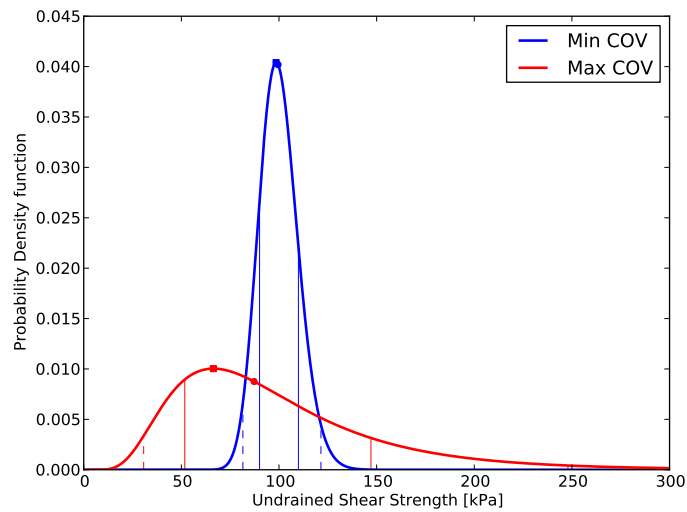


Figure 5.7: Probability density function of Undrained shear strength for minimum and maximum reported COVs based on laboratory tests

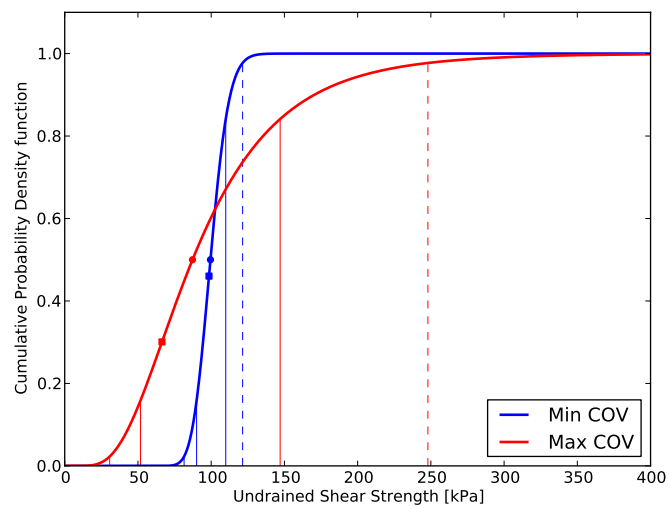


Figure 5.8: Cumulative probability density function of Undrained shear strength for minimum and maximum reported COVs based on laboratory tests

modulus E_{PMT} is often presumed to be roughly equivalent to Young's modulus (Phoon and Kulhawy, 1999b) and published total coefficients of variation for the former range between 20-70%. We may assume that stiffness uncertainty is generally greater than strength uncertainty. Figures 5.17 and 5.18 shows PDF and CDF of Young's modulus uncertainties for PMT tests.

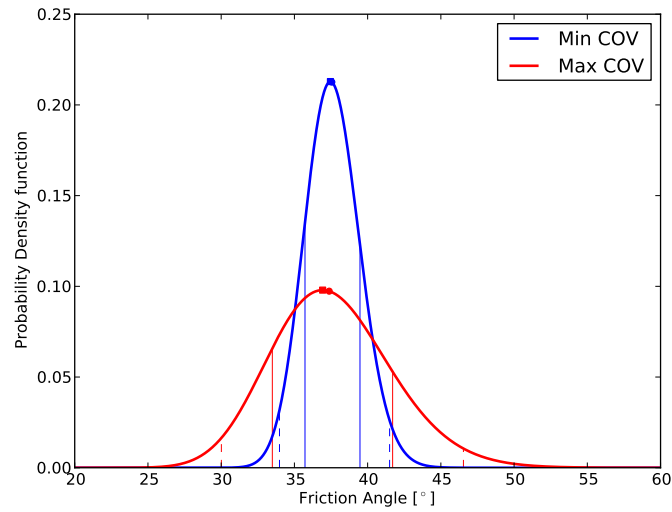


Figure 5.9: Probability density function of friction angle for minimum and maximum reported COVs based on laboratory tests

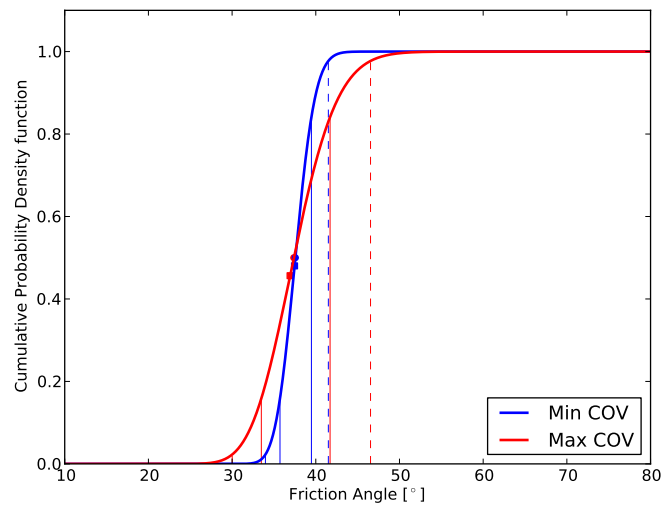


Figure 5.10: Cumulative probability density function of friction angle for minimum and maximum reported COVs based on laboratory tests

Figures 5.19 and 5.20 show values of the residual of Young's modulus based on SPT data Sett et al. (2011).

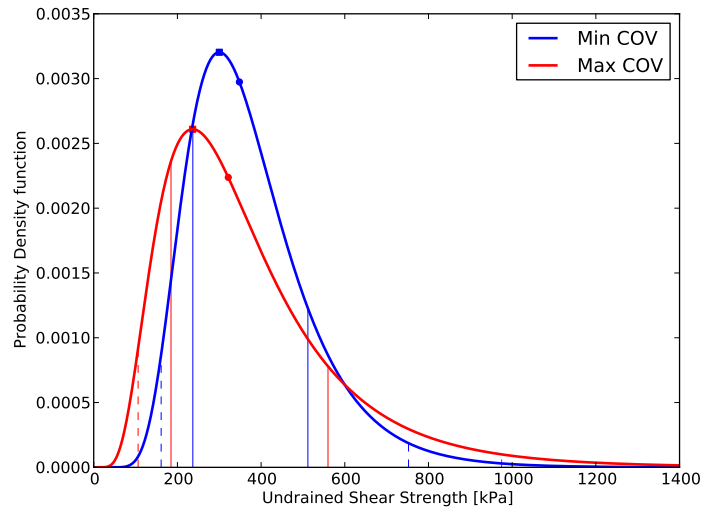


Figure 5.11: Probability density function of Undrained shear strength for minimum and maximum reported COVs based on SPT tests

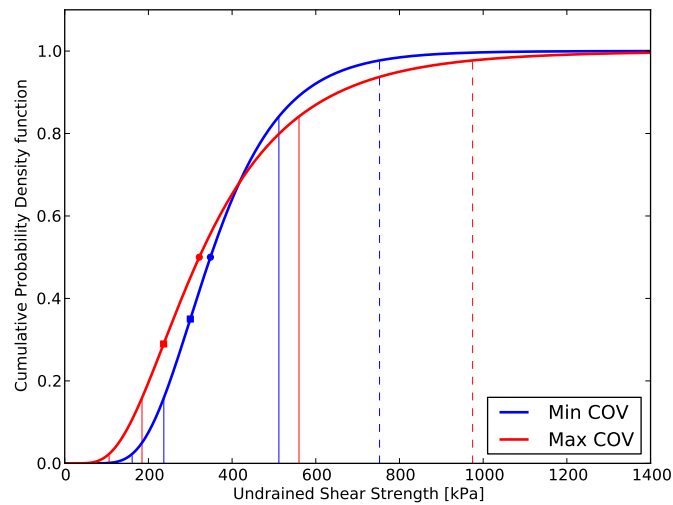


Figure 5.12: Cumulative probability density function of Undrained shear strength for minimum and maximum reported COVs based on SPT tests

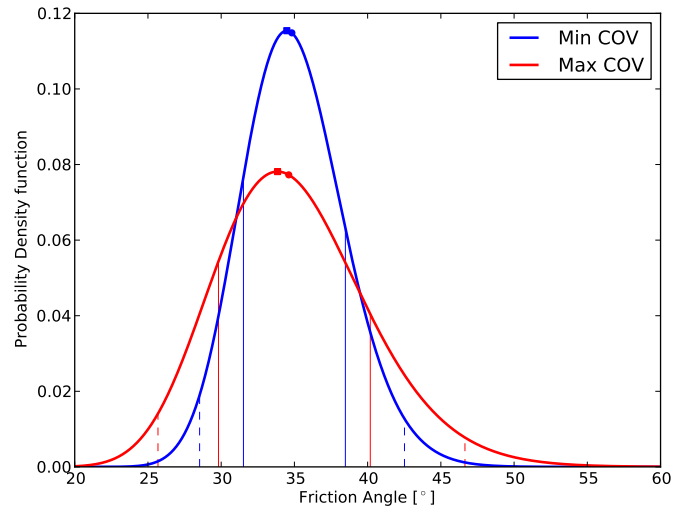


Figure 5.13: Probability density function of friction angle for minimum and maximum reported COVs based on CPT tests

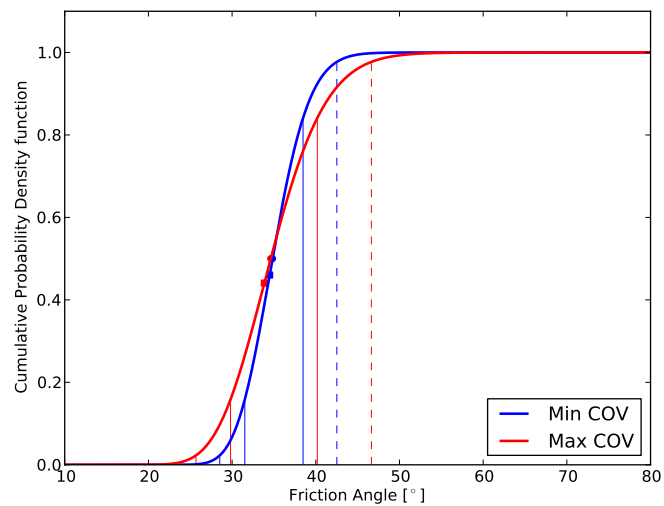


Figure 5.14: Cumulative probability density function of friction angle for minimum and maximum reported COVs based on CPT tests

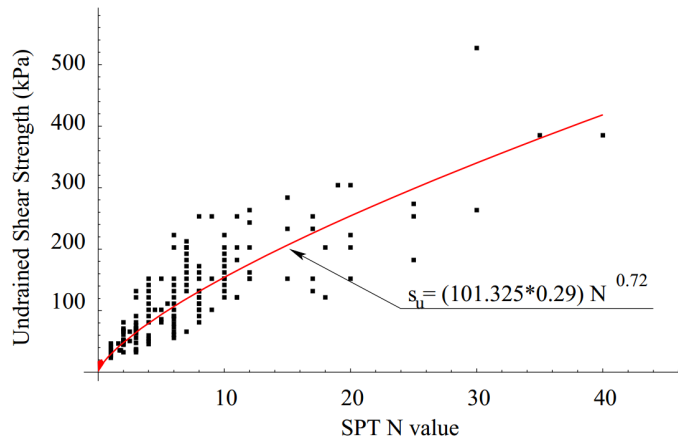


Figure 5.15: Transformation relationship between SPT N-value and undrained shear strength, S_u (Sett et al., 2011)

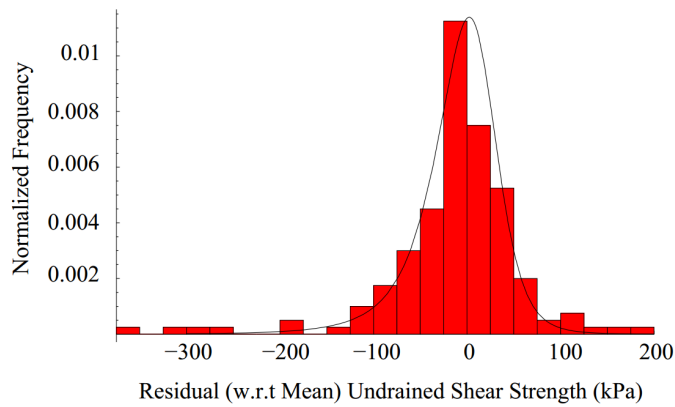


Figure 5.16: Histogram of the residual undrained strength along with fitted pdf (Sett et al., 2011)

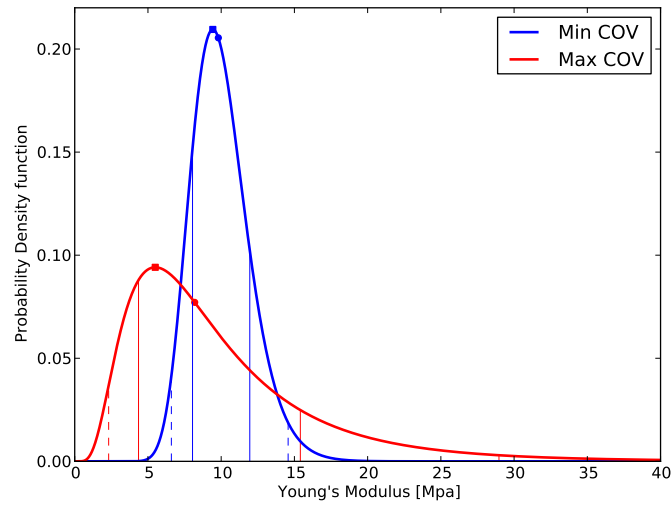


Figure 5.17: Probability density function of Young's Modulus for minimum and maximum reported COVs based on PMT tests

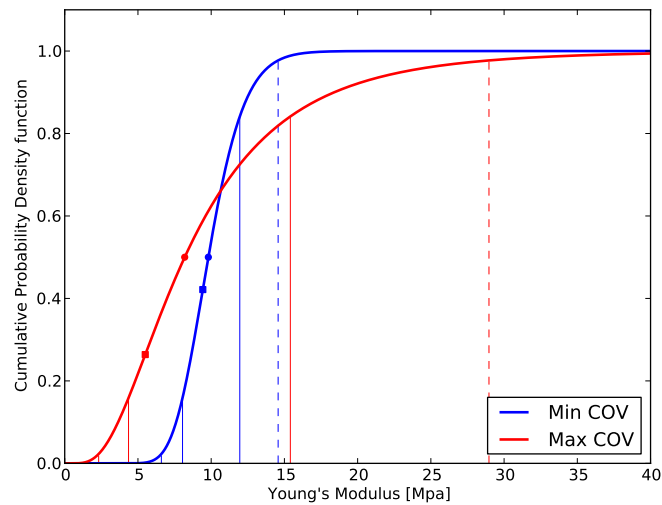


Figure 5.18: Cumulative probability density function of Young's Modulus for minimum and maximum reported COVs based on PMT tests

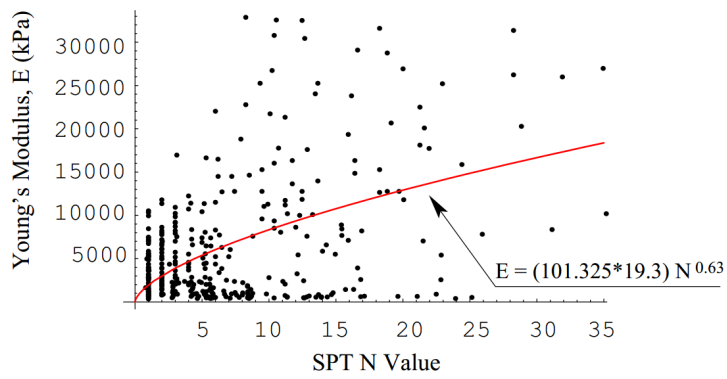


Figure 5.19: Transformation relationship between SPT N-value and pressuremeter Young's Modulus, E (Sett et al., 2011)

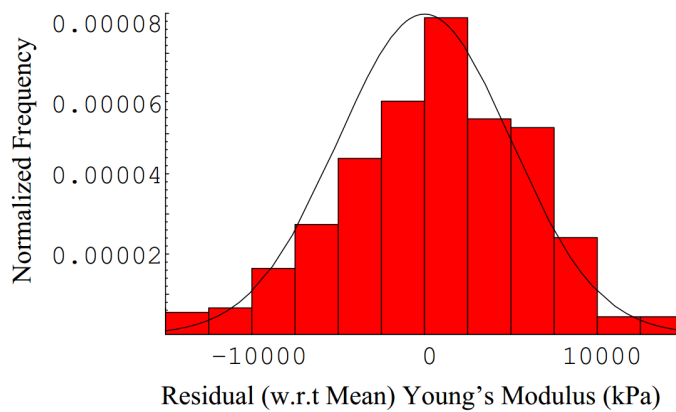


Figure 5.20: Histogram of the residual Young's Modulus along with fitted pdf (Sett et al., 2011)

5.3.2 Lack of Volume Change Data for Soil.

Use of G/G_{max} and damping curves for describing and calibrating material behavior of soil is missing a very important (crucial) information about soil/rock volume change during shearing deformation. Volume change data is very important for soil behavior. It is important to emphasize that soil behavior is very much a function of volumetric response during shear. During shearing of soil there are two essential types of soil behavior:

- Dilative (dense) soils will increase volume due to shearing
- Compressive (loose) soils will decrease volume due to shearing

The soil volume response, that is not provided by G/G_{max} and damping curves data can significantly affect response due to volume constraints of soil. For example, for one dimensional site response (1D wave propagation, vertically propagating (SV) shear waves) the soil will try to change its volume (dilate if it is dense or compress if it is loose). However, such volume change can only happen vertically (since there is no constraint (foundation for example) on top, while horizontally the soil will be constraint by other soil. That means that any intended volume change in horizontal direction will be resisted by change in (increase for dense and decrease for loose soil) horizontal stress. For example for dilative (dense) soil, additional horizontal stress will contribute to the increase in mean pressure (confinement) of the soil, thus increasing the stiffness of that soil. It is the opposite for compressive soil where shearing will result in a reduction of confinement stress. Figure 5.21 shows three responses for no-volume change (left), compressive (middle) and dilative (right) soil with full volume constraint, resulting in changes in stiffness for compressive (reduction in stiffness), and dilative (increase in stiffness).

Changes in stiffness of soil during shearing deformation will influence wave propagation and amplification of different frequencies. Figure 5.22 shows response of no-volume change soil (as it is/should be assumed if only G/G_{max} and damping curves are available, with no volume change data) and a response of a dilative soil which stiffens up during shaking due to restricted intent to dilate. It is clear that dilative soil will show significant amplification of higher frequencies.

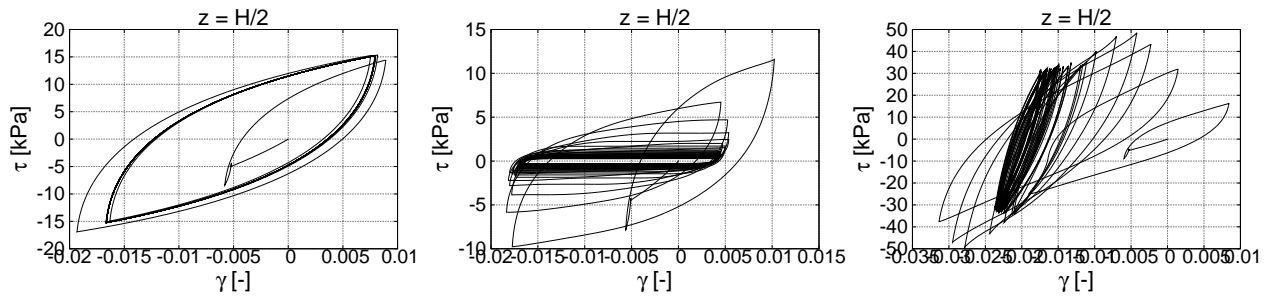


Figure 5.21: Constitutive Cyclic response of soils with constraint volumetric deformation: (left) no volume change (soil is at the critical state); (middle) compressive response with decrease in stiffness; (right) dilative response with increase in stiffness.

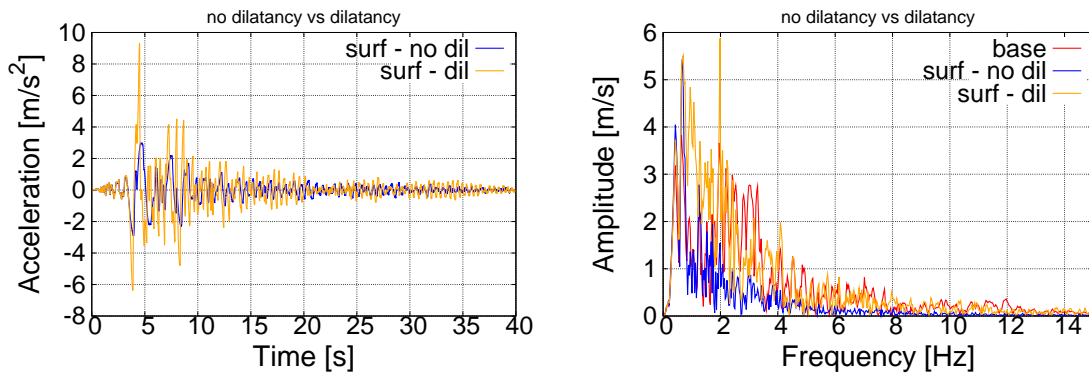


Figure 5.22: One dimensional seismic wave propagation through no-volume change and dilative soil. Please note the (significant) increase in frequency of motions for dilative soil. Left plot is a time history of motions, while the right plot shows amplitudes at different frequencies.

5.3.3 Extrapolation from 1D Data to full 3D Data, Pisano Material Model

This extrapolation from 1D data (G/G_{max} and damping curves) to full 3D model is done through the development of Pisanò model, as described bellow. It is noted that description of material model developed and used is from a recent publication by Pisanò and Jeremić (2014). Detailed description is included here for completeness.

Abstract. Stiffness degradation and damping represent some of the most well-known aspects of cyclic soil behavior. While standard equivalent linear approaches reproduce these features by (separately) prescribing stiffness reduction and damping curves, in this paper a multiaxial, 3D, viscoelastic – plastic model is developed for the simultaneous simulation of both cyclic curves over a wide cyclic shear strain range.

The proposed constitutive relationship is based on two parallel resisting/dissipative mechanisms, purely frictional (elastic-plastic) and viscous. The frictional mechanism is formulated as a bounding surface plasticity model with vanishing elastic domain, including pressure-sensitive failure locus and non-associative plastic flow – which are essential for effective stress analysis. At the same time, the use of the parallel viscous mechanism is shown to be especially beneficial to improve the simulation of the overall dissipative performance.

In order to enable model calibration from stiffness degradation (G/G_{max}) and damping curves, the constitutive equations are purposely kept as simple as possible with a low number of material parameters. Although the model performance is here explored with reference to pure shear cyclic tests, the 3D, multiaxial formulation is appropriate for general loading conditions.

Introduction

Modeling soil behavior under cyclic/dynamic loading is crucial in most Geotechnical Earthquake Engineering (GEE) applications, including e.g. site response analysis and soil structure interaction (SSI) problems. In the last decades, a number of experimental studies (Ishihara, 1996; di Prisco and Wood, 2012) pointed out the complexity of such behavior – especially in the presence of pore fluid(s) – characterized by non-linearity, irreversibility, anisotropy, barotropy, picnotropy, rate-sensitivity, etc. In principle, a comprehensive soil model should be capable of reproducing all the aspects of the mechanical response for any loading condition, as well as predicting the occurrence of liquefaction and cyclic mobility, distinguishing the conditions for shakedown or ratcheting under repeated loads and so forth. However, such a perfect model is expected to require too many data for calibration, which are hardly available in most practical situations.

Conversely, many GEE problems are traditionally solved in the frequency domain by using 1D (equivalent) linear visco-elastic models, to be calibrated on standard stiffness degradation (G/G_{max}) and damping (ζ) curves. Owing to the availability of computer programs for 1D

site response analysis (SHAKE (Schnabel et al., 1972), EERA (Bardet et al., 2000), DEEPSOIL (Hashash and Park, 2001)) and SSI problems (SASSI (Lymser, 1988)), the visco-elastic approach has become more and more popular among practitioners, regardless of the following drawbacks:

- most energy dissipation in soils comes from frictional inter-granular mechanisms, rather than viscous flow;
- G/G_{max} and ζ curves do not allow to evaluate irreversible deformations, nor the influence of pore fluid(s);
- adopting 1D shear constitutive relationships has poor mechanical soundness, since soil behavior exhibits a pronounced deviatoric-volumetric coupling under general multiaxial loading conditions;
- the meaning of cyclic shear strain amplitude for the choice of G/G_{max} and ζ values is not evident in the presence of irregular seismic loads.

From the above observations the need stems for more physically consistent soil models. In the last decades, several approaches to cyclic modeling have been explored and gradually refined in the framework of elasto-plasticity, including e.g. “multi-surface plasticity”, “bounding surface plasticity”, “generalized plasticity” and “hypoplasticity”. A number of valuable contributions are worth citing, such as – to mention only a few – Mróz et al. (1978); Prevost (1985); Wang et al. (1990); Borja and Amies (1994); Manzari and Dafalias (1997); Gajo and Wood (1999); Papadimitriou and Bouckovalas (2002); Elgamal et al. (2003); Dafalias and Manzari (2004b); Taiebat and Dafalias (2008); Andrianopoulos et al. (2010). Recently, it has been also shown how a good simulation of dynamic properties can be achieved by means of even elastic-perfectly plastic models, as long as formulated in a probabilistic elastic-plastic framework (Sett et al., 2011). Comprehensive overviews on cyclic soil modeling are given by Prevost and Popescu (1996), Zienkiewicz et al. (1999b) and di Prisco and Wood (2012).

As is well-known, the major issues about the practical use of incremental elastic-plastic models concerns the potentially high number of material parameters. For a model to appeal to practicing engineers, a tradeoff is needed between the overall accuracy and the number of parameters to

be calibrated, particularly provided the frequent lack of detailed *in situ* or laboratory data. This observation led the authors to set up a constitutive model with main following characteristics:

- multiaxial formulation to cope with a 3D finite element modeling
- capability of reproducing the practical features of dynamic soil behavior, in particular, stiffness reduction and damping over a wide strain range, as well as frictional failure, irreversible deformation and dilatancy;
- low number of material parameters, to be calibrated using usually (practice) available dynamic soil experimental data, the stiffness reduction (G/G_{max}) and damping (ζ) curves.

A constitutive relationship fulfilling the above requirements is hereafter presented as the combination of two resisting/dissipative mechanism:

- Frictional (elastic-plastic, displacement proportional) and
- Viscous (velocity proportional)

The frictional mechanism has been formulated starting from the work by Borja and Amies (1994), who proposed a kinematic-hardening bounding surface von Mises model for the seismic total-stress analysis of the clayey deposits at Lotung site in Taiwan (Borja et al., 1999, 2000). In particular, based on the idea by Dafalias and Popov (1977) and Dafalias (1979), the Borja and Amies's multiaxial model is characterized by the assumption of vanishing elastic domain, implying soil plastification at any load level and a redefinition of the standard loading/unloading criterion. The vanishing elastic region also has a strong bases in micromechanics of particulate media where it can be shown that two particles with any amount of shear on their contact will develop inelastic deformation (Mindlin and Deresiewicz, 1953). Recently, the vanishing elastic region approach has been also employed by Andrianopoulos et al. (2010), in order to improve the previous model by Papadimitriou and Bouckovalas (2002) with respect to numerical implementation and integration.

In this paper, a bounding surface approach with vanishing elastic region is exploited to derive the frictional component of the overall model in the form of a Drucker-Prager effective-stress relationship, incorporating pressure-sensitive failure and non-associative plastic flow. In addition,

the model is endowed with a further viscous mechanism, which can be wisely exploited to improve the simulation of the experimental damping. Although numerical convenience often motivates the use of viscous dissipation into elastic-plastic computations, it has a real physical origin, coming from the time-dependent processes taking place at both inter-granular contacts and grain/pore fluid (water, air, etc.) interfaces.

The proposed formulation should be considered as an attempt at reconciling traditional (equivalent linear) and advanced (elastic-plastic) cyclic modeling within an effective-stress elasto-plasticity framework. In particular, the model is shown to possess reasonable accuracy in reproducing standard modulus reduction and damping curves over a wide strain range, and it is particularly user-friendly because of the low number of material parameters. The literature survey put evidence that these advantages are not easily found in most previous effective-stress models.

In order to clearly illustrate the main modeling ingredients, the basic version of the model is hereafter presented and tested under symmetric cyclic shear loading. Its convenient mathematical structure enables future refinement to model other (other than G/G_{max} and damping) important features of dynamic behavior of soil.

Frictional and viscous dissipative mechanisms

The time-domain finite element (FE) solution of dynamic problems is usually carried out by solving an incremental discrete system of the following form (Bathe and Wilson, 1976; Zienkiewicz and Taylor, 1991):

$$\mathbf{M}\Delta\ddot{\mathbf{U}} + \mathbf{C}\Delta\dot{\mathbf{U}} + \mathbf{K}^t\Delta\mathbf{U} = \Delta\mathbf{F}^{ext} \quad (5.1)$$

where Δ and dots stand respectively for step increment and time derivative, \mathbf{U} is the generalized DOF vector (nodal displacement for example), \mathbf{F}^{ext} the nodal external force vector and \mathbf{M} , \mathbf{C} , \mathbf{K}^t are the mass, damping and (tangent) stiffness matrices, respectively.

In system (5.1) two dissipative sources are readily recognizable, namely the viscous (velocity-proportional) and the frictional (displacement-proportional) terms (Argyris and Mlejnek, 1991). While the latter is given by the elastic-plastic tangent stiffness \mathbf{K}^t , the viscous term related to the damping matrix \mathbf{C} can represent interaction of solid skeleton and pore fluid, and constitutive

rate-sensitiveness of the soil skeleton. The above combination of frictional and viscous dissipation can be interpreted in terms of two distinct effective stress components acting on the soil skeleton:

$$\sigma_{ij} = \sigma_{ij}^f + \sigma_{ij}^v \quad (5.2)$$

where the effective stress tensor σ_{ij} has been split into frictional (elastic-plastic) and viscous stresses¹. From a rheological point of view, the resulting scheme can be defined as visco-elastic-plastic. In what follows, the frictional component is first specified via the formulation of the bounding surface model with vanishing elastic domain; then, the role played by the linear viscous term is discussed.

Index tensor notation is used, along with the standard Einstein convention for repeated indices; the norm of any second-order tensor x_{ij} is defined as $\|x_{ij}\| = \sqrt{x_{ij}x_{ij}}$, whereas the deviatoric component can be extracted as $x_{ij}^{dev} = x_{ij} - x_{kk}\delta_{ij}/3$ (δ_{ij} is the Kronecker delta). In accordance with usual Solid Mechanics conventions, positive tensile stresses/strains are considered, whereas – as is done in Fluid Mechanics – only the isotropic mean pressure is positive if compressive.

Bounding surface frictional model with vanishing elastic domain

The frictional component of the model being proposed is formulated by generalizing the previous constitutive relationship by Borja and Amies (1994). In what follows, the superscript f referring to the frictional component of the global effective stress (Equation (5.2)) is avoided for the sake of brevity.

Elastic relationship

Provided the usual additive combination of (incremental) elastic and plastic strain components $d\epsilon_{ij} = d\epsilon_{ij}^e + d\epsilon_{ij}^p$, the incremental linear elastic Hooke's law is expressed as follows:

$$d\sigma_{ij} = D_{ijhk}^e (d\epsilon_{hk} - d\epsilon_{hk}^p) \implies \begin{cases} ds_{ij} = 2G_{max} (de_{hk} - de_{hk}^p) \\ dp = -K (d\epsilon_{vol} - d\epsilon_{vol}^p) \end{cases} \quad (5.3)$$

¹Henceforth, effective stresses are exclusively accounted for

where d stands for a differentially small increments and D_{ijhk}^e is the fourth-order elastic stiffness tensor. Equation (5.3) also points out the elastic deviatoric/volumetric decoupling, in which $p = -\sigma_{kk}/3$, $\epsilon_{vol} = \epsilon_{kk}$, $s_{ij} = \sigma_{ij}^{dev}$ and $e_{ij} = \epsilon_{ij}^{dev}$ stand for mean stress, volumetric strain, stress deviator and strain deviator, respectively. The shear modulus $G_{max} = E/2(1 + \nu)$ and the bulk modulus $K = E/3(1 - 2\nu)$ are derived from the Young modulus E and the Poisson's ratio ν . Henceforth, G_{max} will be always used for the elastic small-strain shear modulus, whereas the secant cyclic shear stiffness will be referred to as G .

Although soil elasticity is known to be non-linearly pressure-dependent, a classical linear formulation has been here maintained to simulate constant-pressure cyclic shear tests, exclusively.

Drucker-Prager yield and bounding loci

A conical Drucker-Prager yield locus is first introduced, similar to that used by Prevost (1985) and Manzari and Dafalias (1997):

$$f_y = \frac{3}{2} (s_{ij} - p\alpha_{ij}) (s_{ij} - p\alpha_{ij}) - k^2 p^2 = 0 \quad (5.4)$$

where α_{ij} is the so called deviatoric back-stress ratio ($\alpha_{kk} = 0$) governing the kinematic hardening of the yield surface; k is a parameter determining the opening angle of the cone. The variation of the back-stress ratio α_{ij} in (5.4) leads to a rigid rotation of the yield locus and, therefore, a rotational kinematic hardening.

In the spirit of standard bounding surface plasticity, the yield locus must always reside within an outer surface (the so-called bounding surface), here assumed in the form of a further Drucker-Prager cone (non kinematically hardening, fixed in size):

$$f_B = \frac{3}{2} s_{ij} s_{ij} - M^2 p^2 = 0 \quad (5.5)$$

where M provides the bounding cone opening and, as a consequence, the material shear strength.

Plastic flow and translation rules

The plastic flow of soils is in general non-associative (Nova and Wood, 1979) and gives rise to plastic contractancy or dilatancy depending on whether loose or dense materials are considered.

Here, the plastic flow rule is borrowed from Manzari and Dafalias (1997):

$$d\epsilon_{ij}^p = d\lambda \left(n_{ij}^{dev} - \frac{1}{3}D\delta_{ij} \right) \quad (5.6)$$

where $d\lambda$ is the plastic multiplier, n_{ij}^{dev} is a deviatoric unit tensor ($\|n_{ij}^{dev}\| = 1$) and D is a dilatancy coefficient defined as (Manzari and Dafalias, 1997):

$$D = \xi (\alpha_{ij}^d - \alpha_{ij}) n_{ij}^{dev} = \xi \left(\sqrt{\frac{2}{3}}k_d n_{ij}^{dev} - \alpha_{ij} \right) n_{ij}^{dev} \quad (5.7)$$

in which ξ and k_d are two positive constitutive parameters. While the former controls the amount of volumetric plastic strain, the latter determines the position of the so called “dilatancy surface” and rules the transition from contractive ($D > 0$) to dilative ($D < 0$) behavior under undrained triaxial conditions².

For the sake of simplicity (and regardless of some experimental evidences), the kinematic hardening evolution of the yield locus and the direction of the deviatoric plastic strain increment are related through the standard Prager’s rule (Borja and Amies, 1994):

$$d\alpha_{ij} = \|d\alpha_{ij}\| n_{ij}^{dev} \quad (5.8)$$

Vanishing elastic region

As previously mentioned, the main feature of the frictional model concerns the vanishing elastic domain, corresponding with the limit $k \rightarrow 0$ in Equation (5.4). Accordingly, the Drucker-Prager cone reduces to its axis, so that:

$$\lim_{k \rightarrow 0} f_y = 0 \Rightarrow \frac{s_{ij}}{p} = r_{ij} = \alpha_{ij} \Rightarrow d\alpha_{ij} = dr_{ij} = \frac{ds_{ij}}{p} - \frac{s_{ij}}{p^2} dp \quad (5.9)$$

where r_{ij} is the deviatoric stress ratio tensor (Manzari and Dafalias, 1997). After substituting the Prager’s rule (5.8) into (5.9) we obtain:

$$n_{ij}^{dev} = \frac{dr_{ij}}{\|dr_{ij}\|} = \frac{ds_{ij} - \alpha_{ij} dp}{\|ds_{ij} - \alpha_{ij} dp\|} \quad (5.10)$$

From Equation (5.10) it can be inferred that:

²Under different loading conditions this transition is not “exactly” governed only by the location of the current stress state with respect to the dilatancy surface

1. since the direction of the overall plastic strain increment depends on the stress increment $d\sigma_{ij}$, the resulting constitutive formulation is by definition “hypoplastic” (Dafalias, 1986);
2. hydrostatic stress increments ($ds_{ij} = 0$) from initial hydrostatic states ($\alpha_{ij} = 0$) produce $n_{ij}^{dev} = 0 \rightarrow \epsilon_{ij}^{dev} = 0$;
3. the deviatoric plastic strain increment is along the direction of the deviatoric stress ratio increment. This directly comes from the use of the above Prager’s rule in combination with the vanishing elastic region. Although this finding is not in full agreement with general experimental evidences, it will not prevent satisfactory cyclic G/G_{max} and ζ curves to be obtained.

Starting from Equation (5.9), the norm $\|d\alpha_{ij}\| = \|dr_{ij}\|$ can be specified for the case of radial loading paths in the deviatoric plane, which are characterized by $dp = 0$ and the coaxiality of s_{ij} and ds_{ij} . Under these loading conditions, simple manipulations lead to find:

$$\|d\alpha_{ij}\| = \sqrt{\frac{2}{3}} \frac{dq}{p} \quad (5.11)$$

where $q = \sqrt{3/2} \|s_{ij}\|$ stands for the usual deviatoric stress invariant.

Hardening relationship and plastic multiplier

An incremental hardening relationship is directly established (Borja and Amies, 1994):

$$dq = \sqrt{\frac{2}{3}} H \|de_{ij}^p\| \quad (5.12)$$

where H is the hardening modulus. Then, the substitution of both the flow rule (5.6) and the hardening relationship (5.12) into (5.11) leads to:

$$\|d\alpha_{ij}\| = \frac{2}{3} \frac{H d\lambda}{p} \quad (5.13)$$

By equating the two definitions of ds_{ij} arising from Equations (5.3)-deviatoric and (5.9), and then using Equations (5.3)-volumetric and (5.13) the following relationship is obtained:

$$2G_{max} (de_{ij} - d\lambda n_{ij}^{dev}) = \|d\alpha_{ij}\| n_{ij}^{dev} p + \alpha_{ij} dp = \frac{2}{3} \frac{H d\lambda}{p} n_{ij}^{dev} p - \alpha_{ij} K (d\epsilon_{vol} + d\lambda D) \quad (5.14)$$

whence:

$$d\lambda = \frac{2G_{max} de_{ij} n_{ij}^{dev} + K d\epsilon_{vol} \alpha_{ij} n_{ij}^{dev}}{2G + \frac{2}{3} H - K D \alpha_{ij} n_{ij}^{dev}} \quad (5.15)$$

Equation (5.15) represents the consistent frictional generalization of Equation (18) in Borja and Amies (1994), as well as the limit of Equation (12) in Manzari and Dafalias (1997)³ for a vanishing size of the yield locus.

Projection rule, hardening modulus and unloading criterion

The theory of bounding surface plasticity relies on the basic concept that the plastic modulus explicitly depends on the distance between the current stress state and an *ad hoc* stress projection onto the bounding surface. On this issue, benefits and pitfalls of different projection rules have been thoroughly discussed by Andrianopoulos et al. (2005).

Here, the stress projection in the π -plane (deviatoric stress ratio plane) is assumed to be along the direction of $\alpha_{ij} - \alpha_{ij}^0$:

$$\alpha_{ij}^b = \alpha_{ij} + \beta (\alpha_{ij} - \alpha_{ij}^0) \quad (5.16)$$

where β is a scalar distance coefficient, while α_{ij}^0 is the back-stress ratio at the last loading reversal (Figure 5.23). As observed by Andrianopoulos et al. (2010), projection rules of the type (5.16) are “stable”, in the sense that small perturbations of the loading direction do not affect severely the location of the stress projection on the bounding surface.

The coefficient β is obtained by enforcing the projected stress σ_{ij}^b to lie on the bounding surface (Equation (5.5)):

$$\frac{3}{2} s_{ij}^b s_{ij}^b = M^2 (p^b)^2 \iff \frac{3}{2} \alpha_{ij}^b \alpha_{ij}^b = M^2 \quad (5.17)$$

³Different signs result because of the opposite sign conventions adopted by these authors

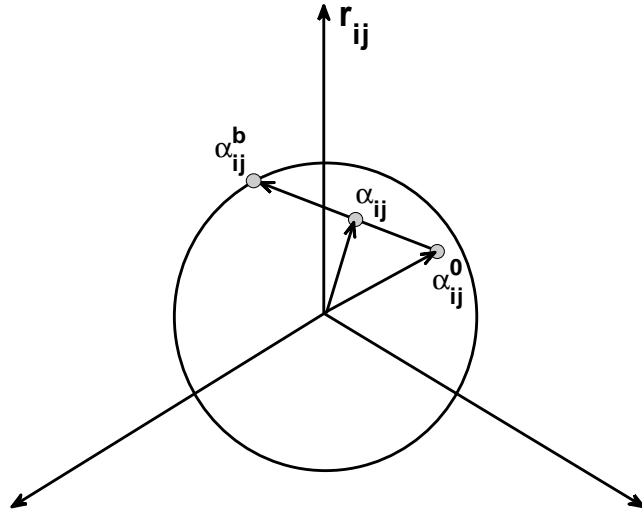


Figure 5.23: Representation of the projection rule (5.16)

that is by substituting (5.16) into (5.17) and then deriving the positive root of the following algebraic equation⁴:

$$\|\alpha_{ij} - \alpha_{ij}^0\|^2 \beta^2 + 2\alpha_{ij} (\alpha_{ij} - \alpha_{ij}^0) \beta + \|\alpha_{ij}\|^2 - \frac{2}{3}M^2 = 0 \quad (5.18)$$

The analytical relationship between H and β is chosen to fulfill the following requirements:

1. $H(\beta = 0) = 0$, that is full mobilization of the material strength when the stress image point lies on the bounding surface;
2. $H(\beta \rightarrow \infty) \rightarrow \infty$, that is (instantaneous) recover of the elastic stiffness at the onset of load reversal (i.e. $\alpha_{ij} = \alpha_{ij}^0$).

In this case, the following $H - \beta$ relationship has been introduced because of its simplicity:

$$H = ph\beta^m \quad (5.19)$$

in which h and m are two additional constitutive parameters.

⁴The adoption of a simple Drucker-Prager-type bounding surface allows β to be analytically obtained. This would not be the case in the presence of more complex π -sections

In the absence of a finite-sized elastic region, the occurrence of unloading cannot be checked by comparing the loading direction and the local normal to the yield locus. This requires the definition of an alternative unloading criterion, coinciding here with providing a rule for updating α_{ij}^0 . Borja and Amies (1994) proposed a criterion based on the observation that the hardening modulus H increases at the onset of unloading, so that – as long as $H(\beta)$ is a monotonically increasing function – instantaneous unloading is assumed whenever $dH > 0$, i.e. $d\beta > 0$. However, the authors experienced that such an unloading criterion lacks robustness in numerical computations under complex/irregular loading paths, because the small values assumed by β (especially close to the bounding surface) can be easily corrupted even by numerical inaccuracies; as a result, unrealistic unloading is often likely to arise. While different proposals are available in literature to overcome this problem (Andrianopoulos et al., 2005, 2010), the following unloading criterion has been here preferred:

$$(\alpha_{ij} - \alpha_{ij}^0) dr_{ij} < 0 \iff (\alpha_{ij} - \alpha_{ij}^0) n_{ij}^{dev} < 0 \quad (5.20)$$

in which the coaxiality of $d\alpha_{ij} = dr_{ij}$ and n_{ij}^{dev} (Prager's rule (5.8)) has been exploited.

It should be also borne in mind that this kind of updating criterion is likely to give rise to “overshooting” phenomena under general loading paths (Dafalias, 1986). Overshooting takes place when, after loading along a given direction, a very small unloading implies an updated α_{ij}^0 before reloading along the original direction. The updated small distance between the current and the reversal stresses determines an unrealistically high reloading stiffness, so that “the corresponding stress-strain curve will overshoot the continuation of the previous curve which would have occurred if no unloading/reverse loading/reloading had taken place” (Dafalias, 1986). While this shortcoming can be usually observed under irregular seismic loading, it will not be detected in the results being presented, exclusively concerning symmetric sinusoidal cyclic loading. A recent discussion on the remediation of overshooting is provided by E-Kan and Taiebat (2014).

Possible refinements

The frictional model has been developed trying to keep the number of material parameters as low as possible, even with a non-associated flow rule. This was done since our primary goal is to create a material model that appeals to practice, and that can be calibrated from stiffness

degradation (G/G_{max}) and damping curves. There are a number of improvements that might be introduced if required by the problem under examination, and, of course, if more (appropriate) experimental data is available.

It should be first noted that, as a Drucker-Prager type bounding surface has been adopted, the material shear strength is unaffected by the Lode angle, so that for instance the same failure obliquity is predicted for triaxial compression and extension. This drawback could be easily remedied by modifying the deviatoric cross-section of the bounding surface itself, e.g. by adopting the well known Mohr-Coulomb deviatoric locus or other smooth loci (Matsuoka and Nakai, 1974; Willam and Warnke, 1974; Lade, 1977). A change in the deviatoric cross-section would negligibly influence the overall formulation, as just the evaluation of the projection distance β (Equation (5.17)).

Secondly, the present version of the model cannot predict a possible softening behavior of the soil, usually taking place in the case of dense materials. Softening could be accounted for by incorporating a further isotropic hardening mechanism at the bounding surface level, allowing for a gradual shrinkage of the outer surface during plastification.

Another relevant point concerns the fact that different parameters must be calibrated for different void ratios of the same granular material, as if distinct materials were indeed considered. As a matter of fact, continuous transitions from loose to dense states (and vice versa) spontaneously take place during straining: this aspect has been successfully addressed and reproduced via the concept of “state parameter” (Been and Jefferies, 1985; Wood et al., 1994; Manzari and Dafalias, 1997), which could be also introduced into a critical-state version of the proposed model. Also, the state parameter concept represents a natural way to reproduce softening as an effect of the material evolution from peak strength to critical state conditions.

While the above aspects concern both monotonic and cyclic loading conditions, further issues could be addressed with more specific reference to cyclic/dynamic loading, as for instance fabric effects (Papadimitriou and Bouckovalas, 2002; Dafalias and Manzari, 2004b) and anisotropy, the evolution toward shakedown or ratcheting under a large number of loading cycles (di Prisco and Wood, 2012), the occurrence of cyclic mobility (Elgamal et al., 2003), rate-sensitiveness and related frequency effects.

Apparently, refining the model formulation in the light of the above observations would

result in more accurate predictions/simulations, implying though higher difficulties in terms of calibration, implementation and, as a consequence, practical employment. It is noted again that the main goal of presented development is to conceive a 3D incremental elastic-plastic model that is reasonably accurate, yet calibrated from (only) stiffness degradation (G/G_{max}) and damping curves, and that provide engineers/modelers with a standard cyclic modeling concepts (modulus reduction and damping curves) in a 3D elastic-plastic fashion.

The role of linear viscous damping

An additional viscous mechanism (Equation (5.2)) is usually available and exploited in most finite element (FE) codes, even though it is not directly included in the constitutive model. Indeed, many numerical programs solve discrete systems with a viscous damping term (Equation (5.1)), usually assembled as a linear combination of the mass and the (elastic) stiffness matrices (Rayleigh formulation (Argyris and Mlejnek, 1991; Chopra, 2000)):

$$\mathbf{C} = a_0\mathbf{M} + a_1\mathbf{K}^e \quad (5.21)$$

where a_0 and a_1 are two constant parameters, related to the n^{th} modal damping ratio ζ_n of the discrete structural system.

It could be easily shown that a constitutive viscosity in the form:

$$\sigma_{ij}^v = D_{ijhk}^v \dot{\epsilon}_{hk} \quad (5.22)$$

gives rise to a stiffness-proportional damping matrix, which can be equivalently reproduced through the following calibration of the Rayleigh damping parameters (Borja et al., 2000; Hashash and Park, 2002):

$$a_0 = 0 \quad a_1 = \frac{2\zeta_0}{\omega} \quad (5.23)$$

The calibration (5.23) establishes the same ratio between tangential/bulk elastic and the viscous moduli, that is $G_{max}^e/G_{max}^v = K^e/K^v$. More importantly, a damping ratio ζ_0 is ensured for a given circular frequency ω , as long as the parallel resisting mechanism (σ_{ij}^f) is purely elastic; as a consequence, provided the a_1 value at the beginning of the analysis, modal frequencies and the corresponding damping ratios are linearly related.

It is also worth remarking some further points about the implications of linear viscous damping in conjunction with non-linear soil models. If a soil element undergoes an imposed shear strain history, the overall shear stress/strain cycles $\tau - \gamma$ differ from the purely frictional component $\tau^f - \gamma$, this difference being due to the viscous shear stress τ^v . As will be shown in next section, the viscous component implies smoother cycles and avoid the sharp transitions at stress reversal usually exhibited by purely elastic-plastic responses (Borja et al., 2000). However, the overall G/G_{max} ratio between the average cyclic stiffness and the elastic shear modulus is unaffected by viscosity.

As far as the damping ratio is concerned, its standard definition (Kramer, 1996) can be easily adapted to point out the frictional/viscous splitting of the energy ΔW dissipated in a loading cycle:

$$\zeta = \frac{\Delta W}{2\pi G \gamma_{max}^2} = \frac{\Delta W^f + \Delta W^v}{2\pi G \gamma_{max}^2} = \zeta^f + \zeta^v \quad (5.24)$$

where γ_{max} is the imposed cyclic shear strain amplitude and G the corresponding (secant) cyclic shear stiffness. As γ_{max} approaches zero, the plastic dissipation tends to zero as well, so that $\zeta = \zeta^v$; therefore, the Rayleigh parameter a_1 can be calibrated to obtain $\zeta(\gamma_{max} \rightarrow 0) = \zeta_0$ for a given circular frequency ω (see Equation (5.23)). This is a desirable feature of the model, as natural soils are well known to dissipate energy at even very small strain amplitudes.

At progressively larger strains, both the frictional and viscous components contribute to the global damping, although the relative quantitative significance is hard to assess *a priori*. In addition, the viscous component of the $\zeta - \gamma_{max}$ curve is not constant, since ζ^v depends on the strain-dependent secant modulus $G(\gamma_{max})$ and, implicitly, on the strain rate. This is different to what has been argued by Borja et al. (2000).

As an example, consider the response of an elastic-perfectly plastic model with additional viscosity under a sinusoidal shear excitation $\gamma(t) = \gamma_{max} \sin(\omega t)$. The simplicity of the elastic-perfectly plastic response allows derivation of instructive analytical formulas for the G/G_{max} and the damping ratios, even in the presence of viscous dissipation. While $\gamma_{max} < \gamma_y$ (yielding shear strain), the material behavior is linear elastic, so that $G/G_{max} = 1$ and ζ equals the purely viscous contribution at $\gamma_{max} = 0$, i.e. $\zeta = \zeta_0$; γ_y depends on the elastic stiffness and the shear strength of the material, $\gamma_y = \tau_{lim}/G_{max}$, where τ_{lim} is the limit (frictional) shear stress for

a given confining pressure. For $\gamma_{max} > \gamma_y$ plastification take place with a flat elastic-perfectly plastic $\tau^f - \gamma$ branch, and the following expressions can be easily derived:

$$\frac{G}{G_{max}} = \frac{\tau_{lim}}{G_{max}\gamma_{max}} \quad (5.25)$$

$$\zeta = \frac{\Delta W^f + \Delta W^v}{2\pi G \gamma_{max}^2} = \underbrace{\frac{2}{\pi} \left(1 - \frac{\tau_{lim}}{G_{max}\gamma_{max}} \right)}_{\zeta^f} + \underbrace{\zeta_0 \frac{G_{max}\gamma_{max}}{\tau_{lim}}}_{\zeta^v} \quad (5.26)$$

In Figure 5.24 the G/G_{max} and ζ ratios are plotted for increasing ζ_0 values. As γ_{max} increases, the frictional damping tends to $2/\pi \approx 0.63$, while the viscous one keeps increasing because of the reduction in the secant stiffness and the increase in the shear strain rate (depending on the strain amplitude). Hence, the value of ζ_0 is to be carefully chosen, in order to avoid excessive dissipation when medium/large strains are induced by the loading process.

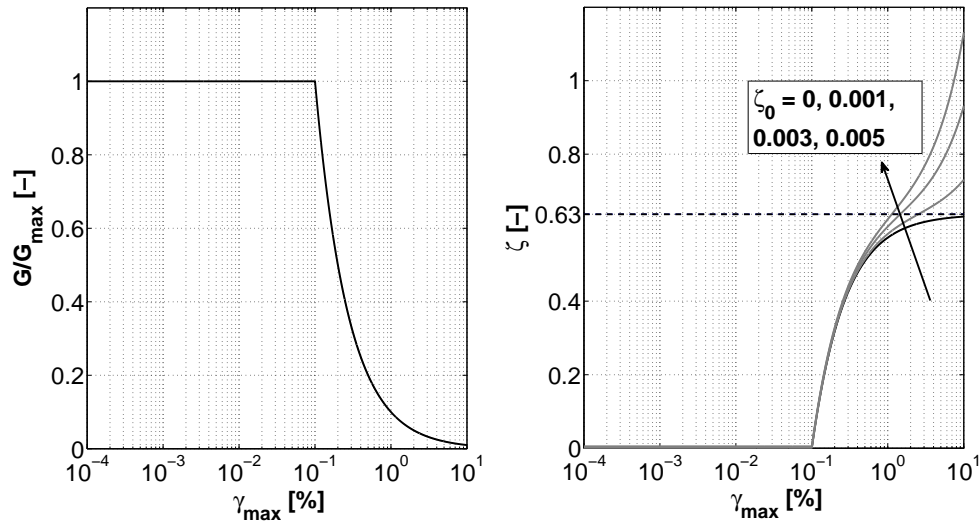


Figure 5.24: G/G_{max} and damping curves for a elastic-perfectly plastic model with linear viscous damping at varying ζ_0 ($\tau_{lim}=100$ kPa, $G_{max}=100$ MPa)

The fact that the viscous mechanism can modify the purely frictional $\zeta - \gamma_{max}$ curve without altering the cyclic stiffness degradation can be fruitfully exploited to improve experimental-numerical agreement in terms of energy dissipation.

Model performance and calibration

The frictional mechanism of the above model is characterized by a very low number of material parameters, namely the following seven:

- two elastic parameters, the Young modulus E (or the shear modulus G_{max}) and the Poisson's ratio ν ;
- the shear strength parameter M for the definition of the bounding surface (Equation (5.5));
- the flow rule parameters, ξ and k_d , governing the increment of the volumetric plastic strain under shearing and the size of the dilatancy surface, respectively (Equation (5.6));
- the hardening parameters h and m for the dependence of the hardening modulus on the distance coefficient β (Equation (5.19)), affecting the pre-failure deformational behavior and, in overall, the resulting dynamic properties (G/G_{max} and damping curves).

Provided a reasonable value for the Poisson's ratio (usually in the range 0.25–0.4), the small-strain elastic stiffness can be evaluated from dynamic laboratory (RC tests) or *in situ* (seismic geophysical surveys) tests. As far as the shear strength is concerned, the parameter M can be related to the friction angle ϕ as follows:

$$M = \frac{6 \sin \phi}{3 \pm \sin \phi} \quad (5.27)$$

to reproduce triaxial compression (sign $-$ in (5.27)) or extension (sign $+$ in (5.27)) failure conditions. While different bounding deviatoric sections would easily capture both compressive and extensive limits (Manzari and Dafalias, 1997), the calibration of a circular deviatoric locus can be tackled – as usual – by setting a trade-off M in between the bounding values in Equation (5.27) (this is appropriate, for instance, for plane strain problems). Also, since no strain-softening is reproduced, the peak strength or the residual ϕ is to be considered on the basis of the specific purpose of the analysis, i.e. depending on whether optimistic or safe assessments are needed. In any case, the present version of the model is not well suited for problems where simulating failure is particularly relevant (e.g. slope stability analysis).

The calibration of the flow rule parameters, ξ and k_d , requires at least a triaxial test to be performed, in order to obtain some information about the volumetric behavior. In particular, under undrained triaxial conditions, k_d coincides with the stress ratio ($\eta = q/p'$) characterizing the so-called “phase transformation line” (Ishihara et al., 1975) and determining the compactive/dilatative transition. In the case of loose (compactive) materials, since fixed bounding and dilatancy surfaces are considered in this version of the model, $k_d = M$ is set to ensure a compactive behavior vanishing as the limit external locus is achieved. Figure 5.25 shows the predicted triaxial response for three different values of k_d (and fixed ξ), that is by varying the opening angle of the dilatancy surface (the employed parameters are reported in the figure caption, where p_0 stands for the initial mean pressure).

While the limit stress deviator q is exclusively given by M , the pre-failure behavior is influenced by the plastic deformability and therefore by k_d . The model possesses sufficient flexibility to reproduce contractive, dilatative or contractive/dilatative behavior; also, such a feature is necessary to reproduce undrained conditions (liquefying and non-liquefying responses), this being a further motivation for non-associativeness when dealing with sandy materials.

Figure 5.26 exemplifies the response predicted under pure shear (PS) cyclic loading, applied as a sinusoidal shear strain history ($\gamma_{max} = 0.2\%, 20\%$, period $T=2\pi$ s) at constant normal stresses (and thus constant mean pressure p_0 as well). This corresponds with a radial loading path on the deviatoric plane); for the sake of clarity, the volumetric plastic response has been inhibited ($\xi=0$), in order to evaluate the deviatoric mechanism exclusively. Both purely frictional (solid line) and frictional/viscous (dashed line) responses are plotted.

Owing to the kinematic hardening of the vanished yield locus, the model can reproduce both the Bauschinger and the Masing effects, the latter implying the stabilization of the cyclic response to take place after more than one loading cycle. As expected, the additional viscous damping increases the area of the cyclic loop and therefore the overall dissipated energy; however, the effect of the viscous dissipation becomes significant only at medium-high shear strains, corresponding – for a given loading frequency – with higher strain rates. Further, viscosity causes the aforementioned “smoothing” of stress reversals, as it can be noticed in Figure 5.27 by comparing the purely frictional and the frictional/viscous responses.

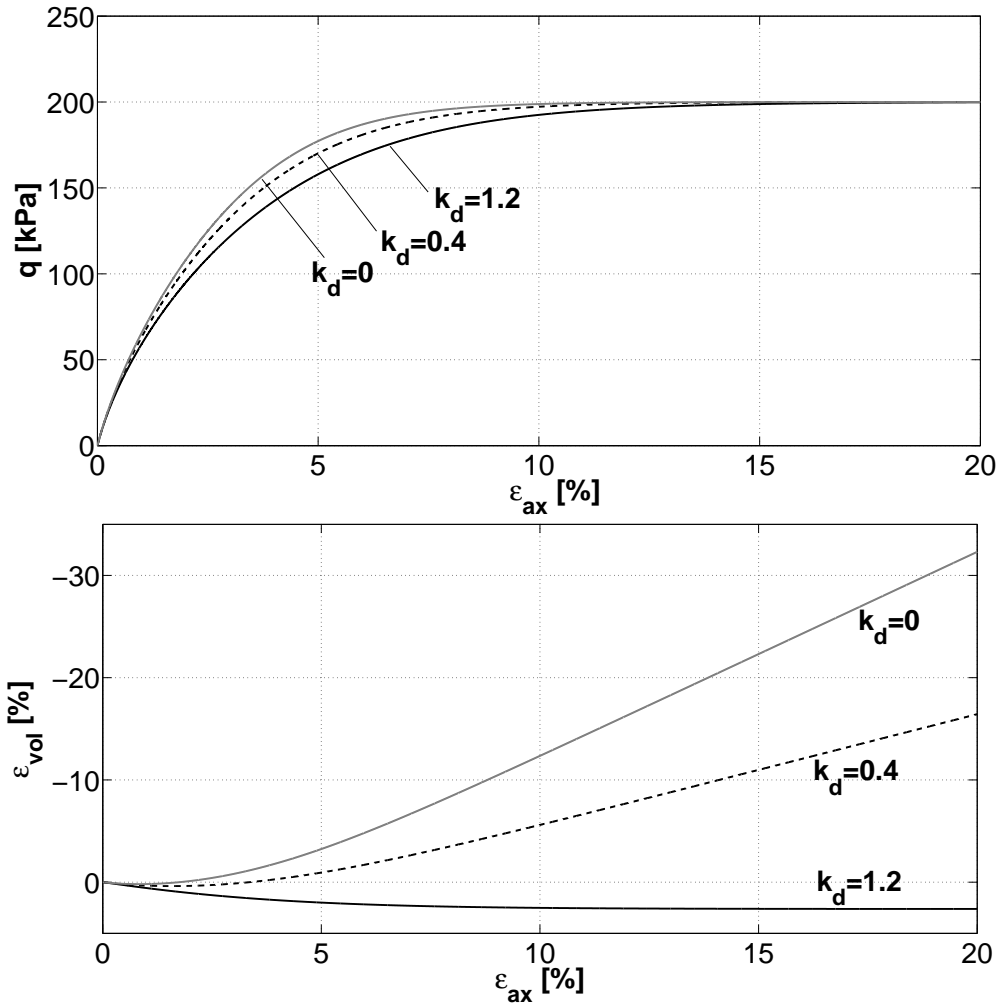


Figure 5.25: Predicted triaxial responses for different dilatancy surfaces ($p_0=100$ kPa, $G_{max} = 4$ MPa, $\nu=0.25$, $M=1.2$, $\xi=1$, $h=G/(1.5p_0)$, $m=1$)

Given the elastic stiffness and the strength of the soil, the shape of the resulting loading cycles is totally governed by the hardening properties, by h and m in Equation (5.19): this directly affects the simulation of experimental G/G_{max} and damping curves, which can be therefore exploited for the calibration of both h and m . The following equality holds under PS loading conditions:

$$1 = \frac{G}{G_{max}} \left[1 + \frac{6G_{max}}{hp_0\gamma_{max}} \int_0^{\gamma_{max}} \left(\frac{\gamma}{\tau_{lim}/G - 2\gamma + \gamma_{max}} \right)^m d\gamma \right] \quad (5.28)$$

where $\tau_{lim} = Mp_0/\sqrt{3}$. Relationship (5.28) has been obtained by integrating the constitutive equations over the first loading cycle, and represents the frictional counterpart of Equation (6)

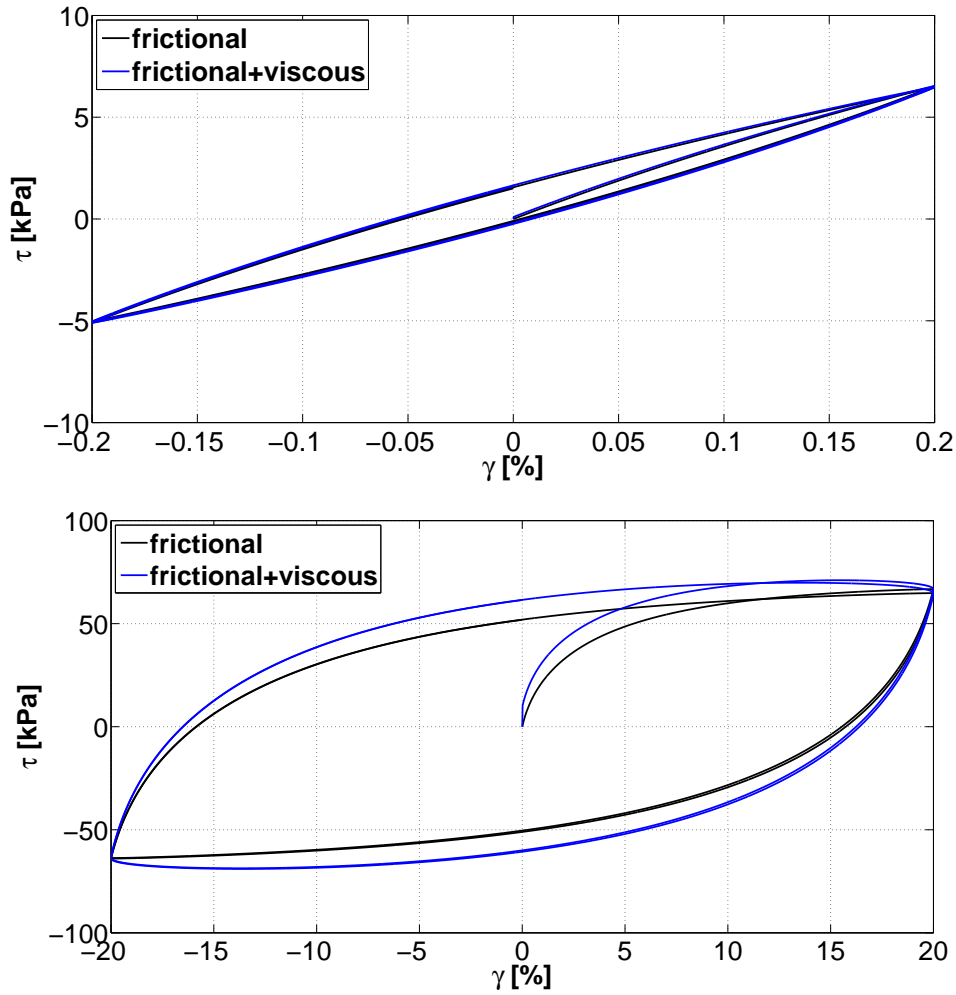


Figure 5.26: Predicted pure shear response at two different shear strain amplitudes ($p_0=100$ kPa, $T=2\pi$ s, $\zeta_0 = 0.006$, $G_{max} = 4$ MPa, $\nu=0.25$, $M=1.2$, $k_d=\xi=0$, $h=G/(1.5p_0)$, $m=1$)

in Borja et al. (2000) – as is testified by the explicit influence of the confining pressure p_0 . The proper use of Equation (5.28) requires first the choice of two meaningful points on the G/G_{max} experimental curve, i.e. two $(\gamma_{max}, G/G_{max})$ couples; then, the unknowns h and m are obtained by solving the integral system arising from the specification of Equation (5.28) for both selected $(\gamma_{max}, G/G_{max})$ couples.

Figure 5.28 illustrates the result of the above calibration procedure, applied on the G/G_{max} and ζ curves for sands implemented into the code EERA (Bardet et al., 2000) and formerly obtained by Seed and Idriss (1970).

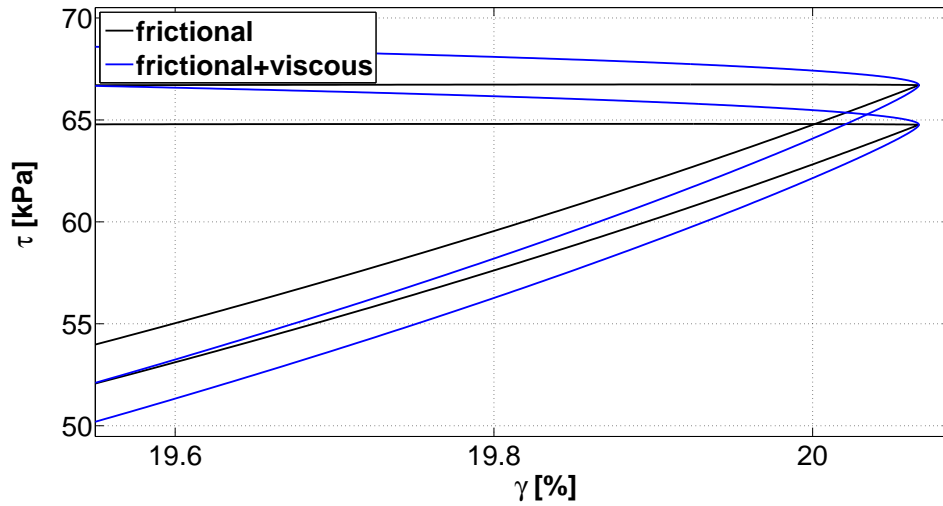


Figure 5.27: Detail of stress reversals for the pure shear response in Figure 5.26 ($\gamma_{max} = 20\%$)

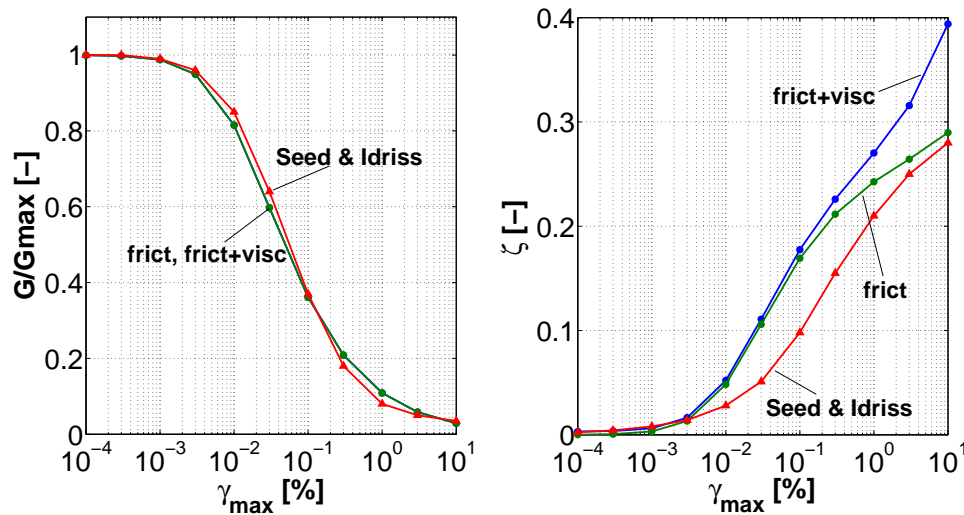


Figure 5.28: Comparison between experimental and simulated G/G_{max} and damping curves ($p_0=100$ kPa, $T=2\pi$ s, $\zeta = 0.003$, $G_{max} = 4$ MPa, $\nu=0.25$, $M=1.2$, $k_d=\xi=0$, $h=G/(112p_0)$, $m=1.38$)

Since Equation (5.28) exclusively accounts for the G/G_{max} curve, the very satisfactory agreement in terms of stiffness degradation (viscosity has no effect on it) should not surprise. On the other hand, once h and m are set, the predicted damping curve may or may not match the experimental outcome irrespective of the calibration procedure. In this respect, Figure 5.28 also presents the comparison between the damping curve by Seed and Idriss and the model pre-

diction. The frictional ζ curve lies in the same experimental range, even though the accuracy at $\gamma_{max} = 0.03 - 1\%$ is not as good as for the G/G_{max} ratio. In this case, the contribution of the viscous mechanism is practically non-existent, as it only increases the total ζ ratio for $\gamma_{max} > 0.1\%$.

Depending on the specific application, a “trial and error” calibration might be preferable, sacrificing some of the accuracy in terms of G/G_{max} ratio to improve the damping performance. A possible outcome of a manual calibration is plotted in Figure 5.29: apparently, while the simulation of the stiffness curve is still acceptable, the damping curve appears to be much better than the previous one. The use of the viscous mechanism seems to be highly beneficial, since it remedies the lack of accuracy in the frictional curve at medium/large cyclic strains.

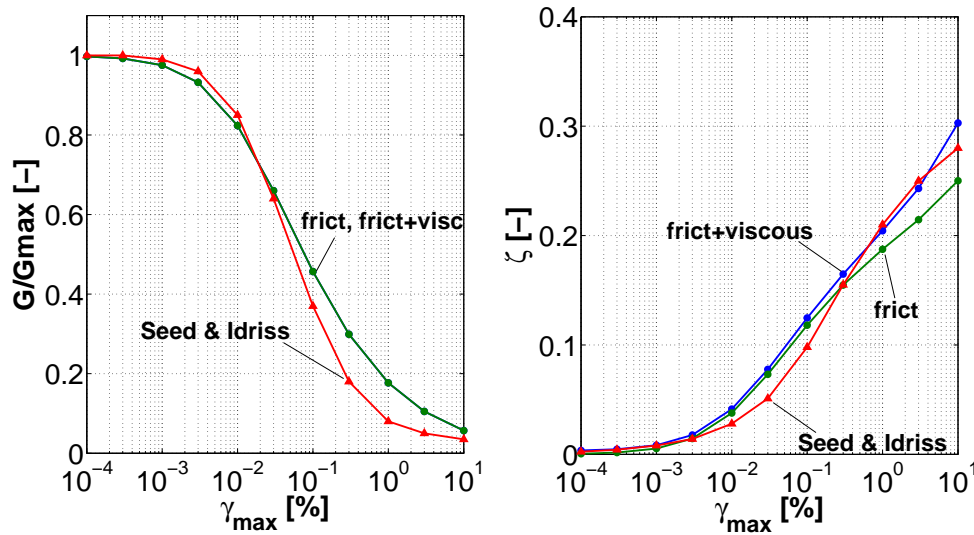


Figure 5.29: Comparison between experimental and simulated G/G_{max} and damping curves ($p_0=100$ kPa, $T=2\pi$ s, $\zeta = 0.003$, $G_{max} = 4$ MPa, $\nu=0.25$, $M=1.2$, $k_d=\xi=0$, $h=G_{max}/(15p_0)$, $m=1$)

It is also worth noting that the experimental/numerical agreement is satisfactory up to even $\gamma_{max} = 10\%$, where substantial plasticity occurs and, in any case, the extrapolation of cyclic curves from experimental data is – to say the least – questionable.

Besides, if the experimental data under examination are unsatisfactorily reproduced for any h and m combination, the user still has the chance of substituting the interpolation function (5.19) with no further changes in the model formulation. In particular, the present model is as flexible

as the one by Borja and Amies (1994) in reproducing, for a given initial mean pressure, usual 1D non-linear laws for soils, such as the exponential, the hyperbolic, the Davidenkov and the Ramberg-Osgood models (for this latter a hardening bounding surface would be needed as well). Matching the aforementioned 1D laws ensures sufficient capability of reproducing experimental curves of usual shape.

Parametric analysis

In this section the influence of some relevant input parameters on the model predictions is parametrically investigated.

Influence of the confining pressure

Figure 5.30 illustrates the sensitivity, under PS loading, of both G/G_{max} and damping frictional curves to the initial confining pressure. As can be noticed, increasing p_0 does enlarge the “pseudo-elastic” range, that is the strain interval within which the deviation by the elastic behavior is negligible even with a vanishing yield locus. It is also noted that the variations in the confining pressure do not imply appreciable changes in the shape of the curves.

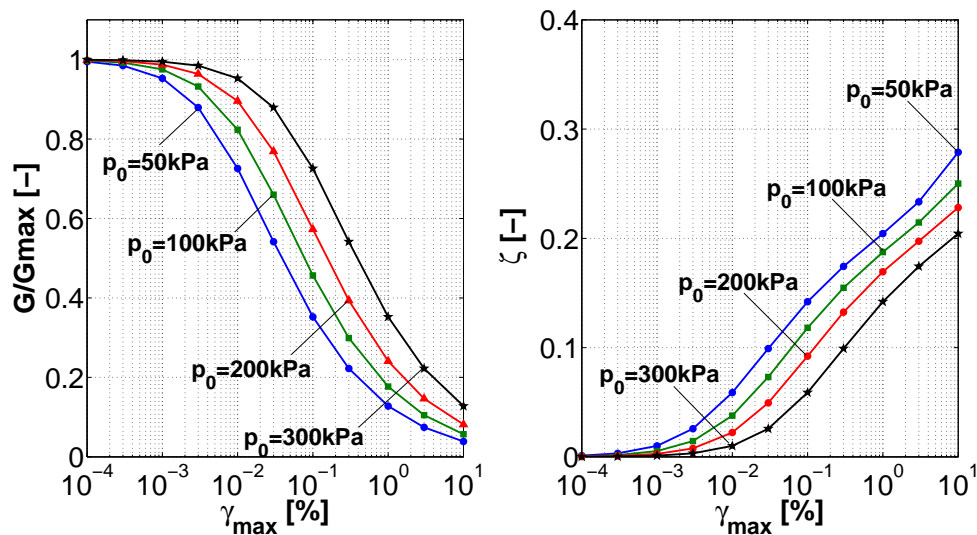


Figure 5.30: Simulated G/G_{max} and damping curves at varying confining pressure ($T=2\pi$ s, $G_{max} = 4$ MPa, $\nu=0.25$, $M=1.2$, $k_d=\xi=0$, $h=G/(15p_0)$, $m=1$)

Although the present version of the model is apparently pressure-dependent, it cannot quantitatively reproduce the pressure-sensitiveness of G/G_{max} and ξ curves arising from real experiments and incorporated into some analytical formulas (Ishibashi and Zhang, 1993; Darendeli, 2001). This stems from the fact that the influence of the mean pressure only concerns the plastic component of the model, while constant elastic (and viscous) moduli have been adopted for the initial simulation of only PS loading tests. From this point of view, two easy improvements are possible and mutually compatible:

1. use of hyper- or hypo-elastic laws with variable moduli (Papadimitriou and Bouckovalas, 2002; Andrianopoulos et al., 2010);
2. adoption of p -dependent hardening parameters (i.e. h and m).

In particular, the latter point does not introduce any further difficulty in terms of analytical/numerical treatment, since it only affects the interpolation rule (5.19). Appropriate $h(p)$ and $m(p)$ relationships could be easily obtained by first calibrating h and m on experimental or analytical cyclic curves for different p values, and then analytically interpolating the parameters values over a meaningful pressure range.

Influence of the hardening parameters

Figures 5.31 and 5.32 show the influence of the hardening parameters h and m on the predicted cyclic curves. In particular, a decrease in either h or m implies a faster development of plastic strains, so that the closely-elastic range tends to disappear and $G/G_{max} < 1$ and $\zeta > 0$ at even $\gamma_{max} = 10^{-4}\%$; conversely, an extended pseudo-elastic behavior can be obtained over a large strain range by increasing the hardening parameters. Apparently, the model ensures high flexibility in terms of cyclic curve shapes, so that the response of standard elastic-plastic models (i.e. with non-vanishing elastic region) can be smoothly approximated (compare for instance the $m = 3$ curves in Figure 5.32 and the analytical elastic-perfectly plastic frictional curves in Figure 5.24).

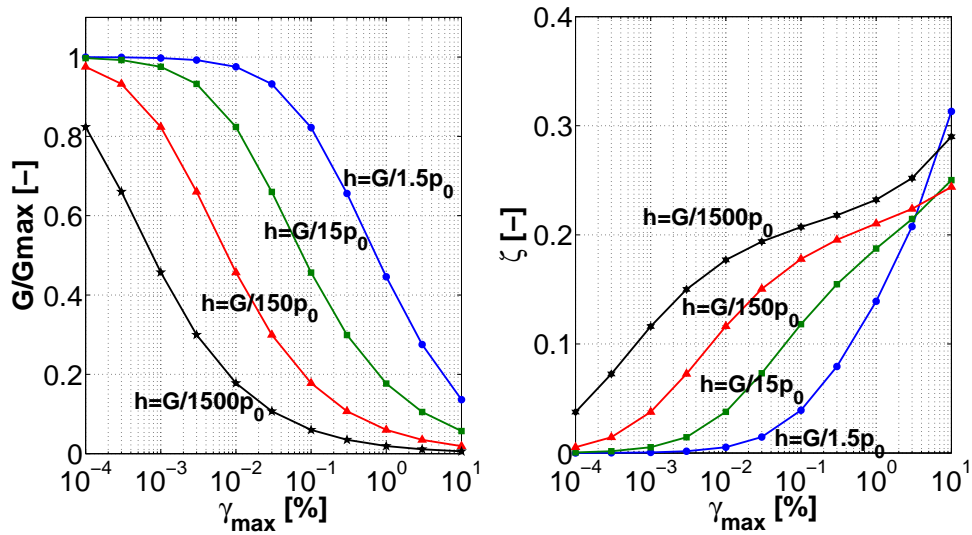


Figure 5.31: Simulated G/G_{max} and damping curves at varying h ($p_0=100$ kPa, $T=2\pi$ s, $G_{max} = 4$ MPa, $\nu=0.25$, $M=1.2$, $k_d=\xi=0$, $m=1$)

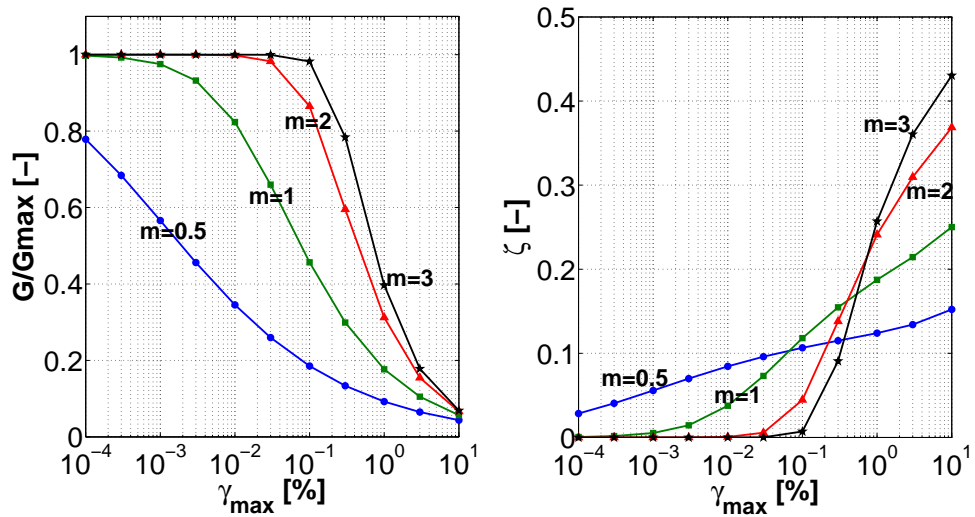


Figure 5.32: Simulated G/G_{max} and damping curves at varying m ($p_0=100$ kPa, $T=2\pi$ s, $G_{max} = 4$ MPa, $\nu=0.25$, $M=1.2$, $k_d=\xi=0$, $h=G_{max}/(15p_0)$)

Influence of the viscous mechanism

The influence of the viscous parameter ζ_0 on the resulting frictional/viscous damping curve is illustrated in Figure 5.33 (the G/G_{max} is not affected by the parallel viscous mechanism). As was expected, an increase in ζ_0 induce larger values of ζ ($\gamma_{max} \rightarrow 0$), as well as a faster increase

of the ζ curve at medium/high cyclic strains. Figure 5.33 confirms the usefulness of the viscous mechanism, which can be exploited as an additional degree of freedom for reproducing the cyclic dissipative soil behavior.

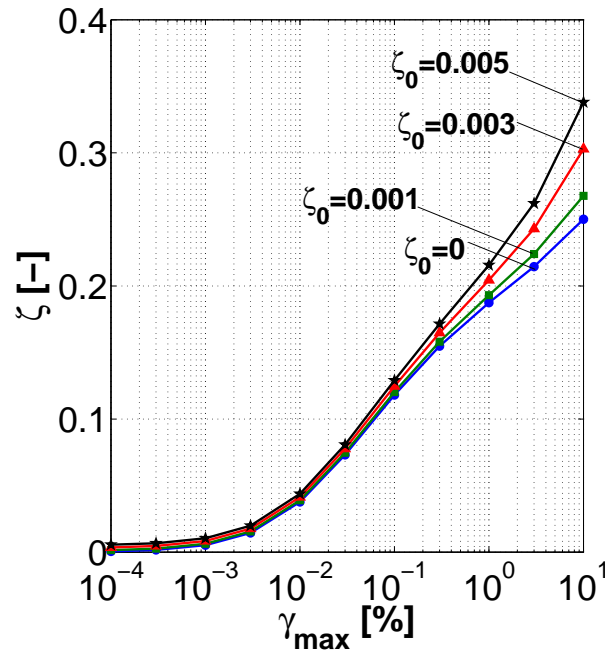


Figure 5.33: Damping curves simulated at varying ζ_0 ($p_0=100$ kPa, $T=2\pi$ s, $G_{max} = 4$ MPa, $\nu=0.25$, $M=1.2$, $k_d=\xi=0$, $h=G_{max}/(15p_0)$, $m=1$)

Interaction between volumetric behavior and kinematic constraints

All the above simulations have been performed by inhibiting the elastic-plastic soil dilatancy ($\xi = 0$), which in most cases cannot be done to represent real soil behavior. As previously shown for triaxial loading conditions (Figure 5.25), in the absence of kinematic boundary constraints, a variation in the volumetric behavior slightly affects only the hardening evolution of the stress-strain response toward the limit shear strength; a similar consideration applies to PS loading conditions, since even in this case the normal confinement is statically determined.

However, computational (FE) models often contain kinematic constraints arising from certain symmetries (consider e.g. plane strain or one-dimensional schemes) (Prevost, 1989; Borja et al., 1999; di Prisco et al., 2012). In addition, for SSI problems, where soil interacts with a (stiff)

structural foundations and wall, the soil volume change plays an important role. The presence of kinematic constraints implies that the value of some stress components directly derives from compatibility requirements (e.g. prevented lateral expansion). That means that the local mean confinement is affected by the tendency of the material to dilate or contract. In particular, dilative frictional materials will increase the limit shear stress (with respect to unconfined conditions), while compactive frictional materials will decrease the limit shear stress. Further, not only the limit shear stress, but also the whole pre-failure response depends on the plastic flow rule whenever kinematic constraints are imposed (di Prisco and Pisanò, 2011; di Prisco et al., 2012).

The above considerations suggest that both experimental and numerical results are certainly affected by the kinematics of the system, even though this effect is not easy to be *a priori* quantified in terms of G/G_{max} and ζ curves. The kinematic conditions of an infinite soil layer during 1D shear wave propagation are experimentally approximated through the well known “simple shear (SS) apparatus” (Wood, 2004), in which the soil specimen is cyclically sheared with no lateral expansion allowed. In order to assess how the kinematic confinement influences the cyclic response, stiffness degradation and damping curves are hereafter simulated under SS conditions by varying the volumetric response of the soil; in particular, three different calibrations of the plastic flow rule (5.6) are considered, namely (i) isochoric ($k_d = \xi = 0$), (ii) compactive ($k_d = M$, $\xi = 1$) and (iii) dilative ($k_d = 0.4$, $\xi = 1$)

The results reported in Figure 5.34 provide an insight into the possible effect of the volumetric response in combination with constrained loading conditions. In the isochoric case, the PS and the SS curves perfectly match (compare e.g. with the $p_0 = 100$ kPa curves in Figure 5.30), as, with no plastic expansion (or contraction), the lateral constraints do not affect the mean pressure during the shear loading; conversely, non-negligible SS-PS differences arise when dilative or contractive materials are considered. As is evident in Figure 5.34, the discrepancy between isochoric and non-isochoric curves becomes evident at medium/high cyclic strains, i.e. when significant plastification take place. Indeed, while the mechanical response is barely inelastic, the deviatoric and the volumetric responses are practically decoupled, so that no variation of the normal confinement takes place.

Apparently, the quantitative relevance of this effect strictly relates to the actual dilational properties of the material: soils undergoing significant volume changes under unconfined shear

will exhibit a high sensitiveness to boundary constraints. The cyclic interaction between volumetric behavior and kinematic constraints seems to be poorly investigated in literature and is worth remarking for both theoretical and practical motivations. Indeed, the cyclic behavior measured through certain experimental devices (triaxial, biaxial, simple shear, torsional shear, etc) can differ from the mechanical response characterizing other kinematic conditions in boundary value problems, so that the employment of volume-insensitive models (such as the linear equivalent) may lead to inaccurate predictions. In particular, Equation (5.19) clearly shows that if any relevant p variation arises from the interaction between dilatancy and boundary constraints, a variation in the hardening modulus H and, therefore, the resulting stiffness will also take place. As a consequence, an influence on the global (non-linear) dynamic response is expected in terms of both amplitude amplification and frequency content (Roten et al., 2013). While this aspect is totally disregarded by most modeling approaches in GEE, further work is currently ongoing to quantitatively investigate the role of soil dilatancy in affecting the outcomes of seismic site response (elastic-plastic) analysis.

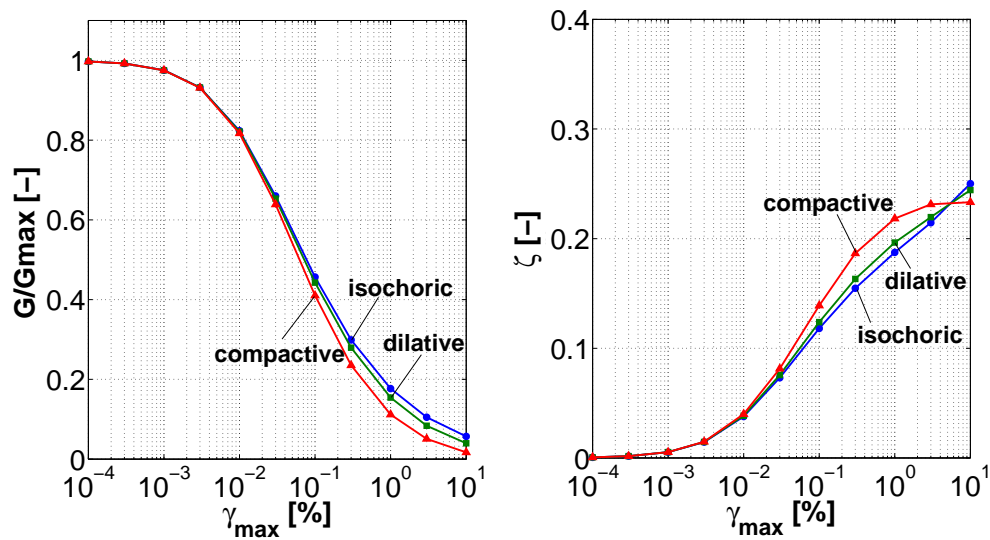


Figure 5.34: G/G_{max} and damping curves simulated under SS conditions and different volumetric responses ($p_0=100$ kPa, $T=2\pi$ s, $G_{max} = 4$ MPa, $\nu=0.25$, $M=1.2$, $k_d=[1.2, 0.4]$, $\xi=[0,1]$, $h=G_{max}/(15p_0)$, $m=1$)

Derivation of Equation (5.28)

Under PS loading conditions (pure shear at constant mean pressure), Equation (5.16) produces the following simple expression for β :

$$\beta = \frac{\tau_{lim} - \tau}{\tau - \tau_0} \quad (5.29)$$

where $\tau_{lim} = Mp_0/\sqrt{3}$ and p_0 is the initial (and constant) mean pressure. Equation (5.12) can be easily specified for PS loading:

$$dq = \sqrt{3}d\tau = \sqrt{\frac{2}{3}}H\|de_{ij}^p\| = \sqrt{\frac{2}{3}}H\frac{d\gamma^p}{\sqrt{2}} \implies d\tau = \frac{H}{3}d\gamma^p \quad (5.30)$$

so that the following form of the PS elastic-plastic response results:

$$d\gamma = d\gamma^e + d\gamma^p = \frac{d\tau}{G_{max}} + \frac{3d\tau}{H} \quad (5.31)$$

and, after substituting (5.29) into (5.19):

$$d\gamma = \frac{d\tau}{G_{max}} + \frac{3d\tau}{p_0h\beta^m} = \frac{d\tau}{G_{max}} + \left(\frac{\tau - \tau_0}{\tau_{lim} - \tau}\right)^m \frac{3d\tau}{p_0h} \quad (5.32)$$

Integration over a strain interval between two stress reversals ($\gamma \in [-\gamma_{max}; \gamma_{max}]$) yields:

$$2\gamma_{max} = \frac{2\tau}{G_{max}} + \frac{3}{hp_0} \int_{-\tau}^{\tau} \left(\frac{\tau' + \tau}{\tau_{lim} - \tau'}\right)^m d\tau' \quad (5.33)$$

where $\tau_0 = -\tau$ has been set. Straightforward variable changes lead to:

$$1 = \frac{G}{G_{max}} + \frac{3}{2hp_0\gamma_{max}} \int_0^{2G\gamma_{max}} \left(\frac{\tau''}{\tau_{lim} - \tau'' + G\gamma_{max}}\right)^m d\tau'' \quad (5.34)$$

$$1 = \frac{G}{G_{max}} \left[1 + \frac{6G_{max}}{hp_0\gamma_{max}} \int_0^{\gamma_{max}} \left(\frac{\gamma}{\tau_{lim}/G - 2\gamma + \gamma_{max}}\right)^m d\gamma \right] \quad (5.35)$$

It is worth highlighting that two approximations are implicitly contained in Equation (5.35): (i) the integration over the first loading cycle does not exactly reproduce the stabilized cyclic response (because of the aforementioned Masing effect); (ii) a symmetric loading cycle in terms of shear strain does not in general ensure the symmetry of the corresponding shear stress range (as it is assumed in Equation (5.33)). However, such approximations do not prevent reasonable values for the hardening parameters h and m to be obtained.

Concluding remarks

An incremental 3D visco-elastic-plastic constitutive model was developed to simulate stiffness degradation (G/G_{max}) and damping in soils under cyclic/dynamic loading. The model is based on an effective-stress formulation with two parallel dissipative mechanisms, purely frictional (elastic-plastic) and viscous.

As far as the frictional mechanism is concerned, a bounding surface formulation with vanishing elastic region was adopted, extending to pressure-sensitive non-associative soils the previous cohesive model by Borja and Amies (1994) for total-stress analysis, but maintaining higher simplicity than later works, such as that e.g. by Andrianopoulos et al. (2010). The main features of the frictional model are: (i) the vanishing yield locus implies an elastic-plastic response at any load levels, as is observed in real experiments; (ii) a minimum number of physically meaningful parameters, which can be easily calibrated on few experimental data; (iii) excellent performance and flexibility in reproducing in the elastic-plastic framework the standard stiffness degradation and damping curves. With reference to these latter, the parallel viscous mechanism – easy to be introduced in FE computations – was shown to provide an additional degree of freedom to improve the simulation of the cyclic energy dissipation, as long as the viscous parameter is properly calibrated. As a matter of fact, the viscous mechanism, used here, does physically exist in the form of viscous interaction between the soil solid skeleton and the pore fluid(s), and needs to be taken into account (as for example done here).

5.3.4 Energy Dissipation of Soil/Rock (Viscous and Frictional).

Dissipation of seismic energy as it propagates through soil/rock layers is mostly due to the displacement proportional frictional damping. There is also a component of energy dissipation that is velocity proportional (viscous) but that component is usually dissipating much less energy than the frictional damping. Both frictional and viscous damping. Use of Pisanò material model allows for direct computation of frictional energy dissipation, while viscous energy dissipation can be calculated from velocity data.

5.3.5 Calibration of Material Model from Available G/G_{max} and Damping Curves.

Usually available data for soil behavior in practical applications and design consists of stiffness reduction (G/G_{max}) and damping curves. The challenge of developing a full 3D, elastic-plastic material model using only such limited data (please note lack of volume change data) is met through the development of Pisanò material model.

5.4 NPP Model with Inelastic Soil

Generic model presented in the last progress report is used for assessing effects nonlinear soil has on seismic response of NPPs. The finite element mesh of this model is shown in Figure 5.35.

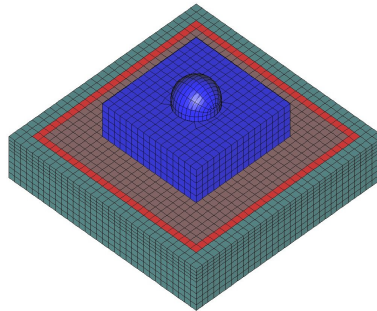


Figure 5.35: Finite element model for a single NPP with the containment and auxiliary buildings on a common base mat, as well as the soil/rock sub-base, DRM layer for seismic motions input and the layers outside of DRM for damping out outgoing waves. The soil sub-base is modeled using elastic-plastic Pisanò model.

Preliminary calculations of energy dissipation per unit volume ($W = \int \sigma_{ij} d\epsilon_{ij}^{pl}$), as shown in Figure 5.36 (Jeremić, 2010) are used to assess effects soil under the foundation has on a response of an NPP.

In addition to energy dissipation, changes in dynamics of an NPP due to reduction of stiffness of underlying soil are observed and will be reported at the June 2014 meeting at CNSC headquarters. In addition to that, finite element models, that are used in this study will be delivered as well.

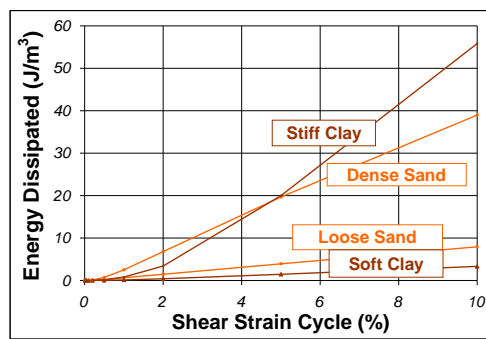


Figure 5.36: Energy dissipation capacity for one cycle at various strains for four generic soils (Jeremić, 2010).

Chapter 6

Task 4.4: Modeling Slipping and Gaping

6.1 Summary of Findings for Task 4.4

The main findings are:

- Contact of foundation concrete and sub-base soil/rock is of great importance for dynamic response of an NPP, as this contact can significantly change NPP response.
- Placement of impermeable plastic sheets under foundation concrete (to prevent ground water contact with concrete) can significantly decrease friction coefficients of concrete on sub-base soil/rock, thus acting as an unintended base isolation system.
- Gap opening/closing modeling is important as it might introduce artificial high frequencies into vertical motions.
- Choice of proper stiffness (penalty) is important in order to reduce potential numerical modeling problems.
- Calibration of slipping resistance is very important, yet such resistance is rarely measured. Both cases, (a) direct contact of foundation to the soil/rock and (b) placement of layers of plastic sheets to prevent water penetration are important and data needs to be collected for each case.

- Importance of modeling fully saturated contact zone, where effective stresses (and pore fluid pressure) will change the mechanics of contact behavior.
- Inelastic behavior of contact zone during earthquakes can have both beneficial and detrimental effects on global dynamic response of an NPP. Such effects have to be analyzed on a case by case basis.
- Significant amount of seismic energy can be dissipated within a contact zone, thus reducing seismic demand on NPP structure, systems and components.

6.2 Methodology

In soil-structure systems, there always exist an interfaces between concrete and soil. These contact zones can detach and open gaps, and can also slip. Modeling of contact is done using contact finite elements. Simplest contact elements are based on a two node elements, the so called joint elements which were initially developed for modeling of rock joints. Typically normal and tangential stiffness were used to model the pressure and friction at the interface (Sheng et al. (2007); Haraldsson and Wriggers (2000); Desai and Siriwardane (1984)).

The study of two dimensional and axisymmetric benchmark examples have been done by Olukoko et al. (1993) for linear elastic and isotropic contact problems. Study was done considering Coulomb's law for frictional behavior at the interface. In many cases the interaction of soil and structure is involved with frictional sliding of the contact surfaces, separation, and re-closure of the surfaces. These cases depend on the loading procedure and frictional parameters. Sheng et al. (2007) discussed how frictional contact is important for structural foundations under loading, pile foundations, soil anchors, and retaining walls. Khoei and Nikbakhti (2006) used the extended finite element method (X-FEM) for modeling of frictional contact problems. In order to be able to simulate discontinuities in model during the analysis without considering the boundary conditions of domain, special functions should be included within standard finite element framework. A finite element method for analysis of frictional contact problems was developed by Chandrasekaran et al. (1987). The nonlinear problem is solved by imposing geometric constraints on equilibrium configuration which compatibility conditions are violated.

Different conditions happening at contact area, such as sticking and slipping, are determined from the relative magnitudes of the normal and tangential nodal forces. Developing contact finite element for analysis of connections between laminated composite plates was done by Barbero et al. (1995). Such element is compatible with a three-dimensional plate element based on constant shear theory. The contact element formulation is based on a simple regularization of the unilateral contact with a Coulomb friction problem.

Two-dimensional frictional polynomial to segment contact elements are developed by Haraldsson and Wriggers (2000) based on non-associated frictional law and elastic-plastic tangential slip decomposition. Several benchmarks are presented by Konter (2005) in order to verify the the results of the finite element analyses performed on 2D and 3D modelings. In all proposed benchmarks the results were approximated pretty well with a 2D or an axisymmetric solutions. In addition, 3D analyses were performed and the results were compared with the 2D solutions. Hjjaj et al. (2004) presented an algorithm for solving frictional contact problems where sliding rule is non-associated. The algorithm is a combination of the classical unilateral contact law and an anisotropic friction model with a non-associated slip rule. It has been observed that slip rule has a strong influence on the frictional behavior.

6.2.1 Formulation

The formulation for contact is represented by a discretization which establishes constraint equations and contact interface constitutive equations on a purely nodal basis. Such a formulation is called *node-to-node contact*. For this discretization the frictional contact formulation is developed below (Wriggers, 2002).

The variables adopted to formulate the model are shown in Figure 6.1: the force (\mathbf{F}) and displacement vectors (\mathbf{u}).

Each vector is composed of three terms: the first one acts along the longitudinal direction whereas the other two components lie on the orthogonal plane. The total relative displacement is the summation of the elastic and plastic displacements (6.2).

$$\mathbf{F} = [p \quad ; \quad \mathbf{t}]^T; \quad \mathbf{u} = [v; \quad \mathbf{g}_s]^T \quad (6.1)$$

$$\mathbf{u}^{el} = [v^{el}; \quad \mathbf{g}_s^{el}]^T; \quad \mathbf{u}^{pl} = [v^{pl}; \quad \mathbf{g}_s^{pl}]^T; \quad \mathbf{u} = \mathbf{u}^{el} + \mathbf{u}^{pl} \quad (6.2)$$

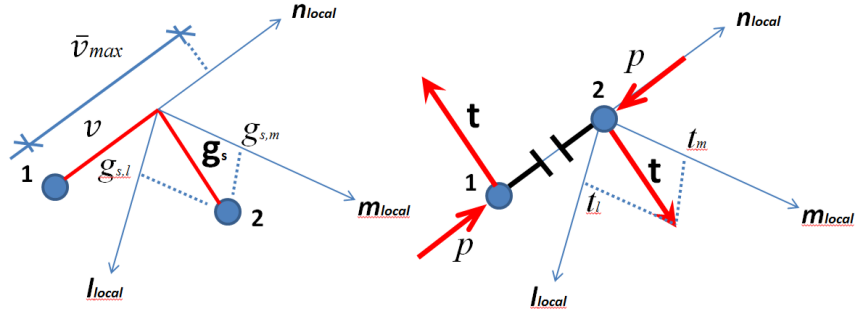


Figure 6.1: Forces and relative displacements of the element.

Elastic behavior

The elastic behavior is defined by the relation:

$$d\mathbf{F} = \mathbf{E} \cdot d\mathbf{u}^{el}; \quad \mathbf{E} = \begin{bmatrix} K_N(p) & 0 & 0 \\ 0 & K_T & 0 \\ 0 & 0 & K_T \end{bmatrix} \quad (6.3)$$

The normal displacement-normal force relationship, valid for loading and unloading conditions, is the same that has been introduced by Gens et al. (1988, 1990) and given by:

$$p = C_N \frac{v^{el}}{(\bar{v}_{max} - v^{el})} \quad (6.4)$$

v^{el} is the normal relative elastic displacement, \bar{v}_{max} represents the maximum closure value and C_N is a constant. This relation is valid only whenever the difference $(\bar{v}_{max} - v^{el})$ is greater than zero, otherwise p is set equal to zero. The derivative of (6.4) gives the normal stiffness K_N (6.5), that depends on both the maximum closure \bar{v}_{max} and the current value of the elastic normal displacement v^{el} . The tangential stiffness K_T is assumed to be constant.

$$K_N = \frac{C_N \bar{v}_{max}}{(\bar{v}_{max} - v^{el})^2} \quad ; \quad K_T = const \quad (6.5)$$

An alternative normal force deformation relationship is given as

$$f_n(u_x, u_y, u_z) = \begin{cases} \frac{1}{2}k_n u_x^2 + 0.0001k_n u_x & ,\text{if } u_x < 0 \\ 0 & ,\text{if } u_x \geq 0 \end{cases} \quad (6.6)$$

Force–displacement equation $f_n(u_x) = \frac{1}{2}k_n u_x^2 + 0.0001k_n u_x$ is a parabola that has a non-zero tangent at $u_x = 0$, as this helps in solving the problem. The value of stiffness $0.0001k_n$ is chosen as stiffness at 1/10 of millimeter (0.0001m)...

This alternative formulation for normal force-displacement behavior has some benefits for concrete - soil modeling and is currently used in the program.

Plastic model

The plastic model is defined in terms of yield surface and plastic potential represented in Figure 6.2. Since the proposed model reproduces an elasto-perfectly plastic behavior of the interface, no hardening rule has been introduced. The expression for the implemented yield surface corresponds to a particular case of the Mohr-Coulomb criteria (6.7), in which the only parameter is the frictional one ($\mu = \tan\phi$) and the cohesion is neglected. On the contrary, the expression adopted for the plastic potential is a von Mises criteria (6.8), in which k is a positive constant. The direction of the normal to the plastic potential G_s is not orthogonal to the yield function (unless the friction angle $\phi = 0$), so the flow rule is non-associated and the plastic normal relative displacement is always zero. This means that the normal elastic displacements (v^{el}) are equal to the total normal displacements (v).

$$f_s \equiv \|\mathbf{t}\| - \mu p = 0 \quad (6.7)$$

$$G_s \equiv \mathbf{t}^2 - k^2 = 0 \quad (6.8)$$

Implementation

The formulation used for the implementation is the Implicit General Backward Euler algorithm in stress space (*GBE*). *GBE* algorithm solves the problem in two steps:

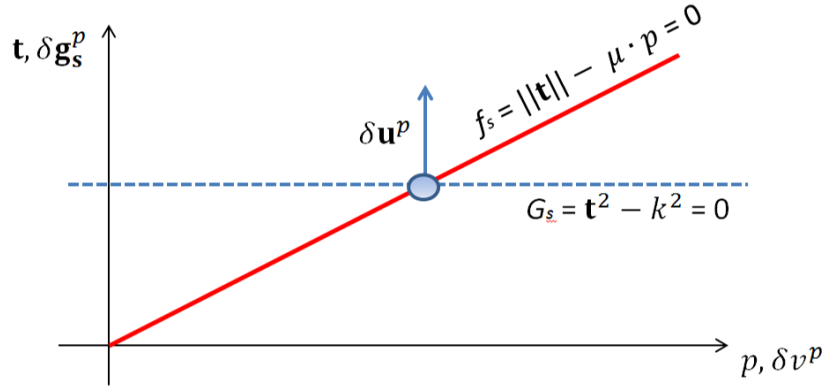


Figure 6.2: Yield surface f_s , plastic potential G_s and incremental plastic displacement $\delta \mathbf{u}^p$.

- the elastic problem is solved - with the prescribed initial conditions - to obtain a trial elastic state;
- if the trial state is outside the yield locus, the plastic problem is solved - at a fixed current configuration - assuming the trial state as initial conditions.

In this simple model the evolution equations, the constraints and the initial conditions are, respectively:

$$\begin{cases} \Delta \mathbf{F}_{n+1} = \mathbf{E} \Delta \mathbf{u}_{n+1}^{\text{el}} = \mathbf{E} [\Delta \mathbf{u}_{n+1} - \Delta \mathbf{u}_{n+1}^{\text{pl}}] \\ \Delta \mathbf{u}_{n+1}^{\text{pl}} = \Delta \lambda_{n+1} \frac{\partial G_{s_{n+1}}}{\partial \mathbf{F}_{n+1}} \end{cases} \quad (6.9)$$

$$\Delta \lambda_{n+1} \geq 0 \quad ; \quad f_s(\mathbf{F}_{n+1}) \leq 0 \quad ; \quad \Delta \lambda_{n+1} f_s(\mathbf{F}_{n+1}) = 0 \quad (6.10)$$

$$\mathbf{F} = \mathbf{F}_n \quad ; \quad \mathbf{u} = \mathbf{u}_n \quad (6.11)$$

During the first step (*elastic predictor*) the plastic flow is frozen ($\Delta \lambda = 0$), the incremental plastic displacements are set to zero and the solution is called *elastic trial state* (6.12):

$$\mathbf{F}_{n+1}^{\text{tr}} = \mathbf{F}_n + \Delta \mathbf{F}_{n+1}^{\text{tr}} = \mathbf{F}_n + \mathbf{E} \Delta \mathbf{u}_{n+1} \quad (6.12)$$

If the yield function $f_s^{tr}(\mathbf{F}_{n+1}^{tr}) \leq 0$, the solution is correct and the force vector is updated; on the contrary, the trial solution has to be corrected during the second step. In fact, the violation of the consistency condition is restored by solving the system of equations during the second step, and it is called *return mapping* (6.13):

$$\mathbf{F}_{n+1} = \mathbf{F}_{n+1}^{tr} - \Delta\lambda_{n+1} \mathbf{E} \frac{\partial G_{s_{n+1}}}{\partial \mathbf{F}} \quad ; \quad f_{s_{n+1}}^{tr} = \|\mathbf{t}_{n+1}^{tr}\| - \mu p_{n+1}^{tr} \leq 0 \quad (6.13)$$

In this case, the yield function and the plastic potential have a particular expression that the process of return mapping has an interesting geometrical interpretation. The state \mathbf{F}_{n+1} represents the closest point projection of the trial state \mathbf{F}_{n+1}^{tr} to the yield surface $f_{s_{n+1}}$ in the plane to which the tangential force belongs. Since the shape of the yield function and the plastic potential is circular in this plane, the return mapping procedure is called *radial return mapping*.

The algorithm is listed below.

$$\mathbf{g}_{s_{n+1}} = \mathbf{g}_{s_n} + \Delta\mathbf{g}_{s_{n+1}}; \quad \mathbf{g}_{s_{n+1}} = \mathbf{g}_{s_{n+1}}^{el} + \mathbf{g}_{s_{n+1}}^{pl} \quad (6.14)$$

$$v_{n+1} = v_n + \Delta v_{n+1}; \quad \delta_{n+1} = \bar{v}_{max} + v_{n+1} \quad (6.15)$$

$$\left\{ \begin{array}{l} \text{if } \delta_{n+1} > 0 \quad K_N = \frac{C_{KN} \bar{v}_{max}}{(\bar{v}_{max} - v_{n+1})^2} \quad K_T = \text{const} \\ \text{else} \quad \quad \quad K_N = K_T = 0.0 \end{array} \right. \quad (6.16)$$

$$\mathbf{t}_{n+1}^{tr} = \mathbf{t}_n + K_T \Delta\mathbf{g}_{s_{n+1}}; \quad p_{n+1}^{tr} = K_N \Delta v_{n+1} + p_n \quad (6.17)$$

$$\text{check if } f_{s_{n+1}}^{tr} = \|\mathbf{t}_{n+1}^{tr}\| - \mu p_{n+1}^{tr} \leq 0 \quad (6.18)$$

$$\text{if } f_{s_{n+1}}^{tr} > 0 \quad \mathbf{t}_{n+1} = \mathbf{t}_{n+1}^{tr} - \Delta\lambda K_T \mathbf{n}_{n+1}$$

$$p_{n+1} = p_{n+1}^{tr}$$

$$\mathbf{n}_{n+1} = \mathbf{n}_{n+1}^{tr} = \frac{\mathbf{t}_{n+1}^{tr}}{\|\mathbf{t}_{n+1}^{tr}\|} \quad (6.19)$$

$$\Delta\lambda = \frac{1}{K_T} (\|\mathbf{t}_{n+1}^{tr}\| - \mu p_{n+1})$$

$$\text{update } \Delta\mathbf{g}_{s_{n+1}}^{pl} = \Delta\lambda \mathbf{n}_{n+1} \quad ; \quad \Delta\mathbf{g}_{s_{n+1}}^{el} = \Delta\mathbf{g}_{s_{n+1}} - \Delta\mathbf{g}_{s_{n+1}}^{pl}$$

$$\mathbf{g}_{s_{n+1}}^{el} = \mathbf{g}_{s_n}^{el} + \Delta\mathbf{g}_{s_{n+1}}^{el} \quad ; \quad \mathbf{g}_{s_{n+1}}^{pl} = \mathbf{g}_{s_n}^{pl} + \Delta\mathbf{g}_{s_{n+1}}^{pl}$$

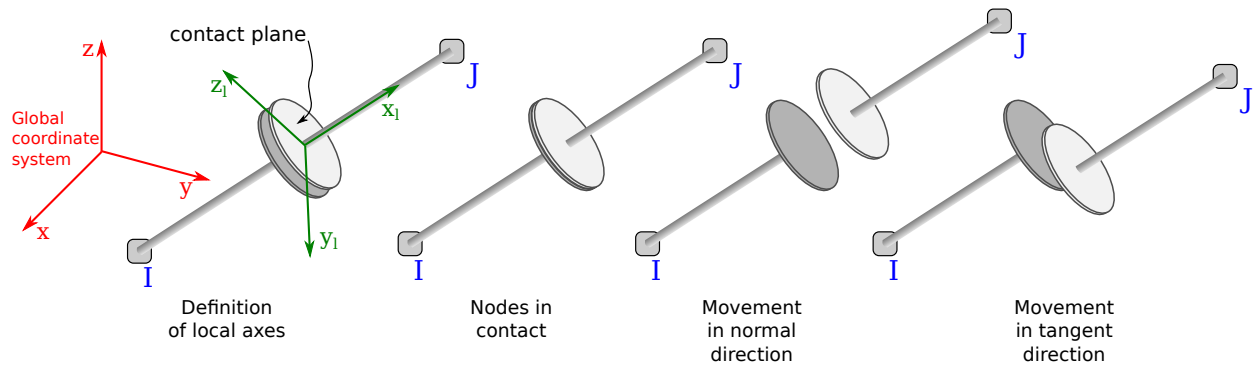


Figure 6.3: Description of contact geometry and displacement responses

Geometry description

Figure 6.3 shows geometry of the two node contact element and its main deformations modes. It is important to note the importance of properly numbering element nodes, consistently with the definition of normal x_1 . Node I is the first node, node J is the second node and normal goes from node I toward node J . If reversed, elements behaves like a hook.

6.3 Work Performed, Subtasks

Gap Opening/Closing Criteria. The criteria for gap opening/closing has been developed with reference to the exponential contact model as suggested by Gens et al. (1990). However, since their model was developed for rock to rock interface, it was changed to fit our case, which is soil to concrete contact. Updated contact stiffness was given in the above equation 6.6. The nonlinear change of stiffness resolve a number of issues, and there is no need to sub-incrementation approach that we initially considered. With continuous, nonlinear function that models stiffness a number of other potential problems are resolved as noted in sections below.

Choice of Contact Element Stiffness. Contact element stiffness is chosen based on experimental data. If such data is not available, than published data can be used, for example material parameters developed by Gens et al. (1990). It is highly recommended to obtain material parameters from experiments as contact behavior can have significant influence on dynamic response of NPPs. Current definition of contact stiffness (by Equation 6.6, on page 113) can use material

data described by Gens et al. (1990), however it is advisable to obtain data directly for contact properties in question.

Calibration of Nonlinear Slipping Resistance with and without Impermeable Barrier.

Data for Friction angles between foundation concrete and sub-base soil or rock is not readily available, but can be obtained in some cases. One reported (Kennedy, 2009-2014) value of friction angle between foundation concrete and the plastic sheeting that is placed on top of foundation soil is $\phi = 22^\circ$ and that value is used in our illustrative analysis. If realistic frictional coefficient values are not available, it is suggested that a parametric study is conducted and sensitivity of response estimated.

Zero Stiffness when Gap Opened. This problem was resolved by using a continuous, exponential stiffness approach (Gens et al., 1990) (with updated stiffness as per equation 6.6), that removes a zero stiffness and provides for a (very) small stiffness even when a gap is opened.

Fully Saturated Contact. Fully saturated contact is being worked on and will be ready for reporting with Task 4.6 on buoyant forces.

6.4 NPP Model with Nonlinear Contact, Illustrative Results

Representative NPP models with full shell structural models are prepared and posted for use. However, in order to gain better understanding of slip – gap behavior a simpler model is used, with stick models for containment and internal structures. Model is very similar to the model what was used in our previous CNSC project, however, now nonlinear contact is added. Model is shown in figure 6.4 below.

A Ricker wave with dominant frequency of $1Hz$ is used for analysis of the model. The maximum amplitude of Ricker function happens at 1 second. Figures (6.5) and (6.6) show the acceleration and displacement time histories as well as the FFT of the Ricker wave respectively.

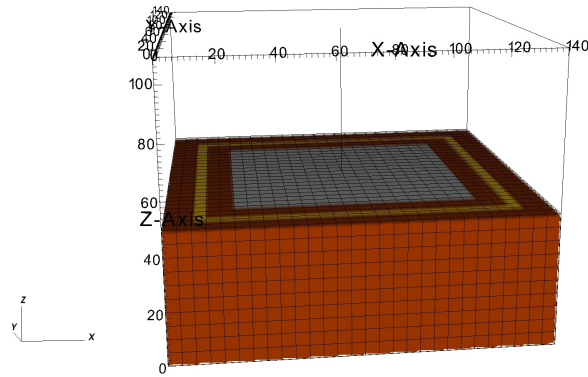


Figure 6.4: Finite element model for slip/gap modeling.

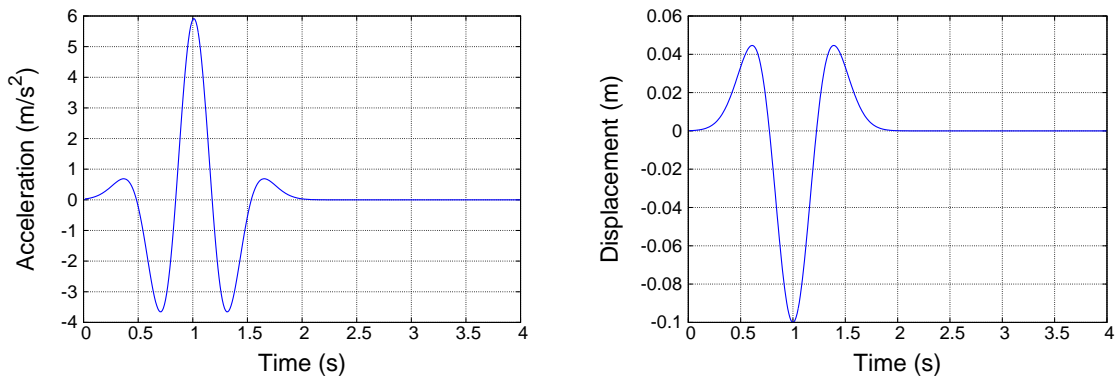


Figure 6.5: Acceleration and displacement time histories of Ricker wave with dominant frequency of $1Hz$

As shown in Figure (6.7), displacement time history of top of the structure along X direction is higher when slipping behavior is not considered, while along Z direction it is higher when considering slipping behavior. Since structural components have rotational degrees of freedom, the slipping behavior and gaps in the model will lead to more rotational movement and rocking of the foundation. There is also a phase lag in response of the structure in slipping behavior model. The displacement time histories at the bottom of the structure are slightly different in X direction. It can also be observed that along Z direction, the response of the structure in slipping model is higher comparing to the no-slipping one.

In this analysis slipping behavior reduces displacements along the X direction. This might be

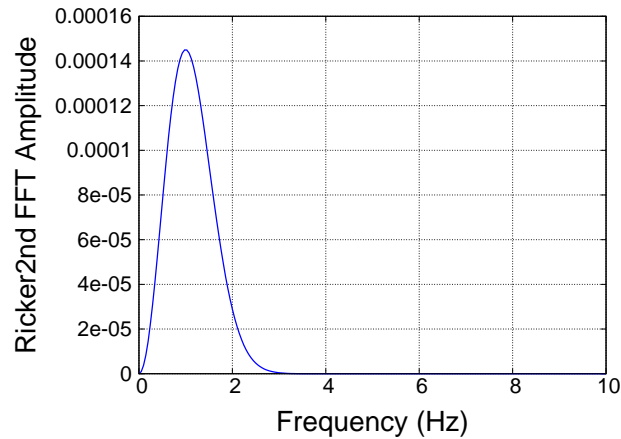


Figure 6.6: FFT of Ricker wave with dominant frequency of $1Hz$

due to the fact that while the foundation and structure are displacing, gaps are created at some parts of the interface, and that affect the rocking of the foundation.

Figure (6.8) shows the FFT of the acceleration at the bottom and top of the structure. As it is observed, there is a slight shift in predominant frequency of the response between the slipping and no-slipping behavior. By considering the slipping behavior, the dominant frequency of the motion is decreased along the X direction while is increased along the Z direction. This means that the system gets softer along X direction and stiffer along Z direction. This is due to the gap openings and sliding at the foundation and soil layer interface. Since sliding happens along the X direction, and also considering the gap openings occur along the Z direction leading to the rocking of the foundation, it makes the system softer along the X direction. In general, this shows that the natural frequency of the system can be changed due to the slipping behavior.

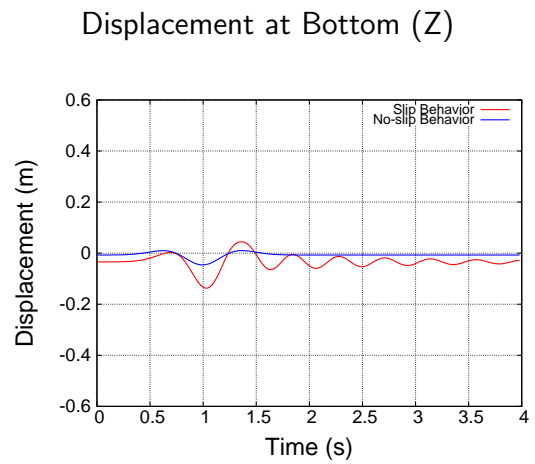
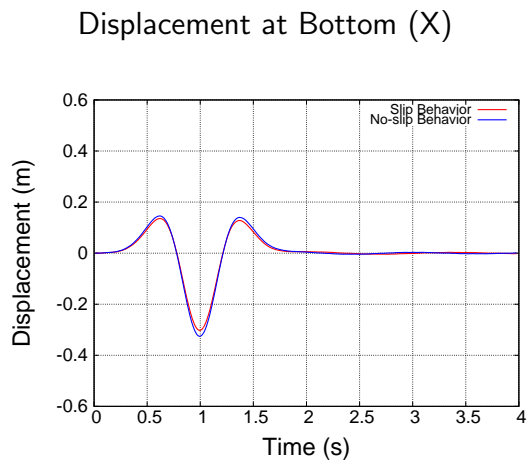
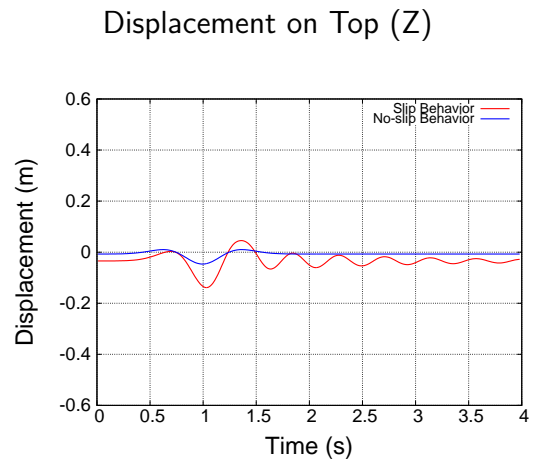
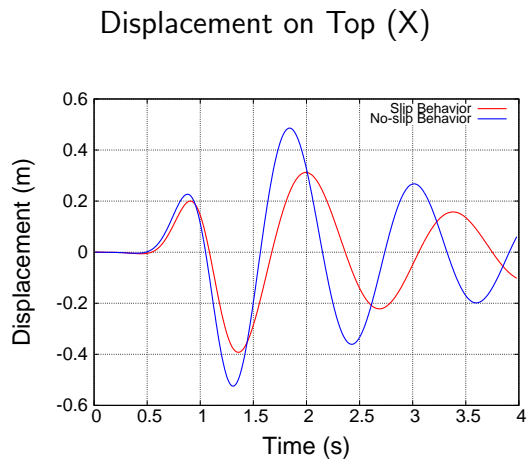


Figure 6.7: Comparison of displacement time histories of the structure between slipping and no-slipping models for Ricker wave

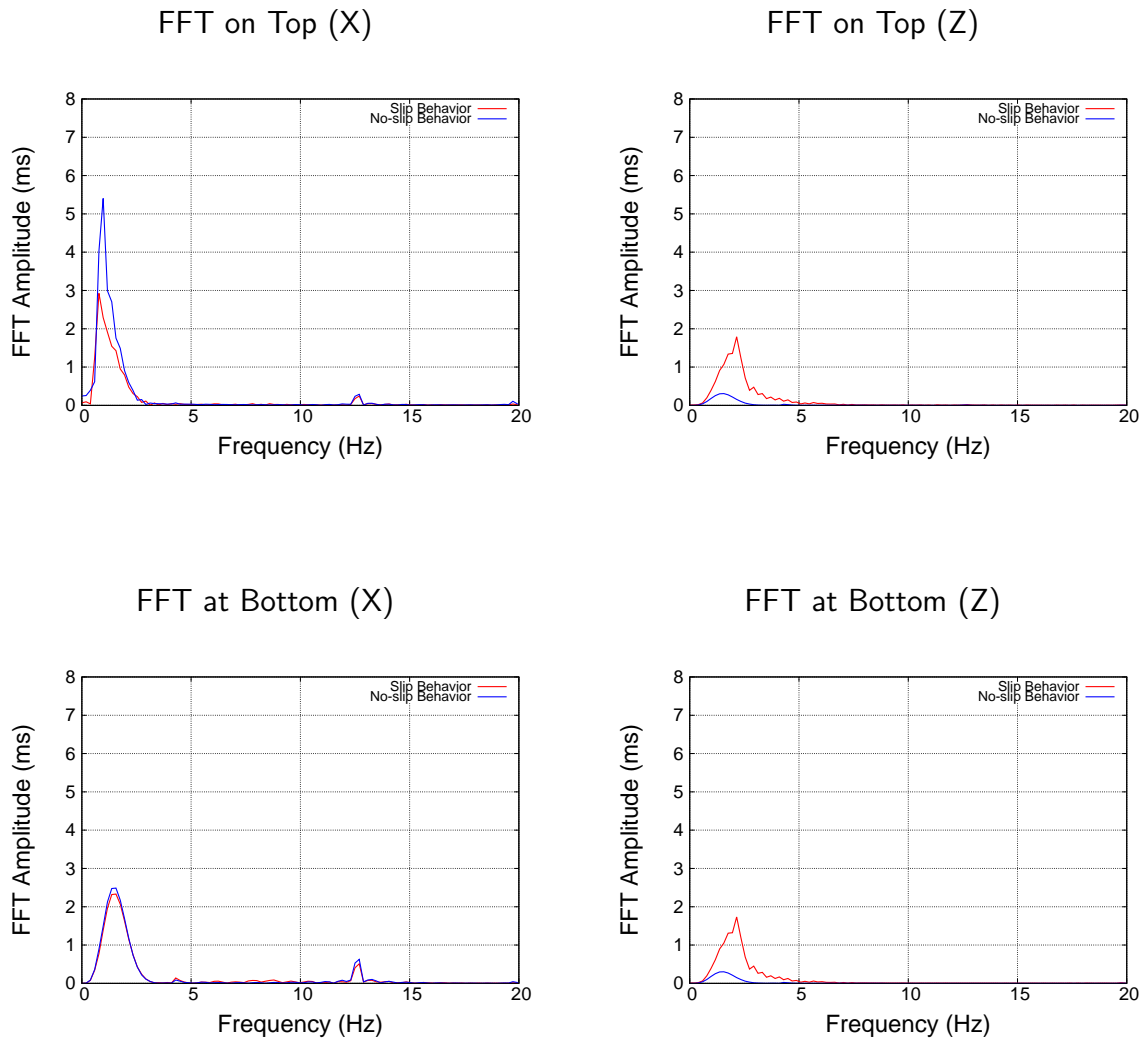


Figure 6.8: Comparison of FFT of the acceleration of the structure between slipping and no-slipping models for Ricker wave

6.4.1 Slipping behavior of SSI models by considering 3D wave propagation

In this section, the same finite element SSI model as previous section is used with 3D wave propagated motions as input motions for simulations. The input motion used here is Ricker wave (as shown in Figure (6.5)).

In order to study the slipping behavior of SSI considering 3D wave propagation for first stage of DRM simulation, a finite element model with dimensions of $10000m \times 50m \times 5000m$ is considered. Two cases are studied here with the source of motion (fault) to be located at $(x = 3000m, y = 0, z = 3000m)$ and $(x = 3000m, y = 0, z = 3000m)$. Figures (6.9) and (6.10) show these two cases respectively.

The size of the elements is chosen to be $50m$ in all directions for both cases in order to reduce the computational time. The soil parameters are: shear wave velocity of $700m/s$ and density of $2200kg/m^3$. Analyses for the fault slip model are done by applying the motion at the nodes of one element. This is done in order to represent the the wave propagation starting from the fault using multiple support excitation pattern. This is representing the first stage of analysis of DRM in which a big model including the fault is considered for free field case in order to obtain the required motions for DRM layer.

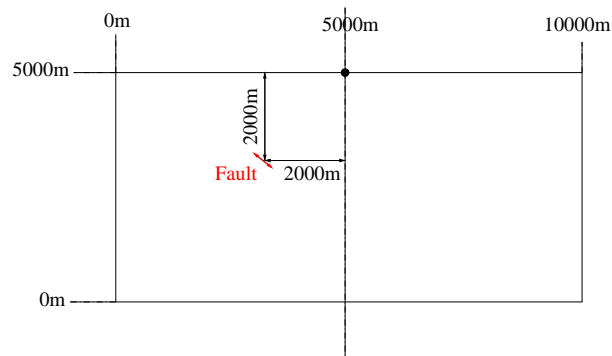


Figure 6.9: Domain to be analyzed for the 1st stage of DRM with fault located at an angle of 45° with respect to the top middle point of the model

For the first case to be studied here, Ricker wavelet is considered as an input motion with dominant frequency of $1Hz$. The fault is located with angle of 45° toward the top middle point

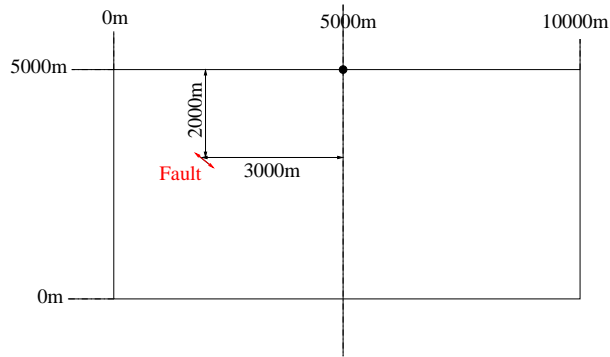


Figure 6.10: Domain to be analyzed for the 1st stage of DRM with fault located at an angle of 34° with respect to the top middle point of the model

of the model (Figure (6.9)).

Displacement time histories of the structure along X and Z directions are shown in Figure (6.11). It is observed that along the X direction, the amplitude of displacement is little less at the beginning of the shaking of the slipping behavior model and a slight phase lag can be observed as well. However, when the actual pick of the motion is gone, it is shown that the motion for no-slipping model will damp out sooner. So the magnitude of displacements are higher at this time range for slipping model which could be because of the gap/sliding at the interface zone. The displacement time histories do not have a significant difference at the bottom of the structure. Displacement time histories observed along the Z direction shows the fact that magnitude of displacements for slipping model is higher and will damp out later comparing to the no-slipping model.

Acceleration time histories along X and Z directions at the bottom and top of the structure are shown in Figure (6.12). It is observed that along the X direction the amplitude of acceleration is less considering the slipping behavior and also there is a phase lag in the observed motion. However, the amplitude of the acceleration along Z direction is much higher in case of considering the slipping case. This is the same behavior observed in 1D wave propagation as well but with higher difference in time histories amplitudes.

As shown in Figure (6.13), the dominant frequency of the response in case of slipping is less than the one observed in no-slipping case along X direction while it is higher along Z direction.

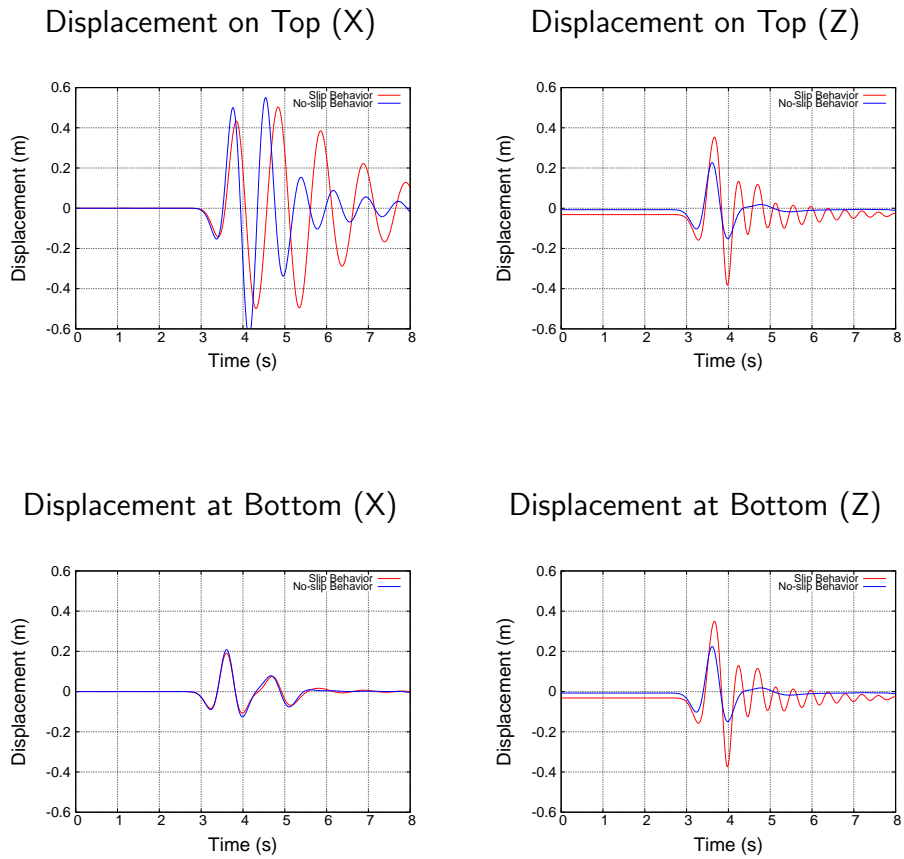


Figure 6.11: Comparison of displacement time histories of the structure between slipping and no-slipping models for Ricker wave

6.4.2 Example Nonlinear Model for Gapping and Slipping, Following Design Provisions and Standards

Presented here is work and findings that were described by Orbović et al. (2015). Presentation follows detail of the above presentation in order to provide completeness.

Abstract

Described here is the use of time domain nonlinear analysis for design and assessment of nuclear power plants. The seismic input is defined as time-history defined by the site specific UHS. Non-linear contact (stick-slip and gapping) at the bottom of the structural model (between foundation slab and soil/rock beneath) represent the only nonlinear behavior of the soil-structure system.

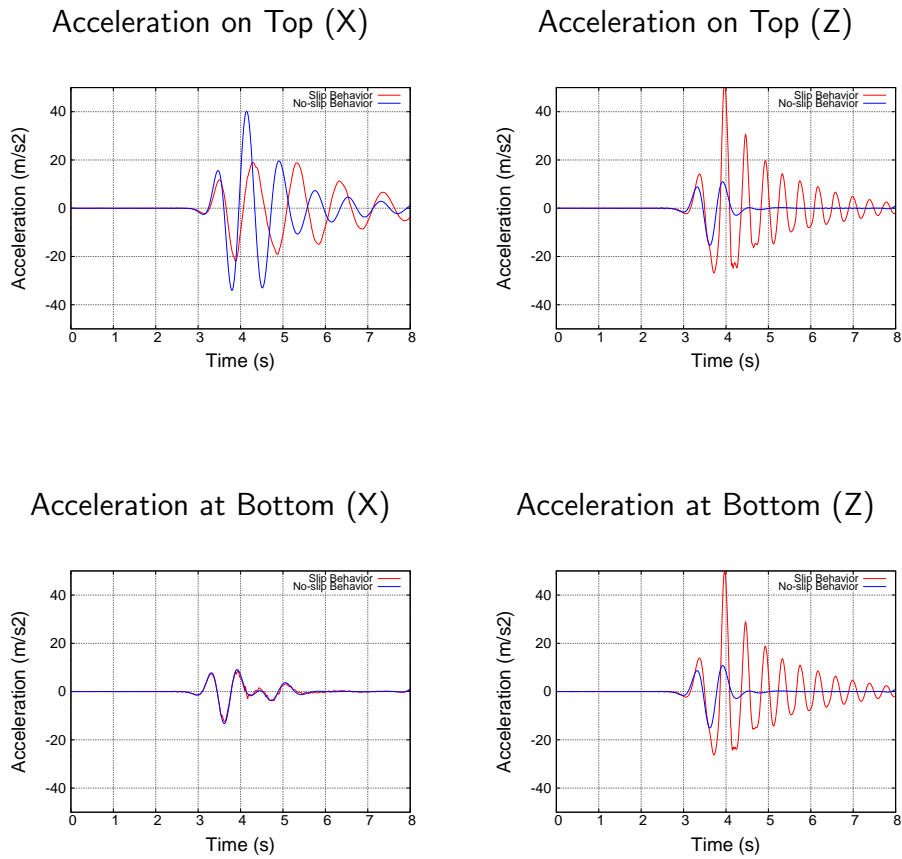


Figure 6.12: Comparison of acceleration time histories of the structure between slipping and no-slipping models for Ricker wave

This model is followed through a nonlinear analysis that is compatible with current design standard. It is important to note that the structure, in this case modeled as a simple stick model, remains elastic. The main purpose of described development is to provide methodology for use of nonlinear, time domain analysis for design based on standard approaches.

Present approach represents the first attempt to use nonlinear soil structure interaction within standard design framework. Of course, a more sophisticated and accurate model for structure (containment and internal) can be developed using shells and beams, however for this initial attempt, simple model suffice.

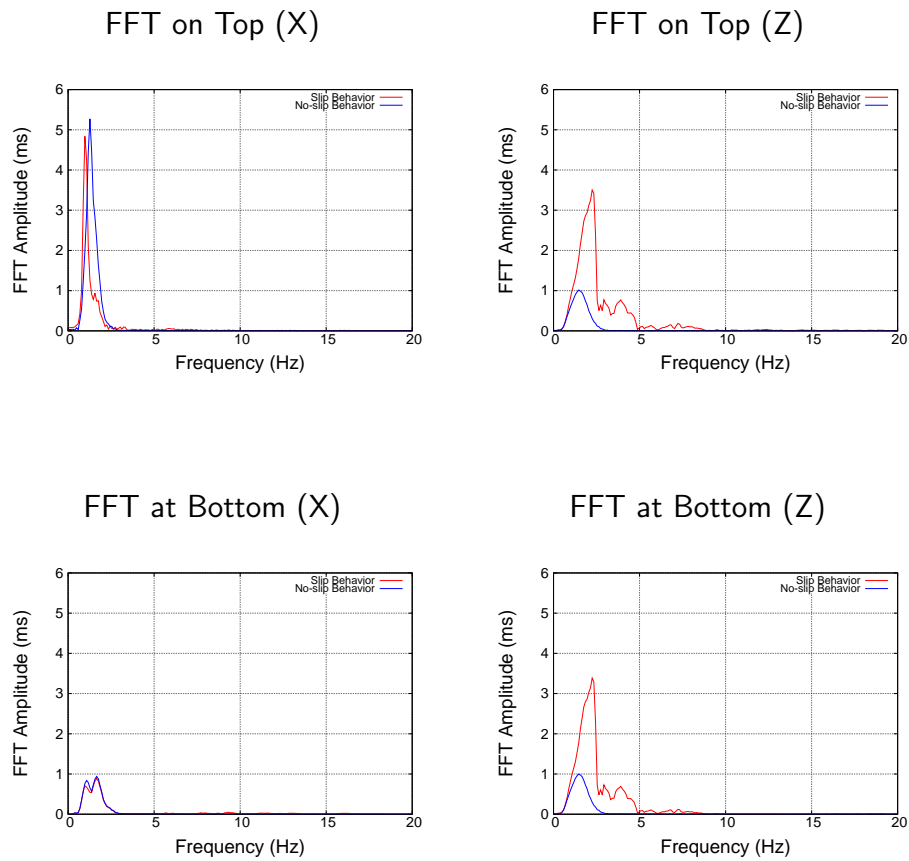


Figure 6.13: Comparison of FFT of the acceleration of the structure between slipping and no-slipping models for Ricker wave

Introduction

The design of nuclear power plants is based on linear structural behavior and the superposition of different loading cases acting simultaneously or quasi-simultaneously. On the other hand, non-linear analysis captures realistic non-linear behavior of soil and the soil-structure interaction. The structural behavior has to remain elastic. This is a requirement for the design of nuclear power plants. In this paper we describe use of nonlinear, time domain, seismic analysis for design and assessment.

The seismic input is defined through time-histories compatible with the design spectrum, a site specific UHS. This is the seismic input for the whole non-linear soil-structure system. The seismic input features a combination of horizontal and vertical motions, acting simultaneously

in non-linear analysis, using different combination methods. In this study, contact between the soil and the structure is modeled as a nonlinear contact with gap opening/closing and shear slip behavior. The model of the structure is represented by a simple stick model representative of a global dynamic behavior. This modeling simplification does not affect the main goal of this paper, as simplification is applied to the structural model, which is assumed to remain elastic. Similar structural model developed using linear elastic shells and beams can be used instead of a stick model, but we opt for a simple stick model as the main focus is on presenting the methodology. In addition, a number of different input motions (different intensities, different return periods, &c.) can be used, with different UHS, different soil/rock site conditions, different depth to bedrock. however the main thrust of the methodology will not change. In other words, main focus of presented work is the use of time domain nonlinear finite element modeling and simulation (in this case using Real ESSI Simulator (Jeremić et al., 2015)) for design, while following current design standards.

The use of nonlinear analysis for design proceeds as follows. The site specific UHS is given on the bedrock. Spectrum compatible accelerograms are generated and propagated through the model. From the bedrock, motions are propagated as 1D waves vertically using 1D wave propagation solutions, as implemented, for example, in the SHAKE program (Idriss and Sun, 1992). Developed motions are then propagated through soil, that can be inelastic, and non-linear contact elements between the soil and the foundation. Following the nonlinear analysis obtained are the accelerograms at the foundation level. This accelerograms include information about the nonlinear behavior of soil (if modeled) and nonlinear contact, for a complete model (soil-structure system). Thus obtained accelerograms, including all the nonlinear effects from the contacts (and possibly soil) will be quite different from the accelerograms obtained for the linear elastic model. Based on this accelerograms, and assuming that the structural behavior is elastic, a response spectrum at the foundation level is calculated. This spectrum will include all information about the soil and contact non-linearities in the model. This spectrum can now be used as a design spectrum applied at the foundation level and design the structure according to ACI349/359. The result of this analysis will also be compared with the classical linear analysis currently used in the design of nuclear power plants.

Modeling

Presented below are details of models used for this study.

Earthquake Motions

Seismic Motions from the Center for Engineering Strong Motion Data (CESMD) data base were used. Earthquake record used for this analysis was from Taiwan SMART1(45), Time: 11/14/1986, Station:SMART1 E02. Figure 6.14 shows time histories, FFT and the response spectra of the free field motions used.

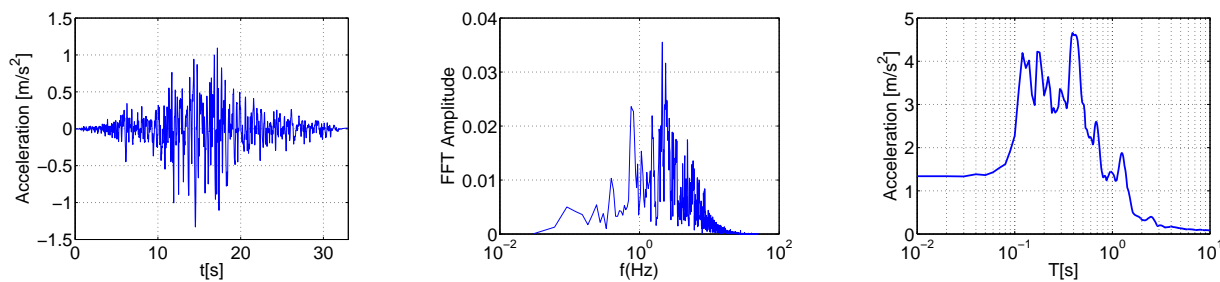


Figure 6.14: Free field seismic motions at the surface: time history, FFT and response spectra.

Motions were applied simultaneously to the soil structure system at 100% in the X (horizontal direction, 40% in the Y (horizontal) direction and 40% in the Z (vertical) direction). It should be noted that the application of vertical motions as P waves, is probably not quite correct, as most vertical motions are a results of a surface Rayleigh wave and not a P wave. Frequency characteristics of a P wave are quite different that those of a surface Rayleigh wave. In fact, frequency characteristics of the vertical waves are similar to those of the horizontal waves, which is only possible if both horizontal and vertical motions are components of a surface, Rayleigh wave, which is happening in reality.

Seismic Input is provided using the Domain Reduction Method (Bielak et al., 2003). Free field motions accelerations \ddot{u}^0 and displacements u^0 , that were developed from a 1D wave propagation

analysis, are used to create effective forces:

$$P^{eff} = \begin{Bmatrix} P_i^{eff} \\ P_b^{eff} \\ P_e^{eff} \end{Bmatrix} = \begin{Bmatrix} 0 \\ -M_{be}^{\Omega+} \ddot{u}_e^0 - K_{be}^{\Omega+} u_e^0 \\ M_{eb}^{\Omega+} \ddot{u}_b^0 + K_{eb}^{\Omega+} u_b^0 \end{Bmatrix} \quad (6.20)$$

These effective forces are applied to a single layer of finite elements surrounding the nonlinear soil-structure domain of interest. Effective force P^{eff} is an exact dynamic replacement for a free field motions from the earthquake source forces. The DRM allows for application of any realistic seismic wave field, including body and surface waves. In this case, focus is on current design procedures which use 1D seismic wave field.

Finite Element Model

Structural Model. The finite element model consists of a soil/rock model, the foundation slab model and the structural model (containment and internal structure model). Between the foundation slab and the soil/rock, a set of contact elements are used. The structural model is simplified to a stick model, as the purpose of this paper is to show the use of nonlinear analysis for design. Figure 6.15 shows the model used.

Soil/rock in the foundation is modeled using linear elastic ($V_s = 750\text{m/s}$) brick finite elements. Brick finite elements are 4m in size, which provides for reliable propagation of seismic motion frequencies of up to 15Hz ($(750\text{m/s}) / (12 \times 4\text{m}) \approx 15\text{Hz}$). It was assumed that 12 linear displacement interpolation finite elements are enough to propagate full wave with minimal distortion and loss of accuracy.

Figure 6.15 also shows the placement of the (single) DRM layer that is used for input of seismic motions. Two more layers of elements are used out of the DRM layer in order to damp out any additional motions that results from radiation damping of the soil-structure system.

Foundation slab is made of concrete ($V_s = 2400\text{m/s}$) and has dimensions of $40\text{m} \times 40\text{m} \times 4\text{m}$. The stick model representing the containment and internal structures is that of one of the standard NPPs.

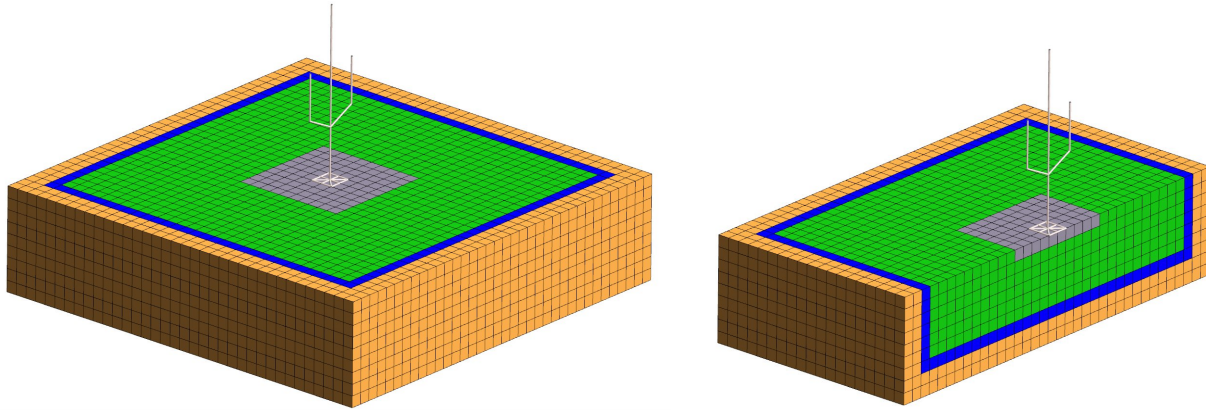


Figure 6.15: Finite element model of an NPP. Soil/Rock and the foundation slab is represented by brick elements, while structure (containment and internal) is represented by a stick model. Contact elements are applied at the bottom of the foundation slab. Note the DRM layer surrounding the soil/rock domain, and the out of DRM layers, used to damp out additional, NPP radiation damping motions.

Contact between foundation slab and the underlying soil/rock is modeled using contact element that allows for normal/axial nonlinear response and a gap opening Gens et al. (1990). In the transversal directions this element allows for Coulomb frictional slip Crisfield (1997). A fairly low friction angle ($\Phi = 25^\circ$), that mimics friction of concrete foundation on layers of plastic sheets (to prevent underground water to wet foundation concrete) over soil/rock.

Modeling and Simulation Software: All modeling and simulations described here were done using Real ESSI Simulator (Jeremić et al., 2015). Real ESSI Simulator is a modeling and simulation system developed by Jeremić, et al. at University of California, Davis and Lawrence Berkeley National Laboratory, with support from the US-DOE, US-NRC, CNSC-CCSN and US-NSF, for high fidelity, realistic modeling and simulation of seismic behavior (Earthquake Soil Structure Interaction, ESSI) of infrastructure objects (Nuclear Facilities, Nuclear Power Plants, Bridges, Buildings, Dams, &c.). Of particular importance for the Real ESSI Simulator modeling and simulation system is the availability of complete verification (Oberkampf et al., 2002; Roy and Oberkampf, 2011) and partial validation for all the software components.

Results

Two models were analyzed.

- Model #1 was a linear elastic model with no contact elements, therefore no slip or gap between foundation slab and underlying soil/rock was possible.
- Model #2 had contact elements between foundation slab and the adjacent soil/rock.

The main idea is to compare response of an NPP with linear elastic model (no contact modeling, foundation slab is glued to soil beneath) and with a nonlinear contact that allows for separation and shear slip. Presented nonlinear approach can be used in design as the main structure (containment, internal and the foundation) are still linear elastic, nonlinearities are contained beneath, in the contact zone.

Foundation – Soil-Rock Slip: Slip was observed at all locations in the contact zone during shaking. Figure 6.4.2 shows a snapshot of a structure during a slip (left) and the amount of slip between foundation slab and rock beneath containment and internal sticks.

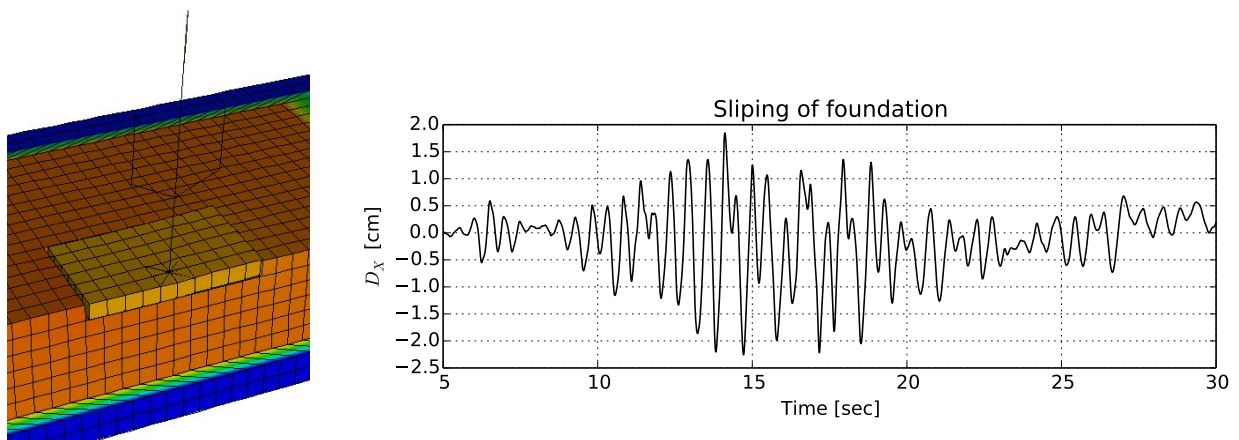


Figure 6.16: Snapshot of a relative displacements between foundation slab and soil/rock (left) and the amount of slip at a center of a foundation slab (beneath containment and internal sticks).

It is noted that it was expected that the contact zone between foundation slab and soil beneath will show gapping. This did not happen. After careful analysis it was determined that

shear slip behavior prevents gapping and liftoff of the foundation slab. That is, when a demand of a horizontal force becomes large enough due to motions of the soil beneath, the structure can shear slip or rock or both. For given material parameters, the response prefers to slip, before rocking, and gapping occurs. This is similar to a response of a car making a sharp turn, rather than tipping over (equivalent of rocking), tire-pavement friction is overcome and car slips sideways.

Spectral Accelerations, Nonlinear vs Linear Response Figures 6.17 and 6.18 show comparison of spectral accelerations in soil beneath foundation slab and at the foundation slab level, respectively, for horizontal and vertical directions.

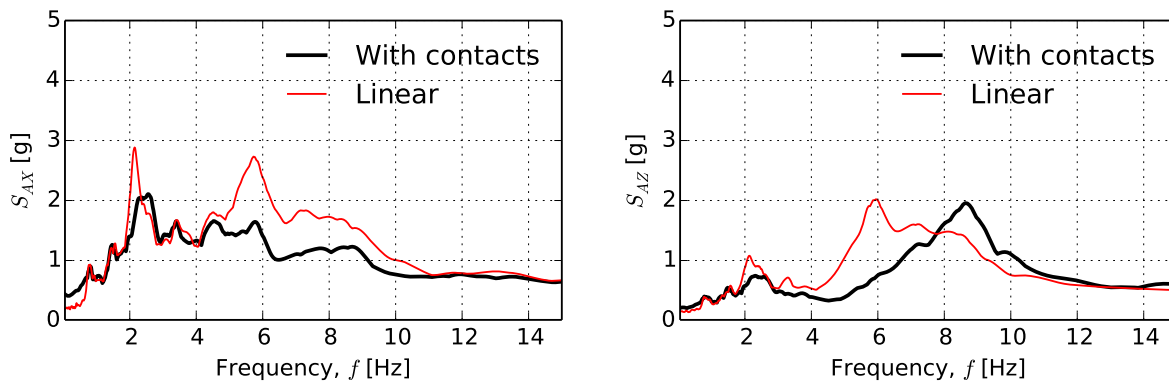


Figure 6.17: Comparison of spectral accelerations at the top of soil, beneath foundation slab for X directions (left), and vertical directions (right).

Figures 6.19 and 6.20 show comparison of spectral accelerations for top of a containment building and internal structure, respectively, for horizontal and vertical directions.

There are a number of observations to be made.

- Response of a linear system (that is, a system with no contact modeling, foundation slab is glued/tightly connected to soil beneath) is in general larger than that of a system where shear slipping and gapping is allowed.

This is apparent in all the plots.

- Vertical response of a contact model for soil beneath foundation has a slightly higher spectral accelerations for higher frequencies (8Hz - 11Hz) than linear system. This is

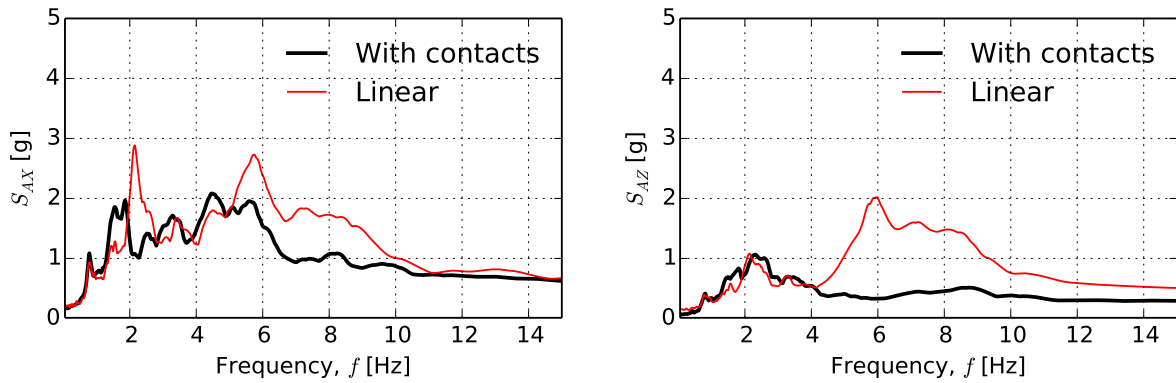


Figure 6.18: Comparison of spectral accelerations at the foundation slab for X directions (left), and vertical directions (right).

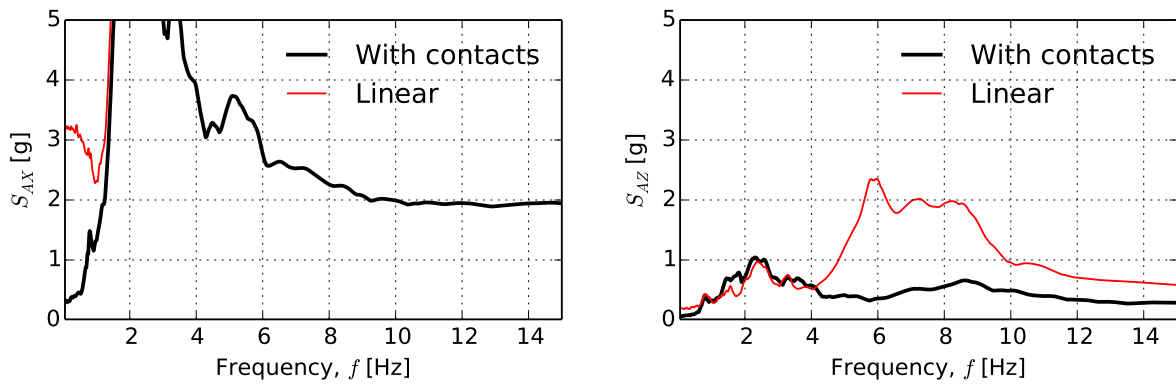


Figure 6.19: Comparison of spectral accelerations at the top of a containment structure for X directions (left), and vertical directions (right).

explained by the fact that small gapping still does occur (even if large gapping is prevented by release of horizontal demand by slipping). Such small gapping will, upon closure, create vertical motions, in the vicinity of the natural frequencies of the structure (8Hz and above).

- Both horizontal and vertical response at the foundation slab are reduced, except for a very low frequency (just below 2Hz) where slip occurs. That this is indeed a frequency of slip, can be observed from response shown in Figure 6.4.2, where there are approximately 2 cycles per second.

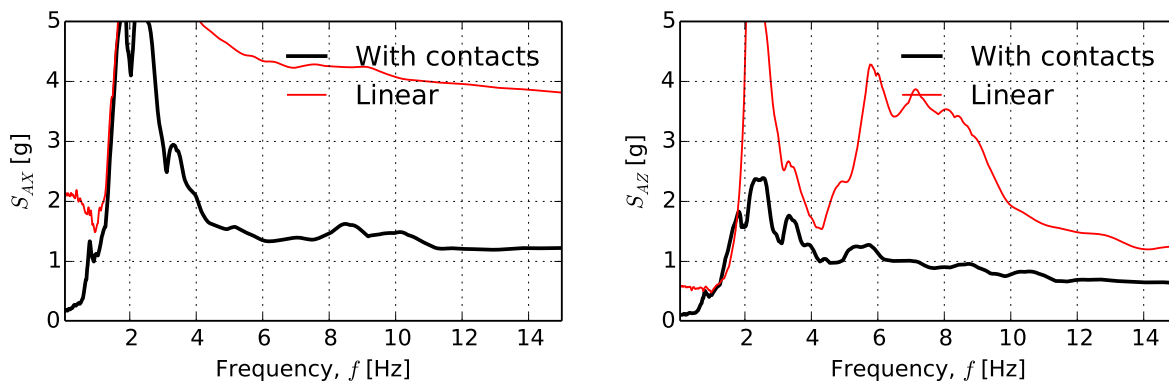


Figure 6.20: Comparison of spectral accelerations at the top of a containment structure for X directions (left), and vertical directions (right).

Reduction of vertical response is significant for frequencies higher than 4Hz, while for horizontal response, reduction starts at about 5Hz.

- Both horizontal and vertical response are significantly reduced for containment building and internal structure. In fact, spectral accelerations were plotted in the same scale as for soil and foundation slab, the linear response (no contact modeling) far exceeds this scale, while nonlinear model (contact) shows significant reduction for all frequencies

Conclusions

In this paper we presented a novel approach to design of NPPs where, structural components (internal, containment, foundation) are assumed and remain linear elastic, while nonlinear behavior is allowed beneath the foundation slab, in the contact zone. It is noted that more nonlinearities will probably be present in the soil and rock beneath, however in this experimental design approach, only nonlinear response of contact zone was allowed.

A significant reduction in demand was observed by allowing nonlinear (inelastic) response in foundation slab – soil/rock contact zone. This reduction in demand, and the underlying seismic energy dissipation can be used to benefit seismic design of NPPs, as, although structural components remain (are modeled as) linear elastic, seismic motions that structure will experience (through foundation slab) are (significantly) reduced. It is very important to note that due to

nonlinear nature of modeling, it is not possible to scale up or down developed results. In other words, if any changes in earthquake scaling are made, a model has to be rerun, as in general response will not scale.

Chapter 7

Task 4.5: Energy Dissipation

7.1 Summary of Findings for Task 4.5

The main findings are:

- Energy dissipation is an important measure of efficiency of the soil structure NPP system.
- Energy dissipation is increasingly viewed as one of the best methods to improve design and consequentially there is an effort to use energy as a design tool by the SEAC (Structural Engineering Association of California) (Trifunac et al., 2001).
- The most important energy dissipation mechanisms for NPPs are:
 - nonlinear (hysteretic, elastic-plastic) response of soil and rock under the foundation of an NPP, and
 - nonlinear response of contact zone between foundation concrete and underlying soil and rock
- Soil under foundations and at some distance from the NPP has a large energy dissipation capacity, due to its large volume.
- Energy dissipation capacity of soil and the contact zone increases with the increase in shaking magnitude, as more plastification (nonlinearities) occur for stronger motions.

- Numerical energy dissipation and production, can occur in nonlinear systems even for non-dissipative integration algorithms, and it should be aware of and carefully controlled.

7.2 Methodology

7.2.1 Seismic energy input into SFS system

Earthquakes release large amounts energy at the source¹ Part of released energy is radiated as mechanical waves ($\approx 1.6 \times 10^{-5}$) and part of that energy makes it to the surface where SFS system is located.

Mechanical seismic wave energy enters the SFS system through a closed surface Γ that encompasses (significant) soil volume as well as foundation system and the structure (see Figure 7.2). Kinetic energy flux through closed surface Γ includes both incoming and outgoing waves and can be calculated using Domain Reduction Method (Bielak et al., 2003) as:

$$E_{flux} = [0; -M_{be}^{\Omega+} \ddot{u}_e^0 - K_{be}^{\Omega+} u_e^0; M_{eb}^{\Omega+} \ddot{u}_b^0 + K_{eb}^{\Omega+} u_b^0]_i \times u_i$$

where $M_{be}^{\Omega+}$, $M_{eb}^{\Omega+}$, $K_{be}^{\Omega+}$, $K_{eb}^{\Omega+}$ are mass and stiffness matrices, respectively for a single layer of elements just outside of the boundary Γ , while \ddot{u}_e^0 and u_e^0 are accelerations and displacements from a free field model for nodes belonging to that layer of elements. Alternatively, energy flux can be calculated using (Aki and Richards, 2002):

$$E_{flux} = \rho A c \int_0^t \dot{u}_i^2 dt$$

Outgoing kinetic energy can be obtained from outgoing wave field w_i , (from DRM, Bielak et al. (2003)), while the difference then represents the incoming kinetic energy that needs to be dissipated with SFS region.

¹for example, some of the recent large earthquake energy releases are listed: Northridge, 1994, $M_{Richter} = 6.7$, $E_r = 6.8 \times 10^{16} J$; Loma Prieta, 1989, $M_{Richter} = 6.9$, $E_r = 1.1 \times 10^{17} J$; Sumatra-Andaman, 2004, $M_{Richter} = 9.3$, $E_r = 4.8 \times 10^{20} J$; Valdivia, Chile, 1960, $M_{Richter} = 9.5$, $E_r = 7.5 \times 10^{20} J$;

7.2.2 Seismic energy dissipation in SFS system

Seismic energy that enters the SFS system is dissipated in a number of ways. part of the energy that enters SFS system can be reflected back into domain outside Γ by

- wave reflection from impedance boundaries (free surface, soil/rock layers...).
- SFS system oscillation radiation.

While the rest of seismic energy is dissipated through one of the following mechanisms within SFS domain:

- Elasto-plasticity of soil
- Viscous coupling of porous solid with pore fluid (air, water)
- Elasto-plasticity/damage of the foundation system
- Elasto-plasticity/damage of the structure
- viscous coupling of structure with surrounding fluids (air, water)

It is also important to note that in numerical simulations (advocated and used in this work), part of the energy can be dissipated or produced by purely numerical means. That is, numerical energy dissipation (damping) or production (negative damping) has to be carefully controlled (Argyris and Mlejnek, 1991), (Hughes, 1987).

Energy Dissipation by Plasticity. Elastic-plastic deformation of soil, foundation and structure is probably responsible for major part of the energy dissipation for large earthquakes. This, displacement proportional dissipation is a result of dissipation of plastic work ($W = \int \sigma_{ij} d\epsilon_{ij}^{pl}$) and is present in all three components of the system (soil, foundation and the structure). Ideally, majority of the incoming energy would be dissipated in soil, before reaching foundation and structures. The possibility to direct energy dissipation to soil can be used in design by recognizing energy dissipation capacity for different soils. For example, simple elastic-plastic models of stiff and soft clay as well as dense and loose sand predict different energy dissipation capacities, as shown in Figure 7.1, for single loading-unloading-reloading cycle. While Figure 7.1 shows

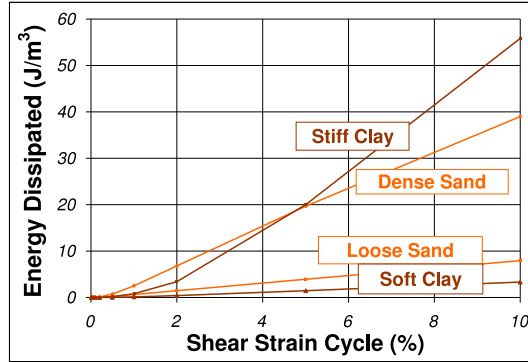


Figure 7.1: Energy dissipation capacity for one cycle at various strains for four generic soils.

that stiff clay and dense sand have much higher dissipation capacity, it is important to note that soft/loose soils can undergo much larger deformation/strain, thus offering increased energy dissipation capacity through flexibility.

Energy Dissipation by Viscous Coupling. Viscous coupling of pore fluid (air, water...) and soil particles and/or foundation or structural components is responsible for velocity proportional energy dissipation. In particular, viscous coupling of porous solid and fluid results in $E_{vc} = n^2 k^{-1} (\dot{U}_i - \dot{u}_i)^2$ energy loss per unit volume. It is noted that this type of dissipation is realistically modeled using $u - p - U$ formulation (Jeremić et al., 2008).

Numerical Energy Dissipation and Production. As noted above, numerical integration of nonlinear equations of motions affects calculated energy in various ways. Most common effect for nonlinear (elastic-plastic) systems is the positive (energy dissipation) and negative (energy production) damping. For example Newmark (N) (Newmark, 1959) and Hilber–Hughes–Taylor (HHT) (Hilber et al., 1977) are energy preserving for linear elastic system with proper choice of constants ($\alpha = 0.0; \beta = 0.25, \gamma = 0.5$). Both methods can also be used to dissipate higher frequency modes for linear elastic models by changing constants so that for N: $\gamma \geq 0.5, \beta = 0.25(\gamma + 0.5)^2$, while for HHT: $-0.3\dot{3} \leq \alpha \leq 0, \gamma = 0.5(1 - 2\alpha), \beta = 0.25(1 - \alpha)^2$. However, for nonlinear problems it is impossible to maintain energy of the system throughout computations (Argyris and Mlejnek, 1991).

7.3 Work Performed, Subtasks

Modeling of input energy. Energy flux can be calculated using Aki and Richards (2002); Trifunac (2008):

$$E_{flux} = \rho Ac \int_0^t \dot{u}_i^2 dt \quad (7.1)$$

Outgoing kinetic energy can be obtained from outgoing wave field w_i , (from DRM, Bielak et al. (2003)), while the difference then represents the incoming kinetic energy that needs to be dissipated within SSI region.

Alternatively, using DRM, mechanical seismic wave energy enters the SSI system through a closed surface Γ that encompasses soil volume as well as foundation system and the structure, thus providing a way to calculate all of the energy that enters the system, as shown in Figure 7.2. Kinetic energy flux through closed surface Γ includes both incoming and outgoing waves and

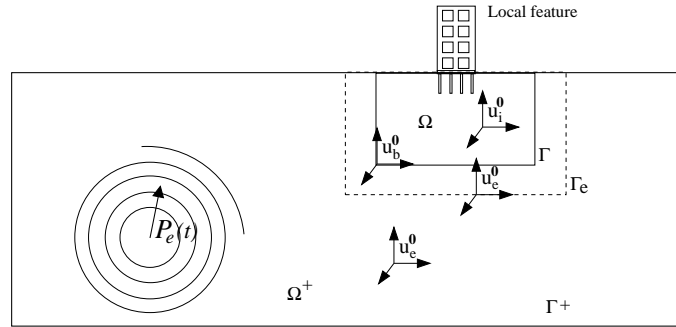


Figure 7.2: Geometry of the SSI system.

can be calculated using DRM:

$$E_{flux} = [0; -M_{be}^{\Omega+} \ddot{u}_e^0 - K_{be}^{\Omega+} u_e^0; M_{eb}^{\Omega+} \ddot{u}_b^0 + K_{eb}^{\Omega+} u_b^0]_i \times u_i \quad (7.2)$$

where $M_{be}^{\Omega+}$, $M_{eb}^{\Omega+}$, $K_{be}^{\Omega+}$, $K_{eb}^{\Omega+}$ are mass and stiffness matrices, respectively for a single layer of elements just outside of the boundary Γ , while \ddot{u}_e^0 and u_e^0 are accelerations and displacements from a free field model for nodes belonging to that layer of elements.

Modeling of radiation dissipation. From the DRM, outside wave field w_i is followed and energy calculated for every node just outside surface Γ , $E_{node} = (m_{node} \times w_e^2)/2$. Energy of all

the nodes outside of Γ is then simply added.

Modeling of energy dissipation in soil/rock. Two main energy dissipation mechanisms in soil and rock are modeled

- **Frictional (elastic-plastic, displacement proportional) energy dissipation mechanism.** Proper way of modeling this energy dissipation mechanism in soil and rock is done by using the incremental elastic-plastic theory. Pisanò Material model (Pisanò and Jeremić, 2014) is used for that purpose. Energy dissipation modeling is based on accurate calculation of plastic work for each part of soil and rock domain adjacent to the NPP. This is done through calculation of plastic work

$$W^{soil/rock} = \int_V \int_{t_n}^{t_{n+1}} \sigma_{ij} d\epsilon_{ij}^{pl} dV \quad (7.3)$$

where integration is done for each time increment and each element volume, σ_{ij} is the current stress state at each integration (Gauss) point within each finite element, and $d\epsilon_{ij}^{pl}$ is the increment of plastic strain at the current increment.

- **Viscous (velocity proportional) energy dissipation mechanism.** There are two main approaches to modeling viscous energy dissipation, namely (a) using Rayleigh damping, which is phenomenological approach, assigning damping ratios to individual finite elements or groups of elements and (b) using fully coupled modeling of pore fluid that interacts with porous solid (soil and rock skeleton). We use the second approach. Modeling viscous damping for soil and rock using fully coupled approach is based on physics of interacting media (fluid and porous solid) and is modeled using coupled finite elements (Jeremić et al., 2008; Taiebat et al., 2010, 2009). To this end, the so called u-p-U finite elements are used (Jeremić et al., 2008, 1989-2016). These elements feature an analytical approach to the pore fluid – porous solid interaction, done through a (physics based) damping matrix (not based on Rayleigh damping) that models viscous energy dissipation based on relative movement of pore fluid and soil/rock skeleton. Such modeling approach ensure that the calculated energy dissipation is physics based and verifiable. This approach is used in this project to calculated (assess) energy dissipation amounts for viscous dissipation mechanism.

Similar to the frictional energy dissipation approach, viscous dissipation approach can also be done for each finite element, in each time step, thus allowing for precise (detailed) spatial and temporal following of viscous dissipation. However, viscous energy dissipation represents a small part of totally dissipated energy when strong material nonlinearities are present.

Modeling of energy dissipation in soil/rock – foundation contact zone. Using contact finite element that models both slip and gap, dissipation from two mechanisms is calculated:

- **Frictional component of energy dissipation.** The energy dissipation during slipping is calculated by integrating nonlinear cyclic response loops of the contact–slipping element. Calculated is dissipated energy for each element (region of soil/rock–foundation contact) at each time step.
- **Viscous component of energy dissipation.** The energy dissipation during gapping (pumping of water in and out of soil/rock pores) is calculated using viscous damping in the top layers of soil/rock, Saturated soil/rock is modeled using u-p-U finite elements, which allows direct calculation of the viscous damping from a physics based damping matrix (Jeremić et al., 2008). The coupling of pore water and porous solid (soil/rock skeleton) results in $E_{vc} = n^2 k^{-1} (\dot{U}_i - \dot{u}_i)^2$ energy loss per unit volume in unit time (Jeremić et al., 1989-2016). Thus, again, viscous energy losses, are calculated for each location and for each time step.

Numerical energy dissipation (positive and negative). This mode of energy dissipation is carefully followed as it influences results of simulations in a significant way (Argyris and Mlejnek, 1991; Krenk, 2006).

Numerical damping (energy dissipation or energy production) is caused by the numerical integration algorithm used for integrating equations of motion, within the finite element method. When a spatial (discretization of a continuum into finite element mesh) and temporal (time stepping) discretization if done for a continuum problem (solids and structures) the new, discretized system contains artificial, higher modes of vibration that are caused by the discretization process.

It is convenient to devise a time domain integration methods that can damp out those higher order modes. Two methods are most commonly used for such purpose, the Newmark method (Newmark, 1959) and the Hilber-Hughes-Taylor (HHT) α method (Hilber et al., 1977). Both methods can be made non-dissipative (no energy dissipation, and no damping of higher order (artificial) modes), by proper choice of integration parameters ($\beta = 0.25, \gamma = 0.5$ for Newmark and $\alpha = 0.0$ for HHT method). However, it is beneficial to remove (damp out) those higher order, artificial modes in order to obtain as accurate as possible dynamic response of the soil/rock – structure NPP system.

Both methods can be used to dissipate higher frequency modes for linear elastic models by changing constants so that for Newmark method numerical energy dissipation is obtained for $\gamma \geq 0.5$, $\beta = 0.25(\gamma + 0.5)^2$, while for HHT method energy dissipation is obtained for $-0.33 \leq \alpha \leq 0$, $\gamma = 0.5(1 - 2\alpha)$, $\beta = 0.25(1 - \alpha)^2$.

When the response is nonlinear (elastic-plastic for example), the time integration algorithm can even have negative energy damping (production of energy) (Argyris and Mlejnek, 1991).

A parametric study is underway with variation of integration parameters and observation of energy dissipation for limited amount of plasticity.

7.4 Illustrative Example

7.4.1 Example #1

Figure 7.3 shows simple illustrative results of energy dissipation calculations for a simple nonlinear soil column, as function of time. It is noted that most of the energy is dissipated toward the surface layers, since that is where the soil experiences most nonlinearities due to low confinement.

Figure 7.4 shows results for the same example, this time as a function of depth. The significant surface dissipation is even more obvious in this plot. Please also note small jumps in dissipation where the material changes from denser to looser, these impedance boundaries usually enhance strains, and hence finite elements at those boundaries experience more nonlinear response.

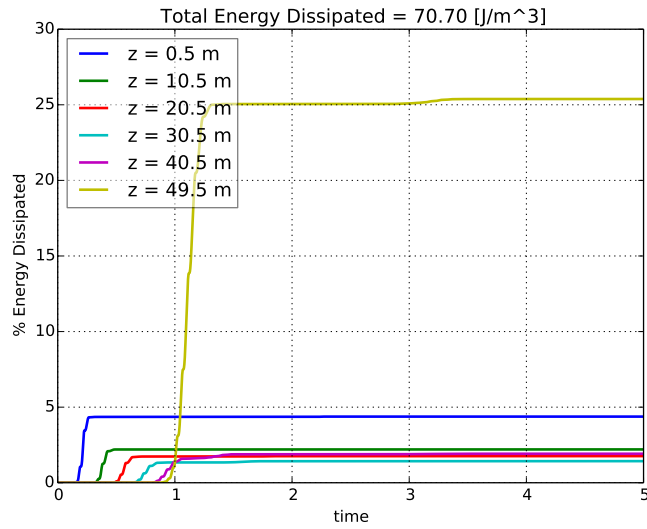


Figure 7.3: Energy dissipation in a vertical column of soil, total energy dissipation in time.

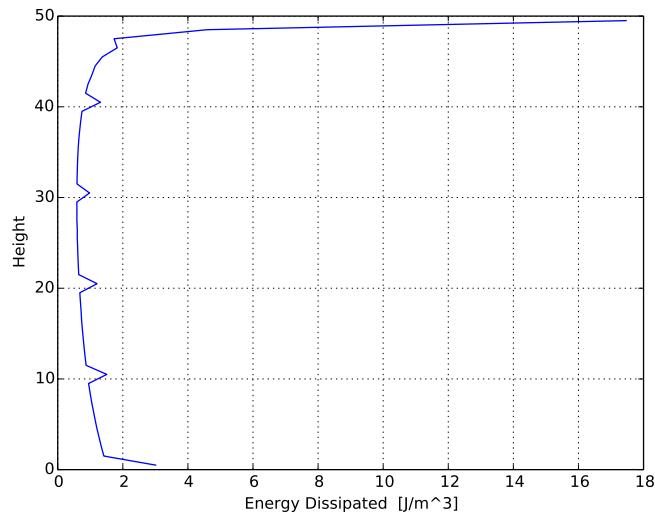


Figure 7.4: Energy dissipation in a vertical column of soil, energy dissipation in the depth.

7.4.2 Example #2

In this example, a full NPP model with nonlinear soil was subjected to seismic motions and energy dissipation followed in the inelastic/nonlinear soil domain. Figure 7.5 shows incremental energy dissipation in one time instant under a realistic model of an NPP.

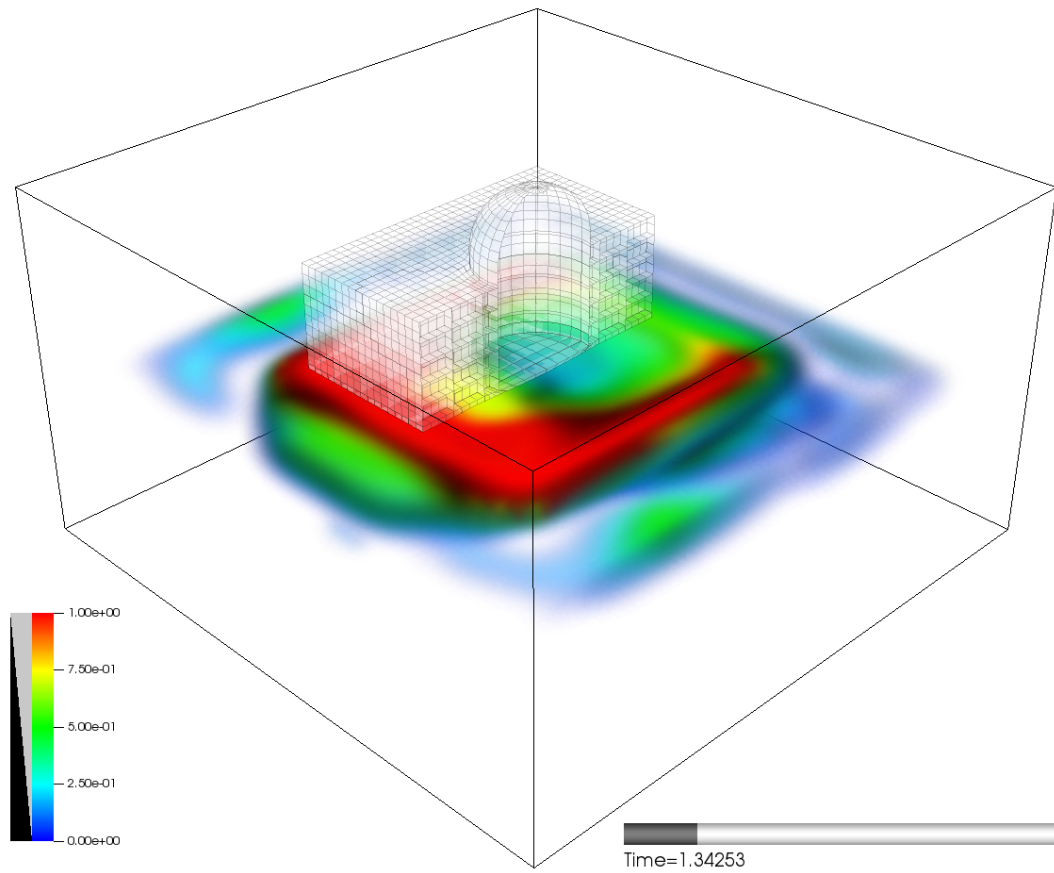


Figure 7.5: Incremental energy dissipation under an NPP, at one time increment.

Energy dissipation at this time instance is localized to one of the edges of the NPP foundation slab. In general, it is noted that most dissipation happens under slab edges.

Chapter 8

Task 4.6: Buoyancy Modeling

8.1 Summary of Findings for Task 4.6

The main findings are:

- Buoyant forces are always present when foundations are located under the water table.
- Simple modeling of buoyant forces by using a single, resultant buoyant force (obtained by integrating volume of a foundation that is under water table) can only be used if foundation (beneath water table) is rigid, and if pore fluid pressures in soil beneath foundation do not change during an earthquake. This is rarely (if ever!) the case.
- Mechanical behavior of fully saturated, fully coupled soil (soil skeleton and pore fluid) beneath the foundation, plays a crucial role in development and dynamic changes of buoyant pressure and consequentially, buoyant forces.
- Water pumping, during dynamic shaking of an NPP (up and down motions, rocking), does create dynamic buoyancy effects.
- A significant problem in modeling buoyancy effects, where dynamics of soils and the contact zone control buoyancy pressures/forces, is the lack of test data. That is, there are only very few tests for dynamic behavior of saturated contacts. and all of them are not element tests, rather they are tests on a small model or full scale full foundations under water

(Allmond et al., 2011) and as such lack detailed measurements of local, element level behavior.

8.2 Methodology

For NPP structures on surface or embedded foundations, with water table that extends over the lowest level of foundation, a buoyant pressure/forces occurs. These buoyant force act on a foundation concrete or on an impermeable barrier that protects concrete from the underground water. These buoyant forces are usually present for both surface and embedded foundation (Kennedy, 2009-2014), where water table is higher than the lowest foundation level,

For self weight and other static loads, and if we assume infinitely stiff structures, buoyant force B can be calculated and applied as a single resultant force directed upward. This is what is currently done for analyzing NPPs (Kennedy, 2009-2014). Calculation of static buoyant force¹ is given as:

$$B = \rho_w g V \quad (8.1)$$

where $\rho_w = 999.972 \text{ kg/m}^3$ is the mass density of water (at temperature of $+4^\circ\text{C}$ with small changes of less than 1% up to $+40^\circ\text{C}$), $g = 9.81 \text{ m/s}^2$ is the gravitational acceleration, and V is the volume of displaced fluid (volume of foundation under water table).

There are a number of effects that the presence of buoyant forces will have on static, and more importantly dynamic behavior of NPPs.

8.3 Work Performed, Subtasks

8.3.1 Background

Provided here is a brief overview of the problem of modeling buoyant forces.

Buoyant forces are resulting from foundations located below water table, in saturated soil and rock. These follower forces (Felippa, 1993-2015) change dynamically as foundation (and the

¹Static buoyant force calculation is based on the Archimedes principle: "Any object immersed in water is buoyed up by a force equal to the weight of water displaced by the object".

structure over it) undergo dynamic motions during earthquake.

For NPP structures founded on soil and permeable rock, with water table above base of concrete foundation, vertical motions and rocking response creates a potential for uplift and opening of the gap, which is significantly affected by the buoyant force. During uplifting motion of the NPP, the pore fluid at the base of a foundation in soil/rock (beneath foundation concrete or beneath impermeable barriers) is "sucked" into the gap (between soil/rock and the foundation concrete) thus reducing potential for lifting up. This reduction in potential for lifting up is due to dynamic change in buoyant pressure/force due to "suction". Fluid volume that is sucked from the soil/rock creates a significant change in pore fluid pressures in soil/rock, and consequentially a pressure gradient, causing water in soil/rock pores to move, change the buoyant pressure and forces and thus add to the nonlinear effects.

Similarly, with bottom of foundation below water table and with vertical motions and rocking response creating a potential for uplift and now closing of the gap, is significantly affected by the buoyant force too. After uplifting motions, when the NPP structure and its foundation, are "falling" back to the ground, water that was "sucked" up into the gap, experiences significant increase in pressure, thus creating excess buoyant pressures, that, in extreme cases, can cause part of foundation to "float", or totally loose contact with the base soil/rock. Fluid volume is pumped back into the soil/rock, creating high pressure gradients (and potentially temporarily liquefying top layers of soil even for very dense soil), changing buoyant pressures and forces and thus adding to the nonlinear effects of Buoyant forces.

The excess pore water pressures or the suction, created in the zone between foundation and underlying soil/rock strongly affect shear deformation as well, due to the changes in contact forces between foundation and soil/rock. In addition, during shear deformation of soil/rock just beneath NPP foundation, dilatancy effects (in dense soil and rock) change (reduce) the void space in soil/rock skeleton, and this changes (reduces) the pore fluid pressures (for dense soil and fissured rock, mostly found under NPP foundations). Such reduction in pore fluid pressure ("suction") reduces buoyant pressures/forces, and creates additional nonlinear buoyant pressure/force effects.

All of these different scenarios create conditions for changes in (static) buoyant force, making this force fully dynamic and nonlinearly changing during dynamic motions.

8.3.2 Modeling Approach

The modeling of buoyancy forces was achieved with two different (yet closely related) approaches.

Approach #1. In cases where a sharp contrast in permeability between soil/rock and foundation concrete exists, that is, where permeability of foundation concrete is much different than permeability of underlying soil (usual case), buoyant forces will be modeled directly, by this sharp contrast in permeability (Cheng and Jeremić, 2009b). Using sharp contrast approach, the buoyant forces are created by providing physical permeabilities for soil (and some highly permeable rock) and for concrete which is quite impermeable (but not absolutely impermeable, permeability of concrete is couple of orders of magnitude lower than that of soil or permeable rock). When the water tries to move (natural process due to pore water pressure gradient) from soil toward foundation concrete (due to static water pressure gradient or during dynamic/earthquake events), it is restricted by the low permeability of the concrete. A region of pressure (hydrostatic for static loading, or a different, dynamic pressure that results from dynamic behavior of soil/rock) is formed. This pressure acts as a buoyant force on the concrete foundation.

However, this approach only works well when there is no gap opening. In addition to that, there are modeling problems, with high pressure gradient close to the boundary between soil/rock and concrete, modeler needs to carefully mesh that region, to overcome too large pressure gradients in single layer of finite elements. A better approach, with or without gap opening is to use special coupled contact finite element described below.

Approach #2. Use of special coupled contact finite element, that explicitly models water displacements and pressures and allows for explicit gap opening, filling of gap with water, slipping (frictional) when the gap is closed, and pumping of water as gap opens and closes, is recommended. This contact element incorporates the pore water pressure information, as well as the information about the displacement (movement) of pore water within a gap. It is based on a dry version of the contact element and has two important new features

- Pore water pressure values from one side of the special coupled contact element (saturated soil/rock side) will be communicated (direct transfer) to the other (concrete) side of this element. With this water pressure information available, the applied water pressure will

be acting on the foundation (concrete) finite elements. Foundation finite element will integrate pressure field on a given face (or faces) of the element and will create a buoyant (nodal) forces. Integration of pressure on an element face into buoyant forces is done using standard finite element procedure for calculating nodal forces (these are the buoyant forces in our case) from face pressures:

$$F_{Ia}^{buoyant} = \int_{S^m} f_a^{buoyant} H_I dS^m \quad (8.2)$$

where $F_{Ia}^{buoyant}$ is the buoyant force at each node of the foundation finite element, f_a^S is the distribution of buoyant pressures on a face the foundation finite element, and H_I is a standard shape function of the foundation finite element (in our case, linear for 8 node brick, or quadratic for a 27 node brick). The integration is performed over a surface area S^m of each finite element face where buoyant pressures are present.

With buoyant forces acting at the bottom (or sides) of a foundation, a proper reduction (change) of contact pressures (forces) will be calculated, according to the effective stress principle (Terzaghi et al., 1996). This means that the slipping (frictional) criteria of the contact element will have all the necessary information about the normal forces (now reduced because of buoyant forces) and will determine if the contact will slip and remain attached (at the location of that contact element).

- Gap opening (physical values obtained from simulations) are used to create suction and compression pore/gap water field. This is achieved by connecting the displacements of the pore fluid from soil/rock finite elements (we will be using u-p-U finite elements for soil/rock modeling (Jeremić et al., 2008)), to the contact element node on the opposite side of the special coupled contact element. This way, if the gap opens, and the contact element now features an opening, the water displacements from the soil/rock side of the contact element is "pulled" to follow the uplifting foundation. This water movement creates a pressure gradients in the soil/rock elements beneath, which is accurately modeled using fully coupled u-p-U finite elements for soil/rock (Jeremić et al., 2008; Jeremić and Cheng, 2009).

8.4 Illustrative Example

A single brick u - p - U finite element is used to model an oedometer compression shown in Figure 8.1. Horizontal displacements and pore pressure are fixed in each node in order to guarantee the one-dimensional and dry conditions. As the ground is modeled as an un-deformable and impermeable layer (1,2,3,4), vertical soil and fluid displacements are fixed. The time-history displacement, shown in Figure 8.2, is applied in vertical direction to each node of the top surface (9,10,11,12). The time-history normal force induced in each contact element is represented in Figure 8.1 and compared with the one obtained with the dry brick element. It is worth noting that the normal force patterns are overlapped: this is due to the fact that excess pore pressure is fixed to zero and the oedometer stiffness are the same in the two cases.

Parameter	Symbol	Value
Young's Modulus	E [kPa]	$1.5 \cdot 10^{10}$
Poisson ratio	ν [-]	0.0
Solid particle bulk modulus	K_s [kPa]	$3.6 \cdot 10^7$
Fluid bulk modulus	K_f [kPa]	$2.17 \cdot 10^6$
Solid density	ρ_s [Mg/m ³]	2.7
Fluid density	ρ_f [Mg/m ³]	1.0
Porosity	n [-]	$1.0 \cdot 10^{-8}$
Darcy permeability	K [m/s]	$1.0 \cdot 10^3$

Table 8.1: Soil parameters.

In what follows an overview of coupled modeling is presented, while more information can be found in recent publications (Jeremić et al., 2008; Shahir et al., 2012; Taiebat et al., 2010)

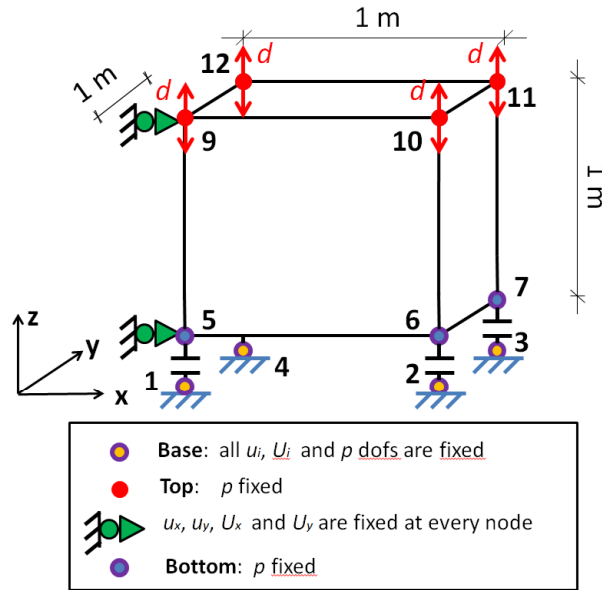


Figure 8.1: Single eight-node brick element. The nodes of the bottom surface are connected to the ground floor through contact elements. Vertical time-history displacement applied to the nodes of the top surface.

8.5 Fully Coupled Formulation for Porous Solid – Pore Fluid

8.5.1 u-p-U Formulation

Background For single-phase material encountered in structural mechanics, the response under ultimate load (failure) can be predicted using very simple calculations, at least for static problems. But for soil mechanics, simple, limit-load calculations can not be fully justified under static situation. However, for problems of soil dynamics, the use of simplified methods is almost never admissible.

As the strength of the soil can be determined once the pore water pressures are known, it is possible to reduce the soil mechanics problem to that of the behavior a single phase. Then we can use again the simple, single-phase analysis approaches. Now we will introduce the concept of effective stress.

The relationship between effective stress, total stress and pore pressure is (assume tensile

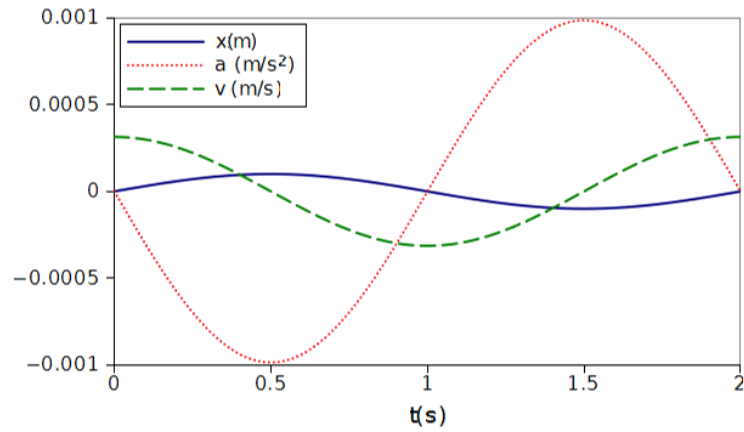


Figure 8.2: Input signal: time history of displacement, acceleration and velocity.

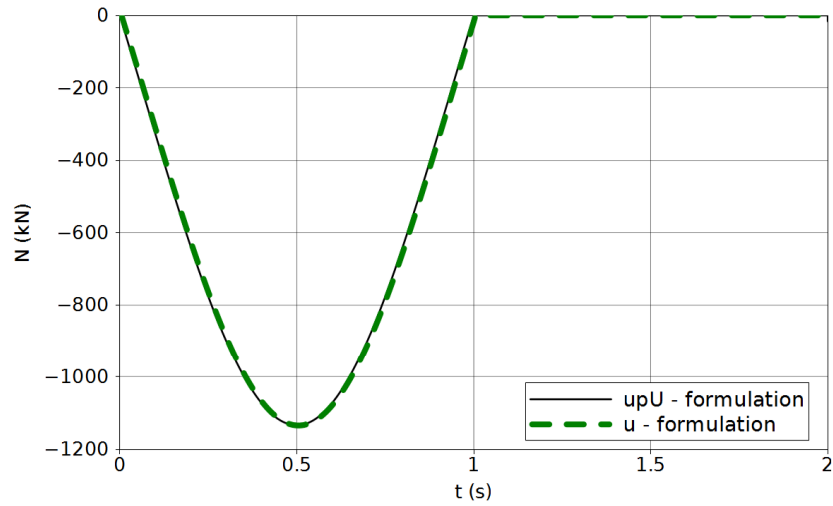


Figure 8.3: Normal force vs time in each contact element. *u-formulation* represents the results for a dry element whereas *upU-formulation* represents the results obtained through the model shown in Figure 8.1.

components of stress as positive and compressive pressure, p is positive) (Zienkiewicz et al., 1999a)

$$\sigma''_{ij} = \sigma_{ij} + \alpha \delta_{ij} p \quad (8.3)$$

where σ''_{ij} is effective stress tensor, σ_{ij} is total stress tensor, δ_{ij} is Kronecker delta. $\delta_{ij} = 1$, when $i=j$, and $\delta_{ij} = 0$, when $i \neq j$. For isotropic materials, $\alpha = 1 - K_T/K_S$. K_T is the total bulk modulus of the solid matrix, K_S is the bulk modulus of the solid particle. For most of the soil mechanics problems, as the bulk modulus K_S of the solid particles is much larger than that of the whole material, $\alpha \approx 1$ can be assumed. Equation (8.3) becomes

$$\sigma''_{ij} = \sigma_{ij} + \delta_{ij}p \quad (8.4)$$

Governing Equations of Porous Media Before proceeding with the general equations, we introduce the associated notation. In this we have

- σ_{ij} the total Cauchy stress in the mixture at any instant
- u_i the displacement of the solid skeleton
- w_i the pseudo-displacement of the fluid phase relative to the skeleton of solid
- p the pore water pressure
- $\varepsilon_{ij} = \frac{1}{2}(du_{i,j} + du_{j,i})$ the strain increment of the solid phase
- $\omega_{ij} = \frac{1}{2}(du_{i,j} - du_{j,i})$ the rotation increment of the solid phase
- ρ, ρ_s, ρ_f the densities of the mixture, and the solid phase and water respectively
- n the porosity
- $\theta = -\dot{w}_{i,i}$ the rate at which volume of water changes per unit total volume of mixture

With these definitions, and others introduced as necessary, we can write the governing equation of the coupled system.

The Equilibrium Equation of the Mixture. The overall equilibrium or momentum balance equation for the soil-fluid 'mixture' can be written as (Zienkiewicz et al., 1999a)

$$\sigma_{ij,j} - \rho \ddot{u}_i - \rho_f [\ddot{w}_i + \dot{w}_j \dot{w}_{i,j}] + \rho b_i = 0 \quad (8.5)$$

Where \ddot{u}_i is the acceleration of the solid part, b_i is the body force per unit mass, $\dot{w}_i + \underline{\dot{w}_j \dot{w}_{i,j}}$ is the fluid acceleration relative to the solid part, \ddot{w}_i is local acceleration, $\underline{\dot{w}_j \dot{w}_{i,j}}$ is convective acceleration.

The underlined terms in the above equation represent the fluid acceleration relative to the solid and convective terms of this acceleration. Generally this acceleration is so small that we shall frequently omit it. And for static problems, equation(8.5) only consists of the first and last terms.

For fully saturated porous media (no air inside), from definition

$$\begin{aligned}
 \rho &= \frac{M_t}{V_t} \\
 &= \frac{M_s + M_f}{V_t} \\
 &= \frac{V_s \rho_s + V_f \rho_f}{V_t} \\
 &= \frac{V_f}{V_t} \rho_f + \frac{V_t - V_f}{V_t} \rho_s \\
 &= n \rho_f + (1 - n) \rho_s \\
 \rho &= n \rho_f + (1 - n) \rho_s \tag{8.6}
 \end{aligned}$$

where M_t , M_s and M_f are the mass of total, solid part and fluid part respectively. V_t , V_s and V_f are the volume of total, solid part and fluid part respectively.

The Equilibrium Equation of the Fluid. For the pore fluid, the equation of momentum balance can be written as (Zienkiewicz et al., 1999a)

$$-p_{,i} - R_i - \rho_f \ddot{u}_i - \rho_f [\ddot{w}_i + \underline{\dot{w}_j \dot{w}_{i,j}}] / n + \rho_f b_i = 0 \tag{8.7}$$

where R is the viscous drag forces. It should be noted that the underlined terms in (8.7) represent again the convective fluid acceleration and are generally small. Also note that, throughout report, the permeability \mathbf{k} is used with dimensions of $[length]^3[time]/[mass]$, which is different from the usual soil mechanics convention, where the permeability has the dimension of velocity, i.e. $[length]/[time]$. Their values are related by $k = K/\rho_f g$, where g is the gravitational acceleration at which the permeability is measured. Assuming the Darcy seepage law: $n\dot{w} = Ki$, here i is

the head gradient. Seepage force is then $R = \rho_f g i$. R can be written as

$$R_i = k_{ij}^{-1} \dot{w}_j \quad \text{or} \quad R_i = k^{-1} \dot{w}_i \quad (8.8)$$

k_{ij} or k are Darcy permeability coefficients for anisotropic and isotropic conditions respectively.

Flow Conservation Equation. The final equation is supplied by the mass conservation of the fluid flow (Zienkiewicz et al., 1999a)

$$\dot{w}_{i,i} + \alpha \dot{\varepsilon}_{ii} + \frac{\dot{p}}{Q} + n \frac{\dot{\rho}_f}{\rho_f} + \dot{s}_0 = 0 \quad (8.9)$$

The first term of equation(8.9) is the flow divergence of a unit volume of mixture. The second term is the volume change of the mixture. In the third term, Q is relative to the compressibility of the solid and fluid. The underlined terms represent change of density and rate of volume expansion of the solid in case of thermal changes. They are generally negligible.

$$\frac{1}{Q} \equiv \frac{n}{K_f} + \frac{\alpha - n}{K_s} \cong \frac{n}{K_f} + \frac{1 - n}{K_s} \quad (8.10)$$

where K_s and K_f are the bulk moduli of the solid and fluid phases respectively.

Thus, we got the total mixture equilibrium equation (8.5), fluid equilibrium equation(8.7) and the flow conservation equation (8.9) for saturated soil. By omitting the convective acceleration (the underline terms in (8.5) and (8.7)), density variation and the volume expansion due to the thermal change (the underline terms in (8.9)), the equations of the total coupled system can be further simplified, they are summarized as below

$$\sigma_{ij,j} - \rho \ddot{u}_i - \rho_f \ddot{w}_i + \rho b_i = 0 \quad (8.11)$$

$$-p_{,i} - R_i - \rho_f \ddot{u}_i - \frac{\rho_f \ddot{w}_i}{n} + \rho_f b_i = 0 \quad (8.12)$$

$$\dot{w}_{i,i} + \alpha \dot{\varepsilon}_{ii} + \frac{\dot{p}}{Q} = 0 \quad (8.13)$$

8.5.2 Modified Governing Equations.

Solid Part Equilibrium Equation. First of all, a new variable U_i is introduced in place of the relative pseudo-displacement w_i , it is defined as

$$U_i = u_i + U_i^R = u_i + \frac{w_i}{n} \quad (8.14)$$

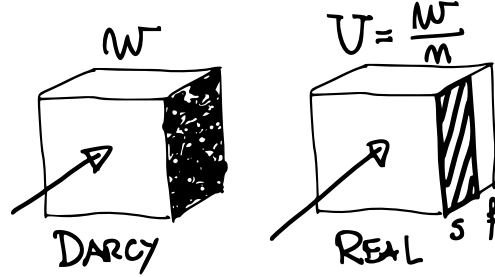


Figure 8.4: Fluid mechanics of Darcy's flow (w_i) versus real flow ($U_i = w_i/n$).

Insertion of definition (8.14) into equation (8.11)(8.12) and subtraction of $[n \times (8.12)]$ from equation (8.11) leads to the equation of skeleton equilibrium

$$\sigma_{ij,j} - \rho \ddot{u}_i + \rho b_i + n p_{,i} + n R_i + n \rho_f \ddot{u}_i - n \rho_f b_i = 0 \quad (8.15)$$

By substituting $\rho = (1 - n)\rho_s + n\rho_f$

$$\begin{aligned} \sigma_{ij,j} - (1 - n)\rho_s \ddot{u}_i - n\rho_f \ddot{u}_i + (1 - n)\rho_s b_i + n\rho_f b_i + n p_{,i} + n R_i + n \rho_f \ddot{u}_i - n \rho_f b_i &= 0 \\ \sigma_{ij,j} + n p_{,i} + (1 - n)\rho_s b_i - (1 - n)\rho_s \ddot{u}_i + n R_i &= 0 \end{aligned} \quad (8.16)$$

By using the definition of effective stress (8.3),(8.15) becomes

$$\sigma''_{ij,j} - (\alpha - n)p_{,i} + (1 - n)\rho_s b_i - (1 - n)\rho_s \ddot{u}_i + n R_i = 0 \quad (8.17)$$

Fluid Part Equilibrium Equation. The fluid part equilibrium equation can be obtained simply by $[n \times (8.12)]$,i.e.

$$\begin{aligned} -n p_{,i} - n R_i - n \rho_f \ddot{u}_i - \rho_f \ddot{w}_i + n \rho_f b_i &= 0 \\ -n p_{,i} - n R_i - n \rho_f \left(\ddot{u}_i + \frac{\ddot{w}_i}{n} \right) + n \rho_f b_i &= 0 \end{aligned} \quad (8.18)$$

From equation (8.14), we have

$$\ddot{U}_i = \ddot{u}_i + \frac{\ddot{w}_i}{n} \quad (8.19)$$

so that equation (8.18) becomes:

$$-np_{,i} + n\rho_f b_i - n\rho_f \ddot{U}_i - nR_i = 0 \quad (8.20)$$

Mixture Balance of Mass. By differentiating equation (8.14) in time space, we have

$$\dot{w}_{i,i} = n\dot{U}_{i,i} - n\dot{u}_{i,i} \quad (8.21)$$

Notice that $\dot{\varepsilon}_{ii} = \dot{u}_{i,i}$, so that equation (8.21) becomes

$$\dot{w}_{i,i} = n\dot{U}_{i,i} - n\dot{\varepsilon}_{ii} \quad (8.22)$$

By substituting (8.22) to (8.13), we obtain

$$n\dot{U}_{i,i} - n\dot{\varepsilon}_{ii} + \alpha\dot{\varepsilon}_{ii} + \frac{\dot{p}}{Q} = 0 \quad (8.23)$$

or:

$$-n\dot{U}_{i,i} = (\alpha - n)\dot{\varepsilon}_{ii} + \frac{1}{Q}\dot{p} \quad (8.24)$$

Thus we got the whole set of modified governing equations (8.17),(8.20) and (8.24). They are summarized as below

$$\sigma''_{i,j,j} - (\alpha - n)p_{,i} + (1 - n)\rho_s b_i - (1 - n)\rho_s \ddot{u}_i + nR_i = 0 \quad (8.25)$$

$$-np_{,i} + n\rho_f b_i - n\rho_f \ddot{U}_i - nR_i = 0 \quad (8.26)$$

$$-n\dot{U}_{i,i} = (\alpha - n)\dot{\varepsilon}_{ii} + \frac{1}{Q}\dot{p} \quad (8.27)$$

From the modified equation set (8.25),(8.26) and (8.27), we can see that only \ddot{u}_i occurs in the first equation, and only \ddot{U}_i in the second, thus leading to a convenient diagonal form in discretization.

Now we have a complete equation system given by (8.25),(8.26) and (8.27). With the basic definitions introduced earlier, there are three essential

1. solid displacement u
2. pore pressure p
3. absolute fluid displacement U

The boundary conditions imposed on these variables will complete the problem. These boundary conditions are: For the momentum balance part, on boundary Γ_t , traction $t_i(t)$ (or $\sigma_{ij}n_j$), where n_i is the i -th component of the normal to the boundary is specified. On boundary Γ_u , the displacement u_i is given. For the fluid part, again the boundary is divided into two parts. On Γ_p , the pressure p is specified, on Γ_w , the normal outflow w_n is specified. For impermeable boundary a zero value for the outflow should be specified.

The boundary conditions can be summarized below

$$\begin{aligned}
 \Gamma &= \Gamma_t \cup \Gamma_u \\
 t_i &= \sigma_{ij}n_j = \bar{t}_i \quad \text{on} \quad \Gamma = \Gamma_w \\
 u_i &= \bar{u}_i \quad \text{on} \quad \Gamma = \Gamma_u
 \end{aligned} \tag{8.28}$$

and

$$\begin{aligned}
 \Gamma &= \Gamma_p \cup \Gamma_w \\
 p &= \bar{p} \quad \text{on} \quad \Gamma = \Gamma_p \\
 n^T w &= w_n \quad \text{on} \quad \Gamma = \Gamma_w
 \end{aligned} \tag{8.29}$$

8.5.3 Numerical Solution of the u-p-U Governing Equations

The solutions to the problems governed by the above equations can be solved using the Finite Element Method.

Matrix form of the governing equations The numerical forms of governing equations can be written together in the matrix form as

$$\begin{aligned}
 \begin{bmatrix} M_s & 0 & 0 \\ 0 & 0 & 0 \\ 0 & 0 & M_f \end{bmatrix} \begin{bmatrix} \ddot{\bar{u}} \\ \ddot{\bar{p}} \\ \ddot{\bar{U}} \end{bmatrix} + \begin{bmatrix} C_1 & 0 & -C_2 \\ 0 & 0 & 0 \\ -C_2^T & 0 & C_3 \end{bmatrix} \begin{bmatrix} \dot{\bar{u}} \\ \dot{\bar{p}} \\ \dot{\bar{U}} \end{bmatrix} + \begin{bmatrix} K^{EP} & -G_1 & 0 \\ -G_1^T & -P & -G_2^T \\ 0 & -G_2 & 0 \end{bmatrix} \begin{bmatrix} \bar{u} \\ \bar{p} \\ \bar{U} \end{bmatrix} \\
 = \begin{bmatrix} \bar{f}_s \\ 0 \\ \bar{f}_f \end{bmatrix} \tag{8.30}
 \end{aligned}$$

or in index form

$$\begin{aligned}
 \begin{bmatrix} (M_s)_{KijL} & 0 & 0 \\ 0 & 0 & 0 \\ 0 & 0 & (M_f)_{KijL} \end{bmatrix} \begin{bmatrix} \ddot{\bar{u}}_{Lj} \\ \ddot{\bar{p}}_N \\ \ddot{\bar{U}}_{Lj} \end{bmatrix} + \begin{bmatrix} (C_1)_{KijL} & 0 & -(C_2)_{KijL} \\ 0 & 0 & 0 \\ -(C_2)_{LjiK} & 0 & (C_3)_{KijL} \end{bmatrix} \begin{bmatrix} \dot{\bar{u}}_{Lj} \\ \dot{\bar{p}}_N \\ \dot{\bar{U}}_{Lj} \end{bmatrix} \\
 + \begin{bmatrix} (K^{EP})_{KijL} & -(G_1)_{KiM} & 0 \\ -(G_1)_{LjM} & -P_{MN} & -(G_2)_{LjM} \\ 0 & -(G_2)_{KiL} & 0 \end{bmatrix} \begin{bmatrix} \bar{u}_{Lj} \\ \bar{p}_M \\ \bar{U}_{Lj} \end{bmatrix} = \begin{bmatrix} \bar{f}_{Ki}^{solid} \\ 0 \\ \bar{f}_{Ki}^{fluid} \end{bmatrix} \tag{8.31}
 \end{aligned}$$

where

$$\begin{aligned}
\mathbf{M}_s &= (M_s)_{KijL} = \int_{\Omega} N_K^u (1-n) \rho_s \delta_{ij} N_L^u d\Omega \\
\mathbf{M}_f &= (M_f)_{KijL} = \int_{\Omega} N_K^U n \rho_f \delta_{ij} N_L^U d\Omega \\
\mathbf{C}_1 &= (C_1)_{KijL} = \int_{\Omega} N_K^u n^2 k_{ij}^{-1} N_L^u d\Omega \\
\mathbf{C}_2 &= (C_2)_{KijL} = \int_{\Omega} N_K^u n^2 k_{ij}^{-1} N_L^U d\Omega \\
\mathbf{C}_3 &= (C_3)_{KijL} = \int_{\Omega} N_K^U n^2 k_{ij}^{-1} N_L^U d\Omega \\
\mathbf{K}^{EP} &= (K^{EP})_{KijL} = \int_{\Omega} N_{K,m}^u D_{imjn} N_{L,n}^u d\Omega \\
\mathbf{G}_1 &= (G_1)_{KiM} = \int_{\Omega} N_{K,i}^u (\alpha - n) N_M^p d\Omega \\
\mathbf{G}_2 &= (G_2)_{KiM} = \int_{\Omega} n N_{K,i}^U N_M^p d\Omega \\
\mathbf{P} &= P_{NM} = \int_{\Omega} N_N^p \frac{1}{Q} N_M^p d\Omega
\end{aligned} \tag{8.32}$$

$$\begin{aligned}
\bar{f}_{Ki}^{solid} &= (f_1^u)_{Ki} - (f_4^u)_{Ki} + (f_5^u)_{Ki} \\
\bar{f}_{Ki}^{fluid} &= -(f_1^U)_{Ki} + (f_2^U)_{Ki} \\
(f_1^u)_{Ki} &= \int_{\Gamma_t} N_K^u n_j \sigma_{ij}'' d\Gamma \\
(f_4^u)_{Ki} &= \int_{\Gamma_p} N_K^u (\alpha - n) n_i p d\Gamma \\
(f_5^u)_{Ki} &= \int_{\Omega} N_K^u (1-n) \rho_s b_i d\Omega \\
(f_1^U)_{Ki} &= \int_{\Gamma_p} n N_K^U n_i p d\Gamma \\
(f_2^U)_{Ki} &= \int_{\Omega} n N_K^U \rho_f b_i d\Omega
\end{aligned} \tag{8.33}$$

Here we have N^u, N^p, N^U as the shape functions of skeleton, pore pressure and fluid, ρ, ρ_s, ρ_f are the density of the total, the solid and the fluid phases, respectively, n is the porosity, and by its definition $\rho = (1-n)\rho_s + n\rho_f$, the symbol n_i is the direction of the normal on the boundary,

u is the displacement of the solid part, p is pore pressure and U is the absolute displacement of the fluid part. Equation (8.30) represents the general form ($u - p - U$) for coupled system which can be written in a familiar form as

$$M\ddot{x} + C\dot{x} + Kx = f \quad (8.34)$$

where x represents the generalized unknown variable. Solution of this equation for each time step will render unknown field for given initial and boundary conditions.

8.5.4 Buoyant Forces: Surface Loads for Solid Bricks

Pore fluid pressures, determined through a dynamic analysis, and available from coupled finite elements, as described above are then used to develop buoyant pressures and consequentially, buoyant nodal forces. These buoyant forces are developed from surface loads on foundation finite elements that are modeled using brick finite elements.

In order to apply surface load on brick elements, equivalent nodal forces have to be applied instead of the surface load. The equivalent force of the i -th node F_i is given by the following equation with shape function N_i and load distribution function f .

$$F_i = \int_S f N_i ds \quad (8.35)$$

When we assume the load distribution is uniform, it turns into

$$F_i = f \int_S N_i ds \quad (8.36)$$

Furthermore, when the magnitude of the load per unit area is 1, and the size of the element is $1 \times 1 \times 1$, equivalent nodal forces are given as shown in Figure 8.5 for 8 node brick element, 20 brick element, and 27 nodes brick element.

Figure 8.5 shows cases of normal loads on vertical upper surface (with nodes: 1, 2, 3, 4 for 8 node brick; 1, 2, 3, 4, 9, 10, 11, and 12 for 20 node brick; and 1, 2, 3, 4, 9, 10, 11, 12 and 26 for the 27 node brick).

Nodal loads from uniform surface loads for 27 node brick are obtained as:

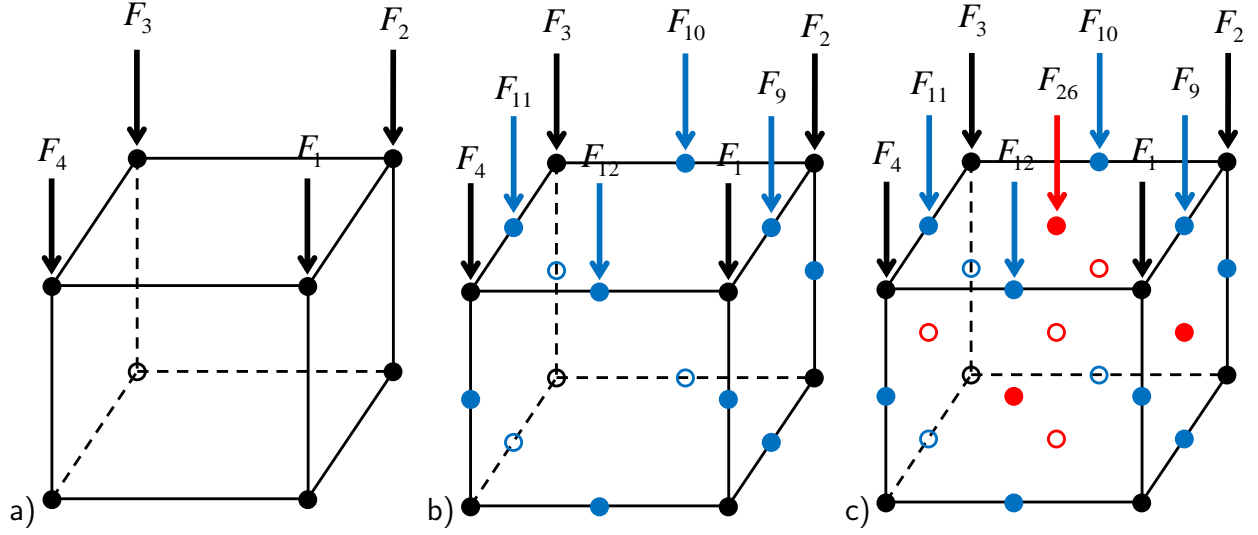


Figure 8.5: Nodal loads for brick elements: (a) $F_1 = F_2 = F_3 = F_4 = +1/4$; (b) $F_1 = F_2 = F_3 = F_4 = -\frac{1}{12}$, $F_9 = F_{10} = F_{11} = F_{12} = +\frac{1}{3}$; (c) $F_1 = F_2 = F_3 = F_4 = +\frac{1}{36}$, $F_9 = F_{10} = F_{11} = F_{12} = +\frac{1}{9}$, $F_{26} = \frac{4}{9}$.

- for nodes 1, 2, 3, and 4, $N_i^{(e)} = \frac{1}{8}(1 + \xi\xi_i)(1 + \eta\eta_i)(1 + \mu\mu_i)(\xi\xi_i)(\eta\eta_i)(\mu\mu_i)$

$$\begin{aligned}
 \int_{-1}^{+1} N_i dS &= \\
 &= \frac{1}{8}(1 + \mu\mu_i)(\mu\mu_i) \int_{-1}^{+1} \int_{-1}^{+1} (1 + \xi\xi_i)(1 + \eta\eta_i)(\xi\xi_i)(\eta\eta_i)(\eta\eta_i) d\xi d\eta \\
 &= \frac{1}{8}(1 + \mu\mu_i)(\mu\mu_i)(\xi_i)^2(\eta_i)^2\left(\frac{2}{3}\right)^2 \\
 &= \frac{1}{18}(1 + \mu\mu_i)(\mu\mu_i)(\xi_i)^2(\eta_i)^2 \tag{8.37}
 \end{aligned}$$

- for nodes 9, 10, 11 and 12, $N_i^{(e)} = \frac{1}{4}(1 - \xi^2)(1 + \eta\eta_i)(1 + \mu\mu_i)(\eta\eta_i)(\mu\mu_i)$

$$\begin{aligned}
 \int_{-1}^{+1} N_i dS &= \\
 &= \frac{1}{4}(1 + \mu\mu_i)(\mu\mu_i) \int_{-1}^{+1} (1 - \xi^2)(1 + \eta\eta_i)(\eta\eta_i) d\xi d\eta \\
 &= \frac{1}{8}(1 + \mu\mu_i)(\mu\mu_i)(\eta_i)^2\left(\frac{4}{3}\right)\left(\frac{2}{3}\right) \\
 &= \frac{2}{9}(1 + \mu\mu_i)(\mu\mu_i)(\eta_i)^2 \tag{8.38}
 \end{aligned}$$

- for nodes 26 $N_i^{(e)} = \frac{1}{2}(1 - \xi^2)(1 - \eta^2)(1 + \mu\mu_i)(\mu\mu_i)$

$$\begin{aligned}
 \int_{-1}^{+1} N_i dS &= \\
 &= \frac{1}{4}(1 + \mu\mu_i)(\mu\mu_i) \int_{-1}^{+1} \int_{-1}^{+1} (1 - \xi^2)(1 - \eta^2) d\xi d\eta \\
 &= \frac{1}{8}(1 + \mu\mu_i)(\mu\mu_i) \left(\frac{4}{3}\right) \left(\frac{4}{3}\right) \\
 &= \frac{8}{9}(1 + \mu\mu_i)(\mu\mu_i) \tag{8.39}
 \end{aligned}$$

Chapter 9

Task 4.7: Piled Foundations

9.1 Summary of Findings for Task 4.7

The main findings are:

- Seismic behavior of piles and pile groups can (should) be modeled using all the piles in a pile group, with nonlinear response of soil, nonlinear pile and the nonlinear pile-soil contact zone
- In some cases, when seismic motions are not too strong, some of the above nonlinearities can be neglected (for example piles will likely remain linear)
- Seismic behavior of piles and pile groups should be modeled using full solid and structural element and not P-Y springs. Noted P-Y springs are developed for monotonic, single plane loading of single piles in uniform soil and such are really not meant for cyclic, 3D analysis of piles and pile groups
- Large pile foundation groups (for example, under a complete NPP), that have end bearing (pile ends on a rock at depth) stiffen up NPP structural system almost as if NPP is sitting on a rock foundation, without any influence of a contact (for a slab foundation, contact of concrete and rock beneath)
- For large pile groups, leading and trailing piles can take a large portion of side (shear and bending) loading, while middle piles can be shielded to a large extent.

9.2 Methodology

Modeling of a single pile and pile groups relies on three main components:

- Modeling of a pile itself. This is mostly done using linear elastic beam-column elements (in general with moment bending around two main cross section axes, torsional (polar) moment twist, shear along two main cross section axes and the axial loading). Material for piles is usually steel, reinforced concrete or reinforced concrete in steel casings. In addition, for design basis motions, it is expected that piles will remain linear. On the other hand, if piles are expected to develop nonlinear deformation (plastic hinges), nonlinear beam elements can be used. It is advisable to use displacement based nonlinear beam elements, that is available in the Real ESSI Simulator program.
- Modeling of soil surrounding the pile (without the pile-soil contact zone). Any elastic (linear or nonlinear) or elastic plastic material model can be used for modeling soil. In general, for most design basis seismic motions, and with the stiffness introduced by the large number of piles under an NPP, it is not expected that soil surrounding large pile group will develop any significant inelastic deformation.
- Modeling of pile-soil contact zone. This zone will develop inelastic (elastic-plastic, nonlinear) before surrounding soil and/or pile(s). As such, it is always a advisable to always use a nonlinear contact model for modeling of this zone. This is particularly important as the interface of a stiff concrete and soft soil will most certainly produce inelastic deformation, even for very small seismic motions.

As usual, it is always a good idea to simulated full nonlinear response, allowing for nonlinear behavior of all the above three components, and then analyze results and decide if some of the nonlinearities really do not play any significant role in the response

9.2.1 Modelling approach

Modeling of large pile groups is done using tree approaches:

Full Detailed Modelling

This approach allows for detailed modeling of all three main sources of nonlinearities (inelasticities) as noted above. With this approach, a model is developed using:

- Solid (dry or saturated), elastic or elastic-plastic finite elements for soil. An opening is developed to house volume of a beam element used to model a pile. In other words, volume occupied by a pile, a pile that is modeled using a beam-column element (which means that the element is really just a line), is explicitly modeled.
- Contact finite elements (dry or saturated) for the pile-soil contact zone, where the contact is developed between connecting elements (elements that connect beam-column element and span across the volume (opening) of the pile to solid element.
- Beam finite elements for pile modeling, with connecting element that replace a volume of the pile and connect beam-column finite element nodes with nodes of solids.

Full Contact Simplified Modelling

Using this approach a model is developed using:

- Solid (dry or saturated), elastic or elastic-plastic finite elements for soil.
- Interaction finite elements (dry or saturated) for the pile-soil contact zone. These contact elements are not explicitly modeling actual normal/gaping and slipping contact. Their purpose is to mimic overall response of a pile-soil interaction, in a sense of P-Y springs. Caution should be exercised with use of these elements as their formulation is not based on rational mechanics, rather it is based on observations of experiments (preferably full scale, centrifuge experiments do not scale up!) and then some generalizations and simplifications.
- Beam finite elements for pile modeling. These finite elements are similar to the previous case, can be linear elastic or fully nonlinear. However, due to simplified interaction of pile and the soil, use of high fidelity nonlinear beam-column finite elements does necessarily increase accuracy of modeling. This is based on a fact that simplified modeling of pile-soil

interaction (see item above) might not provide high enough fidelity to warrant use of high fidelity beam-column finite elements.

Simplified Stiffness Only Modelling

Using this approach a model is developed using:

- Solid (dry or saturated), elastic or elastic-plastic finite elements for soil.
- Beam finite elements for pile modeling. These finite elements are similar to the first case, and can be linear elastic or fully nonlinear. However, due to lack of modeling of interaction of a pile and the soil, there is no need to use nonlinear beam-column finite elements.

This approach works well for large pile groups (similar to what might be used for an NPP) as it is expected that such large pile group will prevent any (significant or any at all) nonlinearity of soil and contact zone (and certainly will not allow for nonlinearity of piles in a pile group).

9.2.2 Modeling Details

Presented are few examples of pile and pile group models in dry and saturated soils.

Piles in Uniform, Liquefiable Soil

In using detailed modeling of piles in their interaction with the soil, it is necessary to carefully model pile, volume that that pile is occupying (since pile is modeled using a beam-column element, which is represented by a line with no volume), contact zone and the volume of soil adjacent to the pile. Figure 9.1 (Cheng and Jeremić, 2009a,b) shows one such model where phases of construction of a pile (from a pile group) are depicted.

Figure 9.2 (Cheng and Jeremić, 2009a,b) shows details of a connection of pile with connecting beam elements to solid finite elements modeling soil. This figure represent connection to coupled finite element used to model saturated soil, and the contact element is placed between the beam element and the solid element.

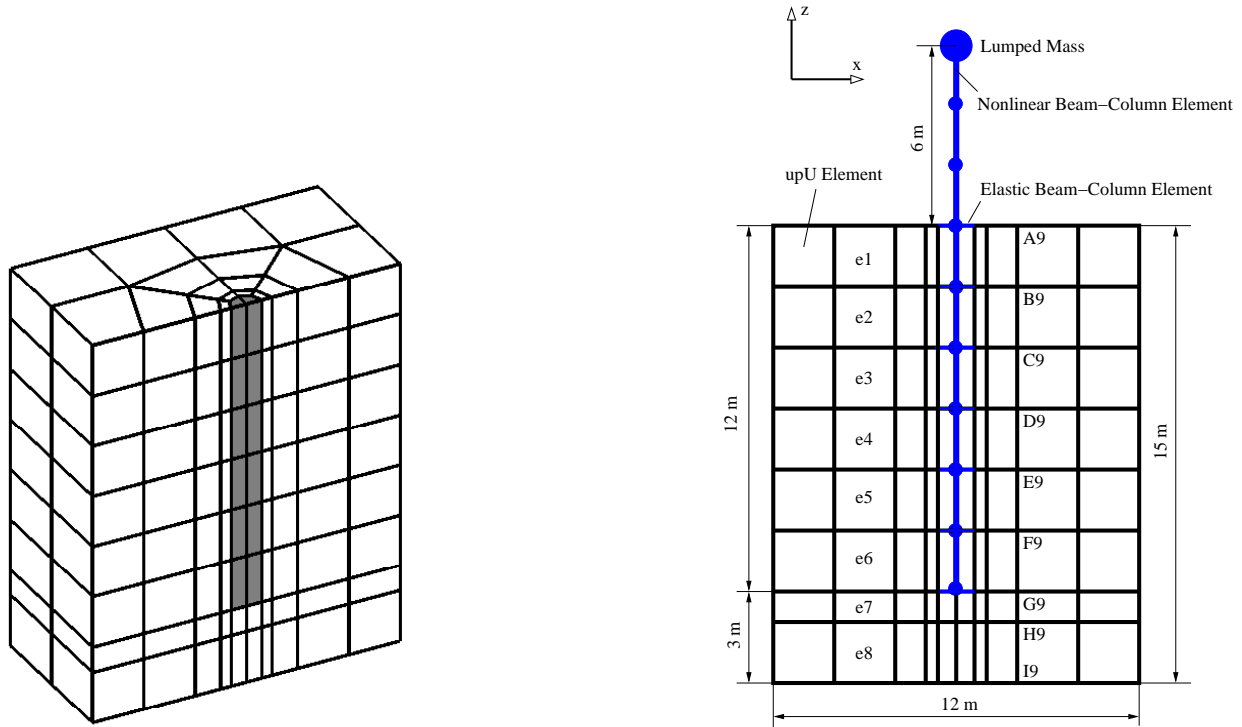


Figure 9.1: Left: Three dimensional finite element mesh featuring initial soil setup, where all the soil elements are present. The gray region of elements is excavated (numerically) and replaced by a pile during later stages of loading; Right: Side view of the pile-soil model.

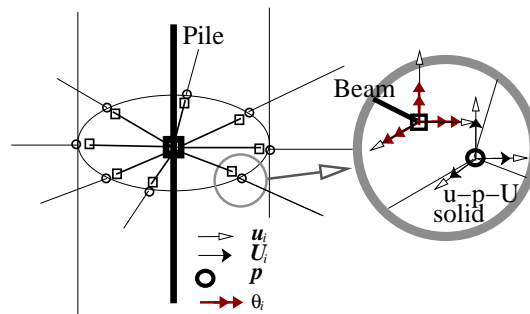


Figure 9.2: Schematic description of coupling of displacement DOFs (u_i) of beam-column element (pile) with displacement DOFs (u_i) of u-p-U elements (soil).

This particular model was used to investigate behavior of piles in liquefiable soils. This might be of particular importance for NPPs and other nuclear facilities that are founded on piles and are located close to bodies of water, which means that water table is close to the surface.

As reported by Cheng and Jeremić (2009b), behavior of piles in liquefiable soils needs to be done using higher than usual modeling sophistication. For example, six models were developed to investigate behavior of piles in liquefiable ground and to compare deformation and response of level and sloping ground with and without piles.

Six models were developed. First three models (model numbers I, II and III) were for level ground, while last three models (model numbers IV, V, and VI) were for sloping ground. First in each series of models (model I for level ground and model IV for sloping ground) were left without the second loading stage, without a pile–column system. Other four models (numbers II, III, V and VI) were analyzed for all three loading stages. Second in each series of models (models number II and V) had all displacements and rotations of pile–column top (where additional mass representing superstructure was placed) left free, without restraints. Thus, these two models represent lateral behavior of a structure. Third in each series of models (model numbers III and VI) had rotations in y directions fixed at the pile–column top, thus representing longitudinal behavior of a structure. Modeling longitudinal behavior of a structure by restraining rotations perpendicular to the structure is appropriate if the stiffness of a structure is large enough, which in this case it was, as it was assumed to be a post–tensioned concrete box girder, so that realistically, the top of a column does not rotate (much) during application of loads. Table 9.1 summarizes models described above.

Figures (9.3) through (9.5) show the R_u time history for up to 30 seconds, for elements (at one of Gauss point) e1, e3, e5 and e7 (refer to right side of Figure (9.1)). It is important to note that R_u is defined as the ratio of the difference of initial mean and current mean effective stresses over the initial mean effective stress:

$$R_u = \frac{p'_{initial} - p'_{current}}{p'_{initial}}$$

where mean effective stress is defined as $p' = \sigma'_{kk}/3$. This is different from traditional definition for R_u , that uses ratio of excess pore pressure over the initial mean effective stress ($p'_{initial}$). However, these two definitions are essentially equivalent, as soil is in the state of liquefaction for $R_u = 1$ (so that $p'_{current} = 0$), while there is no excess pore pressure for $R_u = 0$ (so that $p'_{initial} = p'_{current}$). However, the former definition is advocated here as it avoids the interpolation of pore pressure or extrapolation of the stresses (as the latter definition requires), since for the

Table 9.1: Cases descriptions.

Case	Model sketch	Descriptions
I		horizontal ground, no pile
II		horizontal ground, single pile, free column head
III		horizontal ground, single pile, no rotation at column head
IV		sloping ground, no pile
V		sloping ground, single pile, free column head
VI		sloping ground, single pile, no rotation at column head

u-p-U element, stresses are available at Gauss points while pore pressures are available element nodes. In particular, Figure 9.3 shows R_u time histories for four points for models I (level ground without pile) and model IV (sloping ground without pile). It is noted that differences are fairly small. It is interesting to observe that lower layers do not liquefy as supply of pore fluid for initial void ratio of $e_0 = 0.8$ is too small, and the pore fluid dissipation upward seems to be rapid. On the other hand, the upper soil layers do reach close to or liquefaction state ($R_u = 1$). This is primarily due to the propagation of pore fluid pressure/volume from lower layers upward (pumping effect) and, in addition to that, to a local excess pore fluid production. These results can also be contrasted with those of Jeremić et al. (2008), where similar pumping scenario has been observed. The main difference between soil used by Jeremić et al. (2008) and here is in the coefficient of permeability. Namely, here $k = 1.0 \times 10^{-4} \text{ m/s}$ was used (Čubrinovski et al., 2008; Uzuoka et al., 2008) while Jeremić et al. (2008) used $k = 5.0 \times 10^{-4} \text{ m/s}$. It is important to note that other values of permeability for Toyoura sand have also been reported (Sakemi et al., 1995), but current value was chosen based on Čubrinovski (2007 –).

In addition to that, similar to Jeremić et al. (2008), sloping ground case shows larger R_u

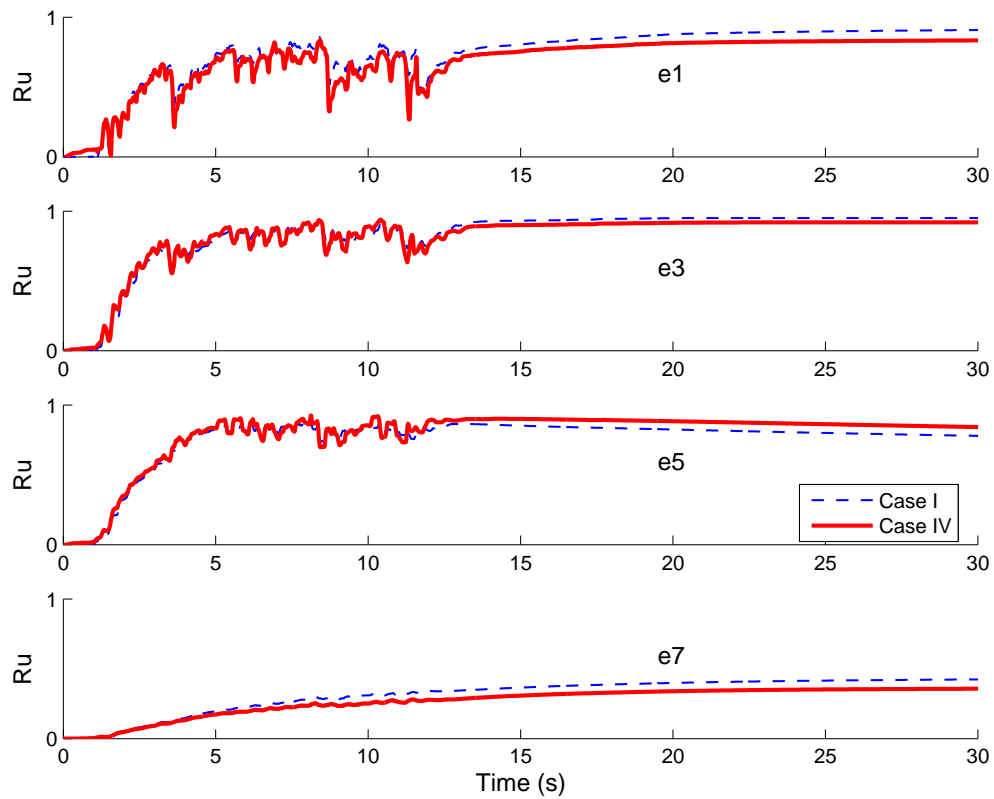


Figure 9.3: R_u times histories for elements e1 (top element), e3, e5, and e7 (bottom element) Gauss point) for Cases I (level ground, no pile) and IV (sloping ground, no pile).

spikes, since there is static shear force (stress) that is always present from gravity load on a slope. This static gravity on a slope will result in an asymmetric horizontal shear stresses in the down-slope direction during cycles of shaking. This asymmetric shear stress induces a more dilative response for down-slope shaking which will help soil regain its stiffness in the dilative parts of the loading cycles. This observation can be used to explain smaller R_u spikes for the sloping ground case. Of course, this asymmetry in loading will result in larger accumulation of down-slope deformation.

While R_u ratios for level and sloping ground cases are fairly similar along the depth of the model, the response changes when the pile is present. Figure (9.4) shows R_u responses at four different points (along the depth) approximately midway between the pile and the model boundary, in the plane of shaking (see location of those elements in Figure (9.1) on page 169). In comparison to behavior without the pile (Figure (9.3)), it is immediately obvious that addition of a pile with a mass on top reduces R_u during shaking for the top element (e1). This is to be expected as presence of a pile-column-mass (PCM) system changes the dynamics of the top layers of soil significantly enough to reduce total amount of shear. This is particularly true for the top layers of soil as effects of column-mass tend to create compressive and extensive movements (compression when the PCM system moves toward soil and extension, and possibly even tension, when PCM system moves away from soil). However, this extension, or possible tension, is not directly observable in presented plots since array of elements where we follow R_u (e1, e3, e5, e7) is some distance away from the pile-soil interface. Middle layers (e3 and e5), on the other hand, display similar response to that of Cases I and IV, as shown in Figure (9.3). It is noted that in a case with of sloping ground with pile, the R_u measurements are always larger than those for level ground (this is also observed for Cases III and VI, as shown in Figure (9.5)). This is expected as presence of a pile in loose sand, and particularly the dynamic movement of a pile during seismic shaking, create an additional shearing deformation field (in the soil adjacent to the pile) that provides for additional (faster) compression of soil skeleton and thus creates additional volume of pore fluid, that is then distributed to adjacent soil (adjacent to the pile).

Particularly interesting are R_u results for soil element e7, which is located below pile tip level (see Figure (9.1)). Observed R_u for Case V in element e7 is significantly larger than for the same element for Case II. Similarly, simulated R_u is larger than what was observed in cases without

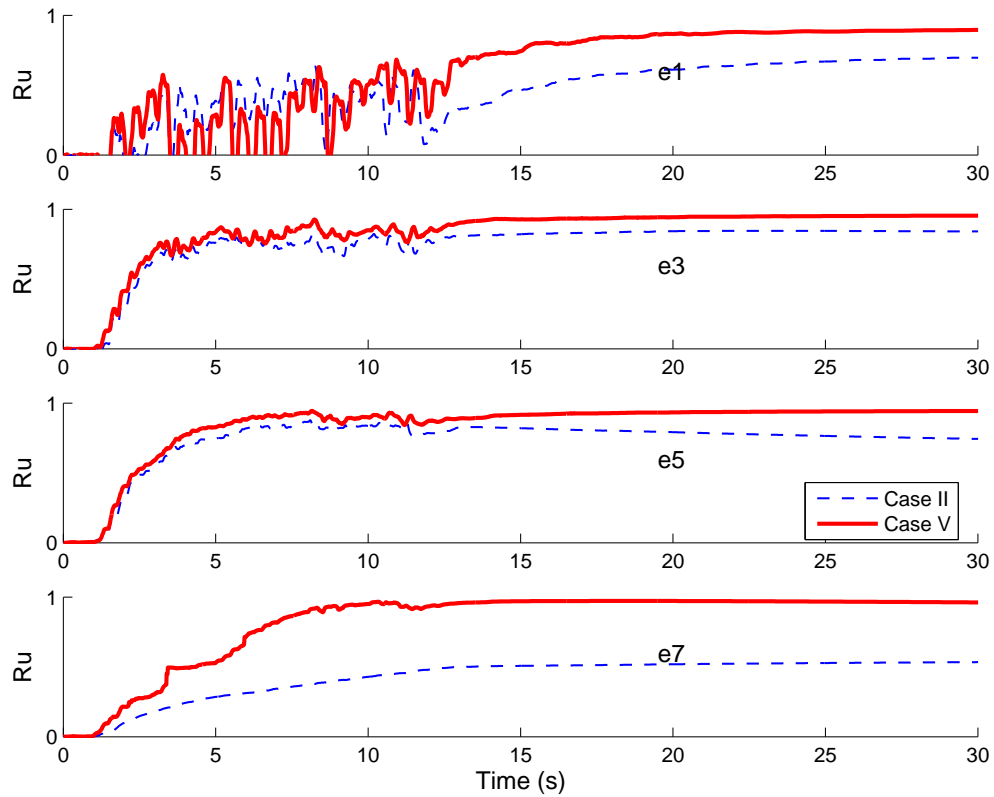


Figure 9.4: R_u times histories for elements e1, e3, e5, and e7 (upper Gauss point) for Cases II (level ground, with pile-column, free column head) and V (sloping ground, with pile-column, free column head).

a pile (see bottom of Figure (9.3)). This increase in R_u for Case V (sloping ground with pile) is explained by noting that the pile “reinforces” upper soil layers and thus prevents excess shear deformation in the upper 12.0 m of soil (above pile tip). The reduction of deformation in upper layers of soil (top 12.0 meters) results in transfer of excessive soil deformation to soil layers below pile tip (where element e7 is located). This, in turn, results in a much larger and faster shearing of those lower loose soil layers. This significantly larger shearing results in a much higher R_u . Deformed shape, shown in Figure (9.6) for Case V, reinforces this explanation, showing much large shearing deformation in lower soil layers, below pile tip. Same observation can be made for Case VI, shown in Figure (9.6).

Observation similar to the above, for Cases II and V can be made for Cases III and VI, results for which are shown in Figure (9.5). One noticeable difference in R_u results between cases with

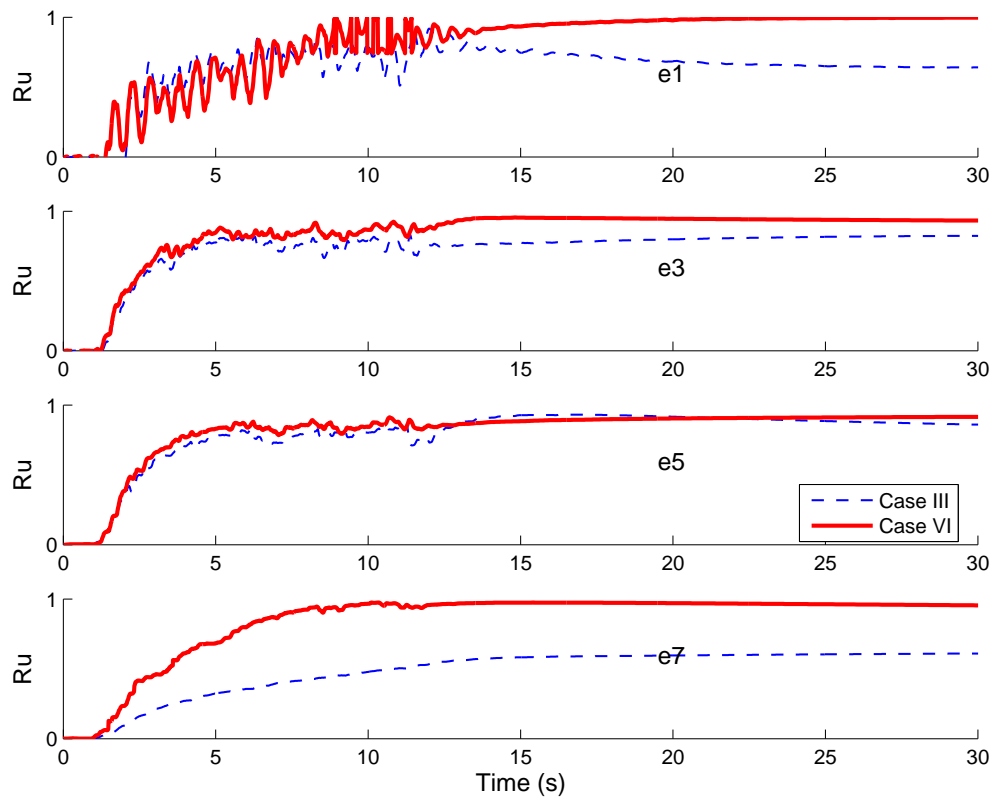


Figure 9.5: R_u times histories for elements e1, e3, e5, and e7 (upper Gauss point) for Cases III (level ground, with pile, no rotation of pile head) and VI (sloping ground, with pile-column, no rotation of column head).

free column head (Cases II and V) and cases with fixed rotation column head (Cases III and VI) is

in significantly larger (and faster) development of R_u close to soil surface for a stiffer, no rotation column cases (Cases III and VI). This much larger R_u observed in a “stiffer” PCM system setup, is due to larger shearing deformation that develops in soils adjacent to the pile during shaking. The stiffer PCM system can displace less (because of additional no rotation condition on column top) while the soil beneath is undergoing shaking (same demand in all cases), thus resulting in larger relative shearing of soil, which then results in larger and faster pore pressure development close to the soil surface, where the column no rotation effect is most pronounced.

A number of deformation modes is observed for both level and sloping ground cases, with or without PCM system. Figure (9.6) shows deformation patterns and excess pore pressures in symmetry plane for all six cases over a period of eighty seconds. A number of observation can be made on both deformation patterns, excess pore fluid patterns and their close coupling.

Level Ground without Pile (Case I). Excess pore pressures and deformations in symmetry plane for level ground without a pile are shown in Figure (9.6) (I). At the very beginning (at $t = 2$ s) there is initial development of excess pore fluid pressure in the middle soil layers. This expected, as the self weight loading stage has densified lower soil layers enough so that their response is not initially contractive enough to produce excess pore pressure. Top soil layers, on the other hand, have a drainage boundary (top surface) too close to develop any significant excess pore pressures. As seismic shaking progresses (for $t = 5, 10$ s), the excess pore pressure increases, and starts developing in lower soil layers as well. It should be noted that a small non-uniformity in results is present. For example, zones of variable, nonuniform excess pore pressures on the lower mid and right side for Case I at $t = 10$ s develop. Nonuniform mesh (many small, long elements in the middle, large elements outside this middle zone) may introduce small numerical errors in results which can be observed by slightly nonuniform results at $t = 10$ s and $t = 15$ s. It should be noted that results for excess pore pressure shown for first 13 seconds (during shaking) in Figure (9.6) (I) are transient in nature, that is, seismic waves are traveling throughout the domain (model) during shaking (first 13 seconds) and slight oscillations in vertical stresses are possible. This oscillations will contribute to the (small) non-uniformity of excess pore pressure results. After the shaking (after 15 seconds) resulting excess pore pressure field is quite uniform.

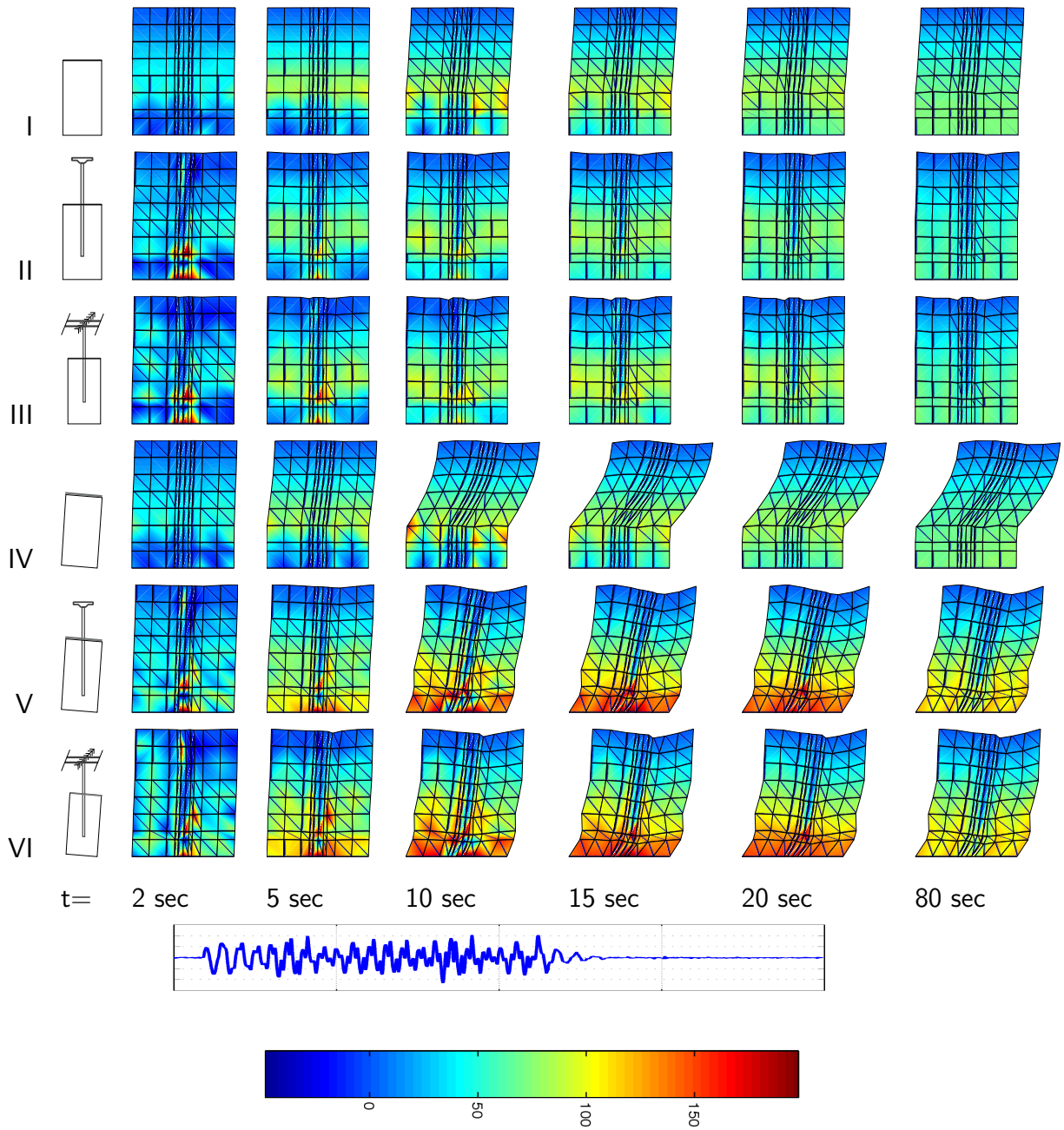


Figure 9.6: Time sequence of deformed shapes and excess pore pressure in symmetry plane of a soil system. Deformation is exaggerated 15 times; Color scale for excess pore pressures (above) is in kN/m^2 . Graph of ground motions used is placed below appropriate time snapshots and is matching for $t = 2, 5, 10, 15, 20$ seconds while at $t = 80$ seconds there is no seismic shaking.

Level Ground with Pile (Cases II and III). Excess pore pressures and deformations in symmetry plane for models with PCM system and with two different boundary conditions at top of column in level ground are shown in Figures (9.6) (II and III). One of the interesting observations is significant shearing and excess pore pressure generation adjacent to the pile tip. The reason for this is that pile is too short, that is, pile tip has significant horizontal displacements during shaking. Those pile tip displacements shear the soil, resulting in excess pore pressure generation. As soon as there is time for dissipation, this localized excess pore pressure dissipates to adjacent soil, and then, after shaking has ceased (at $t = 13$ s and later), it slowly dissipates upward. Addition of pile into the model (construction), with a highly impermeable elements (that mimic permeability of concrete) is apparent as there is a low excess pore pressure region in the middle of model, where pile is located.

Sloping Ground without Pile (Case IV). Excess pore pressures and deformation in symmetry plane for sloping ground without pile is shown in Figures (9.6) (IV). It is noted that initially the excess pore pressure starts developing in middle soil layers, similar to the Case I above. Bottom layers start developing excess pore pressure only after significant shear deformation occurs (at $t = 10$ s) at approximately $2/3$ of the model depth. Lower layers have densified enough during self weight stage of loading that initial shaking is not strong enough to create excess pore water pressure, rather, those layers are fed by the excess pore pressure from above. Lower soil layers also do not develop much deformation, while middle and upper layers together develop excessive horizontal deformation.

Sloping Ground with Pile (Cases V and VI). Excess pore pressures and deformation in symmetry plane for sloping ground with PCM system are shown in Figures (9.6) (V and VI). Similar to the above cases (II and III), pile is too short and there is again excessive shearing of soil at the pile tip, suggesting large movement of that pile tip. In addition to that, pile introduces significant stiffness to upper 12 meters of soil (along the length of pile) and helps reduce deformation of those upper soil layers. Down-slope gravity load is thus transferred to lower soil layers (below pile tip) which exhibit most of the deformation. It should be noted that soil in middle and upper layers (adjacent to pile) does deform, just not as much as the soil below

pile tip. The predominant mode of deformation of middle soil layers is shearing in horizontal plane, around the pile. Deformation in horizontal plane is not significant as the pile is short in this examples (as mentioned above) and does not have enough horizontal support at the bottom. The deformation pattern of a soil – pile system is such that pile experiences significant rotation, and deforms with the soil that moves down-slope. If the pile was longer, and if it had significant horizontal support at the bottom, the middle and upper soil layers would have showed more significant flow around the pile in horizontal planes.

Piles in Layered Soils

Particular attention has to be taken for piles and pile groups in layered soils. In most cases, soils are naturally deposited in layers and proper modeling of layering is very important, particularly when layers are many and not very thick, Recent work in this area by Yang and Jeremić (2002); Yang and Jeremić (2005) shows that for layers of stiff sand and softer clay, reduction of stiffness and ultimate strength of soil can be significant.

Presented in this subsection are representative results related to the behavior of piles in uniform and layered soil systems. These results were first published by Yang and Jeremić (2002); Yang and Jeremić (2005); Jeremić et al. (1989-2016).

Pile Models. A number of static pushover tests for single pile models were simulated using uniform soil and layered soil setups. Figure 9.7 shows the model setups. There are four main setups. Two of these are dealing with uniform sand and clay soils, while two others are featuring layered soils. In particular, the case # 1 is a uniform soft clay soil, case # 2 includes top and bottom layers of soft clay with an in-between layer of medium dense sand. On the other hand, case # 3 features uniform medium dense sand soil, while case # 4 features top and bottom layers of medium dense sand with an in-between layer of soft clay. Detailed layering setup is given in Figure 9.7.

Figure 9.8 shows the finite element mesh for all four cases. Based on symmetry, only half of the model is meshed. Twenty node brick elements are used for both soil, pile and interface. It should be noted that these quadratic elements exhibit high accuracy even for high aspect ratios and can model accurately bending of solid piles with two layers of elements. During mesh design

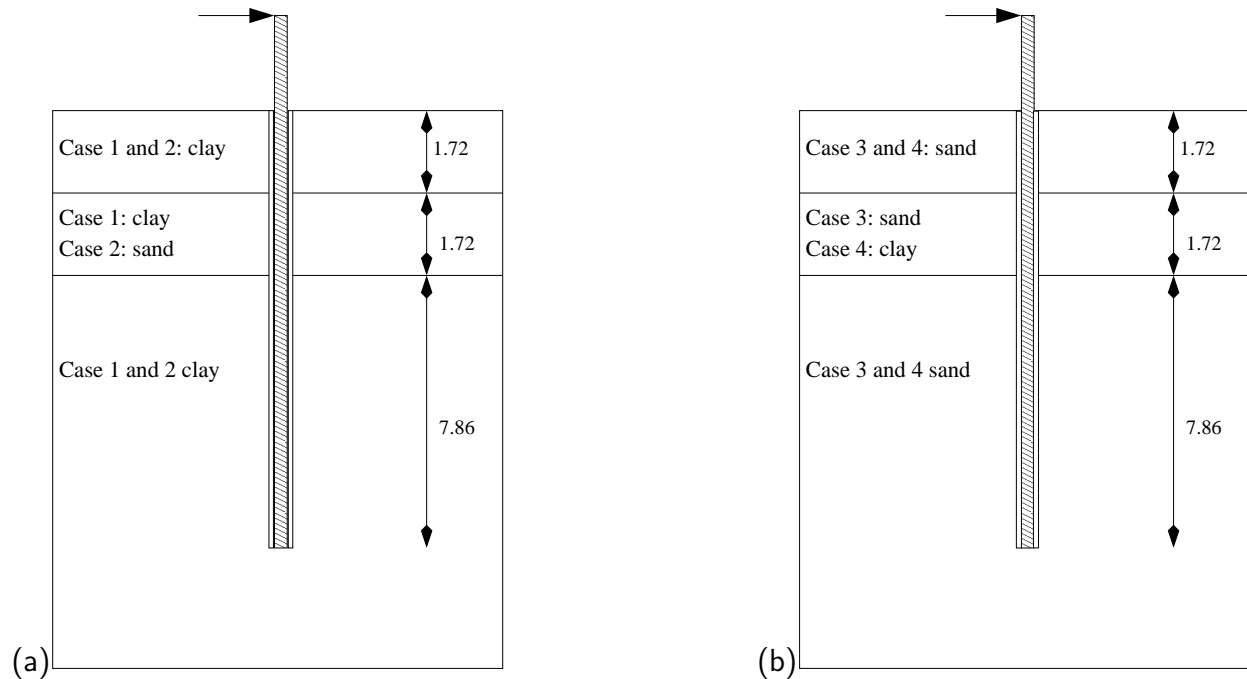


Figure 9.7: (a) Single pile models, dimensions and layers of case #1 and #2. (b) Single pile models, dimensions and layers of case #3 and #4.

stage, a study was performed to decide on appropriate (balanced) mesh size. That study showed that a much larger mesh, with many more elements (with lower aspect ratios) would account for a fairly small change in results, so it was decided that the current mesh is sufficient for our analysis.

The square pile, with a width of 0.429 m, consist of four elements (per cross subsection) with the elastic property of aluminum. The fine mesh in the upper part of the model is to provide data points for the computation of shear forces and $p - y$ curves of sufficient reliability as well as for the investigation of layering effects. The sides and bottom of the model are fixed with the exception of the symmetric boundary, which is only supported in Y direction. The interface layer between aluminum pile and surrounding soil is represented by one thin layer of elements. The purpose of this layer is to mimic the installation effects on piles (drilled or driven). It also serves a purpose of a simplified interface which allows for tension cut-off (gaping) and controlled, coupled horizontal and vertical stiffness. All interface elements were simulated by Drucker–Prager model with a friction angle of 25° , and a dilation angle of 0° .

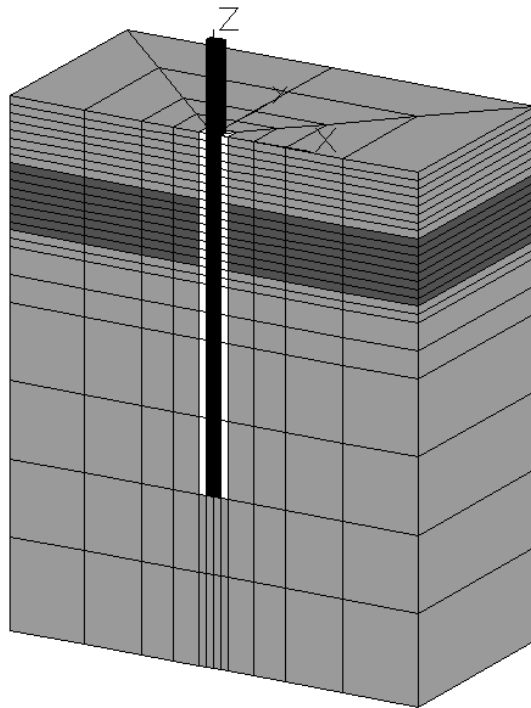


Figure 9.8: Mesh of single pile model, side view, top eight layers of finite elements are either clay or sand (depending on the cases), middle eight layers of finite elements are sand or clay (again depending on the cases) and the bottom is all uniform clay or sand, interface zone around the aluminum pile is also present.

Plastic Zones. The static pushover test were conducted using load control at pile head. The final plastic zones are depicted in Figures 9.9, 9.10. Plastic zones are actually presented by plastified Gauss points. In particular, Figure 9.9(a) shows developed plastic zones for the uniform clay soil (case # 1). It is interesting to note that the plastic zone propagates fairly deep while it does not extend far from the pile in clay. Moreover, compression side (right side) features much larger plastic zone while the plastic zone for the extension side (left side) is confined to the interface layer and a few Gauss points outside the interface layer. The case with clay and sand layer in-between is shown in Figure 9.9(b). The main difference is that the plastic zone is even smaller than for uniform clay layer. It is worth mentioning that this case, which includes sand layer, is stiffer than the uniform clay case, thus displacements are smaller in clay and the plastic zone does not propagate as much as in uniform clay soil.

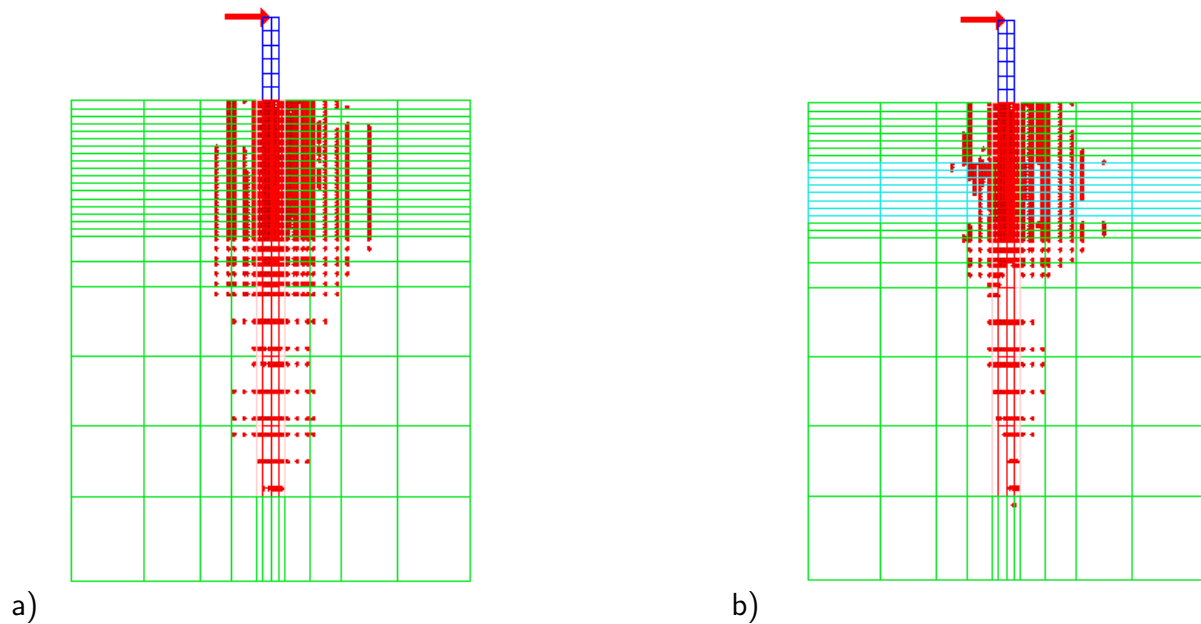


Figure 9.9: The plastic zones for (a) case # 1, and (b) case # 2 at lateral loading of 400kN.

Figure 9.10(a)(b) shows plastic zones at the end of loading process for sand and sand and clay soils. In particular, Figure 9.10(a) shows the plastic zone for uniform sand. It is interesting to note that the plastic zone propagates toward the surface with the collapse mechanics similar to the active and passive failure. In this case of course the system is 3D and so the failure propagation angles do not match the active and passive failure angles, however the difference

between active and passive zones propagation angles is almost exactly $\pi/2$. Figure 9.10(b) shows plastic zone for the case # 4 which includes a layer of clay between -1.72m and -3.44m (Z coordinate, origin is in the pile center at the ground surface) . It is noted that the plastic zone is deeper, but not as nicely defined as in the previous case.

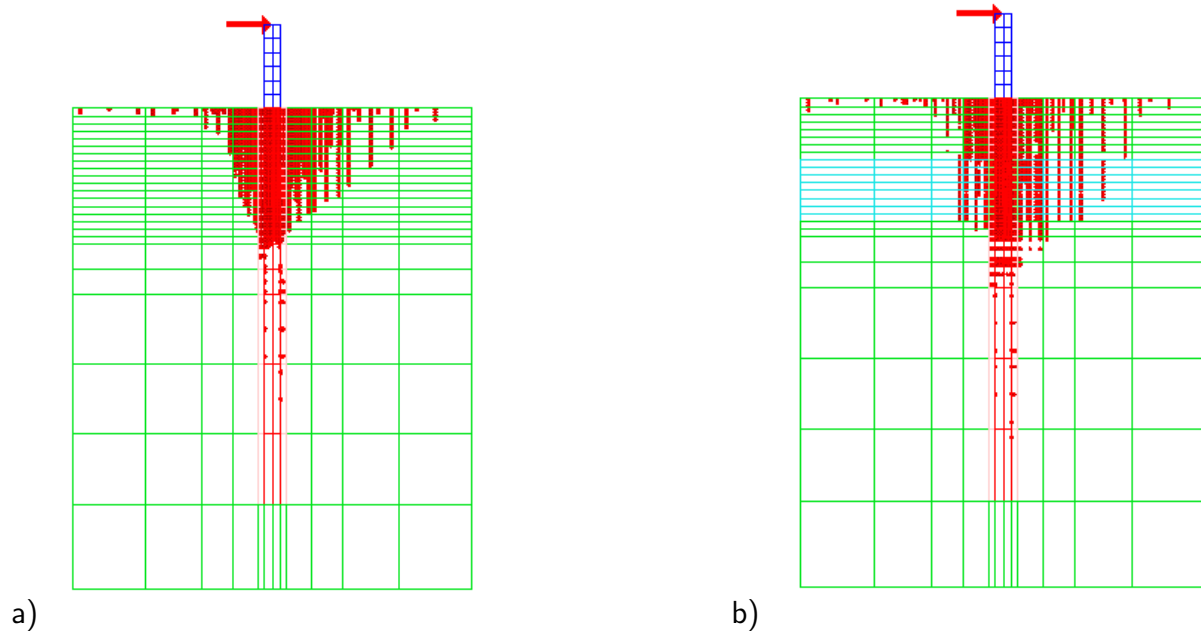


Figure 9.10: The plastic zones of case 3 and 4 at lateral loading of 400kN.

$p - y$ Curves. Results from static pushover tests on piles were used to generate $p - y$ curves. The bending moments derived by integrating vertical stresses are numerically differentiated once and twice to compute the shear force and pressure diagrams, respectively. Direct integration of shear stresses was also performed to check results and it was found that shear forces were within 5% accuracy. The combination of calculated pressures (p) and displacements obtained from the finite element solution, allowed for generation of $p - y$ curves at various depths along the pile.

In what follows, presented are generated $p - y$ curves for both uniform soils (sand and clay) as well as for layered systems. It is noted that the graphical presentation of results for bending moments, shear forces and lateral pressures (load) on a pile beam are shown with 10 lines, each one representing results for one increment ($1/10$) of the total load.

Uniform Clay Soil. Figure 9.11 shows bending moments, shear forces and pressures along the depth of a pile in clay soil. It should be noted that the maximum bending moment, as well as the switching of sign for shear force, moves quite a bit from the depth of approximately -1.7m all the way to the depth of -3.4m . Pressure distribution shows that the top layers are already at the ultimate values of pressures and thus the pressure diagram propagates downward. There is a slight fluctuation of pressures at the depths of $4 - 5\text{m}$, which is attributed to the small numerical problems while doing double differentiations.

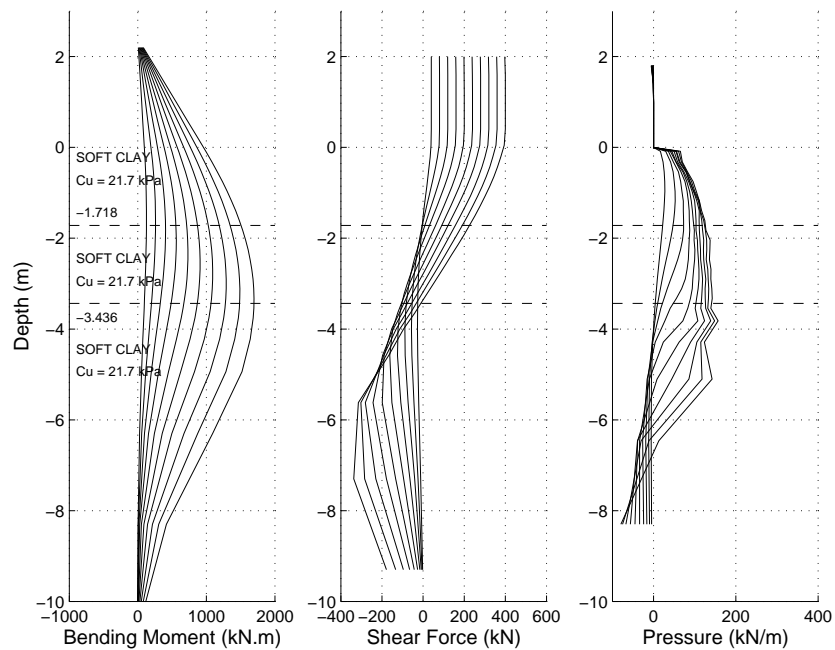


Figure 9.11: Bending moment, shear force and pressure distributions for the uniform clay profile.

Figure 9.12 shows generated $p - y$ curves for uniform clay layer. It is obvious that most of the clay (at least until the depth of -2.6m) has reached its peak resistance.

Uniform Sand Soil. Figure 9.13 shows bending moments, shear forces and pressures for a pile in a uniform sand soil. In this case it is interesting to note that the maximum bending moment, as well as the change of sign for the shear force is moving only between the depths -1.8m and -2.0m . Moreover, the pressure diagram shows steady increase (with top layers reaching ultimate pressures) until the depth of -1.7m and then steadily decreases, and changes sign at greater depths (below -4.0m).

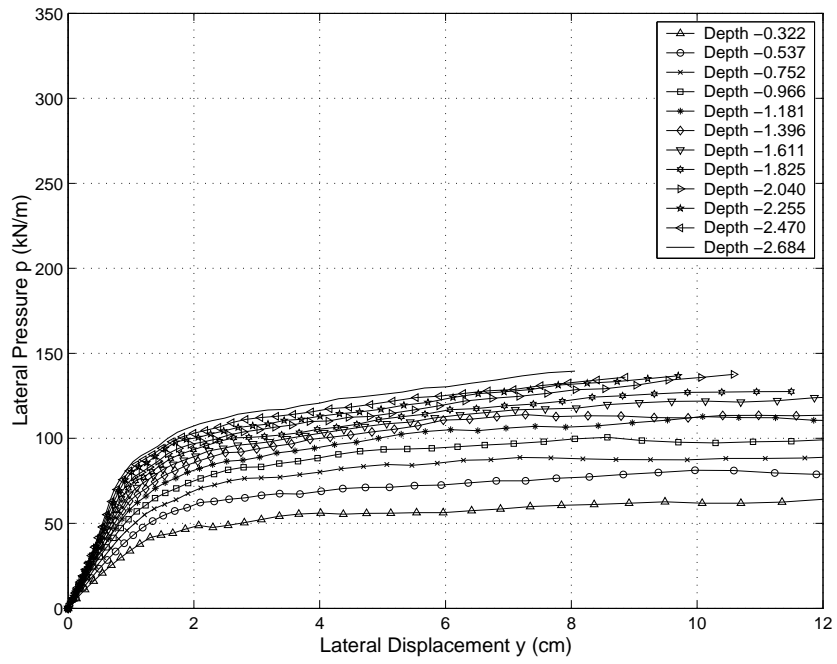


Figure 9.12: Calculated $p - y$ curves for the uniform clay profile.

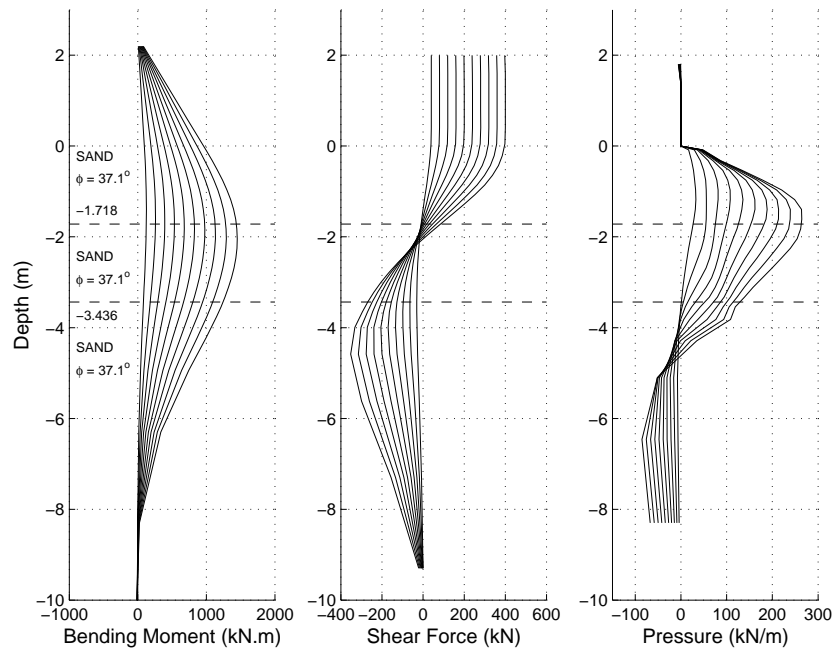


Figure 9.13: Bending moment, shear force and pressure distributions for the uniform sand profile.

Figure 9.14 shows generated $p - y$ curves for the uniform sand case. It is interesting to note that only the top layer at the depth of about -0.3m will reach the ultimate pressure. All the other sand material is far away from corresponding ultimate pressures. It is also worth noting that the displacements in the case of uniform sand are much smaller (almost twice as small) than what has been observed in uniform clay case.

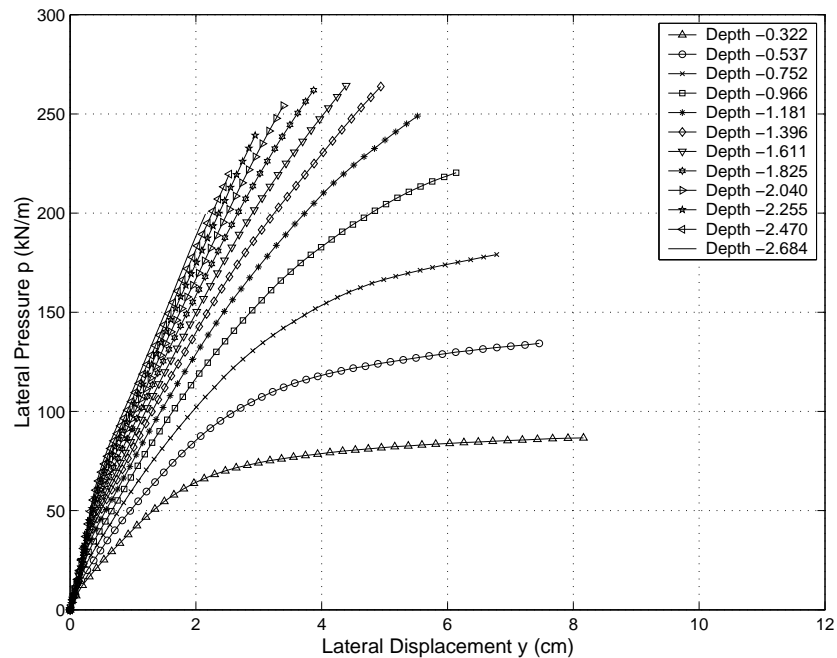


Figure 9.14: Calculated $p - y$ curves for the uniform sand profile.

Clay Soil with a Layer of Sand. Figure 9.15 shows bending moments, shear forces and pressures for a layered soil case. In this case a layer of sand extends from -1.72m to -3.44m . The rest of soil is soft clay. It is interesting to note a large jump in pressures for the sand layer (as expected) and that the pressures in the top clay layer (from the surface to -1.7m) reaches ultimate values. Small non-uniform distribution of the pressures at the interface of sand and clay at -3.44m is attributed to the coarseness of the finite element mesh. In comparing Figure 9.15 with the results for uniform clay case (Figure 9.11) it is obvious that the sand layer arrests the propagation of deformation and forces in depth and fixes the maximum moment to approx. -2.1m .

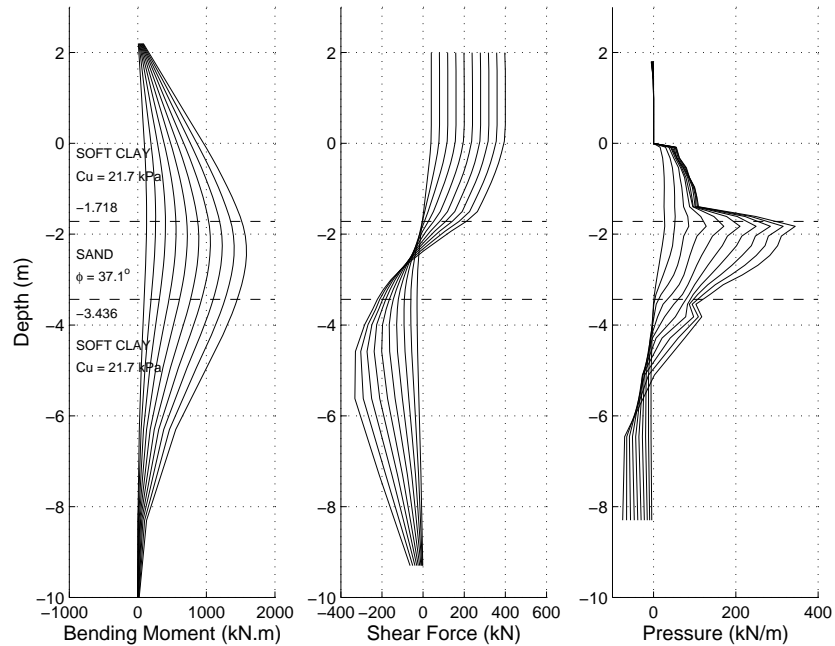


Figure 9.15: Bending moment, shear force and pressure distributions for the clay soil with a sand layer.

Figure 9.16 shows generated $p - y$ curves for the layered case (single layer of sand in clay). The $p - y$ curves were generated only for the top layer of clay and middle layer of sand, to the depth of $-2.7m$. It is interesting to note that the $p - y$ curve for clay at the depth of $-1.61m$ (close to the sand layer) exhibits strong hardening, unlike similar curve for the uniform clay soil, in Figure 9.12. The increase in pressure (transversal loading on the pile) between uniform clay (Fig. 9.12) and clay underlain by a medium dense sand layer (Fig. 9.16) at the displacement of $0.06m$ is more than two times.

Sand Soil with a Layer of Clay. Figure 9.17 shows bending moments, shear forces and transversal pressures for a case where a layer of soft clay is present within sand soil. Unlike the case of uniform sand soil (Figure 9.13) the presence of soft clay layer will change the depth of maximum moment by almost $1m$ (from $-2.0m$ to $-3.0m$). In addition to that, the distribution of pressures on a pile is changed significantly, as seen in the right plot of Figure 9.17. The reduction of pressures will extend into the sand layer and present significant influence of soft clay on pressures in sand.

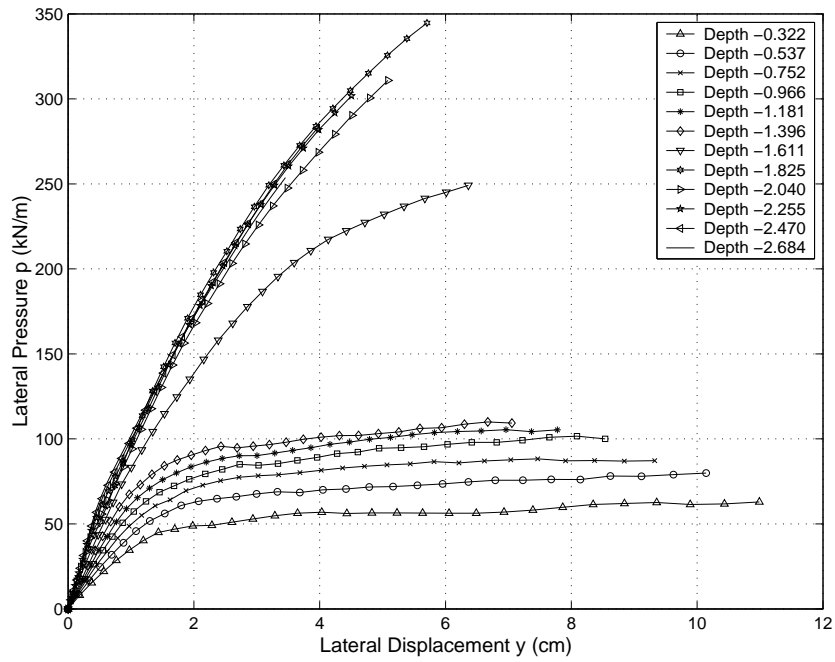


Figure 9.16: Calculated $p - y$ curves for the clay soil underlain by a medium dense sand layer.

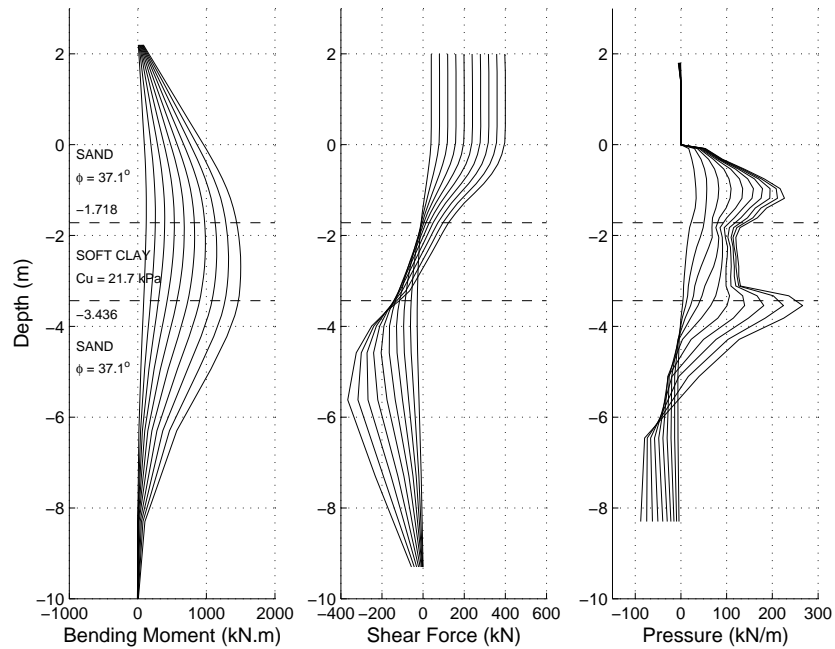


Figure 9.17: Bending moment, shear force and pressure distributions for the sand soil with a soft clay layer.

Figure 9.18 shows generated $p - y$ curves for the case of sand with a soft clay layer. It is noted that the $p - y$ curves for sand that is some distance away from the interface with clay are much the same as for the uniform sand case. However, the $p - y$ curves in sand close to the interface are changed in some cases significantly. For example, the $p - y$ curve at depth of $-1.61m$ is showing pressure of approx. $p = 265kN/m$ at the displacement of $0.042m$ for the uniform sand case, while the same $p - y$ curve, still in sand, has a drop in pressure at the same displacement to $p = 140kN/m$. Similar trend is observed for other $p - y$ curves close to the interface of sand with clay.

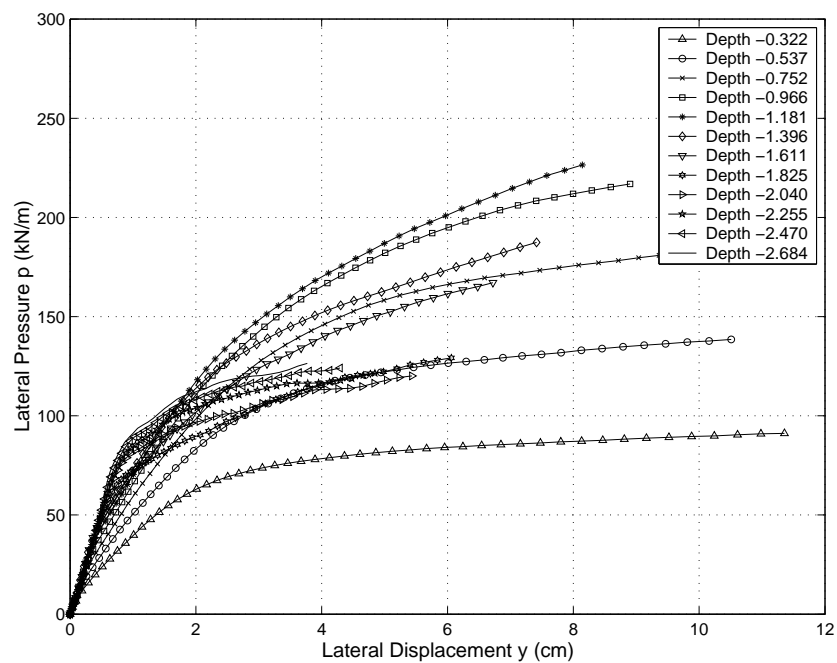


Figure 9.18: Calculated $p - y$ curves for the sand soil underlain by a soft clay layer.

Pile Groups

Pile groups bring certain additional complexities to pile modeling, For example, for a pile group that features more than 2 piles, interaction between piles becomes very important, as front piles tend to pick up majority of loading, while piles in the middle of a pile group are "shaded" and loaded with only relatively small portion of average load. Figure 9.19 (Yang and Jeremić, 2003) shows a setup for a 4×3 pile group.

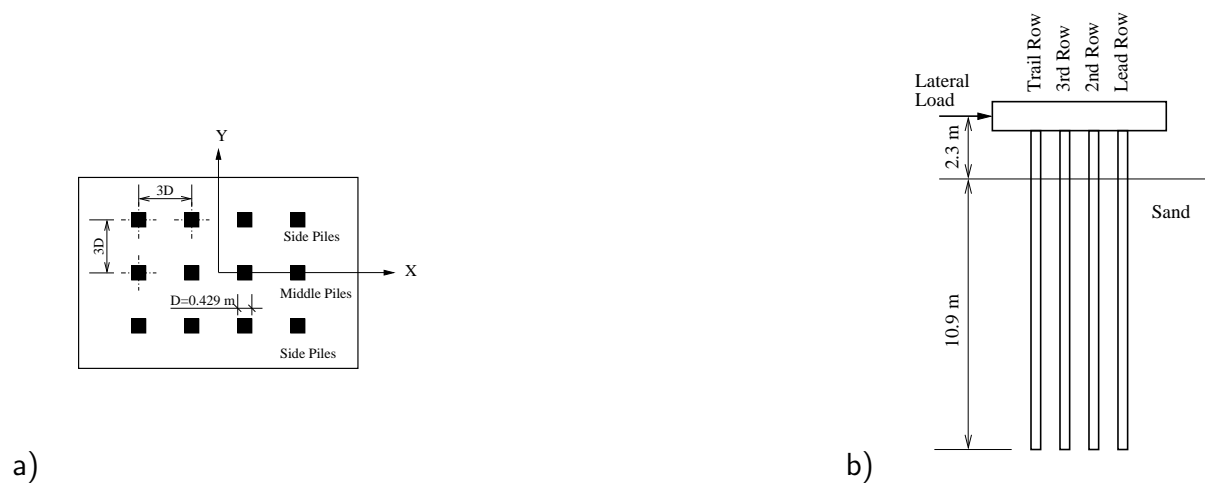


Figure 9.19: Layout of 4×3 pile group: a) top view, b) side view.

Figure 9.20 shows a finite element model for such simple pile group.

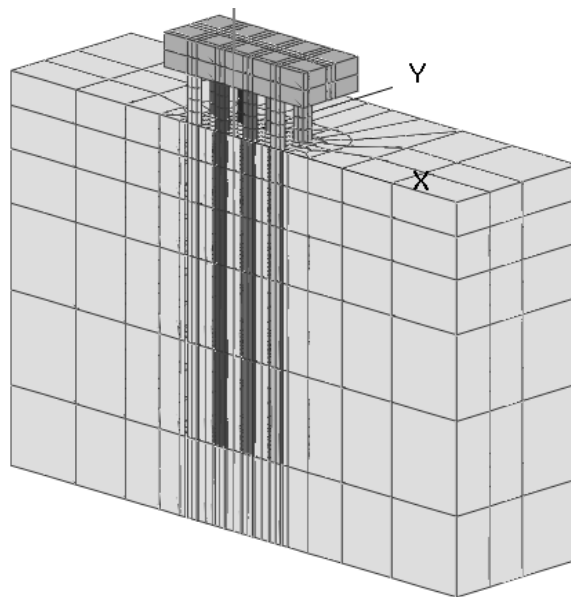


Figure 9.20: Finite element mesh for half of 4×3 pile group.

It is noted that while this pile group is fairly small when compared with a significantly larger pile groups that are potentially placed under NPPs and other nuclear facilities, conclusions on load distribution are very similar.

Figure 9.21 shows variation of percentage of transversal load taken by different piles in this

pile group. It is noted that leading row piles taken majority of loading during transversal loads,

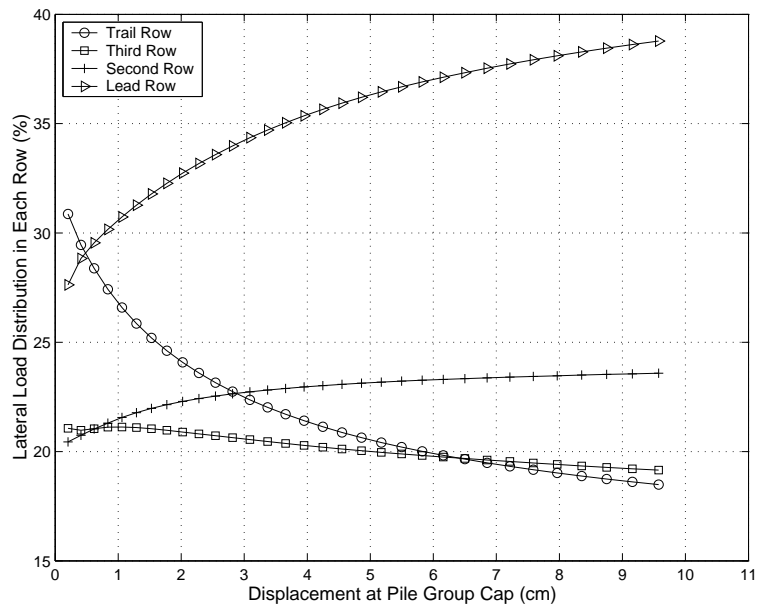


Figure 9.21: Variations of percentage of total load taken by each row in the 4 × 3 group.

almost twice as much as piles behind them, and more than twice as much as piles further behind.

Chapter 10

Task 4.8: Recommendations Regarding Safety Importance of Phenomena 4.1 – 4.7, and Methods to Take Them Into Account

Executive Summary of Findings for Safety Importance of Analyzed Phenomena

Provided here is a summary of recommendations regarding safety importance of phenomena 4.1 – 4.7. It is important to note that summary provides most likely outcomes and recommendations, however, as always with nonlinear analysis, it is recommended to perform full nonlinear analysis for each SSI NPP system and carefully analyze contributions and safety importance of different parts of the system.

4.1 Full, 3D, inclined, body and surface seismic wave fields: Safety concern is that if full (realistic) 3D seismic wave field is not taken into account, some motions are not taken into account, thus (artificially) reducing demand on NPP! Combinations of 100%, 40% in horizontal directions, and 40% in vertical direction do not necessarily convey the real picture of motions as they miss rotational components of motions.

These real 3D ground motions effects that are omitted from current modeling can reduce accuracy of results and render results on unsafe side.

4.2 Incoherence modeling: Safety concern is that current state of art/practice models and motions that are developed using these models do not necessarily cover extended range of incoherent motions from which these models have been developed. In addition, there are concerns over ergodicity, directivity effects, local geology effects.

High fidelity modeling of wave propagation from source, through rock to local site offers much more accuracy and resolution (provided that geology is known in some detail!) and should at least be used in conjunction with current incoherence models, and possible should be used to constrain and expand currently used incoherence models.

These modeling concerns with current incoherence modeling can render results on unsafe side and should be carefully investigated on a case by case basis.

4.3 Soil/rock nonlinearities: currently these nonlinearities are not taken into account in professional practice, and yet, these nonlinearities can, in some cases, reduce seismic demand on NPPs. In some special (somewhat rare) cases demand can also increase. In conclusion, as

with any nonlinear modeling, particular NPP SSI models have to be analyzed as accurately as possible to determine if modeling of nonlinearities/inelasticity is beneficial or detrimental to seismic response of NPPs.

- 4.4 Slipping and gapping at foundation–soil/rock contact: Much like the case of soil/rock nonlinearities/inelasticity, contact can dissipate much seismic energy and by not modeling it, potential beneficial effects are not taken into account. A word of caution is in order, however, as usual reduction of demand is for horizontal motions, while vertical motions can be amplified, depending on axial contact (plasticity and viscous damping) properties.
- 4.5 Timing and location of energy dissipation: If modeled properly, energy dissipation timing and location can provide great insight in dynamic life on an NPP SSI system. In addition, knowledge of timing and location of energy dissipation can help improve safety and economy of NPP SSI systems.
- 4.6 Buoyancy effects: These very important effects need to be modeled properly as buoyant forces will change dynamically, during earthquakes, and can have either beneficial (isolation) or detrimental (loss of stability) effects.
- 4.7 Piles and Pile groups: Modeling of pile groups under NPPs can be done using a number of more or less sophisticated approaches. The main safety concern is if a less sophisticated modeling approach is used, results obtained might not be representative of the actual behavior of an NPP founded on piles.

10.1 Task 4.1: Full 3D, Inclined, Body and Surface Seismic Input

10.1.1 Safety Importance

The importance of properly modeling input motions cannot be overstated. Using simplified methodology, where only motions in one single directions are taken into account can lead to underestimating seismic demand and thus developing results that are on the unsafe side.

A simple example was developed to illustrate the importance of modeling full 3D motions with both body and surface waves and is available through this web site (this example cannot be presented on paper as it comprises a number of animations of simulated results):

http://sokocalo.engr.ucdavis.edu/~jeremic/6D_vs_1D_ESSI_for_NPPs/

In the above example, given combination of body and surface waves produces significant differences in motions (displacements and accelerations) in the containment and auxiliary buildings. Realistic 3D seismic motions do produce larger demand/influences, and thus, use of 1D motions (even if they are combined with a rule of 100% in one horizontal direction, 40% in other horizontal direction and 40% in vertical direction) might not be on the safe side.

10.1.2 Methods to Take into Account

The best method to take into account full 3D seismic motions, that include body and surface waves is the Domain Reduction Method (Bielak et al., 2003; Yoshimura et al., 2003), as described in detail in this report.

10.2 Task 4.2: Incoherence Modeling

10.2.1 Safety Importance

Proper modeling of incoherence in seismic motions is of great importance. Incoherence in seismic motions is a real phenomena that is observed in measurements on closely spaced measuring stations. There are four main sources of incoherence for seismic ground motions (Zerva, 2009):

- Wave passage effects,
- Attenuation effects,
- Scattering effects,
- Extended source effects

When incoherent effects are modeled using site specific geology, site specific seismic sources, a highly accurate ground motions are obtained. Such incoherent ground motions do consist of both body and surface seismic waves, and feature wave passage and attenuation effects, while proper modeling of geology accounts for scattering effects, and proper modeling of source characteristics accounts for extended source effects.

On the other hand, currently predominant incoherence modeling approach is use of statistical models that are developed using measured incoherent motions from few sites, mostly in Taiwan and U.S.A. (California). Use of those models is appropriate if one can assume that ergodic assumption holds. That is, models are developed by using data from a number of earthquakes at these (very) few sites. Then, these models are used to (extrapolate and) predict incoherence at various other sites. Moreover, data recorded at original sites does not account for earthquake directivity effects. In other words, incoherence will be quite different between two points if earthquake epicenter is positioned along the line connecting these two points, or if the earthquake epicenter is at an equal distance from those two points (that is, if it is perpendicular to the line connecting two measurement points). For a number of earthquakes measured at two chosen points, differences in directivity, and path of earthquake waves from sources at different locations, will create a significant spread of data. Hence current models are developed as statistical models. Since current models allow for development of a large number instances of incoherent motions, it

would be appropriate to use a large number of incoherent motions in modeling of SSI for NPPs. That is currently not the case! Currently, statistical models are used to develop (very) few incoherent motions, and those motions are used to excite NPP models. By doing so, realistic incoherent motions that were measured and used to develop original statistical incoherent motion models, are being averaged. Such average incoherent motions (or averaged incoherences) are then used to perform dynamic analysis of NPP SSI systems. This approach might be reducing motions and/or incoherences and as such might not be on a safe side.

10.2.2 Methods to Take into Account

High Fidelity Numerical Modeling: Probably the best method to take incoherent motions into account is to

- Develop a good knowledge about the geology of site (preferably, a detailed picture of distribution of materials in a volume of subsurface geology that is deemed important to the dynamic response of the soil/rock-structure interaction (SSI) NPP system)
- Develop a good knowledge about (number of) potential source(s),
- Develop a reasonable (high fidelity) seismic ground motions that take into account as best as possible knowledge about geology and source(s)
- Develop high fidelity models of the SSI NPP system,
- Apply developed ground motions and analyze obtained SSI for a given NPP

This approach provides for a much higher confidence that results are properly developed and relies on a minimal number of simplifying assumptions that reduce modeling uncertainty.

Current, State of Practice Approach: Currently used methods rely, as noted above, on statistical models developed from observations of incoherence at a very limited number of sites around the world (in Taiwan and California mostly). While these models have so far been almost exclusively used, it is highly advisable to carefully examine their assumptions and use them with great care, while having in mind all the above potential problems. It would be great if in

addition to using statistical incoherence models (with all the potential problems as described above) a real measured values of incoherence are used and applied to SSI problems. These real, measured, values of incoherence, need to be chosen to cover high and low extremes of incoherence in such a way to excite extreme SSI behavior (high and low). This way, one can claim that both beneficial and detrimental incoherence effects have been taken into account and that an NPP under consideration has been numerically (in silico) tested.

10.3 Task 4.3: Soil/Rock Nonlinearities

10.3.1 Safety Importance

Soil and Rock adjacent to NPP foundations undergoes nonlinear, inelastic deformation for even very small loads and seismic motion levels. It can be proven analytically that for any granular material, there does not exist elastic (linear or nonlinear) behavior (Mindlin and Deresiewicz, 1953). In addition to that, a large number of tests on various types of rock material provides evidence that even rock tends to have nonlinear, inelastic response for even small deformation levels (Stavrogin et al., 2001). The decision to make a simplifying assumption of linear elasticity¹ is upon numerical modeler.

The main problem with using a linear elastic assumption for soil and rock adjacent to NPP foundation is the loss of a potential to dissipate seismic energy by that same soil and rock. As seismic motions excite inelastic response of soil and rock, seismic energy, that is propagating from within the soil and rock (as body and surface waves) is dissipated within that soil and rock. This seismic energy dissipation reduces the amount of seismic energy that reaches the NPP, and thus might have a beneficial effect. In addition to dissipating seismic energy, inelastic effects (plastification) of soil and rock will likely change the frequency content of seismic ground motions (in most cases, high frequencies will be cut off, while low frequencies might be amplified).

In that sense, it is believed that nonlinear, inelastic behavior of soils and rock will mostly be beneficial to the safety of NPPs as seismic motions will be reduced due to seismic energy dissipation within soil and rock domain.

10.3.2 Methods to Take into Account

For 3D modeling and simulation of SSI for NPPs, it is highly recommended that full 3D elastic-plastic material models be used. The usual use of 1D equivalent linear or nonlinear material models is not recommended as their generalization from 1D to 3D is questionable.

¹It is very important to note that methods that rely on the so called equivalent elastic models are indeed fully linear elastic approaches, where the linear elastic constant(s) is (are) developed based on a secant approach upon estimating (!) the highest strain level for a nonlinear response of a material (soil).

The other problem that is present is that data that is available for calibration of these 3D elastic plastic models is usually only stiffness degradation (G/G_{max}) and damping curves. There is no volume change data, and this represents a serious drawback as shearing response of soil (during shear wave propagation) is very much a function of such volume change. This serious problem with a lack of data is reported in this report as well (see Chapter 5 on page 61).

The most appropriate way to take nonlinear behavior of soil and rock into account is to use material models that can be calibrated using stiffness degradation and damping curves. One such model, called Pisanò model (Pisanò and Jeremić, 2014) was developed.

10.4 Task 4.4: Contact Problem, Slipping and Gaping

10.4.1 Safety Importance

In addition to nonlinear, inelastic behavior of soil and rock adjacent to structural foundations, contact zone (soil/rock – foundation concrete) shows even more potential for dissipating seismic energy. Contact zone, where a stiff foundation concrete interacts with softer soil and rock beneath, will exhibit nonlinear, inelastic response for even smallest seismic excitation, unless special measure are taken to "glue" foundation concrete to the rock beneath (using post-tensioned cables, grouting, etc.). Usually contact of soil and rock to the foundation concrete is used to prevent ground water to penetrate foundation concrete, and for that purpose, plastic sheets are placed between soil/rock and concrete. These plastic sheets decrease effective friction resistance and almost create an (unintended) base isolated structure. Even without these plastic sheets, contact zone will exhibit significant nonlinear, inelastic response.

This nonlinear, inelastic response serves similar function as the nonlinear/inelastic response of soil and rock adjacent structural foundation. Seismic energy that propagates from within soil and rock toward the structural foundations will be, dissipated, in part, within the contact zone. In addition to dissipating seismic energy, and preventing that energy from propagating further into the structure, nonlinear/inelastic response of the contact zone will alter frequencies of seismic motions propagating through the NPP system (usually, lowering high frequency for horizontal while increasing high frequencies for vertical motions).

10.4.2 Methods to Take into Account

Proper modeling of contact problem that features a normal (axial) response (with gap closing opening capabilities) that is fully coupled to the shear/slip response requires formulation of contact element that takes all those physical phenomena into account. Details of our formulation and implementation of one such element is given in this report (see Chapter 6 on page 109).

It is also very important to note that for contact modeling where contact zone is under water table and is fully saturated, a special contact element is developed/used which explicitly takes into the account pore fluid pressures in soil beneath contact zone, as well as water within the

contact zone.

There were a number of proposal to use linear elastic finite element programs for modeling contact nonlinearity, by resorting to secant stiffness. It is important to not that while such simplification might be acceptable for very minor nonlinearity in the contact zone, that is for a very small seismic motions, any larger nonlinearity simply cannot be modeled using secant approach for two main reasons:

- Secant stiffness approach needs to a-priori determine level of straining in order to decide (choose) secant stiffness. This choice is not unique and will be a function of an overall response, which for a nonlinear system changes in every incremental (time) step.
- By choosing secant stiffness, the system becomes linear elastic, and thus the main potential benefit of nonlinear/inelastic contact, dissipation of seismic energy is completely lost.

10.5 Task 4.5: Timing and Location of Energy Dissipation

10.5.1 Safety Importance

Input of seismic energy and its dissipation within the soil/rock structure interaction system for an NPP controls the dynamic response. Seismic response successes and failures for NPPs (and other structures) are controlled by timing and location of energy dissipation. Energy can be dissipated in a number of different ways. For example, energy dissipation in structural systems and components (SSCs) results in damage (and even failure) of those SSCs. If, on the other hand, seismic energy is dissipated in the soil/rock volume or in the soil/rock–foundation contact zone, then less seismic energy will propagate to the SSCs, and thus potentially reduce damage accumulated in SSCs.

It is thus very important to gain accurate understanding where and when is energy being dissipated within NPP SSI system. It is also important to note that if finite elements used do not allow for modeling of nonlinear/inelastic behavior, energy dissipation will not be accurately measured/analyzed. For example if part of the SSI system finite element model uses linear elastic finite elements, it is very likely that, since those elastic finite elements cannot dissipate seismic energy, seismic energy will be redistributed to other parts of the finite element model that can dissipate energy. While this redistribution might not be much of a problem for parts of the model (SSI system) that are expected to remain close to elastic (for example structure), in other instances, where some parts of SSI system are modeled as elastic (while we know that these parts will have significant nonlinear/inelastic deformation), then energy dissipation results will be much skewed and will not be accurate at all. There is a fine line that needs to be followed in choosing which part of SSI NPP system to model as linear and which part as truly nonlinear/inelastic. It would be best if all parts of the SSI NPP system are modeled with highly accurate models, that can allow realistic nonlinear/inelastic behavior, and allow those models to show that, for example, structure will remain elastic (for the most part it will remain elastic, even for stronger earthquakes, as shown by recent experiences from Japanese earthquakes).

10.5.2 Methods to Take into Account

It is preferable to follow energy dissipation for each finite element in the finite element mesh, and to record dissipation for each time step of a dynamic analysis. This is the philosophy that is developed and implemented in the Real ESSI Simulator.

It is emphasized again that in addition to real, physical dissipation of energy that is modeled using high fidelity finite element models, there exist numerical energy dissipation. This numerical energy dissipation is an artifact of numerical integration of equations of motion. While numerical energy dissipation can be used in linear analysis to damp (dissipate) out energy (usually higher frequencies) artificially introduced into the system by the finite element discretization, for nonlinear systems, energy can also be produced. This feature has to be carefully followed and sensitivity studies have to be performed to establish effects of numerical energy dissipation on simulation results.

10.6 Task 4.6: Buoyancy Effects

10.6.1 Safety Importance

Buoyancy effects are always present when water table is above lower levels of foundation. This is usually the case, as NPPs are mostly located close to bodies of water. Fully saturated soil and rock beneath NPP foundation will closely interact with dynamically excited NPP structure. Water from soil/rock will create uplift forces that will reduce effective (normal) stress between foundation concrete and soil/rock. This reduction in effective stress will reduce shear forces (stress) that is necessary to slip foundation relative to soil/rock. In addition, reduction of effective stress will also allow for easier formation of gaps, and uplift of foundation slab.

Current modeling approach for buoyant forces uses a single static force, calculated using Archimedes principle and applied at the center of volume of submerged part of the NPP system. However, in reality, buoyant force will change dynamically as pore fluid pressures in soil/rock under foundation slab, change during dynamic shaking. This dynamic change of pore fluid pressure adjacent to the foundation slab (including lower foundation surface and walls of embedded foundations) will create dynamic change in buoyant pressures, which will results in a dynamic change in buoyant force(s). This dynamic change of buoyant force(s) can (significantly) affects dynamic response of an NPP. In general one cannot make statements about the benefits or detriments of such dynamically changing buoyant force, each case (NPP model) has to be analyzed and conclusions drawn on a case by case basis. Examples that are forthcoming will demonstrate these beneficial or detrimental effects.

10.6.2 Methods to Take into Account

Instead of a single static buoyant force, water pressures that develop from pore water pressures in saturated soil/rock adjacent to foundation slab and walls need to be integrated. Buoyant (fluid) pressures (forces) will results from such integration and will be appropriately distributed along foundation and submerged wall surfaces. Pressure distributions thus developed will contribute to the proper buoyant forces, which will affect different parts of an NPP in a different way since foundation slab and walls are flexible.

In addition, during earthquakes, pore fluid pressures in soil and rock adjacent to foundation slab and walls, will dynamically change, and will hence change (dynamically) buoyant forces. Details of modeling of buoyant forces are given in Chapter 7 on page 136.

10.7 Task 4.7: Piles and Pile Groups

10.7.1 Safety Importance

As noted in this report, inclusion of pile foundation stem from inadequacy of soil beneath an NPP to properly support such NPP during service and extreme loading events (earthquakes). The main concern is the weak soil that the main reason for inclusion of piles.

Another approach is to use the so called P-Y springs. This approach works well only for monotonic (slow) loading of piles in one plane (pushover analysis) and does not work well for dynamic 3D analysis and as such is discouraged.

10.7.2 Methods to Take into Account

Proper modeling of large pile groups relies on a hierarchy of method from very high sophistication to somewhat lower sophistication methods. Three main approaches are described in detail in Chapter 9 on page 165.

Chapter 11

Task 4.9: Verification and Validation

11.1 Summary of Findings for Task 4.9

Task 4.9 is dealing with a very important subject of verification and validation (V&V) of numerical modeling and simulation tools/programs. A number of verification activities are recommended.

The main findings are related to verification procedures that are recommended (and they should probably be mandatory!) for modeling and simulation, and for validation procedures that are recommended (as there is a general lack of quality validation data!). A list of procedures is provided below that cover all the components of modeling and simulation and is applicable any numerical analysis of NPP systems, structures and components. It is noted that verification and validation procedures are designed in time domain domain, and that for numerical analysis tools that operate in frequency domain, it is required that V&V procedures need to prove/demonstrate adequacy in time domain, since real earthquake soil structure interaction behavior takes place in time domain.

- Source code verification has to be provided in order to prove that the program is free of any bugs and inconsistencies that can diminish results. Modeling and simulation program, written in any programming language (C, C++, FORTRAN, etc/) need to perform source code verification with all the necessary steps, described in some detail in section 11.3 on page 215.
- Verification and validation for constitutive problems addresses issues related to material

modeling and integration of constitutive integration algorithms for nonlinear/inelastic material modeling. Constitutive integration algorithms need to be verified in detail, while material modeling needs to be validated in detail. In addition, seismic energy dissipation is verified at constitutive level calculations. Examples for these activities are provided in section 11.4 on page 216.

- Verification and validation for static and dynamic finite element level solution advancement algorithms address issues related to static and dynamic incremental iterative algorithms that advance (drive) the incremental modeling process forward. These algorithms can introduce (unwanted or wanted) numerical damping/energy production, and as such need to be fully tested against available analytic or very accurate solutions (for example a number of solutions do exist for simple systems in books by Hughes and by Argyris and Mlejnek). Examples of verification activities are provided in section 11.5 on page 223.
- Verification and validation for static and dynamic behavior of single phase, solid elements addresses modeling using solid finite elements. Addressed is accuracy of modeling of various states of stress (uniaxial, multiaxial) and resulting accuracy of stresses, forces and displacements for different models where very accurate or analytic solutions exist (for example, a number of thin and thick plate and shell solutions do exist in books by Timoshenko and by Girkmann). Examples of verification activities are provided in section 11.6 on page 229.
- Verification and validation for static and dynamic behavior of structural elements addresses similar set of issues as previous activity, where forces and displacements for structural elements (truss, beam, shell) are verified against very accurate and/or analytic solutions for trusses, beams and shells (plates, wall elements and combinations). Examples of verification activities are provided in section 11.7 on page 242.
- Verification and Validation for Static and Dynamic Behavior of Special Elements addresses issues with contact elements, for both dry and saturated conditions. Of particular interest here is the accuracy of modeling of axial (normal force – gap) and frictional/slipping behavior, as these elements are known to misbehave for combination of axial and shear

loads. Examples of verification activities for these elements are provided in section 11.8 on page 255.

- Verification and Validation for Coupled, Porous Solid – Pore Fluid Problems addresses issues with solid finite element that model both porous solid and pore fluid, as is very important for soil and rock. In addition, these coupled elements form a basis for modeling coupled contact, where the contact zone (concrete foundation – soil/rock beneath) is beneath water table. Details of verification and validation for these elements is provided as a link to my recent papers, that address these issues, in section 11.9 on page 267.
- Verification and Validation for Seismic Wave Propagation Problems address issues of proper propagation of seismic waves of predetermined frequency range through finite element models. In addition this activity addresses accuracy and adequacy of seismic input, that encompasses body and surface waves, into finite element models. Examples of these verification activities are provided in section 11.10 on page 268.

In addition to comparison with very accurate and analytic solutions, errors tables/plots are also developed. These error table/plots are important as they are used to emphasize that numerical methods used in modeling and simulations are based on approximate methods and that all the obtained results do contain errors. Numerical modelers and analysts need to be aware of these errors and need to address them in presenting their results.

11.2 Introduction to Verification and Validation

Verification and validation (V&V) for numerical modeling and simulation represents a basic development task without which no results of such modeling and simulation should be presented. It is important to set the definitions for V&V (Oberkampf et al., 2002):

- **Verification:** The process of determining that a model implementation accurately represents the developer's conceptual description and specification. It is a mathematics issue. Verification provides evidence that the model is solved correctly.

- **Validation:** The process of determining the degree to which a model is accurate representation of the real world from the perspective of the intended uses of the model. It is a physics issue. Validation provides evidence that the correct model is solved.

With the development of advanced modeling and simulation numerical tools, there is an increased interest in V&V activities, (Roache, 1998; Oberkampf et al., 2002; Oberkampf, 2003; Oden et al., 2005; Babuška and Oden, 2004; Oden et al., 2010a,b; Roy and Oberkampf, 2011)

Importance of V&V activities cannot be overstated! V&V activities and procedures are the primary means of assessing accuracy in modeling and computational simulations. V&V activities and procedures are the tools with which we build confidence and credibility in modeling and computational simulations. Without proper V&V, numerical modeling and simulation results can not/should not be used for design, licensing or any other activity that relies on those results. Errors, inconsistencies and bug in numerical modeling and simulation programs are present and need to be removed and/or documented. A well known study by Hatton and Roberts (1994); Hatton (1997) reveals that all the software (in engineering, databases, control, etc.) contains errors, that can be removed if proper program development procedures are followed. More importantly, the first step is a realization that software/program probably/likely has some errors, bugs and that finding those errors and bugs needs to be done before the program start being used in decision making (design, licensing, etc.). In addition, numerical modeling and simulation are based on approximations and thus approximation errors are always present in results. Those errors need to be documented and information about those errors needs to be presented to potential users of numerical modeling and simulation programs.

The role of V&V activities can be explained by simple graphs. For example graph in Figure 11.1 (developed after Oberkampf et al. (2002)) shows that mathematical models and computer implementation try to mimic reality.

Slightly different view V&V activities is presented by Oden et al. (2010a), as shown in Figure Oden et al. (2010a). In this view, V&V must be available as it is a prerequisite for proper numerical modeling and simulation. Results from such V&V-ed modeling and simulations, are then used to gain knowledge about behavior of infrastructure objects. Such knowledge is then used to make (design, licensing, etc.) decisions.

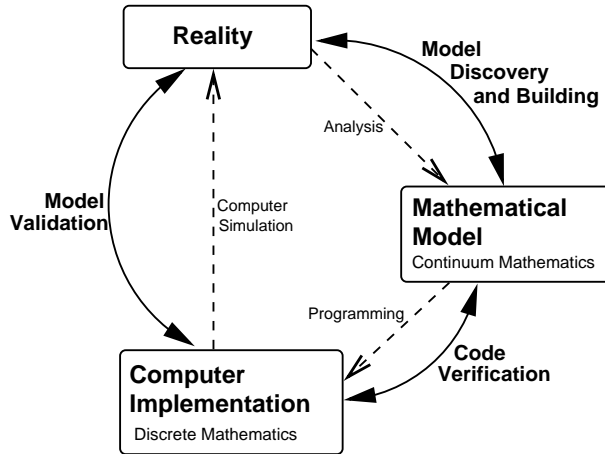


Figure 11.1: Role of Verification and Validation per Oberkamp et al. (2002).

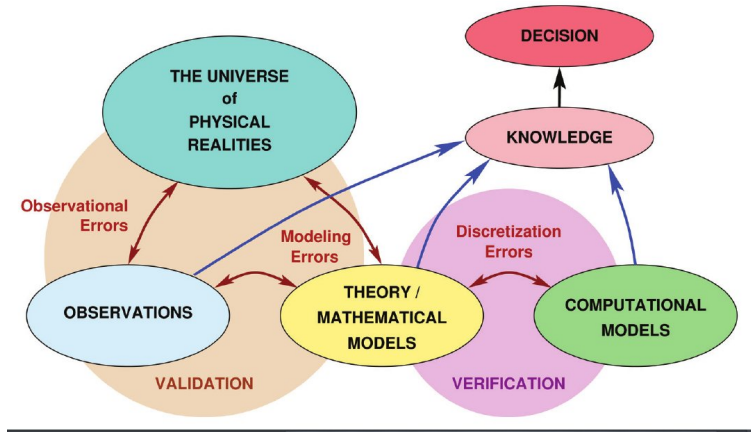


Figure 11.2: Role of Verification and Validation per Oden et al. (2010a).

11.2.1 Detailed Look at Verification and Validation

A detailed view of V&V is presented in Figure 11.3. It is important to note that the "Real World" is meant to represent a high fidelity knowledge about the realistic behavior of our infrastructure objects. Such behavior is represented by conceptual model that is then used as a basis for verification. Physical testing of unit problems or small components of the complete model are used for validation.

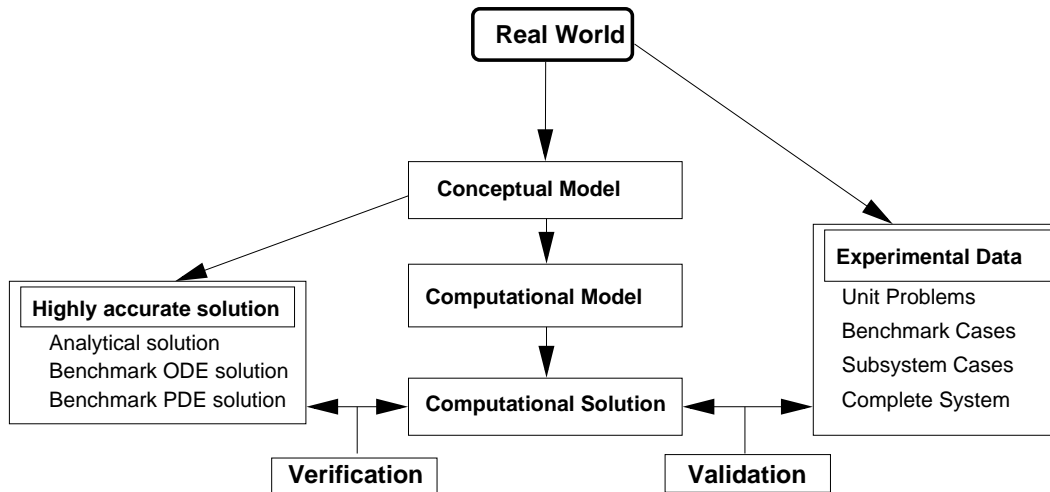


Figure 11.3: Detailed view of V&V.

Verification. The process of determining that a model implementation accurately represents the developer's conceptual description and specification.

Main goals of verification are to:

- Identify and remove errors in computer coding
 - Numerical algorithm verification
 - Software quality assurance practice
- Quantification of the numerical errors in computed solution

Validation: The process of determining the degree to which a model is accurate representation of the real world from the perspective of the intended uses of the model.

Main goals of validation are to:

- Tactical goal: Identification and minimization of uncertainties and errors in the computational model
- Strategic goal: Increase confidence in the quantitative predictive capability of the computational model

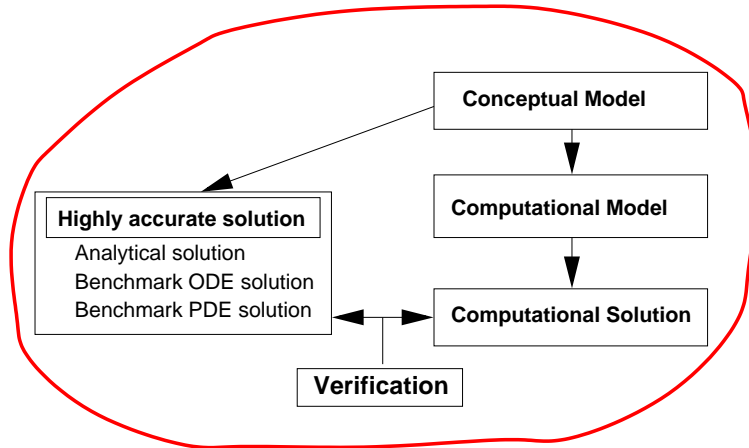


Figure 11.4: Detailed view of Verification.

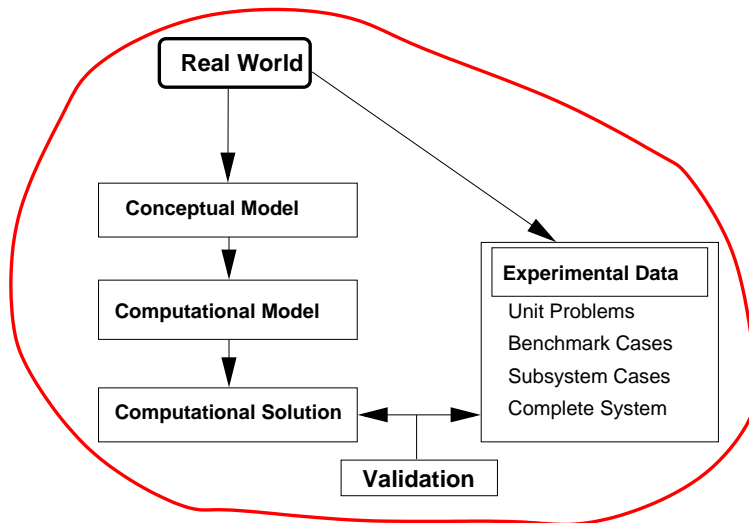


Figure 11.5: Detailed view of Validation.

11.2.2 Prediction

Numerical prediction then uses computational model to foretell the state of a physical system under consideration under conditions for which the computational model has not been validated. Validation does not directly make a claim about the accuracy of a prediction as:

- Computational models are easily misused (unintentionally or intentionally),
- It will depend on how closely related are the conditions of the prediction and specific cases

in validation database, and

- How well is physics of the problem understood.

11.2.3 Forward Toward Verification and Validation

In what follows, a set of verification and validation examples are presented. It is noted that a complete or nearly complete set of verification examples exists (nearly complete as any time new closed form solution is discovered, it is used for further verification), while validation only exists where fully documented, controlled validation experiments are present.

It is noted that presented are select verification example as full presentation of all the example would take much space. The main aim here is to present verification methodology and to show illustrative verification examples. Full set of examples is available and it is run frequently, during regular verification checks of the Real ESSI Simulator program.

11.3 Source Code Verification

Source code verification is very important component of verification process. This verification component tends to reveal problems with programming and various simple bugs that can destroy accuracy of results. Hatton (1997) reports that a large majority (if not all) of programs have a number of pre-coded problems that need to be analyzed and cleared/fixed before further verification and validation is to proceed. There are two main types of source code verification:

- **Software Quality Assurance** aims to clear all software coding (programming) errors. Proper following of good software practice ensures that these errors are minimized, and hopefully completely eliminated. A number of activities have to be undertaken in order to assure software quality. For example, all the warnings from compilers (use of multiple compilers is recommended) have to be resolved. In addition source code coverage has to be documented, that is, what part of code was covered during testing, and, more importantly, what part of code was not covered. Moreover, various tools exist to check consistency of code for managing memory (memory leaks), that guaranty consistency of variables and arrays.

- **Numerical Algorithm Verification** aims to verify errors in numerical algorithms used. This is needed in order to quantify numerical error introduced in solutions, and in particular sensitivity of solutions to such numerical errors.

11.4 Verification and Validation for Constitutive Problems

11.4.1 Verification of Constitutive Integration

Presented is an example of accuracy analysis of the implicit constitutive algorithm. Examples for a simple model (von-Mises) for accuracy analysis are demonstrated to verify general implicit algorithm. Convergence performance analysis is conducted.

Error Assessment

There are various error measures for the integration algorithms. Manzari and Prachathananukit (2001) used the relative stress norm by Equation 11.1,

$$\delta^r = \frac{\sqrt{(\sigma_{ij} - \sigma_{ij}^*)(\sigma_{ij} - \sigma_{ij}^*)}}{\sqrt{\sigma_{pq}^* \sigma_{pq}^*}} \quad (11.1)$$

where σ_{ij}^* is the 'exact' stress solution, and σ_{ij} the calculated stress solution. Alternatively, Jeremić and Sture (1997) used the normalized energy norm by Equation 11.2,

$$\delta^n = \frac{\|\sigma_{ij} - \sigma_{ij}^*\|}{\|p^{unit}\|} \quad (11.2)$$

where $\|\sigma_{ij}\|^2 = \sigma_{ij} D_{ijkl} \sigma_{kl}$, and D_{ijkl} is the elastic compliance fourth-order tensor, p^{unit} is the 'unit' energy norm for normalization.

The relative stress norm by Equation 11.1 is more reasonable since two points having the same $\|\sigma_{ij} - \sigma_{ij}^*\|$ but different $\sigma_{pq}^* \sigma_{pq}^*$ should have different error measures. However, this norm becomes singular and possible meaningless when $\sigma_{pq}^* \sigma_{pq}^*$ is close to zero. The normalized energy norm by Equation 11.2 have no such singularity problem but it may give the same error index for two points having the same $\|\sigma_{ij} - \sigma_{ij}^*\|$ but different $\sigma_{pq}^* \sigma_{pq}^*$. In this work, we use these two error measure methods, but for simplicity, Equation (11.2) is modified into

$$\delta^r = \frac{\sqrt{(\sigma_{ij} - \sigma_{ij}^*)(\sigma_{ij} - \sigma_{ij}^*)}}{\sqrt{\sigma_{pq}^0 \sigma_{pq}^0}} \quad (11.3)$$

where $\sigma_{pq}^0 \sigma_{pq}^0$ is evaluated at some non-zero initial isotropic stress state. That is, the normalized error is evaluated by Equation 11.3, and the relative error is evaluated by Equation 11.1.

In presented examples, the initial stress state point is set $p^0 = 100$ kPa, $q^0 = 0$ kPa, $\theta^0 = 0$, which is the σ_{pq}^0 in Equation 11.3. The one-step predicted stress state point for the implicit algorithm is within the range of $0.1 \leq p \leq 100$ kPa, $0 \leq q \leq 100$ kPa, $0 \leq \theta \leq \pi/3$. The ‘exact’ solution is actually unknown for most elasto-plastic problems. Here the ‘exact’ solution is simply replaced by 50 sub step solution of the explicit algorithm in the same one-step prediction incremental. All these error evaluations are within the material constitutive level.

The test example presents Von-Mises model with the uniaxial yield strength $k = 50$ kPa, where linear elasticity parameters are Young’s modulus $E = 1 \times 10^5$ kPa, and Poisson’s ratio $\nu = 0.25$.

Figures 11.6 and 11.7 show the iso-error maps for the von-Mises model with linear isotropic hardening. The linear hardening modulus $H = 2 \times 10^4$ kPa. The blue lines represents the yield surface boundary. It can be seen that the error magnitudes are as small as 10^{-10} to 10^{-9} , which implies that the solutions by implicit algorithm for this linear isotropic hardening Von-Mises model are numerically accurate.

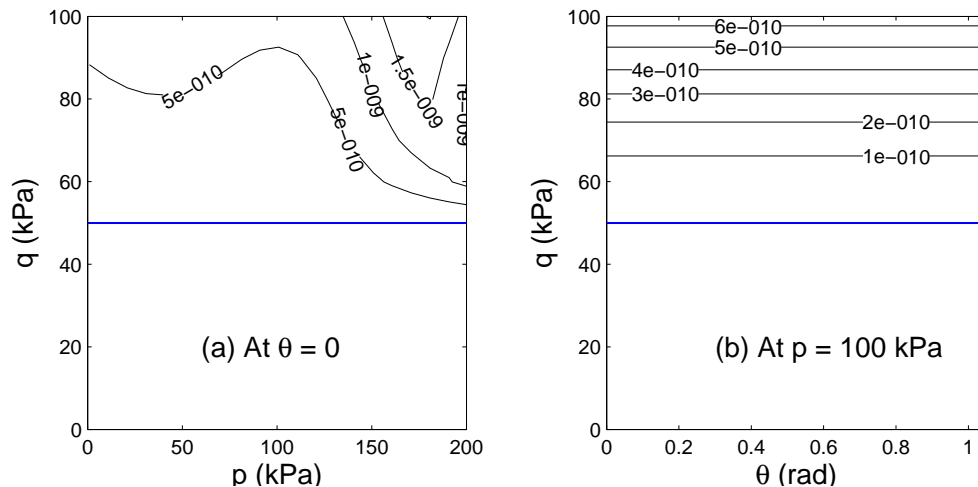


Figure 11.6: Normalized iso-error maps of Von-Mises model with linear isotropic hardening.

Figures 11.8 and 11.9 show the iso-error maps for the Von-Mises model with Armstrong-Frederick translational kinematic hardening. The hardening parameters are $h_a = 5 \times 10^4$ kPa and

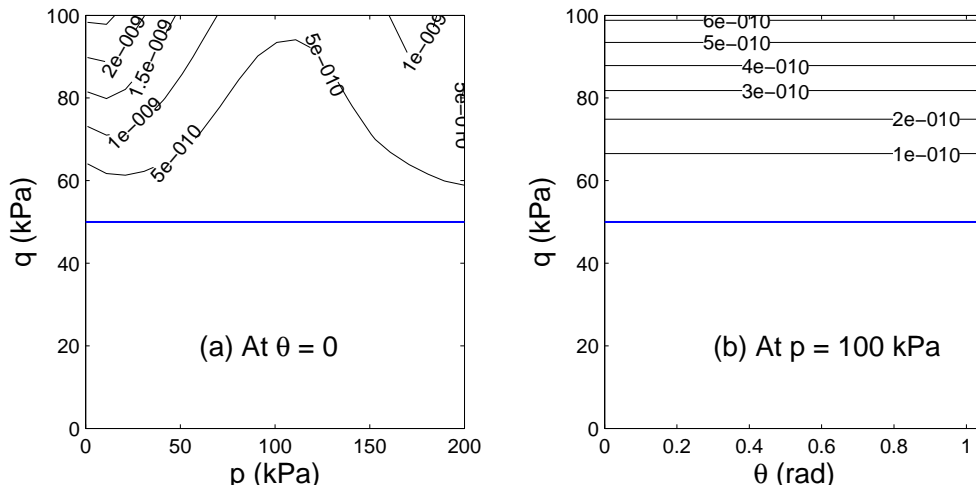


Figure 11.7: Relative iso-error maps of Von-Mises model with linear isotropic hardening.

$C_r = 2.5 \times 10^3$. It can be seen that errors are very small which proves the good performance of the implicit algorithm. The iso-error map gives a good trend, i.e., the further away from the yield surface, the errors become more pronounced; the normalized errors are pressure-independent, which fits well the feature of Von-Mises model; the iso-error lines in the $q - \theta$ figure are parallel to the yield surface and are independent of the Lode's angle θ , which again fits well with Von-Mises model which is only q -related.

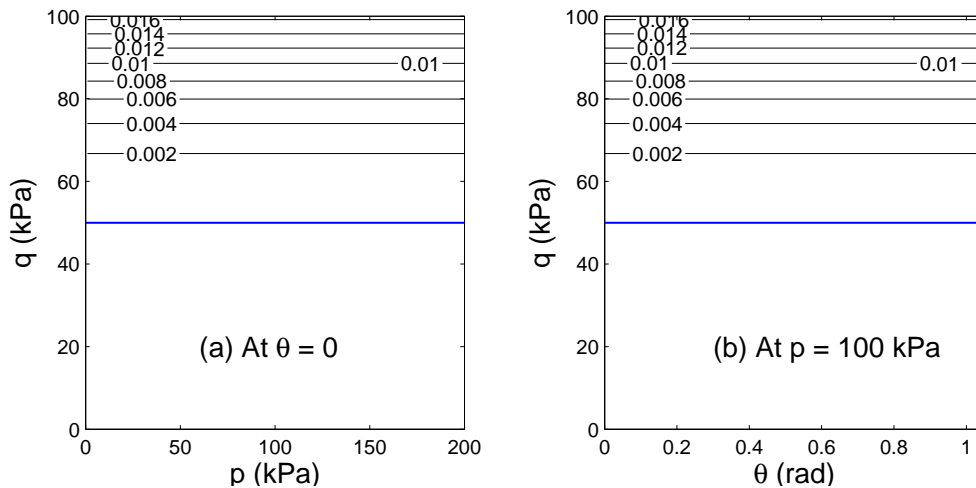


Figure 11.8: Normalized iso-error maps of Von-Mises model with Armstrong-Frederick kinematic hardening.

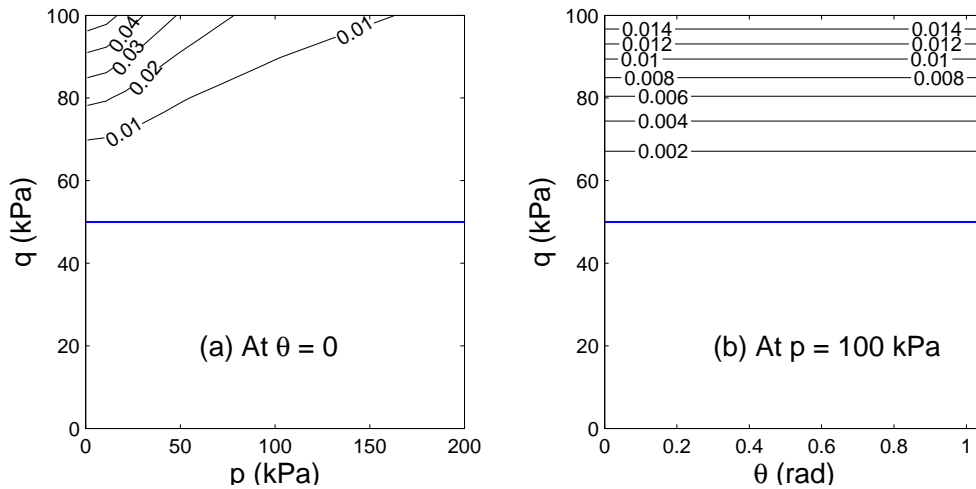


Figure 11.9: Relative iso-error maps of Von-Mises model with Armstrong-Frederick kinematic hardening.

11.4.2 Validation of Constitutive Model Predictions

Dafalias Manzari Material Model

Validation is performed by comparing experimental (physical) results and numerical (constitutive) simulations for the Toyoura sand. The material parameters used are from Dafalias and Manzari (2004a) and are listed in Table (11.1). Several simulated results are compared with the experimental data published by Verdugo and Ishihara (1996).

Figure (11.10) presents both loading and unloading triaxial drained test simulation results for a relatively low triaxial isotropic pressure of 100 kPa but with different void ratios of $e_0 = 0.831, 0.917, 0.996$ at the end of isotropic compression. During the loading stage, one can observe the hardening and then softening together with the contraction and then dilation for the denser sand, while only hardening together with contraction for the looser sand. The significance of the state parameter to the soil modeling is clear from the very different responses with different void ratios at the same triaxial isotropic pressure.

Figure (11.10) also shows both loading and unloading triaxial drained test simulation results for a relatively high triaxial isotropic pressure of 500 kPa but with different void ratio of $e_0 = 0.810, 0.886, 0.960$ at the end of isotropic compression. Similar phenomenon are observed as with tests (physical and numerical) for relatively low triaxial isotropic pressure. However, due to the higher

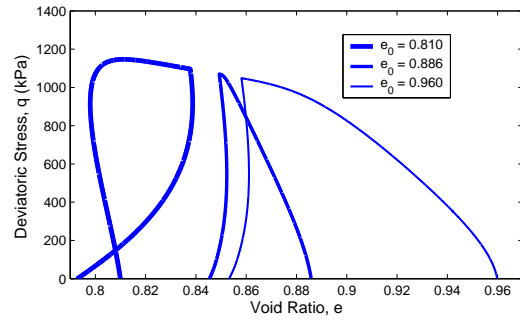
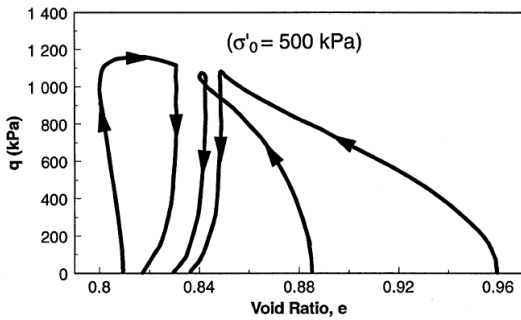
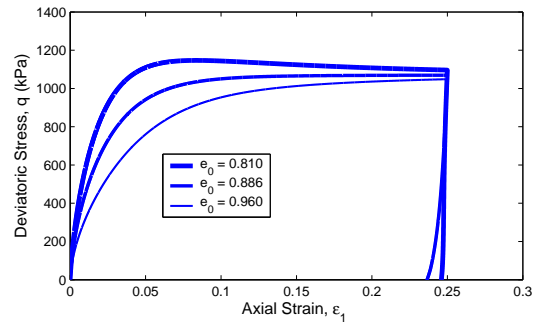
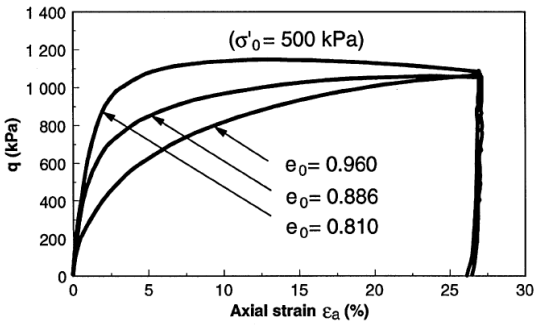
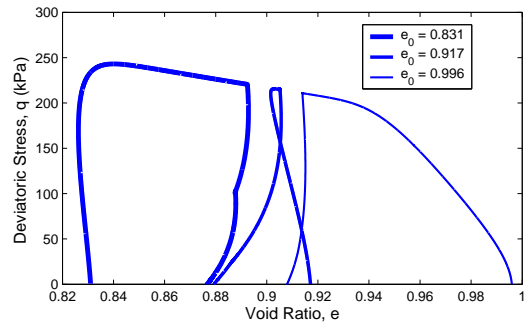
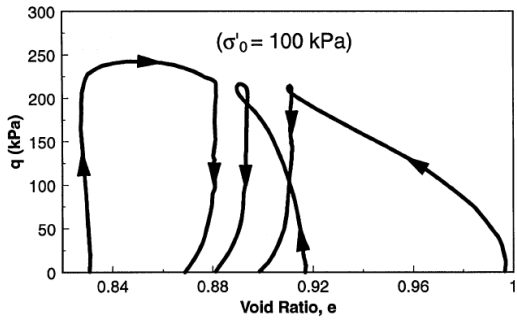
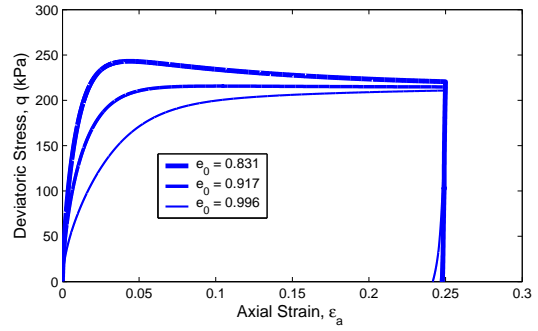
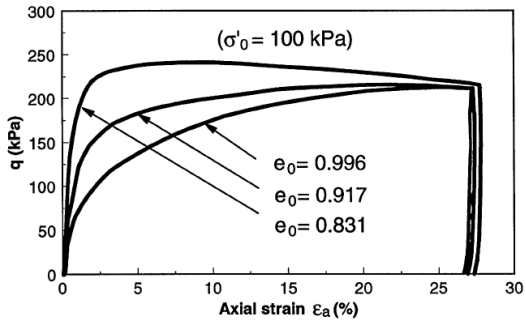


Figure 11.10: Left: Experimental data; Right: Simulated results.

Table 11.1: Material parameters of Dafalias-Manzari model.

material parameter		value	material parameter		value
Elasticity	G_0	125 kPa	Plastic modulus	h_0	7.05
	ν	0.05		c_h	0.968
Critical state	M	1.25	Dilatancy	n_b	1.1
	c	0.712		A_0	0.704
	λ_c	0.019		n_d	3.5
	ξ	0.7		Fabric-dilatancy	z_{max}
e_r	0.934	c_z	600.0		
Yield surface	m	0.01			

confinement pressure, the stress-strain responses are higher at the same strain, which proves the significant pressure dependent feature for the sands.

Figure (11.11) presents both loading and unloading triaxial undrained test simulation results for a dense sand with the void ratio of $e_0=0.735$ at the end of isotropic compression but with different isotropic compression pressures of $p_0 = 100, 1000, 2000, 3000$ kPa. During the loading stage, one observes that each of responses are close to the critical state line for the very various range of isotropic compression pressures. For the higher isotropic compression pressure, the contraction response with softening is clearly observed, while for the smaller isotropic compression pressure, it is a dilation response without softening.

Close matching of physical testing data with constitutive predictions represents a satisfactory validation of our material model. This validation with previous verification gives us confidence that predictions (presented in next section) represent well the real, prototype behavior.

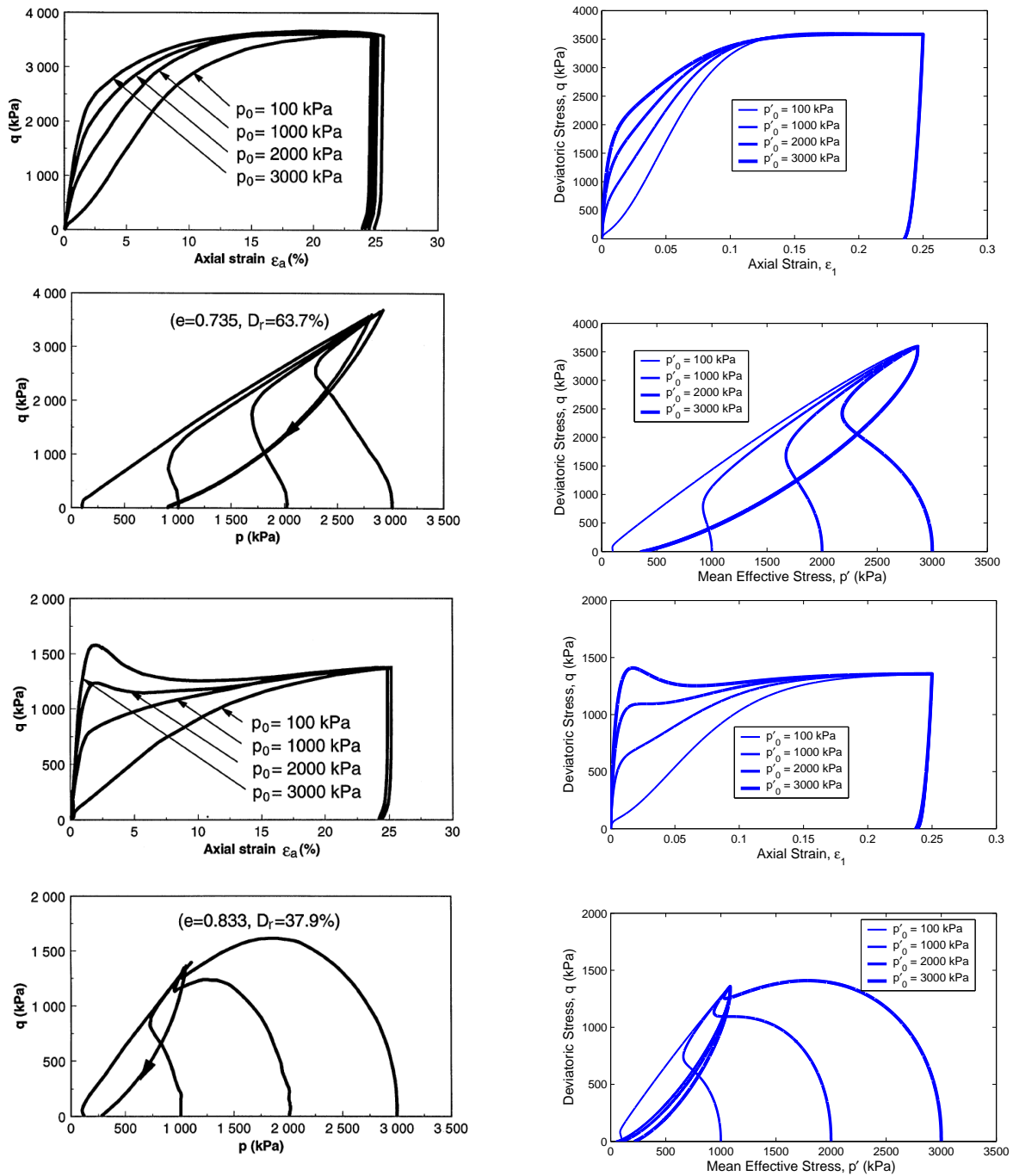


Figure 11.11: Left: Experimental data; Right: Simulated results.

11.5 Verification and Validation for Static and Dynamic Finite Element Level Solution Advancement Algorithms

11.5.1 Verification for Dynamic Solution Advancement

Newmark solution advancement algorithm for dynamic problems (Newmark, 1959) relies on parameters β and γ to control accuracy and numerical damping. For cases where

$$\gamma \geq \frac{1}{2}, \quad \beta \geq \frac{1}{4}\left(\gamma + \frac{1}{2}\right)^2 \quad (11.4)$$

the procedure is unconditionally stable and second-order accurate.

Different values for γ and β can be used to create various integration methods:

- For $\gamma = 0.5$ (and corresponding $\beta = 0.25$) there is no numerical damping.
- Any γ value greater than 0.5 will introduce numerical damping.
- Trapezoidal rule or average acceleration method for $\beta = 1/4$ and $\gamma = 1/2$,
- Linear acceleration method for $\beta = 1/6$ and $\gamma = 1/2$,
- Explicit, central difference method for $\beta = 0$ and $\gamma = 1/2$.
- Strongest numerical damping values is obtained for values $\beta = 1$ and $\gamma = 2/3$, as spectral ratio $\rho_\infty = 0$ (Hughes (1987), page 502)

Following Argyris and Mlejnek (1991); Hughes (1987), to calculate numerical damping ξ and numerical period elongation $\bar{\omega}$ a amplification matrix A is constructed. It proves convenient to define amplification matrix A for the Hilber Hughes Taylor (HHT) family of algorithms and then obtain the same matrix for Newmark algorithm by setting $\gamma = 0$:

$$A = \frac{1}{D} \begin{bmatrix} 1 + \alpha\beta\Omega^2 & 1 & \frac{1}{2} - \beta \\ -\gamma\Omega^2 & 1 - (1 + \alpha)(\gamma - \beta)\Omega^2 & 1 - \gamma - (1 + \alpha)\left(\frac{1}{2}\gamma - \beta\right)\Omega^2 \\ -\Omega^2 & -(1 + \alpha)\Omega^2 & -(1 + \alpha)\left(\frac{1}{2} - \beta\right)\Omega^2 \end{bmatrix} \quad (11.5)$$

where

$$\begin{aligned}
 D &= 1 + (1 + \alpha)\beta\Omega^2 \\
 \Omega &= \omega\Delta t \\
 \omega &= (K/M)^{\frac{1}{2}}
 \end{aligned}
 \tag{11.6}$$

The eigenvalue of amplification matrix A are two complex conjugate roots $\lambda_{1,2}$ and a so-called spurious root λ_3 which satisfy $|\lambda_3| < |\lambda_{1,2}| \leq 1$. The roots $\lambda_{1,2}$ are

$$\lambda_{1,2} = A \pm Bi
 \tag{11.7}$$

Then, the analytic damping ratio ξ and analytic period $\bar{\omega}$ become

$$\begin{aligned}
 \bar{\xi} &= -\ln(A^2 + B^2) \\
 \bar{\omega} &= \bar{\Omega}/\Delta t \\
 \bar{\Omega} &= \arctan(B/A)
 \end{aligned}
 \tag{11.8}$$

Verification Example Description.

A single degree of freedom (SDOF) example is developed to verify the Newmark algorithm as implemented within the Real ESSI simulator. The example, shown in Fig.(11.12) has a stiffness and mass to have a natural period of $T = 1s$. In the first loading stage, the beam is loaded with a horizontal force to generate an initial displacement. The second loading stage then removes initial load and the beam start free vibrations.

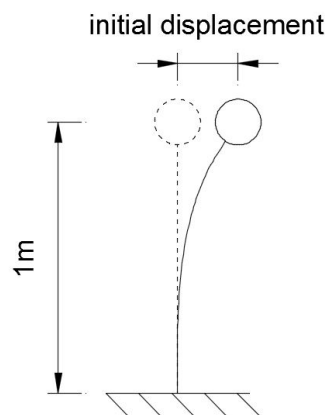


Figure 11.12: Verification example description.

The results are listed and plotted below.

Table 11.2: Verification results for the Newmark solution advancement algorithm.

dt/T	γ	Measured ξ	Analytic ξ	Measured T shift	Analytic T shift
0.005	0.5	0.0030	0.0000	0.0000	0.0001
0.01	0.5	0.0030	0.0000	0.0000	0.0003
0.05	0.5	0.0037	0.0000	0.0101	0.0082
0.1	0.5	0.0034	0.0000	0.0309	0.0321
0.005	0.6	0.0035	0.0016	0.0000	0.0001
0.01	0.6	0.0042	0.0031	0.0000	0.0003
0.05	0.6	0.0160	0.0155	0.0101	0.0084
0.1	0.6	0.0296	0.0295	0.0309	0.0329
0.005	0.7	0.0042	0.0031	0.0000	0.0001
0.01	0.7	0.0063	0.0063	0.0000	0.0004
0.05	0.7	0.0311	0.0309	0.0101	0.0091
0.1	0.7	0.0590	0.0590	0.0309	0.0356
0.005	0.8	0.0051	0.0047	0.0000	0.0001
0.01	0.8	0.0093	0.0094	0.0000	0.0004
0.05	0.8	0.0465	0.0464	0.0101	0.0103
0.1	0.8	0.0882	0.0886	0.0309	0.0399
0.005	0.9	0.0063	0.0063	0.0000	0.0001
0.01	0.9	0.0130	0.0126	0.0000	0.0005
0.05	0.9	0.0618	0.0618	0.0101	0.0120
0.1	0.9	0.1180	0.1181	0.0417	0.0460

Verification Results for Newmark Solution Advancement Algorithm.

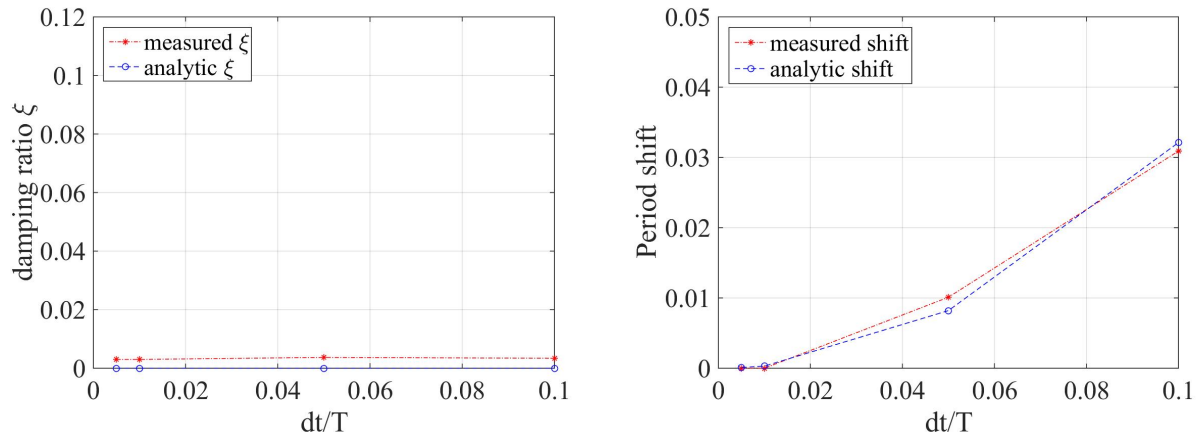


Figure 11.13: Comparison for Newmark algorithm with $\gamma = 0.5$. Left: Damping ratio comparison, Right: Period shift comparison.

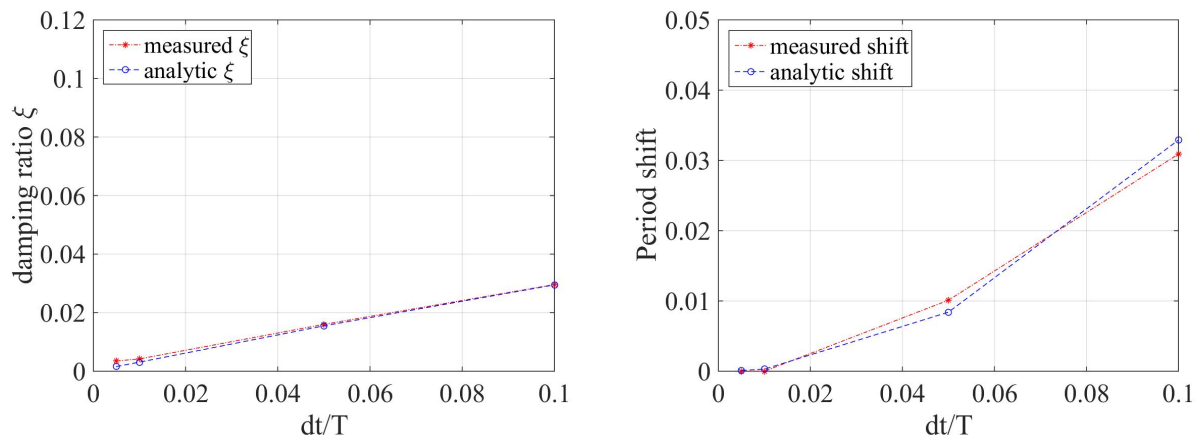


Figure 11.14: Comparison for Newmark algorithm with $\gamma = 0.6$. Left: Damping ratio comparison, Right: Period shift comparison.

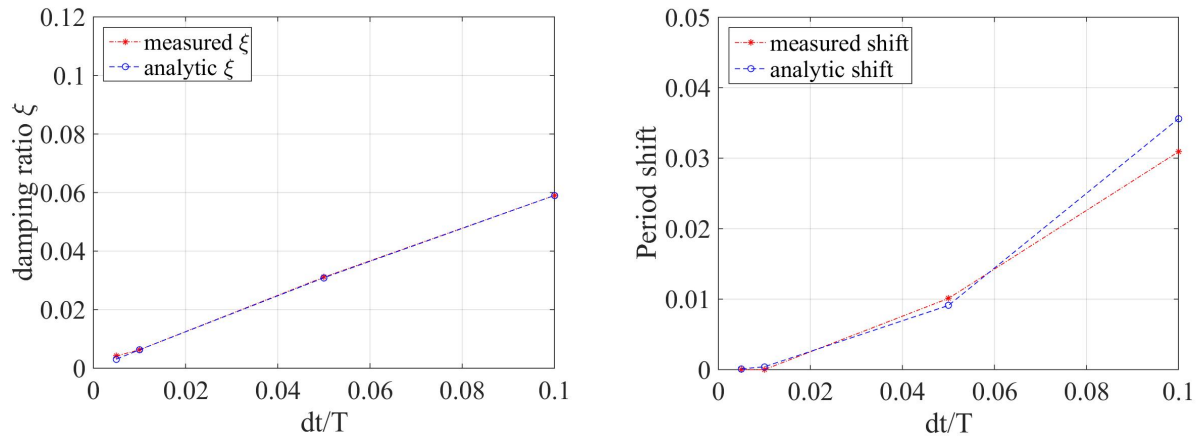


Figure 11.15: Comparison for Newmark algorithm with $\gamma = 0.7$. Left: Damping ratio comparison, Right: Period shift comparison.

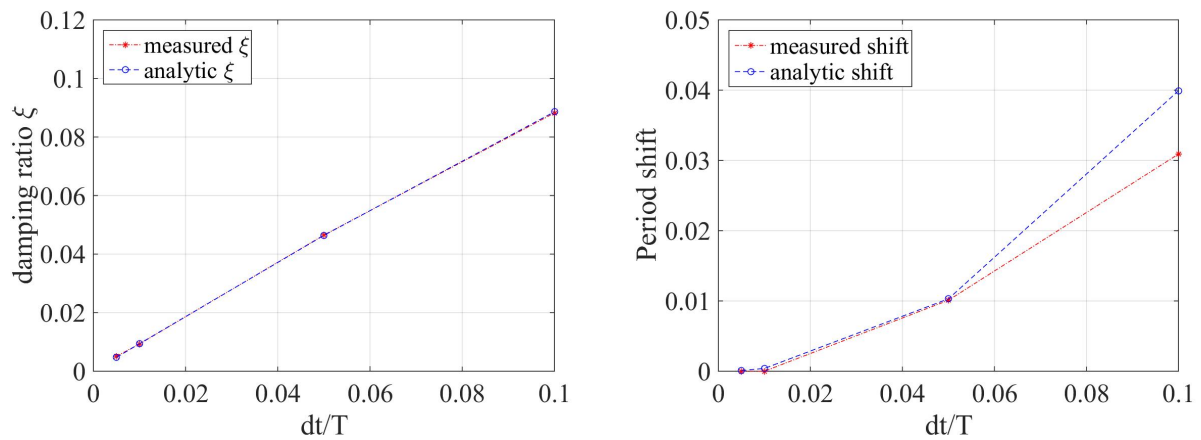


Figure 11.16: Comparison for Newmark algorithm with $\gamma = 0.8$. Left: Damping ratio comparison, Right: Period shift comparison.

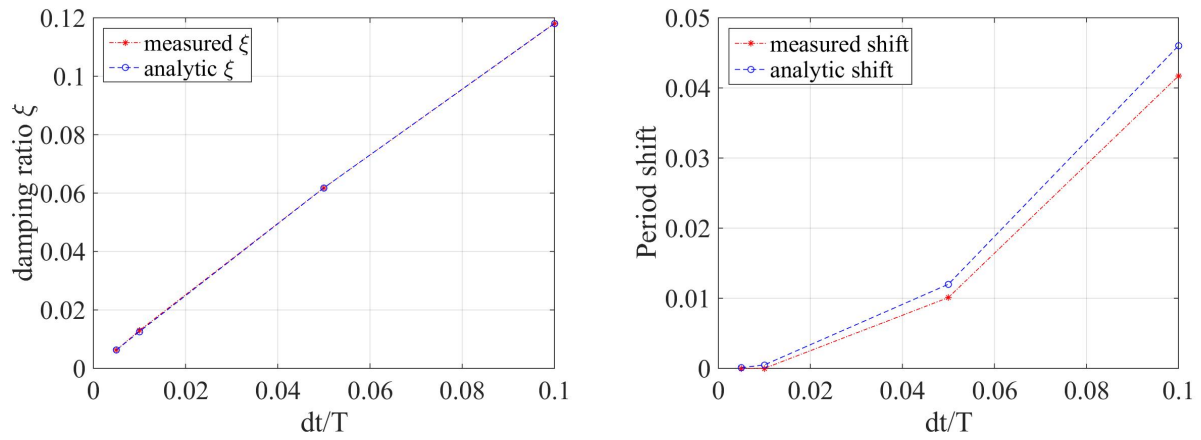


Figure 11.17: Comparison for Newmark algorithm with $\gamma = 0.9$. Left: Damping ratio comparison, Right: Period shift comparison.

11.6 Verification and Validation for Static and Dynamic Behavior of Single Phase Solid Elements

11.6.1 Verification of Static, Single Phase Solid Modeling and Simulation

Verification of 8 node brick cantilever beam (static)

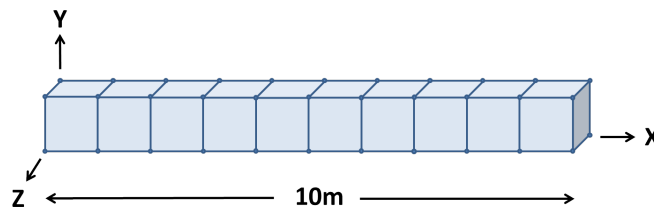
Problem description: Length=10m, Force=4N, $E=100000\text{Pa}$, $I = \frac{1}{12}$

Theoretical displacement:

$$d = \frac{PL^3}{3EI} = \frac{4 \times 1000}{3 \times 100000 \times \frac{1}{12}} = 0.16\text{m} \quad (11.9)$$

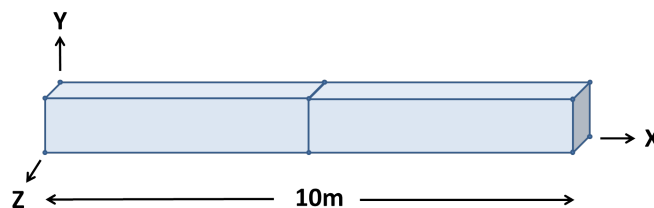
Numerical simulation results:

1m element size (10 elements):



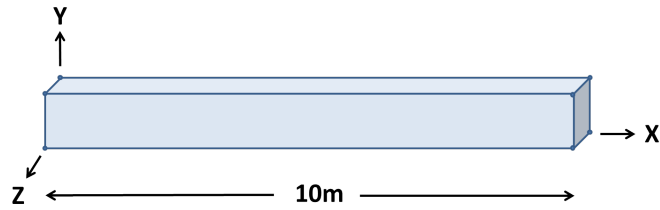
$$error = \frac{0.16 - 0.1072}{0.16} = 33\% \quad (11.10)$$

5m element size (2 elements):



$$error = \frac{0.16 - 0.011911}{0.16} = 92.5\% \quad (11.11)$$

10m element size (1 element):



$$error = \frac{0.16 - 0.00315}{0.16} = 98\% \quad (11.12)$$

Verification of 27 node brick cantilever beam (static)

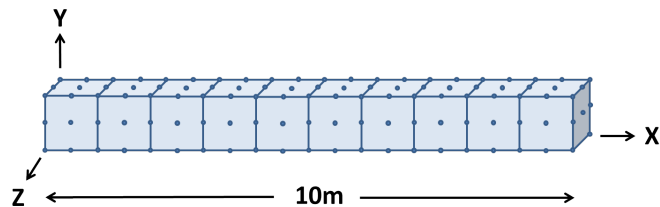
Problem description: Length=10m, Force=9N, $E=100000\text{Pa}$, $I = \frac{1}{12}$

Theoretical displacement:

$$d = \frac{PL^3}{3EI} = \frac{9 \times 1000}{3 \times 100000 \times \frac{1}{12}} = 0.36\text{m} \quad (11.13)$$

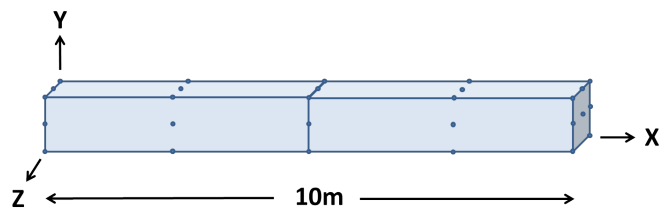
Numerical simulation results:

1m element size (10 elements):



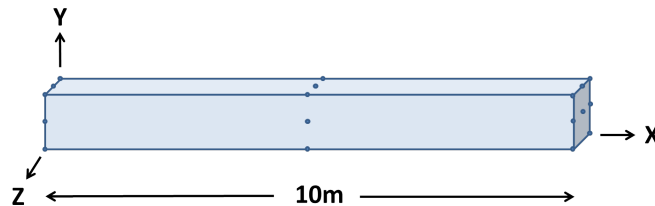
$$error = \frac{0.361721 - 0.36}{0.36} = 0.47\% \quad (11.14)$$

5m element size (2 elements):



$$error = \frac{0.36 - 0.345719}{0.36} = 3.96\% \quad (11.15)$$

10m element size (1 element):



$$error = \frac{0.36 - 0.279989}{0.36} = 22\% \quad (11.16)$$

Verification of 27NodeBrick cantilever beam for different Poisson's ratio

Problem description: Length=6m, Width=1m, Height=1m, Force=100N, $E=1E8Pa$, $\nu = 0.0 - 0.49$. The force direction was shown in Figure (11.18).

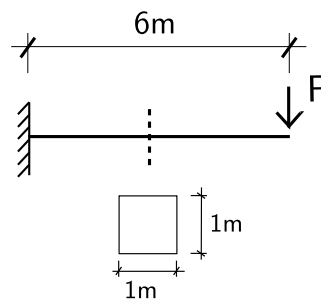


Figure 11.18: Problem description for cantilever beams of different Poisson's ratios.

The theoretical solution for $\nu = 0.0$ was calculated below, while the solution for other Poisson's ratio is calculated by the similar process.

Theoretical displacement (bending and shear deformation):

$$\begin{aligned}
 d &= \frac{FL^3}{3EI} + \frac{FL}{GA_v} \\
 &= \frac{FL^3}{3E \frac{bh^3}{12}} + \frac{FL}{\frac{E}{2(1+\nu)} \frac{bh}{\kappa}} \\
 &= \frac{100N \times 6^3 m^3}{3 \times 10^8 N/m^2 \times \frac{1}{12} m^4} + \frac{100N \times 6m}{\frac{10}{2} \times 10^7 N/m^2 \times 1m^2 \times \frac{5}{6}} \\
 &= 8.64 \times 10^{-4} m + 0.144 \times 10^{-4} m \\
 &= 8.784 \times 10^{-4} m
 \end{aligned} \tag{11.17}$$

The rotation angle at the end:

$$\theta = \frac{FL^2}{2EI} = \frac{100N \times 6^2 m^2}{2 \times 10^8 N/m^2 \times \frac{1}{12} m^4} = 2.16 \times 10^{-4} \text{ rad} = 0.0124^\circ \tag{11.18}$$

The 27NodeBrick elements for cantilever beams of different Poisson's ratios are shown in Figure (11.19).

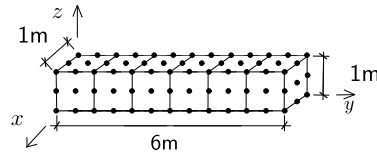


Figure 11.19: Model for 27NodeBrick cantilever beam with different Poisson's ratio.

All the displacement results are listed in Tables (11.3) - (11.5).

Table 11.3: Displacement results for 27NodeBrick cantilever beams with element side length 1 m.

Poisson's ratio	27NodeBrick displacement	Theory displacement (bending)	Theory displacement (shear)	Theory displacement(all)	Error
0.00	8.755E-04 <i>m</i>	8.640E-04 <i>m</i>	1.440E-05 <i>m</i>	8.784E-04 <i>m</i>	0.34%
0.05	8.757E-04 <i>m</i>	8.640E-04 <i>m</i>	1.512E-05 <i>m</i>	8.791E-04 <i>m</i>	0.39%
0.10	8.751E-04 <i>m</i>	8.640E-04 <i>m</i>	1.586E-05 <i>m</i>	8.799E-04 <i>m</i>	0.54%
0.15	8.735E-04 <i>m</i>	8.640E-04 <i>m</i>	1.659E-05 <i>m</i>	8.806E-04 <i>m</i>	0.80%
0.20	8.708E-04 <i>m</i>	8.640E-04 <i>m</i>	1.734E-05 <i>m</i>	8.813E-04 <i>m</i>	1.19%
0.25	8.667E-04 <i>m</i>	8.640E-04 <i>m</i>	1.808E-05 <i>m</i>	8.821E-04 <i>m</i>	1.74%
0.30	8.608E-04 <i>m</i>	8.640E-04 <i>m</i>	1.884E-05 <i>m</i>	8.828E-04 <i>m</i>	2.50%
0.35	8.520E-04 <i>m</i>	8.640E-04 <i>m</i>	1.959E-05 <i>m</i>	8.836E-04 <i>m</i>	3.57%
0.40	8.385E-04 <i>m</i>	8.640E-04 <i>m</i>	2.035E-05 <i>m</i>	8.844E-04 <i>m</i>	5.18%
0.45	8.147E-04 <i>m</i>	8.640E-04 <i>m</i>	2.111E-05 <i>m</i>	8.851E-04 <i>m</i>	7.96%
0.49	7.711E-04 <i>m</i>	8.640E-04 <i>m</i>	2.173E-05 <i>m</i>	8.857E-04 <i>m</i>	12.94%

Table 11.4: Displacement results for 27NodeBrick cantilever beams with element side length 0.5 m.

Poisson's ratio	27NodeBrick displacement	Theory displacement (bending)	Theory displacement (shear)	Theory displacement(all)	Error
0.00	8.804E-04 <i>m</i>	8.640E-04 <i>m</i>	1.440E-05 <i>m</i>	8.784E-04 <i>m</i>	0.23%
0.05	8.808E-04 <i>m</i>	8.640E-04 <i>m</i>	1.512E-05 <i>m</i>	8.791E-04 <i>m</i>	0.19%
0.10	8.805E-04 <i>m</i>	8.640E-04 <i>m</i>	1.586E-05 <i>m</i>	8.799E-04 <i>m</i>	0.08%
0.15	8.796E-04 <i>m</i>	8.640E-04 <i>m</i>	1.659E-05 <i>m</i>	8.806E-04 <i>m</i>	0.12%
0.20	8.778E-04 <i>m</i>	8.640E-04 <i>m</i>	1.734E-05 <i>m</i>	8.813E-04 <i>m</i>	0.40%
0.25	8.752E-04 <i>m</i>	8.640E-04 <i>m</i>	1.808E-05 <i>m</i>	8.821E-04 <i>m</i>	0.78%
0.30	8.715E-04 <i>m</i>	8.640E-04 <i>m</i>	1.884E-05 <i>m</i>	8.828E-04 <i>m</i>	1.28%
0.35	8.663E-04 <i>m</i>	8.640E-04 <i>m</i>	1.959E-05 <i>m</i>	8.836E-04 <i>m</i>	1.95%
0.40	8.588E-04 <i>m</i>	8.640E-04 <i>m</i>	2.035E-05 <i>m</i>	8.844E-04 <i>m</i>	2.89%
0.45	8.465E-04 <i>m</i>	8.640E-04 <i>m</i>	2.111E-05 <i>m</i>	8.851E-04 <i>m</i>	4.36%
0.49	8.248E-04 <i>m</i>	8.640E-04 <i>m</i>	2.173E-05 <i>m</i>	8.857E-04 <i>m</i>	6.88%

Table 11.5: Displacement results for 27NodeBrick cantilever beams with element side length 0.25 m.

Poisson's ratio	27NodeBrick displacement	Theory displacement (bending)	Theory displacement (shear)	Theory displacement(all)	Error
0.00	8.797E-04 <i>m</i>	8.640E-04 <i>m</i>	1.440E-05 <i>m</i>	8.784E-04 <i>m</i>	0.15%
0.05	8.801E-04 <i>m</i>	8.640E-04 <i>m</i>	1.512E-05 <i>m</i>	8.791E-04 <i>m</i>	0.11%
0.10	8.799E-04 <i>m</i>	8.640E-04 <i>m</i>	1.586E-05 <i>m</i>	8.799E-04 <i>m</i>	0.01%
0.15	8.792E-04 <i>m</i>	8.640E-04 <i>m</i>	1.659E-05 <i>m</i>	8.806E-04 <i>m</i>	0.16%
0.20	8.778E-04 <i>m</i>	8.640E-04 <i>m</i>	1.734E-05 <i>m</i>	8.813E-04 <i>m</i>	0.40%
0.25	8.758E-04 <i>m</i>	8.640E-04 <i>m</i>	1.808E-05 <i>m</i>	8.821E-04 <i>m</i>	0.71%
0.30	8.730E-04 <i>m</i>	8.640E-04 <i>m</i>	1.884E-05 <i>m</i>	8.828E-04 <i>m</i>	1.12%
0.35	8.692E-04 <i>m</i>	8.640E-04 <i>m</i>	1.959E-05 <i>m</i>	8.836E-04 <i>m</i>	1.63%
0.40	8.641E-04 <i>m</i>	8.640E-04 <i>m</i>	2.035E-05 <i>m</i>	8.844E-04 <i>m</i>	2.29%
0.45	8.567E-04 <i>m</i>	8.640E-04 <i>m</i>	2.111E-05 <i>m</i>	8.851E-04 <i>m</i>	3.21%
0.49	8.452E-04 <i>m</i>	8.640E-04 <i>m</i>	2.173E-05 <i>m</i>	8.857E-04 <i>m</i>	4.58%

Verification of 27NodeBrick square plate with four edges clamped

Problem description: Length=20m, Width=20m, Height=1m, Force=100N, $E=1E8Pa$, $\nu = 0.3$.

The four edges are clamped. The load is the uniform normal pressure on a plate.

The plate flexural rigidity is

$$D = \frac{Eh^3}{12(1-\nu^2)} = \frac{10^8 N/m^2 \times 1^3 m^3}{12 \times (1-0.3^2)} = 9.1575 \times 10^6 N \cdot m \quad (11.19)$$

The theoretical solution is

$$d = \alpha_c \frac{qa^4}{D} = 0.00406 \times \frac{100 N/m^2 \times 20^4 m^4}{9.1575 \times 10^6 N \cdot m} = 2.2015 \times 10^{-3} m \quad (11.20)$$

where α_c is a coefficient, which depends on the ratio of plate length to width. In this problem, the coefficient¹ α_c is 0.00406.

The 27NodeBrick are shown in Figure (11.20) - (11.25).

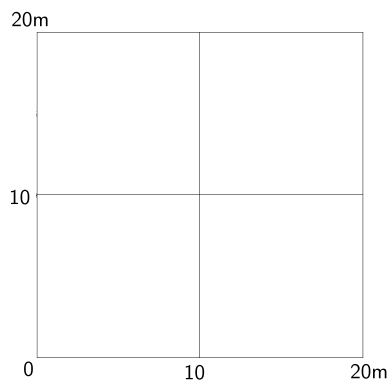


Figure 11.20: 27NodeBrick edge clamped square plate with element side length 10m.

The results are listed in Table (11.6).

The errors are listed in Table (11.7).

The errors are plotted in Figure (11.26).

The ESSI model fei files for the table above are here

¹Stephen Timoshenko, Theory of plates and shells (2nd edition). MrGRAW-Hill Inc, page120, 1959.

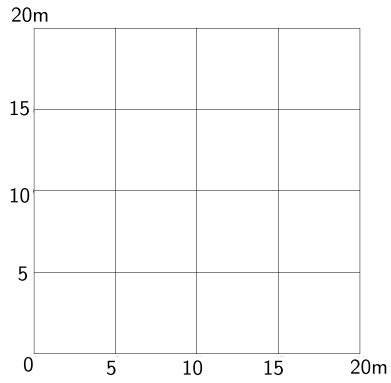


Figure 11.21: 27NodeBrick edge clamped square plate with element side length 5m.

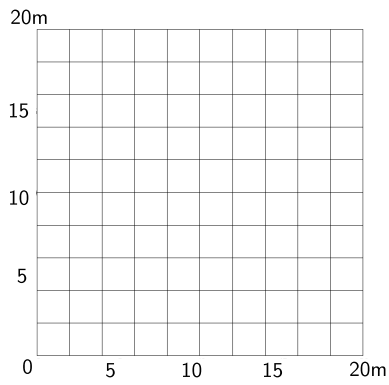


Figure 11.22: 27NodeBrick edge clamped square plate with element side length 2m.

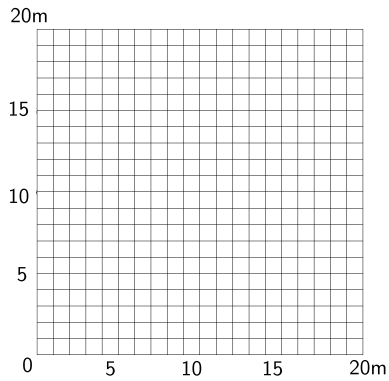


Figure 11.23: 27NodeBrick edge clamped square plate with element side length 1m.

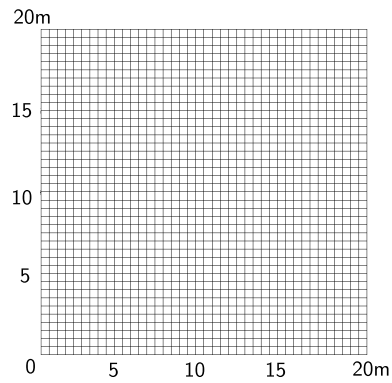


Figure 11.24: 27NodeBrick edge clamped square plate with element side length 0.5m.

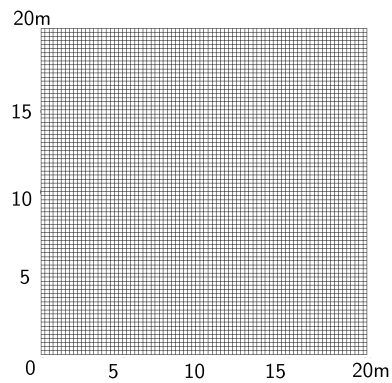


Figure 11.25: 27NodeBrick edge clamped square plate with element side length 0.25m.

Table 11.6: Results for 27NodeBrick square plate with four edges clamped.

Element type	27NodeBrick	27NodeBrick	27NodeBrick	Theoretical displacement
Number of layers	1layer	2layers	4layers	
Element side length	Height:1.00m	Height:0.50m	Height:0.25m	
10m	4.82E-004 m	4.82E-004 m	4.82E-004 m	2.20E-03 m
5m	1.97E-003 m	1.98E-003 m	1.98E-003 m	2.20E-03 m
2m	2.25E-003 m	2.26E-003 m	2.26E-003 m	2.20E-03 m
1m	2.28E-003 m	2.29E-003 m	2.29E-003 m	2.20E-03 m
0.5m	2.29E-003 m	2.30E-003 m	2.30E-003 m	2.20E-03 m
0.25m	2.29E-003 m	2.30E-003 m	-	2.20E-03 m

Table 11.7: Errors for 27NodeBrick square plate with four edges clamped.

Element type	27NodeBrick	27NodeBrick	27NodeBrick
Number of layers	1layer	2layers	4layers
Element side length	Height:1.00m	Height:0.50m	Height:0.25m
10m	78.11%	78.10%	78.10%
5m	10.67%	10.19%	10.16%
2m	2.23%	2.79%	2.83%
1m	3.56%	4.16%	4.22%
0.5m	3.96%	4.58%	4.65%
0.25m	4.08%	4.70%	-

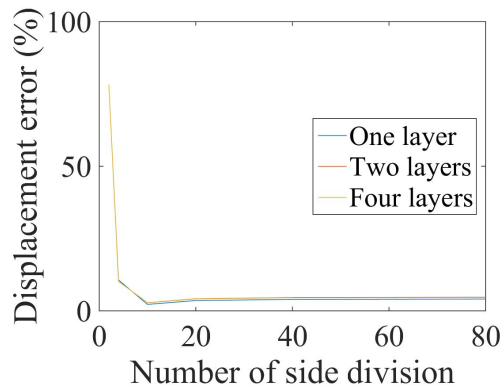


Figure 11.26: 27NodeBrick square plate with edge clamped' Displacement error versus Number of side division

Verification of 27NodeBrick circular plate with all edges simply supported

Problem description: Diameter=20m, Height=1m, Force=100N, $E=1E8Pa$, $\nu = 0.3$.

The four edges are simply supported.

The load is the uniform normal pressure on the whole plate.

The plate flexural rigidity is

$$D = \frac{Eh^3}{12(1-\nu^2)} = \frac{10^8 N/m^2 \times 1^3 m^3}{12 \times (1-0.3^2)} = 9.1575 \times 10^6 N \cdot m \quad (11.21)$$

The theoretical solution² is

$$d = \frac{(5+\nu)qa^4}{64(1+\nu)D} = \frac{(5+0.3) \times 100 N/m^2 \times 10^4 m^4}{64 \times (1+0.3) \times 9.1575 \times 10^6 N \cdot m} = 6.956 \times 10^{-3} m \quad (11.22)$$

The 27NodeBrick are shown in Figure (11.27) - (11.32).

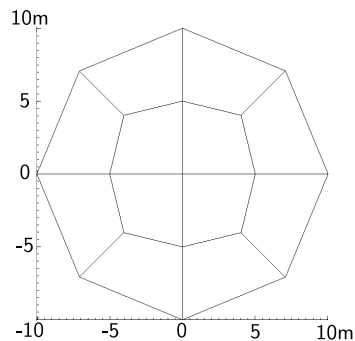


Figure 11.27: 27NodeBrick edge simply supported circular plate with element side length 10m.

The results are listed in Table (11.8).

The errors are listed in Table (11.9).

The errors are plotted in Figure (11.33).

The ESSI model fei files for the table above are here

²Stephen Timoshenko, Theory of plates and shells (2nd edition). MrGRAW-Hill Inc, page55, 1959.

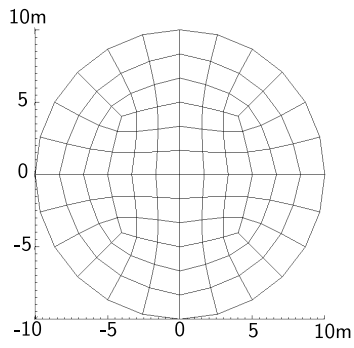


Figure 11.28: 27NodeBrick edge simply supported circular plate with element side length 5m.

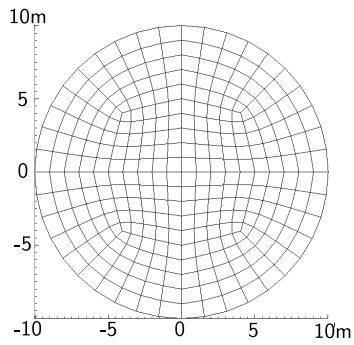


Figure 11.29: 27NodeBrick edge simply supported circular plate with element side length 2m.

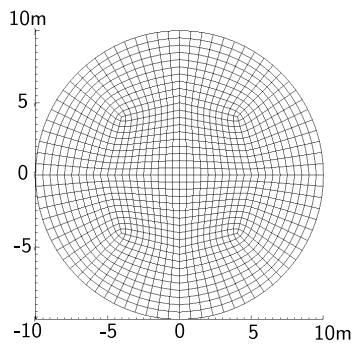


Figure 11.30: 27NodeBrick edge simply supported circular plate with element side length 1m.

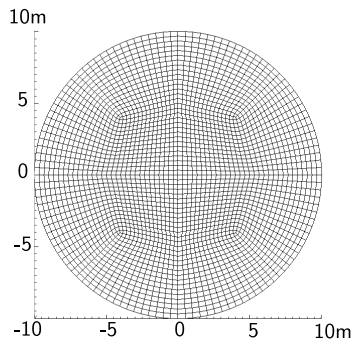


Figure 11.31: 27NodeBrick edge simply supported circular plate with element side length 0.5m.

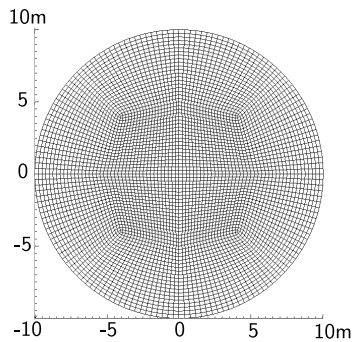


Figure 11.32: 27NodeBrick edge simply supported circular plate with element side length 0.25m.

Table 11.8: Results for 27NodeBrick circular plate with four edges simply supported.

Element type	27NodeBrick	27NodeBrick	Theoretical displacement
Number of layers	2layers	4layers	
Number of diameter divisions	Height:0.50m	Height:0.25m	
4	7.259E-03 m	7.261E-03 m	6.956E-03 m
12	7.083E-03 m	7.084E-03 m	6.956E-03 m
20	7.064E-03 m	7.065E-03 m	6.956E-03 m
40	7.018E-03 m	7.019E-03 m	6.956E-03 m
60	7.029E-03 m	7.030E-03 m	6.956E-03 m
80	7.032E-03 m	7.034E-03 m	6.956E-03 m

11.7 Verification and Validation for Static and Dynamic Behavior of Structural Elements

11.7.1 Verification of Shell (Felippa-ANDES) Finite Element Modeling and Simulation

Table 11.9: Errors for 27NodeBrick circular plate with four edges simply supported.

Element type	27NodeBrick	27NodeBrick
Number of layers	2layers	4layers
Number of diameter divisions	Height:0.50m	Height:0.25m
4	4.36%	4.38%
12	1.82%	1.83%
20	1.56%	1.57%
40	0.88%	0.90%
60	1.04%	1.06%
80	1.09%	1.11%

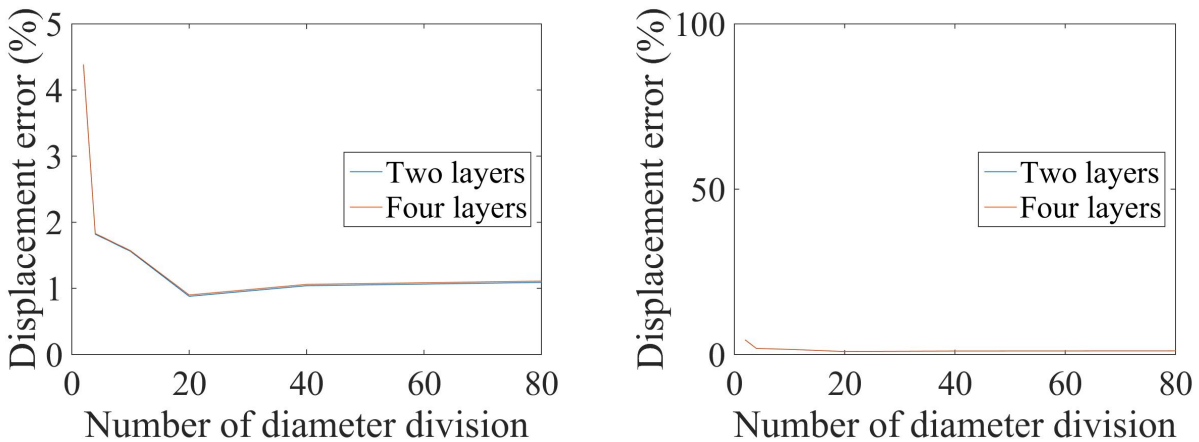


Figure 11.33: 27NodeBrick circular plate with edge simply supported Displacement error versus Number of side division, Left: error scale 0% - 5%, Right: Error scale 0% - 100%.

split up into several cases intended to test different aspects of the implementation. The tests are based on well-known closed form solutions to elasticity problems which can be modelled using shells. Further, the verification is divided into static and dynamic tests.

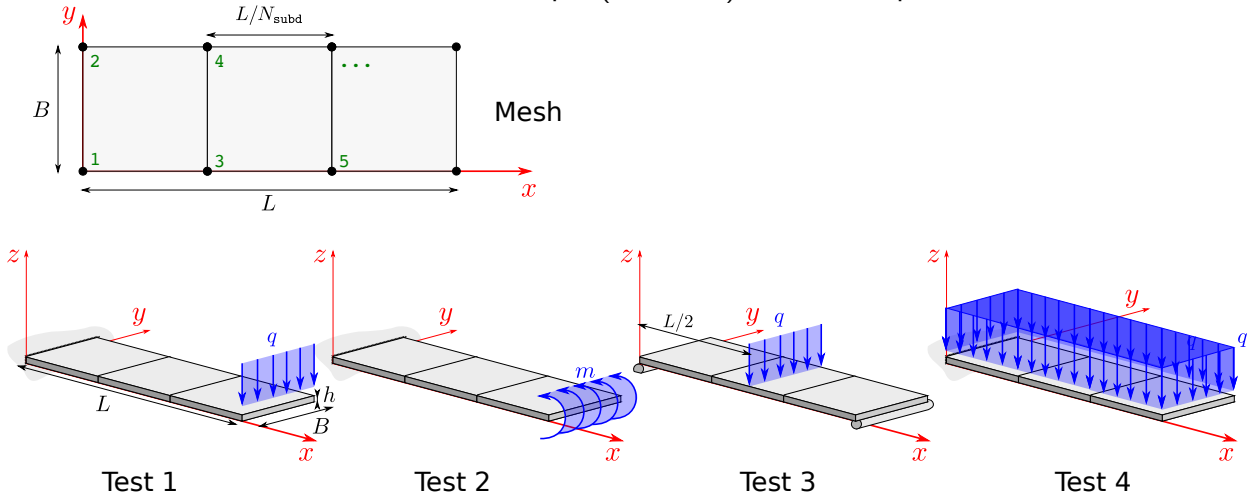
Static Tests

The purpose of the static tests is to verify that the stiffness matrices generated by the 4 Node ANDES Shell are useful to approximate well known cases of solutions to beam theory.

Tests are done to verify the bending component and the membrane component independently,

because the behavior of both is assumed de-coupled in this linear implementation.

Bending Component Verification These tests compare the bending performance of a simple mesh of ANDES shells for the case of simple (Bernoulli) beam examples.



Test 1: Concentrated transversal tip load For a prismatic beam made of a homogeneous elastic isotropic material of modulus of elasticity E , cross section I and length L we have that, under Bernoulli-Euler theory, the displacement at the tip due to a concentrated load P is

$$\delta_{\text{tip}} = \frac{PL^3}{3EI}$$

and for this test case's geometry

$$\delta_{\text{tip}} = \frac{qBL^3}{3EBh^3/12} = \frac{4qL^3}{Eh^3}$$

With the purpose of measuring the errors as percent agreement with the theoretical results, the load q is computed such that the tip displacement is 100 units. Thus, in terms of the geometry of the problem.

$$q = 100 \times \frac{Eh^3}{4L^3}$$

This force is translated into nodal equivalent forces by applying half the total load qB to each tip node in the vertical direction and fixing the x direction rotational degrees of freedom for the tip nodes.

The parameters chosen for this case are

```

1 h          = 1*m;          // Shell thickness
2 Eshell    = 1*N/m^2;      // Elastic modulus
3 nu        = 0.0;          // Poisson's ratio
4 L         = 1*m;          // Beam length
5 B         = 0.2*m;        // Beam width
6 rho       = 0*kg/m^3;    // Mass density

```

For different number of subdivisions, here are the results of the tip displacement.

N_{subd}	u_z	N_{subd}	u_z	N_{subd}	u_z
2	96.2118	42	100.009	83	100.002
7	100.096	48	100.007	89	100.002
13	100.068	54	100.006	95	100.002
19	100.039	60	100.005	101	100.002
25	100.024	66	100.004	107	100.001
31	100.016	72	100.003	112	100.001
37	100.012	77	100.003		

The element displays sensitivity to the aspect ratio of its sides. Indeed, choosing a different set of parameters

```

1 h          = 1*m;          // Shell thickness
2 Eshell    = 1*N/m^2;      // Elastic modulus
3 nu        = 0.0;          // Poisson's ratio
4 L         = 1*m;          // Beam length
5 B         = 0.2*m;        // Beam width
6 rho       = 0*kg/m^3;    // Mass density

```

yields slightly different results

N_{subd}	u_z	N_{subd}	u_z	N_{subd}	u_z
2	93.7897	42	99.9958	83	100.001
7	99.5267	48	99.998	89	100.001
13	99.8587	54	99.9993	95	100.001
19	99.9409	60	100.	101	100.001
25	99.9713	66	100.001	107	100.001
31	99.985	72	100.001	112	100.001
37	99.992	77	100.001		

Test 2: Concentrated tip moment Analogous to the previous test, for a cantilever beam with a tip moment the tip rotation is

$$\theta_{\text{tip}} = \frac{ML}{EI}$$

and for this test case's geometry

$$\theta_{\text{tip}} = \frac{mBL}{EBh^3/12} = \frac{12mL}{Eh^3}$$

In this case, the parameters are selected such that this tip rotation is of 100 units. Execution of the test case shows that with $N_{\text{subd}} = 2$ the theoretical value is met with 100% accuracy. This is because the moment field is constant inside the beam and the elements are capable of reproducing this field with accuracy.

Test 3: Concentrated mid-span transversal load This case is similar to test case 1. The accuracy for 2 elements is 96.2% agreement with the theoretical solution. For $N_{\text{subd}} = 4$ (4 elements total) the accuracy climbs to 99.7%. The test file for this case can be found in

Test 4: Transversal distributed load The distributed load is generated by accelerating the beam transversally with an acceleration which produces a 100 (unit) displacement. This provides an indirect test to the mass matrix which will be further tested in dynamic tests. The uniformly distributed load q which produces the δ_{tip} unit displacement and the corresponding tip rotation are

$$q = 8 \frac{EI}{L^4} \delta_{\text{tip}} \quad \text{and} \quad \theta_{y\text{tip}} = \frac{4}{3L} \delta_{\text{tip}}$$

from this value, the required acceleration is computed as

$$a = \frac{q}{\rho BH}$$

where ρ is the unit-weight of the material used to compute the mass matrix.

For two subdivisions (6 nodes) the results of the two nodes located at the tip of the beam are

```

1 Node : 5
2 ux = 0.000000, rx = 30.550500
3 uy = 0.000000, ry = -133.333000
4 uz = 102.541000, rz = 0.000000
5 Node : 6
6 ux = 0.000000, rx = -30.550500
7 uy = 0.000000, ry = -133.333000
8 uz = 102.541000, rz = 0.000000

```

First, a 2.5% accuracy is reached in the tip displacement. Second, it is noteworthy to mention that the current formulation of the mass matrix will produce rotations around the x axis for the nodes. One reason for this is that the chosen mass matrix is not consistent with the stiffness matrix instead, it is borrowed from a similar element^{3 4 5}. The reason behind this decision is the fact that the very accurate ANDES stiffness formulation lacks a displacement interpolation scheme which is necessary to produce a consistent mass matrix. Furthermore, restraining these x rotation degrees of freedom does not lead to an improved solution.

For 4 subdivisions, the results at the tip are:

```

1 Node : 9
2 ux = 0.000000, rx = 31.671000
3 uy = 0.000000, ry = -133.333000
4 uz = 100.891000, rz = 0.000000
5 Node : 10
6 ux = 0.000000, rx = -31.671000
7 uy = 0.000000, ry = -133.333000
8 uz = 100.891000, rz = 0.000000

```

and for 20.

```

1 Node : 41
2 ux = 0.000000, rx = 32.095800
3 uy = 0.000000, ry = -133.333000
4 uz = 100.039000, rz = 0.000000
5 Node : 42
6 ux = 0.000000, rx = -32.095800

```

³The First ANDES Elements: 9-DOF Plate Bending Triangles Carmello Militello & Carlos A. Felippa December 1989 Report No. CU-CSSC-89-22

⁴Chapter 32 of Felippa's Lecture Notes Finite element templates for bending

⁵C. A. Felippa and P. G. Bergan, A triangular plate bending element based on an energy-orthogonal free formulation, Comp. Meth. Appl. Mech. Engrg., 61, 129160, 1987.

```
7  uy =      0.000000, ry =   -133.333000
8  uz =     100.039000, rz =      0.000000
```

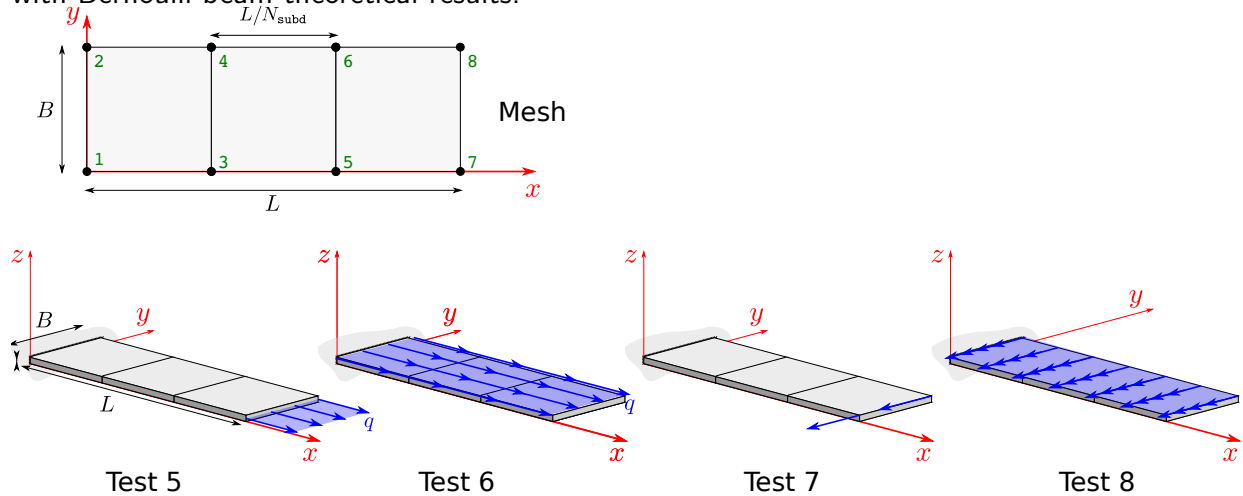
and back to 2 subdivisions but this time with an aspect ratio $L/B = 2$, by changing B so that the expected tip displacement remains the same, we get

```
1  Node : 5
2  ux =      0.000000, rx =      3.890200
3  uy =      0.000000, ry =   -133.333000
4  uz =     99.810100, rz =      0.000000
5  Node : 6
6  ux =      0.000000, rx =     -3.890200
7  uy =      0.000000, ry =   -133.333000
8  uz =     99.810100, rz =      0.000000
```

which shows that the effect of the inconsistent mass matrix is ameliorated for elements with a better aspect ratio. The elements in this case are square in shape since $L/B = 2$ and $N_{\text{subd}} = 2$.

In conclusion increasing accuracy for bending problems not only involves making the elements smaller but also improving their aspect ratio. This is especially critical in dynamic problems (or self weight problems).

Membrane Component Verification These tests compare the performance of the membrane component of the ANDES Shell by modelling simple beams and comparing the approximation with Bernoulli-beam theoretical results.



Test 5: Longitudinal tip load The parameters used to test this case are,

```

1 h = 0.2*m; // Shell thickness
2 Eshell = 1*N/m^2; // Elastic modulus
3 nu = 0.0; // Poisson's ratio
4 L = 30*m; // Beam length
5 B = 3*m; // Beam width
6 rho = 0.0*kg/m^3; // Mass density
7 delta_tip = 100*m; // Target tip displacement
8
9 Nsubd = 2; // Number of side subdivisions

```

the tip load was computed to give $\delta_{\text{tip}} = 100$ from

$$F_{\text{tip}} = \frac{AE}{L} \delta_{\text{tip}}$$

Additionally, the tip rotation degrees of freedom about z axis (rz) are fixed to enforce the uniform loading condition. The results for 2 subdivisions observed at the two tip nodes is

```

1 Node : 5
2 ux = 100.000000, rx = 0.000000
3 uy = -0.000000, ry = 0.000000
4 uz = 0.000000, rz = 0.000000
5 Node : 6
6 ux = 100.000000, rx = 0.000000
7 uy = -0.000000, ry = 0.000000
8 uz = 0.000000, rz = 0.000000

```

Test 6: Longitudinal self-weight load As in test 4, the distributed load for this test was generated by using an acceleration field with a magnitude such that it generates 100 units of displacement in dof u_x . The required body force q (per unit length) is derived from linear elasticity to be

$$q = \frac{2EA}{L^2} \delta_{\text{tip}}$$

from which the acceleration is found to be given by $a = \frac{q}{\rho BH}$. The tip nodes are fixed to move only in the x direction. The model parameters used for this test are,

```

1 h = 1*m; // Shell thickness
2 Eshell = 1*N/m^2; // Elastic modulus
3 nu = 0.0; // Poisson's ratio
4 L = 1*m; // Beam length
5 B = 1*m; // Beam width
6 rho = 100*kg/m^3; // Mass density
7 delta_tip = 100*m; // Target tip displacement
8
9 Nsubd = 2; // Number of side subdivisions

```

and the tip displacements

```

1 Node : 5
2 ux = 100.000000, rx = 0.000000
3 uy = 0.000000, ry = 0.000000
4 uz = 0.000000, rz = 0.000000
5 Node : 6
6 ux = 100.000000, rx = 0.000000
7 uy = 0.000000, ry = 0.000000
8 uz = 0.000000, rz = 0.000000

```

Which means that in the quadratic displacement field coming from a uniform external load can be captured exactly by this element.

Test 7: Transversal tip load This test is identical to test 1, except the beam mesh is placed sideways so that the membrane component is used instead of the bending one. Since the membrane part can capture deformation due to shear, the ratio L/B is set to 10 so that this does not affect the results.

```

1 h = 0.2*m; // Shell thickness
2 Eshell = 1*N/m^2; // Elastic modulus

```

```

3 nu    = 0.0;    // Poisson's ratio
4 L     = 10*m;   // Beam length
5 B     = 1.0*m;   // Beam height
6 rho   = 0*kg/m^3; // Mass density
7 d_tip = 100*m;  // Target tip displacement
8
9 Nsubd  = 10;    // Number of side subdivisions

```

Results at the tip show less than 1% error with theoretical results when shear component is made small.

```

1 Node : 21
2 ux =   -7.513920, rx =    0.000000
3 uy =  -100.650000, ry =    0.000000
4 uz =    0.000000, rz =   -15.072400
5 Node : 22
6 ux =    7.513920, rx =    0.000000
7 uy =  -100.650000, ry =    0.000000
8 uz =    0.000000, rz =   -15.072400

```

It would be interesting to test this component vs. a beam theory which incorporates deformation due to shear such as Timoshenko beams.

Test 8: Transversal self-weight load This test is analogous to test 4, except the membrane component is being tested instead of the bending. Again, the L/B ratio is kept at 10 to avoid shear deformation creeping into the results perceptively.

```

1 h     = 1*m;    // Shell thickness
2 Eshell = 1*N/m^2; // Elastic modulus
3 nu    = 0.0;    // Poisson's ratio
4 L     = 10*m;   // Beam length
5 B     = 0.5*m;   // Beam width
6 rho   = 100*kg/m^3; // Mass density
7 delta_tip = 100*m; // Target tip displacement
8
9 Nsubd  = 10;    // Number of side subdivisions

```

Displacement results at the tip nodes show less than 1% error when compared to Bernoulli beam theory.

```

1 Node : 21
2 ux =    3.325110, rx =    0.000000
3 uy =   99.780900, ry =    0.000000
4 uz =    0.000000, rz =   13.301200

```

```
5 Node : 22
6 ux = -3.325110, rx = 0.000000
7 uy = 99.780900, ry = 0.000000
8 uz = 0.000000, rz = 13.301200
```

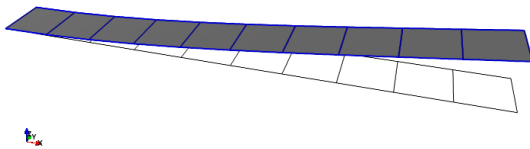
Dynamic Tests

The purpose of the dynamic tests is to verify that the mass matrix adopted for these elements (which is not consistent with the stiffness) is adequate for Dynamic analysis. Also tested herein are the geometric transformations.

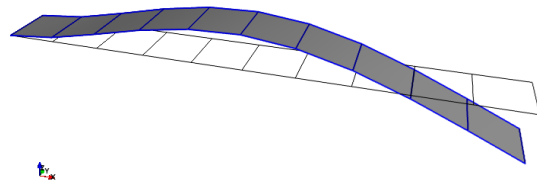
Again, the tests are divided into bending and membrane components which are tested independently. Also, an eigenvalue analysis is performed to verify accordance with theoretical results for continuous Bernoulli beams. Finally, geometric transformations are tested by performing an eigenvalue analysis for the same (unrestrained) beam in different orientations (pitch, yaw and roll) which should have invariant eigenvalues.

Bending Component

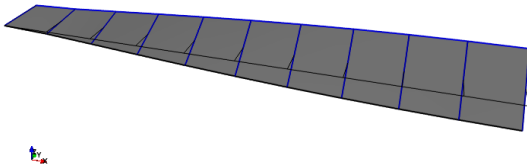
Mode 1, $T = 0.999959s$



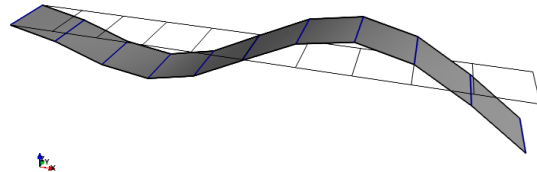
Mode 2, $T = 0.159539s$



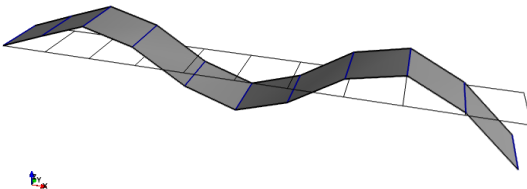
Mode 3, $T = 0.0858275s$



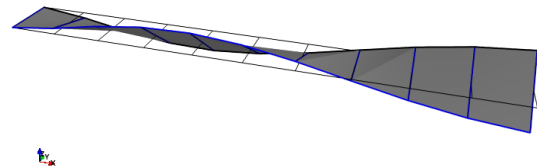
Mode 4, $T = 0.0569888s$



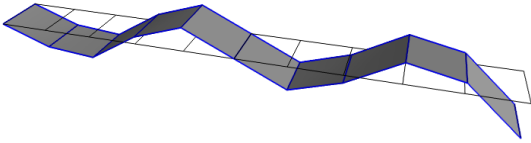
Mode 5, $T = 0.0291146s$



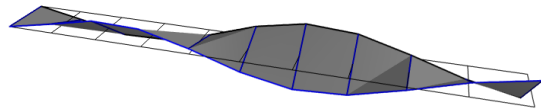
Mode 6, $T = 0.027886s$



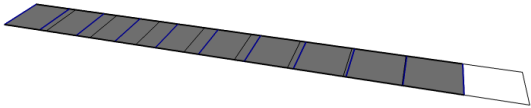
Mode 7, $T = 0.0176583s$



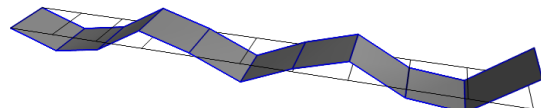
Mode 8, $T = 0.015962s$



Mode 9, $T = 0.0129099s$

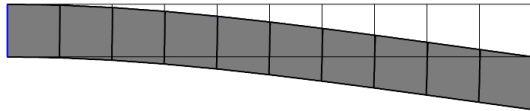


Mode 10, $T = 0.0118701s$

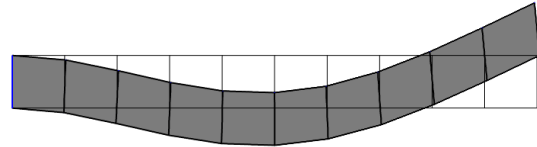


Membrane Component

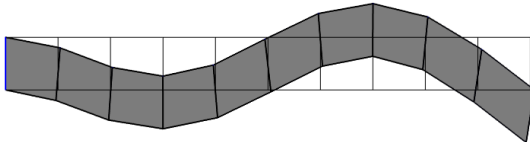
Mode 1, $T = 0.998022s$



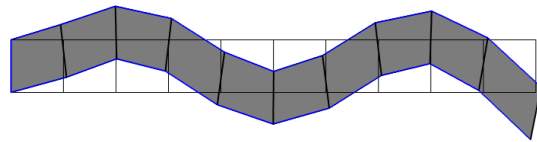
Mode 2, $T = 0.15862s$



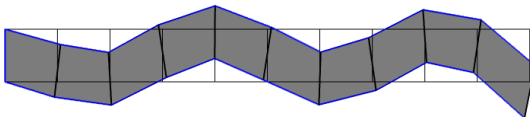
Mode 3, $T = 0.0564893s$



Mode 4, $T = 0.0287508s$

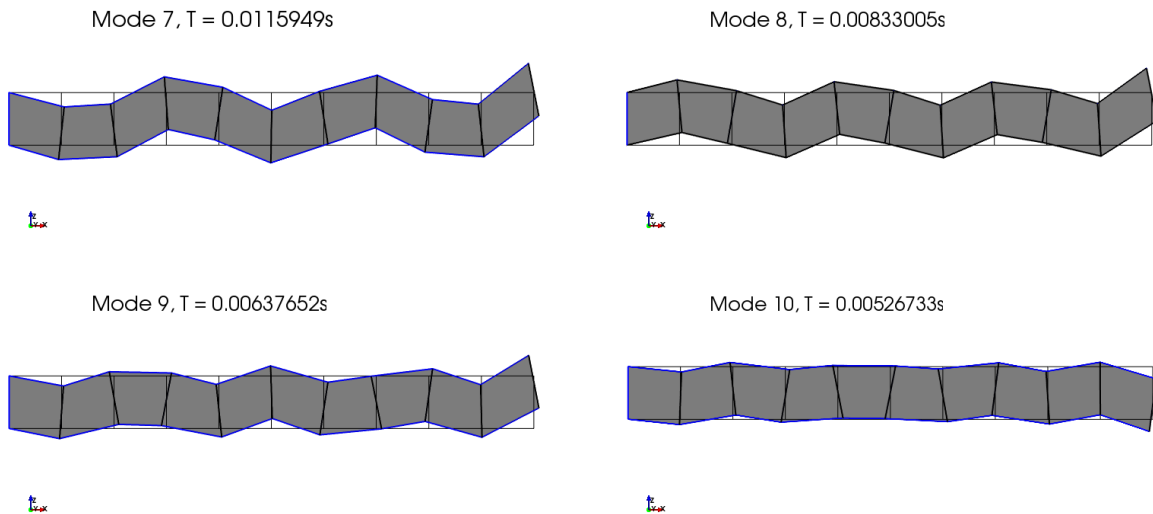


Mode 5, $T = 0.0173475s$



Mode 6, $T = 0.0129099s$





11.8 Verification and Validation for Static and Dynamic Behavior of Special Elements

11.8.1 Verification of Static and Dynamic Contact Element Modeling and Simulation

Solution verification of the contact element formulation and its implementation is presented in what follows. Analytical simple solutions for the frictional contact element are used to verify numerical solutions obtained by application of the developed model. The examples provided show the response of the contact element in several situations. Initially, the element is tested by connecting two nodes that each have $3dof$, subsequently, the element is even implemented to simulate a contact between two nodes that each have $7dof$ and two nodes with different dofs: $3dof$ for the first one and $7dof$ for the second one.

The parameters used for the contact element are listed in Table 11.10.

Truss Examples

The first example (Figure 11.35) represents five nodes: 1,2,3,4,5. Nodes 2,3,4,5 are connected by three truss elements and a contact element links node 1 and 2. All degrees of freedom

Parameter	Value
C_N [kN/m]	10420
\bar{v}_{max} [m]	0.001
K_T [kN/m]	1e7
μ [-]	0.6

Table 11.10: Contact element parameters.

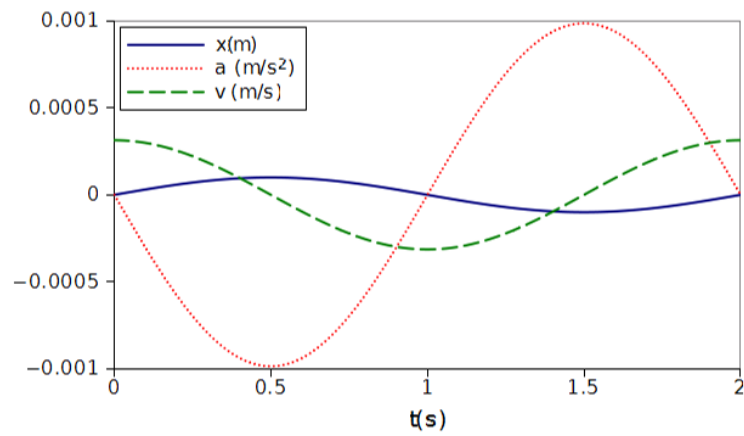


Figure 11.34: Input signal: time history of displacement, acceleration and velocity.

of nodes 1,3,4,5 are fixed, whereas a sine wave displacement time-history (Figure 11.34) is applied to node 2 along x direction and the normal force acting within the contact element is recorded. The results, represented in Figure 11.36, show the normal response of this new contact element. As the time-step decreases, the force-displacement curves tends to be similar to the one represented by (6.4).

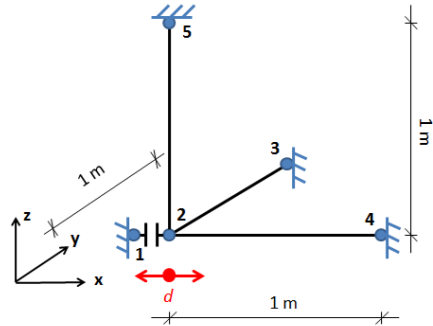


Figure 11.35: System composed of one contact element and three truss elements. A sine wave displacement time-history is applied to node (2).

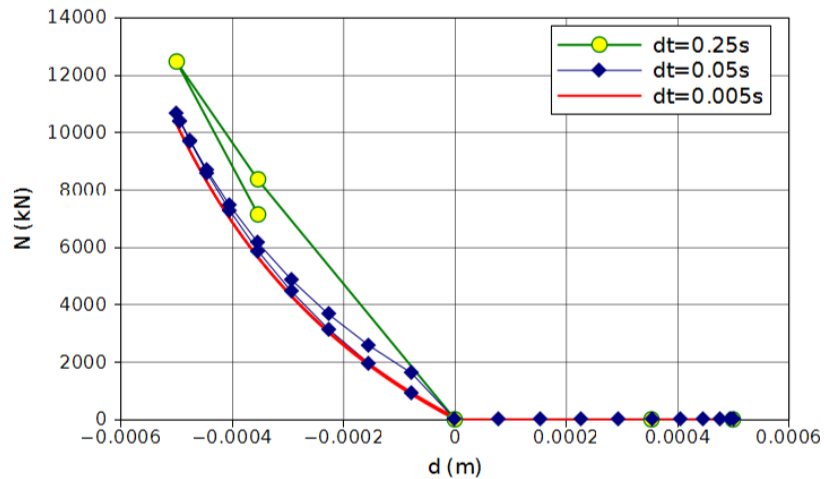


Figure 11.36: Normal force vs normal-relative displacement in contact element.

The second example (Figure 11.37) shows the tangential response of this new contact element. The geometry of the problem is the same as Figure 11.35, but an axial force ($p = 1140$

kN), constant in time, and a sine wave time-history displacement are applied to node 2. The results, represented in Figure 11.38, show that the response is not dependent on the time-step used for the analysis. Due to the elastic-perfectly-plastic behavior, associated with Mohr-Coulomb yield criteria, the maximum shear force (t_{max}) that the contact element can sustain is 684 kN, equal to $t_{max} = \mu \cdot p = 0.6 \cdot 1140kN$.

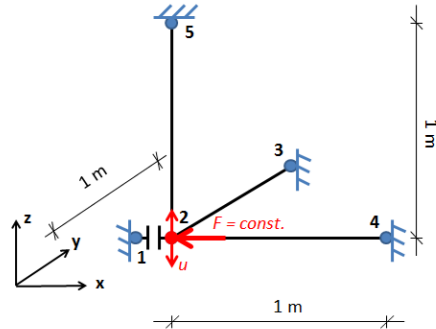


Figure 11.37: Same system used in Figure 11.35. A normal force constant in time ($F = 1140$ kN) and a sine wave displacement time history are applied to node (2).

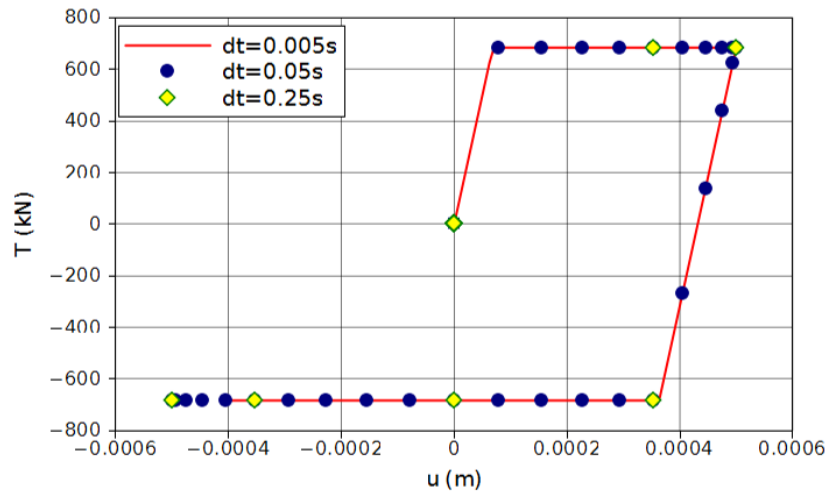


Figure 11.38: $p = 1140$ kN. Transversal force in the contact element vs transversal-relative displacement

Single Brick Element Examples

The contact element is now used to connect each node (5, 6, 7, 8) of the bottom face of an eight node hexahedral element (hex8) to the corresponding node attached to the ground (1, 2, 3, 4).

A linear elastic constitutive model is used for the eight node brick and the parameters are listed in Table 11.11.

Parameter	Value
E [kPa]	1.5e10
ν [-]	0.0

Table 11.11: Brick Element Parameters

In the first example (Figure 11.39) the time-history displacement, shown in Figure 8.2, is applied in the vertical direction to each node of the top surface of the brick element (9, 10, 11, 12) and the time-history normal force induced in each contact element is represented in Figure 11.40. It is worth noting that the normal force is positive if the displacement of the top surface is downward, whereas it is zero if the detachment occurs caused by the upward movement.

Through the second example, shown in Figure 11.41, the transversal response of the contact elements is highlighted. The vertical normal force ($F_v = 50kN$), constant in time, and a horizontal time-history displacement are applied to each node of the top surface and the transversal response is shown in Figure 11.42. As stated in section 11.8.1, the maximum shear force that the contact element can sustain is 30 kN , equal to $t_{max} = \mu \cdot p = 0.6 \cdot 50kN$.

The third example is focused on the transversal response of the contact element under variable normal forces. In fact, a sine wave time-history horizontal displacement and a vertical force are applied to each node of the top surface of the brick. The normal force is variable in time according to the factor ($Fact(t)$) shown in Figure 11.44 and the vertical force is computed as $F_v(t) = Fact(t) \cdot F_{v,max}$, and $F_{v,max}$ equal to 50 kN. The response of the contact element, shown in Figure 11.45, is independent of the time-step used for the analysis emphasizing the correct numerical implementation.

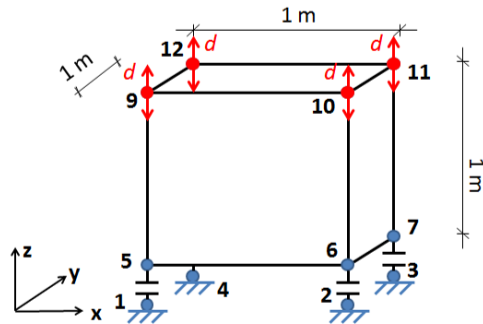


Figure 11.39: Eight-node brick element over four contact elements. A sine wave time-history vertical displacement applied to each node of the top surface.

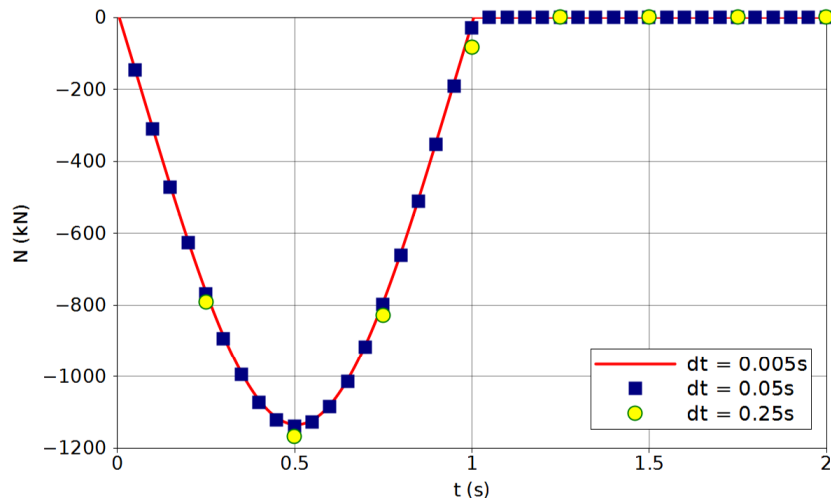


Figure 11.40: Normal force vs time in each contact element.

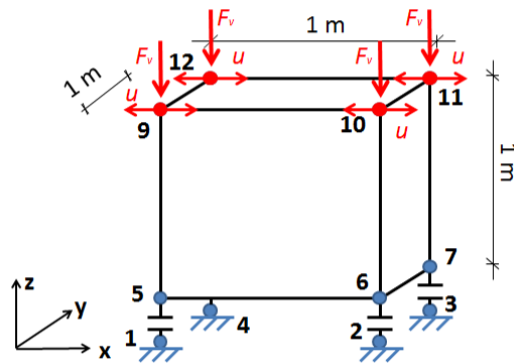


Figure 11.41: Eight-node brick element over four contact elements. $F_v = 50$ kN and a sine wave time-history horizontal displacement applied to each node of the top surface.

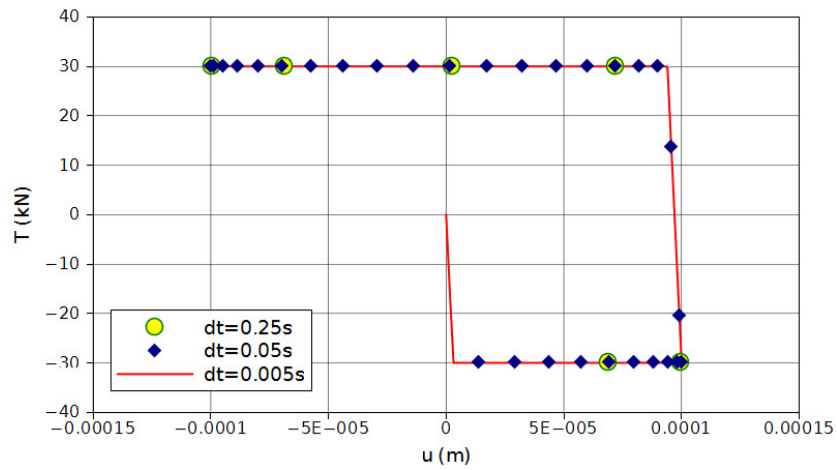


Figure 11.42: Transversal force vs transversal relative-displacement in the contact element with normal force F equal to 50 kN.

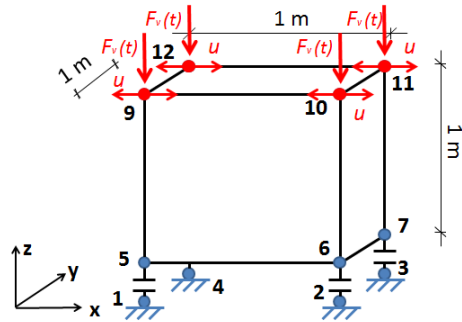


Figure 11.43: Eight-node brick element over four contact elements. Variable vertical force ($F_v(t)$) and a sine wave time-history horizontal displacement applied to each node of the top surface.

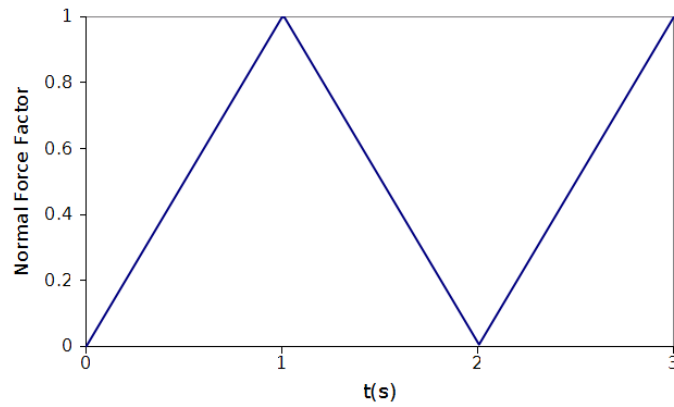


Figure 11.44: Time-history of the normal force factor $Fact(t)$.

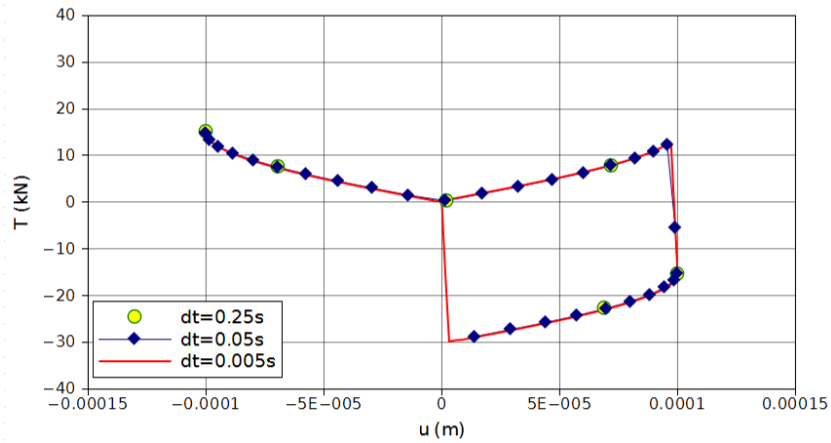


Figure 11.45: Variable normal force. Transversal force vs transversal relative-displacement in each contact element.

Double Brick Element Examples

Few other examples are produced taking in consideration two brick elements. The constitutive model used for these two brick elements is linear elastic with the same parameters listed in Table 11.11. Vertical and horizontal time-history displacement are applied to the top surface, shown in Figure 11.46 and Figure 11.47, and variable vertical forces are considered in the example represented in Figure 11.48. The results are the same shown in Figure 11.40, Figure 11.42 and Figure 11.43.

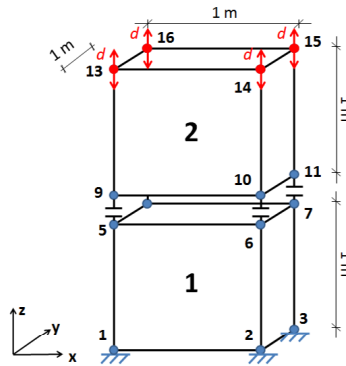


Figure 11.46: Two eight-node brick elements connected by four contact elements. Vertical time-history displacement applied to the nodes of the top surface.

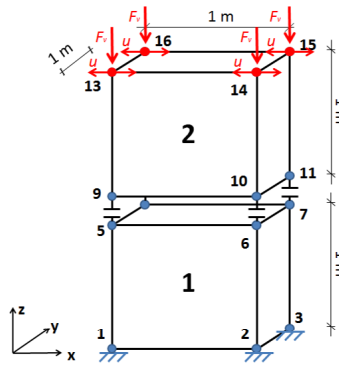


Figure 11.47: Two eight-node brick elements connected by four contact elements. Vertical force, equal to 50 kN and constant in time, and horizontal time-history displacement applied to the nodes of the top surface.

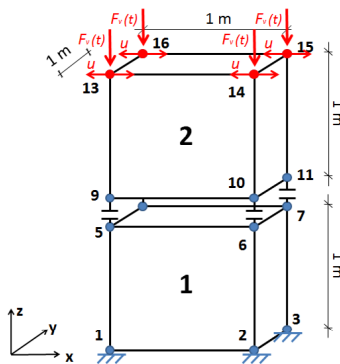


Figure 11.48: Two eight-node brick elements connected by four contact elements. Vertical force, variable in time, and horizontal time-history displacement applied to the nodes of the top surface.

11.8.2 Verification of Static and Dynamic Coupled (Saturated) Contact Element Modeling and Simulation

Dry u-p-U Contact to the ground

A single brick $u-p-U$ finite element is used to model an oedometer compression shown in Figure 11.49. Horizontal displacements and pore pressure are fixed in each node in order to guarantee the one-dimensional and dry conditions. As the ground is modeled as an un-deformable and impermeable layer (1,2,3,4), vertical soil and fluid displacements are fixed. The time-history displacement, shown in Figure 8.2, is applied in vertical direction to each node of the top surface (9,10,11,12).

The time-history normal force induced in each contact element is represented in Figure 11.40 and compared with the one obtained with the dry brick element with u formulation, shown in Figure 11.39. It is worth noting that the normal force patterns are perfectly overlapped: this is due to the fact that excess pore pressure is fixed to zero and the oedometer stiffness are the same in the two cases.

Parameter	Symbol	Value
Young's Modulus	E [kPa]	$1.5 \cdot 10^{10}$
Poisson ratio	ν [-]	0.0
Solid particle bulk modulus	K_s [kPa]	$3.6 \cdot 10^7$
Fluid bulk modulus	K_f [kPa]	$2.17 \cdot 10^6$
Solid density	ρ_s [Mg/m ³]	2.7
Fluid density	ρ_f [Mg/m ³]	1.0
Porosity	n [-]	$1.0 \cdot 10^{-8}$
Darcy permeability	K [m/s]	$1.0 \cdot 10^3$

Table 11.12: Soil parameters.

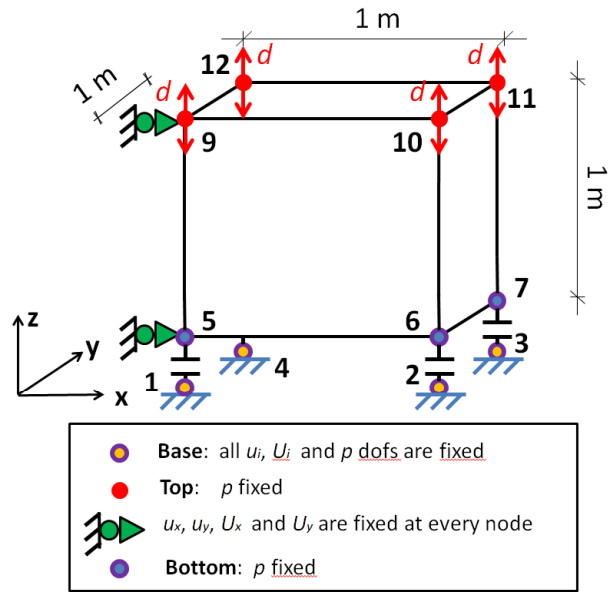


Figure 11.49: Single eight-node brick element. The nodes of the bottom surface are connected to the ground floor through contact elements. Vertical time-history displacement applied to the nodes of the top surface.

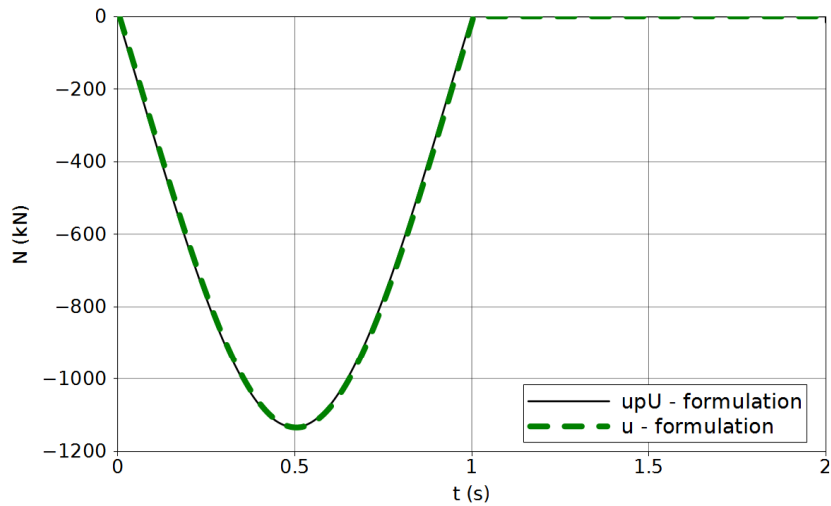


Figure 11.50: Normal force vs time in each contact element. *u-formulation* represents the results shown in Figure 11.40 whereas *upU-formulation* represents the results obtained through the model shown in Figure 11.49.

11.9 Verification and Validation for Coupled, Porous Solid – Pore Fluid Problems

Full verification and validation of coupled finite element modeling is given in our very recent papers and Tasiopoulou et al. (2015a) and Tasiopoulou et al. (2015b) and will not be detailed here.

11.10 Verification and Validation for Seismic Wave Propagation Problems

Verification of seismic wave propagation is split into two main components:

- Verification of wave propagation through discrete finite element mesh,
- Verification of seismic wave input into finite element models.

Validation of seismic wave propagation relies on carefully documented seismic events. One such example will be shown, from a Lotung seismic array, using an earthquake from 1986.

11.10.1 Verification of the Seismic Input (Domain Reduction Method) for 3D, Inclined Seismic Wave Fields

Inclined, 3D Seismic Waves in a Free Field

In this section verification of the 3D wave propagation problem using Domain Reduction Method will be studied. In order to do so, a finite element model with dimensions of $10000m \times 50m \times 5000m$ is considered. Two cases are studied here with the source of motion (fault) to be located at $(x = 3000m, y = 0, z = 3000m)$ and $(x = 3000m, y = 0, z = 3000m)$. Figures (11.51) and (11.52) show these two models respectively.

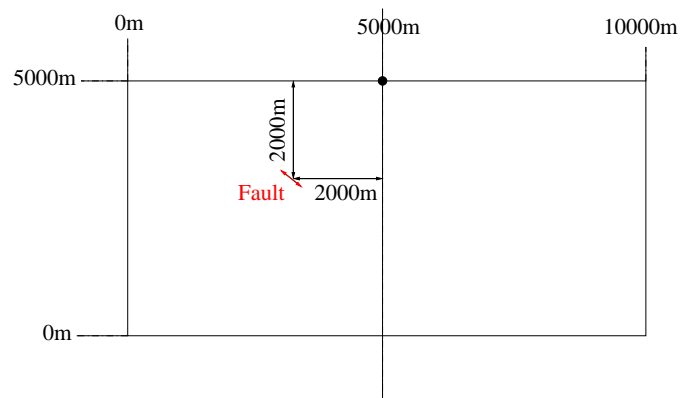


Figure 11.51: Domain to be analyzed for the 1st stage of DRM with fault located at an angle of 45° with respect to the top middle point of the model

The size of the elements is chosen to be $50m$ in all directions for both cases in order to reduce the computational time. The soil parameters are: shear wave velocity of $700m/s$, density of $1800kg/m^3$, and Poisson's ration of 0.1. Analyses for the fault slip model are done by applying the motion at the nodes of one element. This is done in order to represent the the wave propagation starting from the fault using Multiple Support Excitation. This is representing the first stage of analysis of DRM in which a big model including the fault is considered for free field case in order to obtain the required motions for DRM layer. For simulating the second stage of DRM, a smaller model with dimensions of $240m \times 5m \times 70m$ is considered as shown in Figure (11.53). The size of the plastic bowl is $200m \times 5m \times 50m$. Size of the elements for this model is chosen to be $5m$.

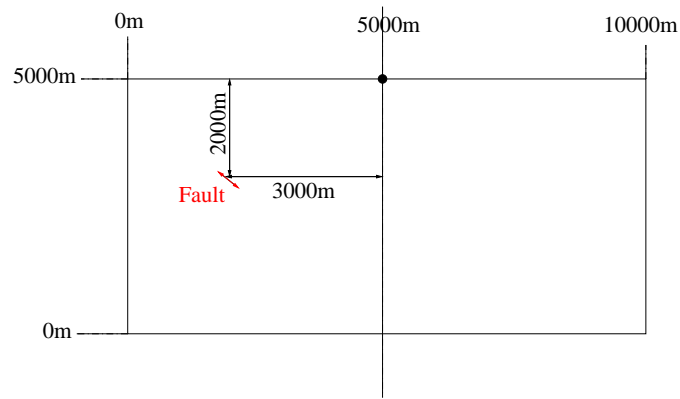


Figure 11.52: Domain to be analyzed for the 1st stage of DRM with fault located at an angle of 34° with respect to the top middle point of the model

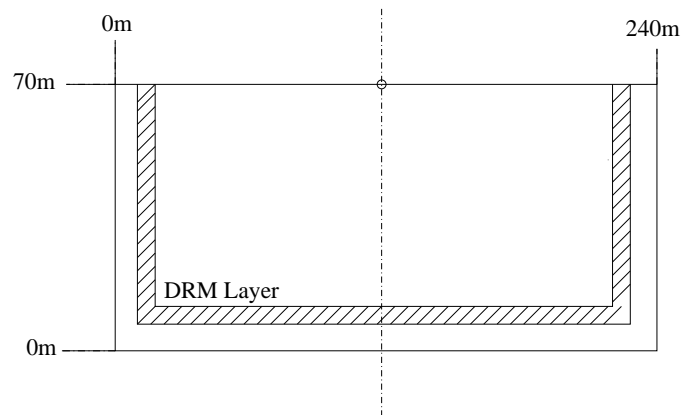


Figure 11.53: Domain to be analyzed for the 2nd analysis stage of DRM with smaller size comparing to the original model

Displacement and acceleration time histories of corresponding nodes of DRM layer are obtained by interpolating between the the results obtained from the first model. These displacement and accelerations are used to calculate the effective forces as an input for DRM analysis. Input motions to be used here are Ricker wave, Morgan Hill, and Kocaeli earthquakes. The maximum allowable frequency to be propagated through this model can be calculated based on Equation (11.23):

$$\Delta h \leq \lambda/10 = V_s/(10 f_{max}) \quad (11.23)$$

Based on the shear wave velocity of $700m/s$ and element size of $50m$, maximum allowable frequency to be propagated through this model would be $1.4Hz$ for the original model and based on element size of $5m$ would be $14Hz$ for the DRM model.

Ricker Wavelets Figure (11.54) show the displacement time history and FFT of Ricker wave of 2^{nd} order with dominant frequency of $1Hz$ and maximum amplitude occurring at 1 second.

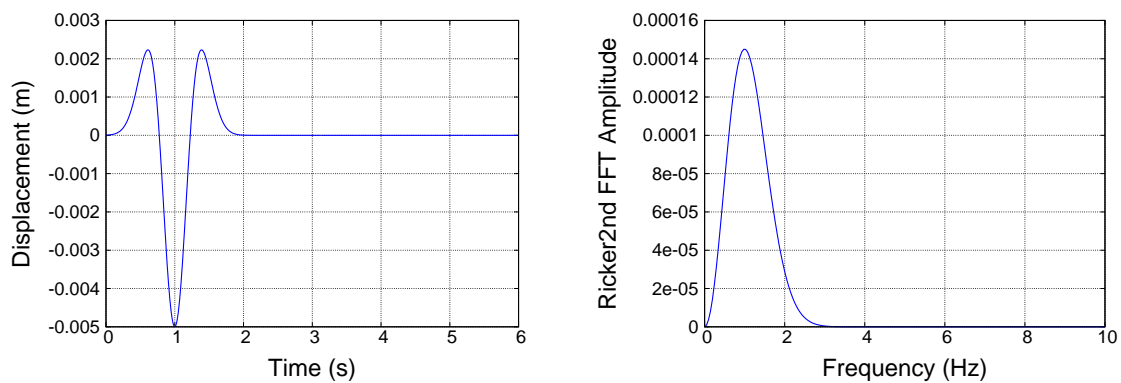


Figure 11.54: Displacement time history and FFT of Ricker wave with dominant frequency of $1Hz$

The first case to be studied here is the one with the fault source located at $(x = 3000m, y = 0, z = 3000m)$ which has the angle of 45° with respect to the top middle point of the model. Results to be discussed here are comparison of displacement and acceleration time histories at the top middle point of the model $(x = 5000m, y = 0, z = 5000m)$ between the fault slip and

DRM models. Comparison of displacement time histories in X and Z directions are shown in Figure (11.55). As it can be observed, the results of DRM model matches perfectly with the ones obtained from the fault slip model.

Figure (11.57) is the displacement and acceleration time history of a point located outside of DRM layer in X direction ($x = 10m, y = 0, z = 40m$). As mentioned before in definition of DRM, no motion should come out of the DRM layer in case of free field. As shown in these figures, displacement and acceleration time histories at this point are zero which verifies this fact.

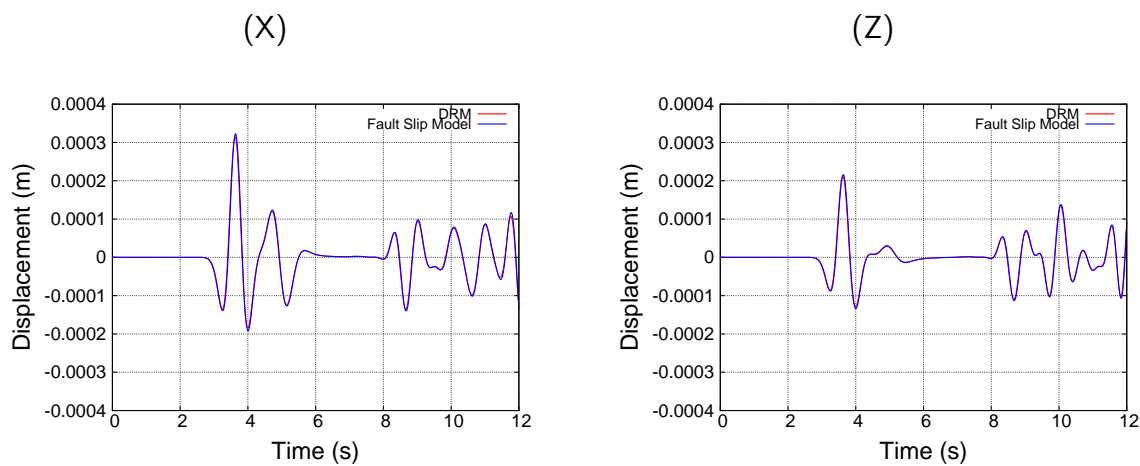


Figure 11.55: Comparison of displacements for top middle point using Ricker wave ($f = 1Hz$) as an input motion

The same motion is applied to the model with fault source located at ($x = 2000m, y = 0, z = 3000m$) which has the angle of 34° with respect to the top middle point of the model. Displacement time histories of the top middle point show the perfect match between results obtained from fault slip model with the ones obtained from DRM mode.

As shown in Figure (11.59), the second motion to be used for analysis is Ricker wave with frequency of $0.5Hz$ and maximum amplitude occurring at 3 seconds. Figure (11.60) shows the displacement time histories of X and Z directions for the same point as before ($x = 5000m, y = 0, z = 5000m$). As it is shown, results of the fault slip and DRM model are the same which verifies the solution from DRM formulation for this motion as well.

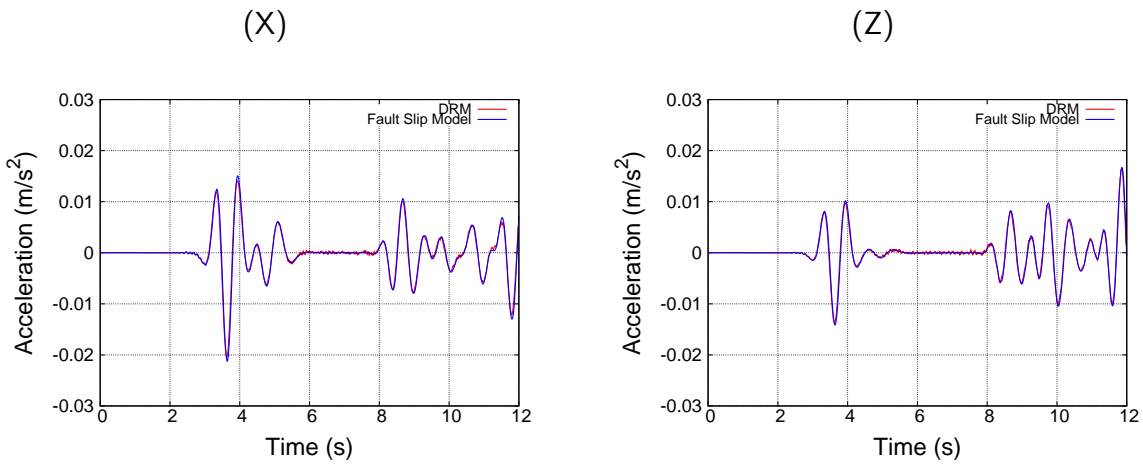


Figure 11.56: Comparison of accelerations for top middle point using Ricker wave ($f = 1Hz$) as an input motion

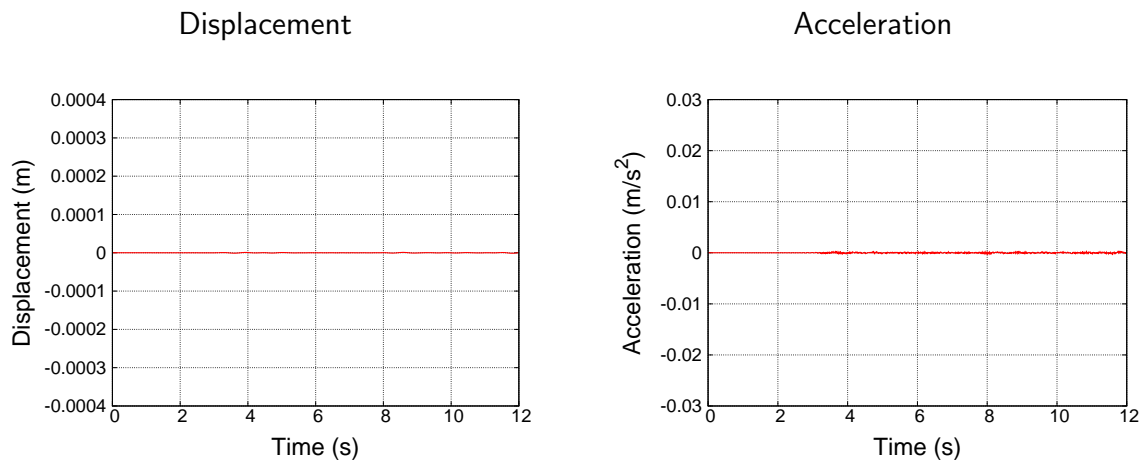


Figure 11.57: Displacement and acceleration time history for a point outside of DRM layer in (x) direction

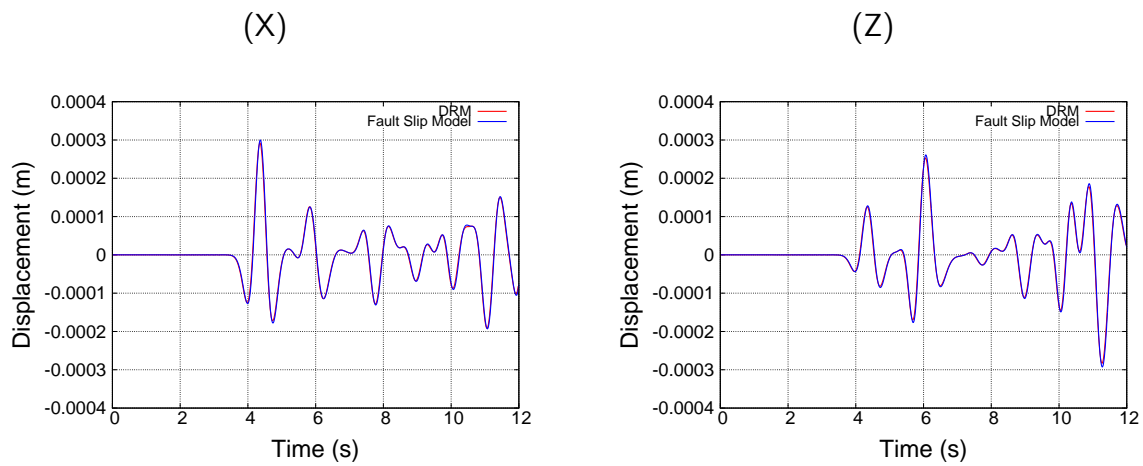


Figure 11.58: Comparison of displacements for top middle point using Ricker wave ($f = 1Hz$) as an input motion

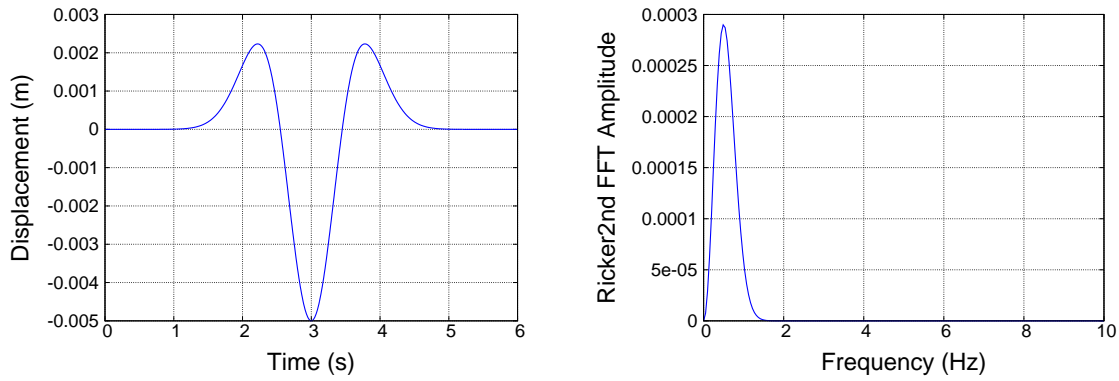


Figure 11.59: Displacement time history and FFT of Ricker wave with dominant frequency of $0.5Hz$

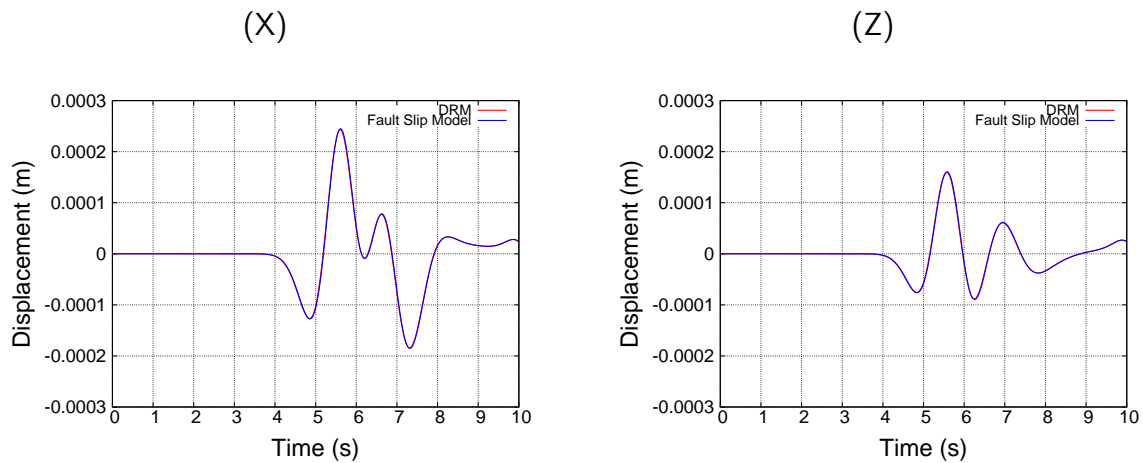


Figure 11.60: Comparison of displacements for top middle point using Ricker wave ($f = 0.5Hz$) as an input motion

The third motion to be used is Ricker wave with frequency of $2Hz$ and maximum amplitude happening at 1 second as shown in Figure (11.61). Comparison of displacement time histories between the fault slip and DRM model has been done and shown in Figure (11.62) along X and Z directions respectively.

In this case, results do not match for the top middle point of the model. The main reason is due to the frequency of the motion. The maximum allowable frequency to be propagated in the fault slip model is $1.4Hz$ while it is $14Hz$ in DRM model. Dominant frequency of the Ricker wave as input motion is $2Hz$. Frequencies above the $1.4Hz$ can not be propagated in the fault slip model while they will propagate in the DRM model. this can change the characteristics of the motion propagating through the model and is the main reason of differences between the obtained results.

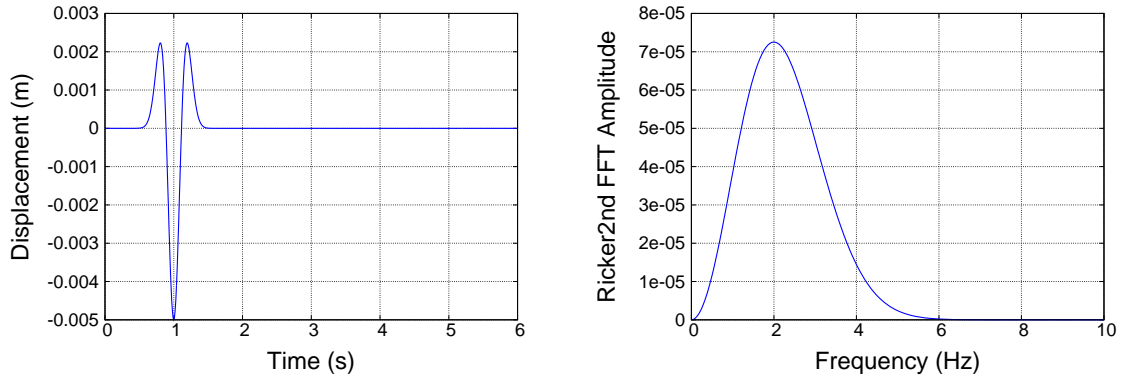


Figure 11.61: Displacement time history and FFT of Ricker wave with dominant frequency of $2Hz$

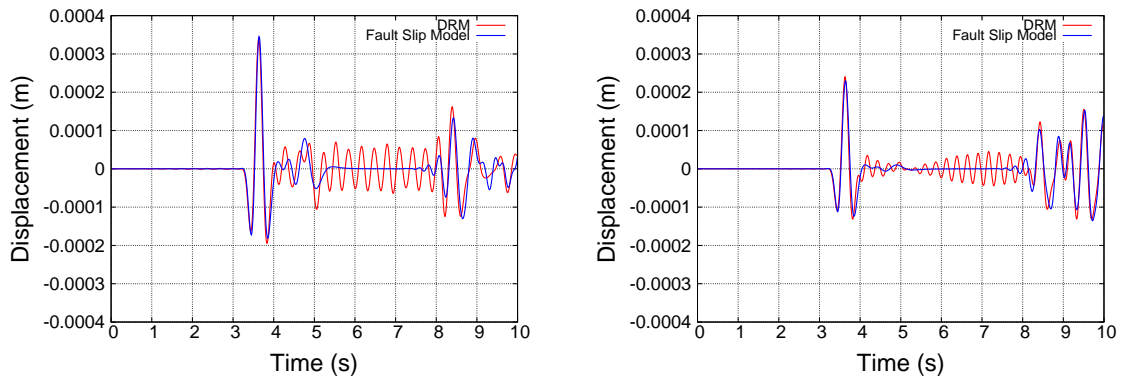


Figure 11.62: Comparison of displacements for top middle point in X and Z direction using Ricker wave ($f = 2Hz$) as an input motion.

11.10.2 Validation: Lotung Large Scale Seismic Test (LLSST) Earthquake 07

Presented here is validation of seismic wave propagation using data from an earthquake that was recorded at Lotung site in 1986. To date, this is only recorded earthquake which featured only two horizontal components, while the vertical component was very small. Validation is done using 1D data, which is actually wrong as soil has seen a full 2D set of motions, however this seismic event is used in every validation presentation. The purpose of using this example here is to show that modeling of this (famous) 2D motion earthquake, in 1D only is possible using Pisano model. However, it is noted, that despite good (excellent) matching of data and simulations, there is still an unresolved question of actual earthquake featuring 2D motions, while only 1D motions are used. This is particularly important as modeling is done using nonlinear/inelastic material, for which principle of superposition does not apply.

Introduction

Figure 11.63 shows the G/G_{max} and Damping data used for Pisano model.

Input motion and input method

We use the data from Lotung Large Scale Seismic Test (LLSST) which is operated by TaiPower and IES during the period from 1985 to 1990. We choose event 07 to validate modeling.

Results

Results present comparison of recorded and simulated motions at different depths.

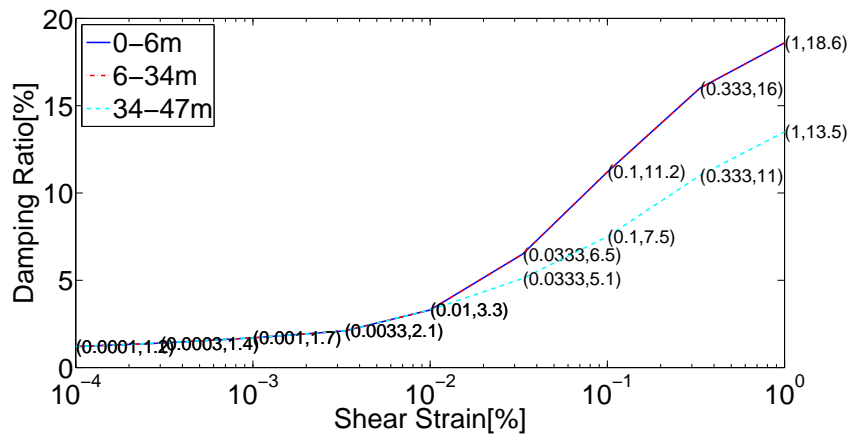
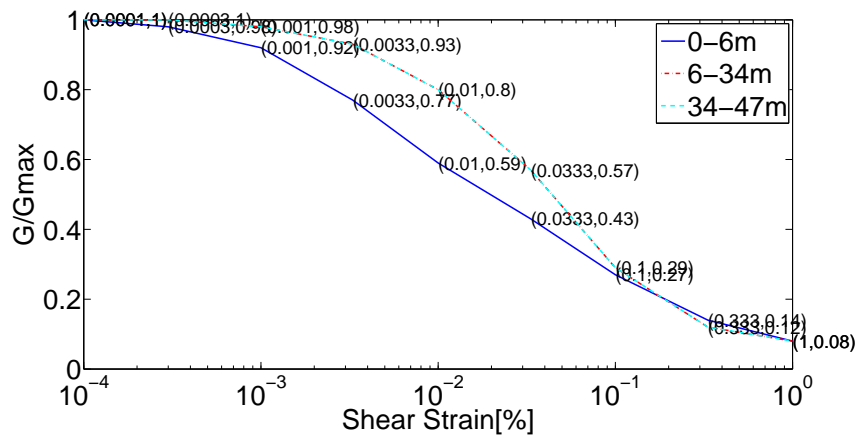


Figure 11.63: G/Gmax and Damping Curves

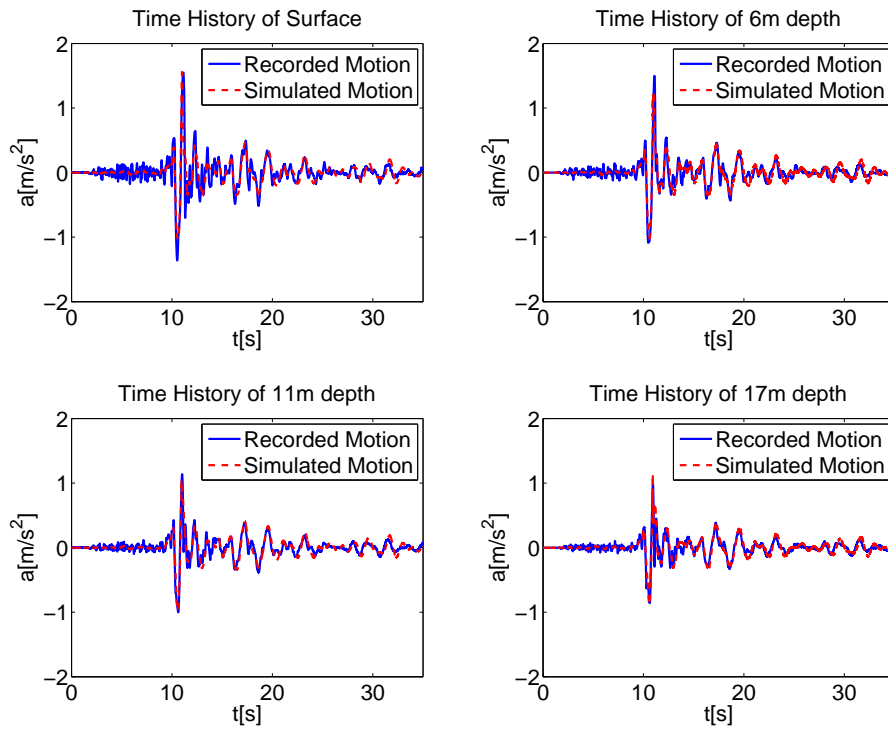


Figure 11.64: Time history comparison at different depths

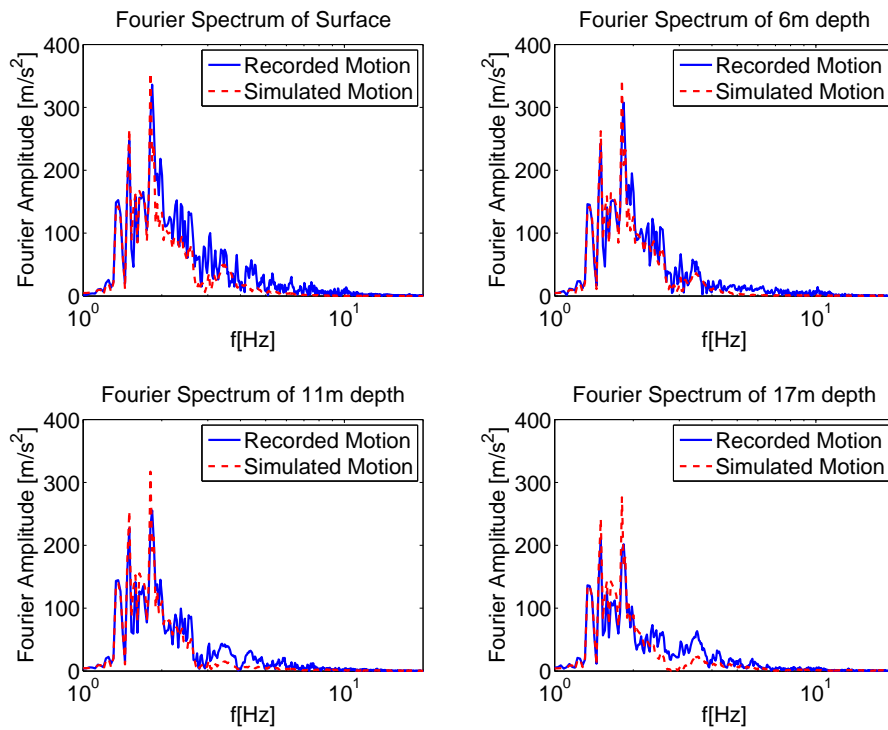


Figure 11.65: Fourier spectrum comparison at different depths

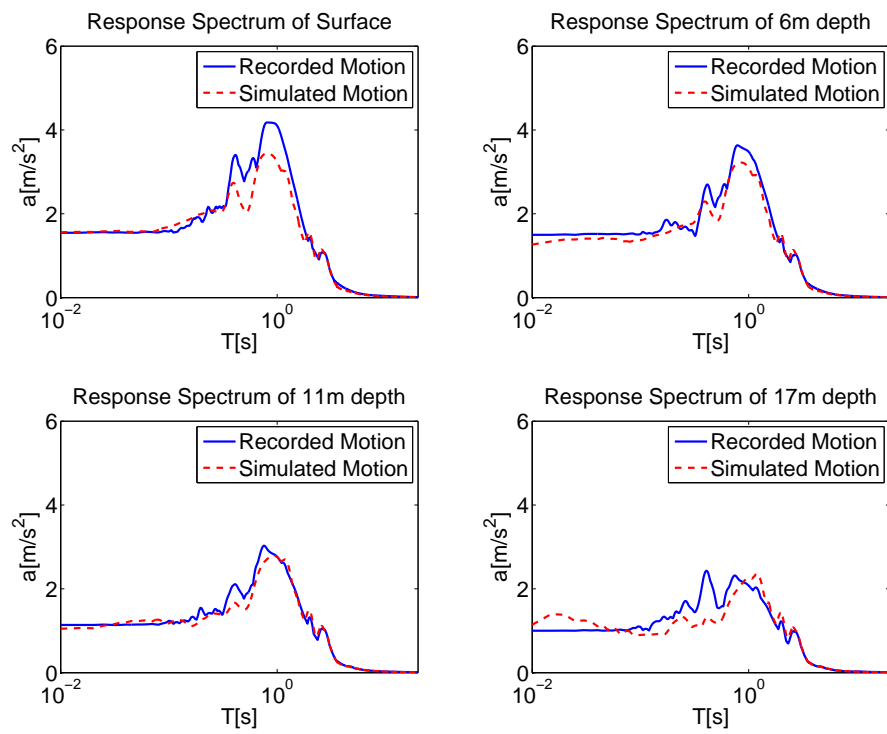


Figure 11.66: Response spectrum comparison at different depths (damping ratio 5%)

Chapter 12

Summary

Earthquake Soil Structure Interaction (ESSI) during earthquakes represent a complex phenomena that requires highly sophisticated experts and high fidelity numerical modeling and simulation tools for proper analysis. Improvements in seismic design (and retrofit) and of soil structure system, and in particular for very important objects, like Nuclear Power Plants (NPPs), are only possible if design and licensing experts have access to high fidelity simulation data. Such data allows experts to make proper design and licensing decisions, that are based on low modeling uncertainty results. The main goal of developed numerical prediction (modeling and simulations) tools is to predict and inform rather than (force) fit. Development of the Real ESSI Simulator, a system for high fidelity modeling and simulation of ESSI behavior epitomizes this philosophy.

Chapter 13

References

Bibliography

- N. Abrahamson. Spatial variation of earthquake ground motion for application to soil-structure interaction. *EPRI Report No. TR-100463, March.*, 1992a.
- N. Abrahamson. Generation of spatially incoherent strong motion time histories. In A. Bernal, editor, *Earthquake Engineering, Tenth World Conference*, pages 845–850. Balkema, Rotterdam, 1992b. ISBN 90 5410 060 5.
- N. Abrahamson. Spatial variation of multiple support inputs. In *Proceedings of the First U.S. Seminar, Seismic Evaluation and Retrofit of Steel Bridges*, San Francisco, CA, October 1993. UCB and CalTrans.
- N. Abrahamson. Updated coherency model. *Report Prepared for Bechtel Corporation, April*, 2005.
- N. A. Abrahamson. Estimation of seismic wave coherency and rupture velocity using the smart 1 strong-motion array recordings. Technical Report EERC-85-02, Earthquake Engineering Research Center, University of California, Berkeley, 1985.
- N. A. Abrahamson. Hard rock coherency functions based on Pinyon Flat data. unpublished data report, 2007.
- N. A. Abrahamson, J. F. Schneider, and J. C. Stepp. Empirical spatial coherency functions for applications to soil–structure interaction analysis. *Earthquake Spectra*, 7(1):1–27, 1991.
- K. Aki and P. G. Richards. *Quantitative Seismology*. University Science Books, 2nd edition, 2002.

- J. Allmond, L. Deng, and B. Kutter. Centrifuge testing of rocking foundations on saturated and submerged sand,. In *Eighth International Conference on Urban Earthquake Engineering*, pages 467–472, Tokyo, Japan, 7-9 March 2011.
- K. Alvin, H. M. de la Fuente, B. Haugen, and C. A. Felippa. Membrane triangles with corner drilling freedoms – I. the EFF element. *Finite Elements in Analysis and Design*, 12:163–187, 1992.
- B. Amadei. *Rock anisotropy and the theory of stress measurements*. Lecture notes in engineering. Springer-Verlag, 1983.
- T. Ancheta, J. Stewart, and N. Abrahamson. Frequency dependent windowing: A non-stationary method for simulating spatially variable earthquake ground motions. *Earthquake Spectra*, 2012. in review.
- T. D. Ancheta. *Engineering characterization of spatially variable earthquake ground motions*. PhD thesis, University of California at Los Angeles, 2010.
- T. D. Ancheta, J. P. Stewart, and N. A. Abrahamson. Frequency dependent windowing: A non-stationary method for simulating spatially variable earthquake ground motions. Technical report, Pacific Earthquake Engineering Center, 2013.
- K. Andrianopoulos, A. Papadimitriou, and G. Bouckovalas. Bounding surface models of sands: Pitfalls of mapping rules for cyclic loading. In *Proceedings, 11 th International Conference on Computer Methods and Advances in Geomechanics*, pages 241–248, 2005.
- K. I. Andrianopoulos, A. G. Papadimitriou, and G. D. Bouckovalas. Bounding surface plasticity model for the seismic liquefaction analysis of geostuctures. *Soil Dynamics and Earthquake Engineering*, 30(10):895–911, 2010.
- J. Argyris and H.-P. Mlejnek. *Dynamics of Structures*. North Holland in USA Elsevier, 1991.
- I. Babuška and J. T. Oden. Verification and validation in computational engineering and science: basic concepts. *Computer Methods in Applied Mechanics and Engineering*, 193(36-38):4057–4066, Sept 2004.

- G. B. Baecher and J. T. Christian. *Reliability and Statistics in Geotechnical Engineering*. John Wiley & Sons Ltd., The Atrium, Southern Gate, Chichester, West Sussex PO19 8SQ, England, 2003. ISBN 0-471-49833-5.
- E. J. Barbero, R. Luciano, and E. Sacco. Three-dimensional plate and contact/friction elements for laminated composite joints. *Computers and Structures*, 54:689–703, 1995.
- J. P. Bardet, K. Ichii, and C. H. Lin. Eera, a computer program for equivalent-linear earthquake site response analyses of layered soil deposits. Technical report, University of Southern California, 2000.
- K.-J. Bathe and L. Wilson, Edward. *Numerical Methods in Finite Element Analysis*. Prentice Hall Inc., 1976.
- K. Been and M. Jefferies. A state parameter for sands. *Geotechnique*, 35(2):99–112, 1985.
- T. Benz and R. Schwabb. A quantitative comparison of six rock failure criteria. *International Journal of Rock Mechanics and Mining Sciences*, 45(7):1176–1186, October 2008.
- P. G. Bergan and C. A. Felippa. A triangular membrane element with rotational degrees of freedom. *Computer Methods in Applied Mechanics and Engineering*, 50:25–69, 1985.
- J. Bielak, K. Loukakis, Y. Hisada, and C. Yoshimura. Domain reduction method for three-dimensional earthquake modeling in localized regions. part I: Theory. *Bulletin of the Seismological Society of America*, 93(2):817–824, 2003.
- R. Borja and A. Amies. Multiaxial cyclic plasticity model for clays. *Journal of Geotechnical Engineering*, 120(6):1051–1070, 1994.
- R. Borja, C. Lin, K. Sama, and G. Masada. Modelling non-linear ground response of non-liquefiable soils. *Earthquake Engineering and Structural Dynamics*, 29:63–83, 2000.
- R. I. Borja, H. Yih Chao, F. J. Montána, and C. Hua Lin. Nonlinear ground response at Lotung LSST site. *ASCE Journal of Geotechnical and Geoenvironmental Engineering*, 125(3):187–197, March 1999.

- N. Chandrasekaran, W. E. Haisler, and R. E. Goforth. Finite element analysis of hertz contact problem with friction. *Finite Elements in Analysis and Design*, 3:39–56, 1987.
- Z. Cheng and B. Jeremić. Numerical modeling and simulation of soil lateral spreading against piles. In *In proceedings of the GeoOrlando, Geo Institute Annual Conference*, Orlando, Florida, March 2009a.
- Z. Cheng and B. Jeremić. Numerical modeling and simulations of piles in liquefiable soil. *Soil Dynamics and Earthquake Engineering*, 29:1405–1416, 2009b.
- A. K. Chopra. *Dynamics of Structures, Theory and Application to Earthquake Engineering*. Prentice Hall, second edition, 2000. ISBN 0-13-086973-2.
- M. A. Crisfield. *Non-Linear Finite Element Analysis of Solids and Structures Volume 2: Advanced Topics*. John Wiley and Sons, Inc. New York, 605 Third Avenue, New York, NY 10158–0012, USA, 1997.
- M. Čubrinovski. Private communications. ..., 2007 –.
- M. Čubrinovski, R. Uzuoka, H. Sugita, K. Tokimatsu, M. Sato, K. Ishihara, Y. Tsukamoto, and T. Kamata. Prediction of pile response to lateral spreading by 3-d soil-coupled dynamic analysis: Shaking in the direction of ground flow. *Soil Dynamics and Earthquake Engineering*, 28(6):421–435, June 2008.
- Y. Dafalias. A model for soil behavior under monotonic and cyclic loading conditions. In *Proceedings of the 5th international conference on SMiRT*, volume K 1/8, 1979.
- Y. Dafalias and E. Popov. Cyclic loading for materials with a vanishing elastic region. *Nuclear Engineering and Design*, 41(2):293–302, 1977.
- Y. F. Dafalias. Bounding surface plasticity. I: Mathematical foundations and hypoplasticity. *ASCE Journal of Engineering Mechanics*, 112(9):966–987, September 1986.
- Y. F. Dafalias and M. T. Manzari. Simple plasticity sand model accounting for fabric change effects. *Journal of Engineering Mechanics*, 130(6):622–634, 2004a.

- Y. F. Dafalias and M. T. Manzari. Simple plasticity sand model accounting for fabric change effects. *ASCE Journal of Engineering Mechanics*, 130(6):622–634, June 2004b.
- M. Darendeli. *Development of a new family of normalized modulus reduction and material damping curves*. PhD thesis, University of Texas at Austin, 2001.
- C. S. Desai and H. J. Siriwardane. *Constitutive Laws for Engineering Materials With Emphasis on Geologic Materials*. Prentice–Hall, Inc. Englewood Cliffs, NJ 07632, 1984.
- C. di Prisco and F. Pisanò. An exercise on slope stability and perfect elasto-plasticity. *Géotechnique*, 61(11):923–934, 2011.
- C. di Prisco and D. Wood. *Mechanical Behaviour of Soils Under Environmentally-Induced Cyclic Loads*. Springer, 2012.
- C. di Prisco, M. Pastor, and F. Pisan. Shear wave propagation along infinite slopes: A theoretically based numerical study. *International Journal for Numerical and Analytical Methods in Geomechanics*, 36(5):619–642, 2012. ISSN 1096-9853. doi: 10.1002/nag.1020. URL <http://dx.doi.org/10.1002/nag.1020>.
- M. E-Kan and H. A. Taiebat. On implementation of bounding surface plasticity models with no overshooting effect in solving boundary value problems. *Computers and Geotechnics*, 55: 103–116, 2014.
- A. Elgamal, Z. Yang, E. Parra, and A. Ragheb. Modeling the cyclic mobility in saturated cohesionless soils. *International Journal of Plasticity*, 19(6):883–905, 2003.
- C. A. Felippa. Nonlinear finite element methods. Lecture Notes at CU Boulder, 1993-2015.
- C. A. Felippa and S. Alexander. Membrane triangles with corner drilling freedoms – III. implementation and performance evaluation. *Finite Elements in Analysis and Design*, 12:203–239, 1992.
- C. A. Felippa and C. Militello. Membrane triangles with corner drilling freedoms – II. the ANDES element. *Finite Elements in Analysis and Design*, 12:189–201, 1992.

- A. Gajo and D. Wood. A kinematic hardening constitutive model for sands: the multiaxial formulation. *International Journal for Numerical and Analytical methods in Geomechanics*, 23:925 – 965, 1999.
- A. Gens, I. Carol, and E. E. Alonso. An interface element formulation for the analysis of soil–reinforcement interactions. *Computers and Geotechnics*, 7:133–151, 1988.
- A. Gens, I. Carol, and E. Alonso. A constitutive model for rock joints formulation and numerical implementation. *Computers and Geotechnics*, 9(1-2):3–20, 1990.
- A. Haraldsson and P. Wriggers. A strategy for numerical testing of frictional laws with application to contact between soil and concrete. *Computer Methods in Applied Mechanics and Engineering*, 190:963–977, 2000.
- R. Harichandran and E. Vanmarcke. Stochastic variation of earthquake ground motion in space and time. *ASCE Journal of Engineering Mechanics*, 112:154–174, 1986.
- Y. Hashash and D. Park. Non-linear one-dimensional wave propagation in the Mississippi embayment. *Engineering Geology*, 62(1–3):185–206, 2001.
- Y. Hashash and D. Park. Viscous damping formulation and high frequency motion in non-linear site response analysis. *Soil Dynamics and Earthquake Engineering*, 22:611–624, 2002.
- L. Hatton. The T experiments: Errors in scientific software. *IEEE Computational Science and Engineering*, 4(2):27–38, April–June 1997.
- L. Hatton and A. Roberts. How accurate is scientific software? *IEEE Transaction on Software Engineering*, 20(10):185–797, October 1994.
- H. M. Hilber, T. J. R. Hughes, and R. L. Taylor. Improved numerical dissipation for time integration algorithms in structural dynamics. *Earthquake Engineering and Structure Dynamics*, 5(3):283–292, 1977.
- M. Hjiiaj, Z.-Q. Feng, G. de Saxce, and Z. Mroz. Three-dimensional finite element computations for frictional contact problems with non-associated sliding rule. *Journal for Numerical Methods in Engineering*, 60:2045–2076, 2004.

- T. Hughes. *The Finite Element Method ; Linear Static and Dynamic Finite Element Analysis*. Prentice Hall Inc., 1987.
- I. M. Idriss and J. I. Sun. *Excerpts from USER'S Manual for SHAKE91: A Computer Program for Conducting Equivalent Linear Seismic Response Analyses of Horizontally Layered Soil Deposits*. Center for Geotechnical Modeling Department of Civil & Environmental Engineering University of California Davis, California, 1992.
- I. Ishibashi and X. Zhang. Unified dynamic shear moduli and damping ratios of sand and clay. *Soils and Foundations*, 33(1):182–191, 1993.
- K. Ishihara. *Soil behaviour in earthquake geotechnics*. Clarendon Press, Oxford University Press, 1996.
- K. Ishihara, F. Tatsuoka, and S. Yasuda. Undrained deformation and liquefaction of sand under cyclic stresses. *Soils and Foundations*, 15(1):29–44, 1975.
- J. Jaeger, N. Cook, and R. Zimmerman. *Fundamentals of rock mechanics*. Blackwell Pub., 2007. ISBN 9780632057597.
- B. Jeremić. High fidelity modeling and simulation of sfs interaction: energy dissipation by design. In R. P. Orense, N. Chouw, and M. Pender, editors, *Soil-Foundation-Structure Interaction*, pages 125–132. CRC Press, Taylor & Francis Group, 2010. ISBN 978-0-415-60040-8 (Hbk); 978-0-203-83820-4 (eBook).
- B. Jeremić and Z. Cheng. Numerical modeling and simulations of piles in liquefied soils. *Soil Dynamics and Earthquake Engineering*, in Print, 2009.
- B. Jeremić and S. Sture. Implicit integrations in elasto–plastic geotechnics. *International Journal of Mechanics of Cohesive–Frictional Materials*, 2:165–183, 1997.
- B. Jeremić, Z. Yang, Z. Cheng, G. Jie, K. Sett, N. Tafazzoli, P. Tasiopoulou, J. A. A. Mena, F. Pisanò, K. Watanabe, K. Karapiperis, Y. Feng, and S. K. Sinha. Lecture notes on computational geomechanics: Inelastic finite elements for pressure sensitive materials. Technical Report UCD-CompGeoMech–01–2004, University of California, Davis, 1989-2016.

- B. Jeremić, Z. Cheng, M. Taiebat, and Y. F. Dafalias. Numerical simulation of fully saturated porous materials. *International Journal for Numerical and Analytical Methods in Geomechanics*, 32(13):1635–1660, 2008.
- B. Jeremić, S. Kunnath, and T. D. Ancheta. Assessment of seismic input and soil structure interaction for deeply embedded, large foundations. Report to the Canadian Nuclear Safety Commission, Consulting Engineers, Ottawa, Canada 2011.
- B. Jeremić, J. A. Abell, G. Jie, Z. Cheng, N. Tafazzoli, and S. K. Sinha. *The Real ESSI Simulator*. University of California, Davis and Lawrence Berkeley National Laboratory, 2015. http://sokocalo.engr.ucdavis.edu/~jeremic/ESSI_Simulator/.
- A. L. Jones, S. L. Kramer, and P. Arduino. Estimation of uncertainty in geotechnical properties for performance-based earthquake engineering. Technical Report PEER 2002/16, Pacific Earthquake Engineering Research Center, Dec. 2002.
- R. P. Kennedy. Private communications. RPK Structural Mechanics Consulting, 2009-2014.
- A. R. Khoei and M. Nikbakhti. Contact friction modeling with the extended finite element method (x-fem). *Journal of Materials Processing Technology*, 177:58–62, 2006.
- K. Konakli, A. Der Kiureghian, and D. Dreger. Coherency analysis of accelerograms recorded by the upsar array during the 2004 parkfield earthquake. *Earthquake Engineering & Structural Dynamics*, pages n/a–n/a, 2013. ISSN 1096-9845. doi: 10.1002/eqe.2362. URL <http://dx.doi.org/10.1002/eqe.2362>.
- A. W. A. Konter. Advanced finite element contact benchmarks. Technical report, Netherlands Institute for Metals Research, 2005.
- S. L. Kramer. *Geotechnical Earthquake Engineering*. Prentice Hall, Inc, Upper Saddle River, New Jersey, 1996.
- S. Krenk. Energy conservation in newmark based time integration algorithms. *Computer Methods in Applied Mechanics and Engineering*, 195(44-47):6110–6124, September 2006.

- S. Lacasse and F. Nadim. Uncertainties in characterizing soil properties. In C. D. Shackelford and P. P. Nelson, editors, *Uncertainty in Geologic Environment: From Theory to Practice, Proceedings of Uncertainty 1996, July 31-August 3, 1996, Madison, Wisconsin*, volume 1 of *Geotechnical Special Publication No. 58*, pages 49–75. ASCE, New York, 1996.
- P. V. Lade. Elastoplastic stress strain theory for cohesionless soil with curved yield surfaces. *International Journal of Solids and Structures*, 13:1019–1035, 1977.
- S. Liao and A. Zerva. Physically compliant, conditionally simulated spatially variable seismic ground motions for performance-based design. *Earthquake Engineering & Structural Dynamics*, 35:891–919, 2006.
- C. Loh and Y. Yeh. Spatial variation and stochastic modeling of seismic differential ground movement. *Earthquake Engineering and Structural Dynamics*, 16:583–596, 1988.
- J. Lymser. SASSI: A computer program for dynamic soil structure interaction analysis. *Report UBC/GT81-02. University of California, Berkeley, CA, USA.*, 1988.
- M. T. Manzari and Y. F. Dafalias. A critical state two-surface plasticity model for sands. *Géotechnique*, 47(2):255–272, 1997.
- M. T. Manzari and R. Prachathananukit. On integration of a cyclic soil plasticity model. *International Journal for Numerical and Analytical Methods in Geomechanics*, 25:525–549, 2001.
- H. Matsuoka and T. Nakai. Stress, deformation and strength characteristics under three different principal stresses. *Proceedings of Japanese Society of Civil Engineers*, 232:59–70, 1974.
- C. Militello and C. A. Felippa. The first ANDES elements: 9-dof plate bending triangles. *Computer Methods in Applied Mechanics and Engineering*, 93:217–246, 1991.
- R. D. Mindlin and H. Deresiewicz. Elastic spheres in contact under varying oblique forces. *ASME Journal of Applied Mechanics*, 53(APM-14):327–344, September 1953.
- Z. Mróz, V. A. Norris, and O. C. Zienkiewicz. An anisotropic hardening model for soils and its application to cyclic loading. *International Journal for Numerical and Analytical Methods in Geomechanics*, 2:203–221, 1978.

- N. M. Newmark. A method of computation for structural dynamics. *ASCE Journal of the Engineering Mechanics Division*, 85:67–94, July 1959.
- R. Nova and D. M. Wood. A constitutive model for sand in triaxial compression. *International Journal for Numerical and Analytical Methods in Geomechanics*, 3:255–278, 1979.
- W. Oberkampf. Material from the short course on verification and validation in computational mechanics. Albuquerque, New Mexico, July 2003.
- W. L. Oberkampf, T. G. Trucano, and C. Hirsch. Verification, validation and predictive capability in computational engineering and physics. In *Proceedings of the Foundations for Verification and Validation on the 21st Century Workshop*, pages 1–74, Laurel, Maryland, October 22-23 2002. Johns Hopkins University / Applied Physics Laboratory.
- J. T. Oden, I. Babuška, F. Nobile, Y. Feng, and R. Tempone. Theory and methodology for estimation and control of errors due to modeling, approximation, and uncertainty. *Computer Methods in Applied Mechanics and Engineering*, 194(2-5):195–204, February 2005.
- T. Oden, R. Moser, and O. Ghattas. Computer predictions with quantified uncertainty, part i. *SIAM News*, 43(9), November 2010a.
- T. Oden, R. Moser, and O. Ghattas. Computer predictions with quantified uncertainty, part ii. *SIAM News*, 43(10), December 2010b.
- C. S. Oliveira, H. Hao, and J. Penzien. Ground motion modeling for multiple-input structural analysis. *Structural Safety*, 10:79–93, 1991.
- O. A. Olukoko, A. A. Becker, and R. T. Fenner. Three benchmark examples for frictional contact modelling using finite element and boundary element methods. *Journal of Strain Analysis*, 28(4):293–301, 1993.
- N. Orbović, B. Jeremić, J. A. A. Mena, C. Luo, R. P. Kennedy, and A. Blaihoanu. Use of nonlinear, time domain analysis for NPP design. In *Transactions, SMiRT-23*, Manchester, United Kingdom, August 10-14 2015.

- A. G. Papadimitriou and G. D. Bouckovalas. Plasticity model for sand under small and large cyclic strains: A multi-axial formulation. *Soil Dynamics and Earthquake Engineering*, 22(3): 191–204, 2002.
- K.-K. Phoon and F. H. Kulhawy. Characterization of geotechnical variability. *Canadian Geotechnical Journal*, 36:612–624, 1999a.
- K.-K. Phoon and F. H. Kulhawy. Evaluation of geotechnical property variability. *Canadian Geotechnical Journal*, 36:625–639, 1999b.
- F. Pisanò and B. Jeremić. Simulating stiffness degradation and damping in soils via a simple visco-elastic-plastic model. *Soil Dynamics and Geotechnical Earthquake Engineering*, 63:98–109, 2014.
- J. Prevost. A simple plasticity theory for frictional cohesionless soils. *International Journal of Soil Dynamics and Earthquake Engineering*, 4(1):9–17, 1985.
- J. H. Prevost. DYNA1D: A computer program for nonlinear site response analysis, technical documentation. technical report no. nceer-89-0025. Technical report, National Center for Earthquake Engineering Research, State University of New York at Buffalo, 1989.
- J. H. Prevost and R. Popescu. Constitutive relations for soil materials. *Electronic Journal of Geotechnical Engineering*, October 1996. available at <http://139.78.66.61/ejge/>.
- P. J. Roache. *Verification and Validation in Computational Science and Engineering*. Hermosa Publishers, Albuquerque, New Mexico, 1998. ISBN 0-913478-08-3.
- C. Roblee, W. Silva, G. Toro, and N. Abrahamson. Variability in site-specific seismic ground-motion predictions. In *Proceedings: Uncertainty in the Geologic Environment*, page 21p, Madison WI., August 1-2 1996. American Society of Civil Engineers.
- D. Roten, D. Fäh, and L. Bonilla. High-frequency ground motion amplification during the 2011 tohoku earthquake explained by soil dilatancy. *Geophysical Journal International*, 193:898–904, 2013.

- C. Roy, A. J. Roffel, S. Bolourchi, L. Todorovski, and M. Khoncarly. Study of seismic structure-soil-structure interaction between two heavy structures. In *Transactions, SMiRT-22*, pages 1–7, San Francisco, August 2013. IASMiRT.
- C. J. Roy and W. L. Oberkampf. A comprehensive framework for verification, validation, and uncertainty quantification in scientific computing. *Computer Methods in Applied Mechanics and Engineering*, 200(25-28):2131 – 2144, 2011. ISSN 0045-7825. doi: 10.1016/j.cma.2011.03.016. URL <http://www.sciencedirect.com/science/article/pii/S0045782511001290>.
- H. Ryan. Ricker, Ormsby, Klander, Butterworth - a choice of wavelets. *Canadian Society of Exploration Geophysicists Recorder*, 19(7):8–9, September 1994. URL <http://www.cseg.ca/publications/recorder/1994/09sep/sep94-choice-of-wavelets.pdf>.
- T. Sakemi, M. Tanaka, Y. Higuchi, K. Kawasaki, and K. Nagura. Permeability of pore fluids in the centrifugal fields. In *10th Asian Regional Conference on Soil Mechanics and Foundation Engineering (10ARC)*, Beijing, China, August 29 - Sept 2 1995.
- P. Schnabel, J. Lysmer, and H. B. Seed. Shake – a computer program for equation response analysis of horizontally layered sites. report eerc 72-12. Technical report, University of California Berkeley, 1972.
- H. B. Seed and I. M. Idriss. Soil moduli and damping factors for dynamic response analyses. report eerc 70-10. Technical report, University of California Berkeley, 1970.
- K. Sett, B. Unutmaz, K. Önder Çetin, S. Koprivica, and B. Jeremić. Soil uncertainty and its influence on simulated G/G_{max} and damping behavior. *ASCE Journal of Geotechnical and Environmental Engineering*, 137(3):218–226, 2011. 10.1061/(ASCE)GT.1943-5606.0000420 (July 29, 2010).
- H. Shahir, A. Pak, M. Taiebat, and B. Jeremić. Evaluation of variation of permeability in liquefiable soil under earthquake loading. *Computers and Geotechnics*, 40:74–88, 2012.
- D. Sheng, P. Wriggers, and S. W. Sloan. Application of frictional contact in geotechnical engineering. *International Journal of Geomechanics*, 7(3):176–185, 2007.

- A. Stavrogin, B. Tarasov, and e. C. Fairhurst. *Experimental physics and rock mechanics*. A.A. Balkema, Lisse ; Exton PA, 2001. ISBN 9058092135.
- S. Stošić. Private communications, 1984-2013.
- M. Taiebat and Y. F. Dafalias. SANISAND: Simple anisotropic sand plasticity model. *International Journal for Numerical and Analytical Methods in Geomechanics*, 2008. (in print, available in earlyview).
- M. Taiebat, B. Jeremić, Y. F. Dafalias, and A. M. Kaynia. Earthquake-induced shear deformation of slopes for performance-based engineering. In Kokusho, Tsukamoto, and Yoshimine, editors, *Performance-Based Design in Earthquake Geotechnical Engineering: From Case History to Practice*, pages 907–914, Tsukuba, Japan, 2009. Taylor & Francis Group, London. ISBN 978-0-415-55614-9.
- M. Taiebat, B. Jeremić, Y. F. Dafalias, A. M. Kaynia, and Z. Cheng. Propagation of seismic waves through liquefied soils. *Soil Dynamics and Earthquake Engineering*, 30(4):236–257, 2010.
- P. Tasiopoulou, M. Taiebat, N. Tafazzoli, and B. Jeremić. Solution verification procedures for modeling and simulation of fully coupled porous media: Static and dynamic behavior. *Coupled Systems Mechanics Journal*, 4(1):67–98, 2015a. DOI: <http://dx.doi.org/10.12989/csm.2015.4.1.067>.
- P. Tasiopoulou, M. Taiebat, N. Tafazzoli, and B. Jeremić. On validation of fully coupled behavior of porous media using centrifuge test results. *Coupled Systems Mechanics Journal*, 4(1):37–65, 2015b. DOI: <http://dx.doi.org/10.12989/csm.2015.4.1.037>.
- K. Terzaghi, R. B. Peck, and G. Mesri. *Soil Mechanics in Engineering Practice*. John Wiley & Sons, Inc., third edition, 1996.
- M. Trifunac. Energy of strong motion at earthquake source. *Soil Dynamics and Earthquake Engineering*, 28(1):1–6, January 2008.

- M. D. Trifunac, T. Ying Hao, and M. I. Todorovska. Energy of earthquake as a design tool. In *Proceedings of 13th Mexican Conference on Earthquake Engineering, XIII MCEE*, pages 1–49, Guadalajara, Mexico, 31th October – 3rd November 2001.
- R. Uzuoka, M. Čubrinovski, H. Sugita, M. Sato, K. Tokimatsu, N. Sento, M. Kazama, F. Zhang, A. Yashima, and F. Oka. Prediction of pile response to lateral spreading by 3-d soil–coupled dynamic analysis: Shaking in the direction perpendicular to ground flow. *Soil Dynamics and Earthquake Engineering*, 28(6):436–452, June 2008.
- R. Verdugo and K. Ishihara. The steady state of sandy soils. *Soils and Foundations*, 36(2): 81–91, 1996.
- M. A. Walling. *Non-Ergodic Probabilistic Seismic Hazard Analysis and Spatial Simulation of Variation in Ground Motion*. PhD thesis, University of California at Berkeley, Spring 2009. Under guidance of Professor Norman Abrahamson.
- Z.-L. Wang, Y. F. Dafalias, and C.-K. Shen. Bounding surface hypoplasticity model for sand. *Journal of engineering mechanics*, 116(5):983–1001, 1990.
- K. J. Willam and E. P. Warnke. Constitutive model for the triaxial behaviour of concrete. In *Proceedings IABSE Seminar on Concrete Bergamo*. ISMES, 1974.
- D. Wood, K. Belkheir, and D. Liu. Strain softening and state parameter for sand modelling. *Geotechnique*, 44(3):335–339, 1994.
- D. M. Wood. *Geotechnical Modeling*. Spoon Press, 2004. ISBN 0-415–34304.
- P. Wriggers. *Computational Contact Mechanics*. John Wiley & Sons, 2002.
- Z. Yang and B. Jeremić. Numerical analysis of pile behaviour under lateral loads in layered elastic-plastic soils. *International Journal for Numerical and Analytical Methods in Geomechanics*, 26(14):1385–1406, 2002.
- Z. Yang and B. Jeremić. Numerical study of the effective stiffness for pile groups. *International Journal for Numerical and Analytical Methods in Geomechanics*, 27(15):1255–1276, Dec 2003.

- Z. Yang and B. Jeremić. Soil layering effects on lateral pile behavior. *ASCE Journal of Geotechnical and Geoenvironmental Engineering*, 131(6):762–770, June 2005.
- C. Yoshimura, J. Bielak, and Y. Hisada. Domain reduction method for three-dimensional earthquake modeling in localized regions. part II: Verification and examples. *Bulletin of the Seismological Society of America*, 93(2):825–840, 2003.
- A. Zerva. *Spatial variation of seismic ground motions: modeling and engineering applications*. CRC Press, 2009. ISBN ISBN-10: 0849399297; ISBN-13: 978-0849399299.
- A. Zerva and V. Zervas. Spatial variation of seismic ground motions: An overview. *ASME Applied Mechanics Review*, 55(3):271–297, May 2002.
- L. Zhang. *Engineering properties of rocks*. Elsevier geo-engineering book series ;v. 4. Elsevier,, Amsterdam ; London, 2005. ISBN 0080446728.
- O. Zienkiewicz, A. Chan, M. Pastor, B. Schrefler, and T. Shiomi. *Computational Geomechanics—with Special Reference to Earthquake Engineering*. John Wiley and Sons Ltd., Baffins Lane, Chichester, West Sussex PO19 1UD, England, 1999a.
- O. C. Zienkiewicz and T. Shiomi. Dynamic behaviour of saturated porous media; the generalized Biot formulation and its numerical solution. *International Journal for Numerical and Analytical Methods in Geomechanics*, 8:71–96, 1984.
- O. C. Zienkiewicz and R. L. Taylor. *The Finite Element Method*, volume 1. McGraw - Hill Book Company, fourth edition, 1991.
- O. C. Zienkiewicz, A. H. C. Chan, M. Pastor, B. A. Schrefler, and T. Shiomi. *Computational Geomechanics with Special Reference to Earthquake Engineering*. John Wiley and Sons., 1999b. ISBN 0-471-98285-7.

Appendix A

Real ESSI Program and Computer

Latest version of the Real ESSI Program is installed on CNSC-CCSN parallel computer. In addition to that, a system was setup so that future updates of the Real ESSI Program can be easily downloaded over the Internet and installed on the CNSC-CCSN computer. It is noted that initial plan was to add additional nodes to the parallel computer, in order to speed up execution of the program. Recent developments in template metaprogramming and advanced use of computers resources made it possible to speed up program and fit large problems in a current parallel computer. Addition of other nodes, connected via network would have actually slowed down computations. In view of such developments, effort was focused on optimizing code so that it runs most efficiently on current parallel computer.

It is anticipated that, as new capabilities become available (for example, nonlinear structural elements) in the Real ESSI Program, updates will be available and down-loadable by the CNSC-CCSN over Internet. Regular updates will be available approximately every three months.

Appendix B

Program Command Manual

B.1 Introduction

This section overviews a command language used for model input and analysis. Presented are all the commands, both those that are fully tested and running and also those that are in testing phase (work but have not been fully verified). For example, all the planned material models and finite element commands are presented, although, for example, seismic isolator elements are not fully available yet.

It is important to note that an up to date command manual (Domain Specific Language manual) is maintained at the Real ESSI web site.

Syntax is used to self-document models, provide physical-unit safety, provide common flow control structures, provide modularity to scripting via user functions and “include” files, and provide an interactive environment within which models can be created, validated and verified. Although finite element analysis within a computer is unitless, this command language uses units, in order to enforce consistency of input data. The language provides modularity through the `include` directive/command. This allows complex analysis cases to be parameterized into modules which can be reused in other models.

B.2 Domain Specific Language (DSL), English Language Binding

Main features of the command language are:

- Each command line has to end with a semicolon (;)
- Models have to be named: `model name "model_name_string";`
- Comment on a line begins with either `//` or `!` and last until the end of current line.
- Units are required (see more below) for all quantities and variables.
- Include statements allow splitting source into several files
- All variables are double precision with a unit attached.
- All standard arithmetic operations are implemented, and are unit sensitive.
- Internally, all units are represented in the base SI units ($m - s - kg$).
- The syntax ignores extra white spaces, tabulations and newlines. Wherever they appear, they are there for code readability only. (This is why all commands need to end with a semicolon).

B.2.1 Running the Program

From the command line type `essi`, to get to the prompt.

Command line output

```
Real ESSI

Compiled: Apr 29 2013 at 10:06:52
Now: Apr 29 2013 at 10:07:33

Static startup tips:
* Remember: Every command ends with a semicolon ';'.
* Type 'help;' to display available commands.
* Type 'quit;' or 'exit;' to finish.
```

```
* Run 'essi -h- to see available command line options.
Input: STDIN
ESSI>
```

at which point ESSI starts in interactive mode. From here, commands can be input manually or a file may be included via the `include` command which is as follows.

```
1 include "foobar.fei";
```

to include the file `foobar.fei`.

Additionally, one can pass a file to the command line ESSI call to execute a file immediately by issuing `essi -f foobar.fei` to execute `essi` with `foobar.fei` as input. After executing the file, the interpreter will continue in interactive mode unless the command line flag `-n` or `--no-interactive` is set. A list of command line options is available by calling `essi` from the command line as `essi -h`.

Command line output

```
Real ESSI
Compiled: Apr 29 2013 at 10:06:52
      Now: Apr 29 2013 at 10:08:28
Static startup tips:
* Remember: Every command ends with a semicolon ';'.
* Type 'help;' to display available commands.
* Type 'quit;' or 'exit;' to finish.
* Run 'essi -h- to see available command line options.

Real ESSI: Real Earthquake-Soil-Structure-Interaction ↵
      Simulator

Usage: essi [-h -n -c -f FILENAME]
  -c --cpp-output          : Output cpp version of the ↵
      analysis done.
  -f --filename [FILENAME] : Input file name in FEI format.
  -h --help                : Print this message.
  -n --no-interactive      : Disable interactive mode.
  -s --set-variable       : Set a variable from the command ↵
      line.
```

To exit ESSI, type `bye;` in the prompt. If `bye;` command is included at the end of a script, the `essi` program will exit upon execution of the script regardless of any errors which occur during execution.

B.2.2 Variables, basic units and flow control

Variables are defined using the assignment (`=`) operator. For example,

```
1 x = 7;           //Results in the variable x be set to 7 (↔
   unitless)
2 y = 3.972e+2;   //Scientific notation is available.
```

The language contains a list of reserved keywords. Throughout this documentation, reserved keywords are highlighted in **blue** or **red**.

All standard arithmetic operations are available between variables. These operations can be combined arbitrarily and grouped together with parentheses.

```
1 a = x + y;      // Addition
2 b = x - y;      // Subtraction
3 c = x*y;        // Product
4 d = x/y;        // Quotient
5 e = y%x;        // Modulus (how many times x fits in y)
```

The `'print'` command can be used to display the current value of a variable.

```
1 print x;
2 print y;
3 print a;
4 print b;
5 print c;
6 print d;
7 print e;
```

Command line output

```
x = 7 []
y = 397.2 []
a = 404.2 []
b = -390.2 []
c = 2780.4 []
d = 0.0176234 []
e = 5.2 []
```

Here the “unit” (sign) [] means that the quantities are unitless. The command 'whos' is used to see all the currently defined variables and their values. After executing all the above code 'whos;' produces the following output.

Command line output

```
ESSI> whos;

Declared variables:
* GPa = 1 [GPa]
* Hz = 1 [Hz]
* Km = 1 [km]
* MPa = 1 [MPa]
* N = 1 [N]
* Pa = 1 [Pa]
  a = 404.2 []
  b = -390.2 []
  c = 2780.4 []
* cm = 1 [cm]
  d = 0.0176234 []
  e = 5.2 []
* g = 9.81 [m*s^-2]
* kN = 1 [kN]
* kPa = 1 [kPa]
* kg = 1 [kg]
* m = 1 [m]
* mm = 1 [mm]
* ms = 1 [ms]
* ns = 1 [ns]
* s = 1 [s]
  x = 7 []
  y = 397.2 []

* = locked variable
```

Along with the variables which were defined above, several predefined variables appear (shown with a preceding asterisk to show they are locked variables which cannot be modified). The purpose of these locked variables are to provide names for units. The units for variable are shown between the brackets. Note that unit variables have the same name as their unit, which is not the case for user defined variables. Variables prepended by a star (*) are locked variables which can't be modified.

For example, the variable 'm' defines the 'meter'. So to define a new variable L1 which has meter units we do:

```

1 L1 = 1*m;      // Defines L1 to 1 m.
2 L2 = 40*mm;   // Defines L2 to be 40 millimeters.

```

Even though L2 was created with millimeter units, it is stored in base units.

`print L2;` displays

Command line output

```
L2 = 0.04 [m]
```

As additional examples, let us define few forces:

```

1 F1 = 10*kN;
2 F2 = 300*N;
3 F3 = 4*kg*g;

```

Here g is the predefined acceleration due to gravity.

Arithmetic operations do check (and enforce) for unit consistency. For example, `foo = L1 + F1;` produces an error because units are not compatible. However, `bar = L1 + L2 + L3;` is acceptable. On the other hand, multiplication, division and modulus, always work because the result produces a quantity with new units (except when the adimensional quantity is involved).

```

1 A = L1*L2;
2 pressure = F1 / A;

```

Units for all variables are internally converted to SI units ($kg-m-s$) and stored in that unit system. Variables can be *displayed* using different units by using the `[]` operator. This does not change the variable, it just displays the value of variable with required unit. For example,

```

1 print pressure;           //Print in base SI units.
2 print pressure in Pa;     //Print in Pascals
3 print pressure in kPa;    //Print in KiloPascals

```

Command line output

```

pressure = 250000 [kg*m^-1*s^-2]

pressure = 250000 [Pa]

pressure = 250 [kPa]

```

The DSL provides functions to test the physical units of variables. For example,

```
print isForce(F1);
```

Will print an adimensional 1 because F1 has units of force. While,

```
print isPressure(F);
```

will print an adimensional 0. The language also provides comparison of quantities with same units (remember all values are compared in SI Units).

```
print F1 > F2;
```

will print an adimensional 1 since F1 is greater than F2.

The program flow can be controlled with `if` and `while` statements, ie:

```
1 if (isForce(F1))
2 {
3   print F1;    // This will be executed
4 };
5
6 if (isForce(L1))
7 {
8   print L1;    // This will not.
9 };
```

Note the necessary semicolon (;) at the closing brace. Unlike C/C++, the braces are always necessary. Closing colon is also always necessary.

The “else” statement is also available:

```
1 if (isForce(L1))
2 {
3   print L1;    // This will not execute
4 }
5 else
6 {
7   print L2;    // This will execute instead
8 };
```

While loops are also available:

```
1 i = 0;
2 while( i < 10)
3 {
4   print i;
5   i = i +1;
6 };
```

B.2.3 Modeling

This section details ESSI modeling commands. Angle brackets $\langle \rangle$ are used for quantity or variable placeholder, that is, they indicate where user input goes. Within the angle brackets, the expected unit type is given as well, ie. $\langle L \rangle$ means the command expects an input with a value and a length unit. The symbol $\langle . \rangle$ represents the adimensional quantity.

In addition to that, the vertical bar | (“OR” sign)) is used to separate two or more keyword options, i.e. $[a|b|c]$ is used indicate keyword options a or b or c. The symbol $|\dots|$ is used to denote where several long options exist and are explained elsewhere (an example of this is available below in a material model definitions).

All commands require unit consistency. Base units, SI or other can be used as indicated below:

- length, symbol L , units [m, in, ft]
- mass, symbol M , units [kg, lb],
- time, symbol T , units [s]

Derived units can also be used:

- angle, symbol rad (radian), unit [*dimensionless*, L/L]
- force, symbol N (Newton), units [N , kN , MN , $M * L/T^2$],
- stress, symbol Pa (Pascal), units [Pa , kPa , MPa , N/L^2 , $M/L/T^2$]
- strain, symbol (no symbol), units [L/L]
- mass density, symbol (no symbol), units [M/L^3]
- force density, symbol (no symbol), units [$M/L^2/T^2$]

Starting a new loading stage

```
new loading stage "loading_stage_name_string";
```

Example, starting a new loading stage called "self weight loading stage": `new loading stage "self weight loading stage";`

Modeling: Material Models

General command for adding constitutive material models:

```
1  add material  # <.> type |...|  
2                algorithm = explicit | implicit  
3                mass_density = <M/L^3>  
4                (more model dependent parameters) ;
```

- Material number # (or alternatively No) is a distinct integer number used to uniquely identify this material.
- Algorithm type used to integrate constitutive equations
- Mass density should be defined for each material (even if only static analysis is performed, for example if self weight is to be used as a loading stage).
- Depending on material model, there will be additional material parameters that are defined for each material model/type below:

Choices for `material_type` are listed below

Material Model: `linear_elastic_isotropic_3d`,

for which a full command is:

```
1 add material # <.> type linear_elastic_isotropic_3d
2   mass_density = <M/L^3>
3   elastic_modulus = <F/L^2>
4   poisson_ratio = <.>;
```

where:

- `mass_density` is the mass density of material [M/L^3]
- `elastic_modulus` is an isotropic modulus of elasticity of a material (units: stress)
- `poisson_ratio` is a Poisson's ratio [dimensionless]

Material Model: `linear_elastic_crossanisotropic`

for which a full command is:

```
1  add material # <.> <material_number>
2      type linear_elastic_crossanisotropic
3      mass_density = <M/L^3>
4      elastic_modulus_horizontal = <F/L^2>
5      elastic_modulus_vertical = <F/L^2>
6      poisson_ratio_h_v = <.>
7      poisson_ratio_h_h = <.>
8      shear_modulus_h_v = <F/L^2>;
```

where:

- `mass_density` is the mass density of material [M/L^3]
- `elastic_modulus_horizontal` is an anisotropic modulus of elasticity for horizontal plane of a material [F/L^2]
- `elastic_modulus_vertical` is an anisotropic modulus of elasticity for vertical direction of a material [F/L^2]
- `poisson_ratio_h_v` is a Poisson's ratio for horizontal-vertical directions [dimensionless]
- `poisson_ratio_h_h` is a Poisson's ratio for horizontal-horizontal directions [dimensionless]
- `shear_modulus_h_v` is a shear modulus for horizontal-vertical directions [F/L^2]

Material Model: `non_linear_elastic_isotropic_3d` (command syntax is in development) ,

...

Material Model: von_mises_perfectly_plastic,

for which a full command is:

```
1  add material # <.> type vonmises_perfectly_plastic
2      mass_density = <M/L^3>
3      elastic_modulus = <F/L^2>
4      poisson_ratio = <.>
5      von_mises_radius = <F/L^2>
6      initial_confining_stress = <F/L^2>
7      algorithm = explicit (or) implicit
8      number_of_subincrements = <.>
9      maximum_number_of_iterations = <.>
10     tolerance_1 = <.>
11     tolerance_2 = <.>;
```

where:

- `mass_density` is the mass density of material [M/L^3]
- `elastic_modulus` is an isotropic modulus of elasticity of a material [stress]
- `poisson_ratio` is a Poisson's ratio [dimensionless]
- `von_mises_radius` is the radius of von Mises yield surface in (deviatoric) stress space [stress].
- `initial_confining_stress` is the initial confining stress $p = -1/3\sigma_{ii}$ and it is positive in compressions (since there is that – (minus) sign in front of sum of normal stresses (σ_{ii} indicial notation summation convention applies) that are positive in tension [stress].
- `algorithm` can be explicit or implicit.
- `number_of_subincrements` number of subincrements in constitutive simulation
- `maximum_number_of_iterations` maximum number of iterations
- `tolerance_1` Explicit: tolerance for intersection point (distance between two consecutive points) Implicit: yield function tolerance
- `tolerance_2` Implicit: residual tolerance

Material Model: von_mises_perfectly_plastic_accelerated,

for which a full command is:

```
1  add material # <.> type ←  
    vonmises_perfectly_plastic_accelerated  
2      mass_density = <M/L^3>  
3      elastic_modulus = <F/L^2>  
4      poisson_ratio = <.>  
5      von_mises_radius = <F/L^2>  
6      initial_confining_stress = <F/L^2>  
7      maximum_number_of_iterations = <.>  
8      tolerance_1 = <.>  
9      tolerance_2 = <.>;
```

where:

- `mass_density` is the mass density of material [M/L^3]
- `elastic_modulus` is an isotropic modulus of elasticity of a material [stress]
- `poisson_ratio` is a Poisson's ratio [dimensionless]
- `von_mises_radius` is the radius of von Mises yield surface in (deviatoric) stress space [stress].
- `initial_confining_stress` is the initial confining stress $p = -1/3\sigma_{ii}$ and it is positive in compressions (since there is that – (minus) sign in front of sum of normal stresses (σ_{ii} indicial notation summation convention applies) that are positive in tension [stress].
- `number_of_subincrements` number of subincrements in constitutive simulation
- `maximum_number_of_iterations` maximum number of iterations
- `tolerance_1` Explicit: tolerance for intersection point (distance between two consecutive points) Implicit: yield function tolerance
- `tolerance_2` Implicit: residual tolerance

Material Model: von_mises_isotropic_hardening,

for which a full command is:

```
1  add material # <.> type vonmises_isotropic_hardening
2      mass_density = <M/L^3>
3      elastic_modulus = <F/L^2>
4      poisson_ratio = <.>
5      von_mises_radius = <F/L^2>
6      isotropic_hardening_rate = <.>
7      initial_confining_stress = <F/L^2>
8          algorithm = explicit (or) implicit
9          number_of_subincrements = <.>
10         maximum_number_of_iterations = <.>
11         tolerance_1 = <.>
12         tolerance_2 = <.>;
```

where:

- `mass_density` is the mass density of material [M/L^3]
- `elastic_modulus` is an isotropic modulus of elasticity of a material [stress]
- `poissons_ratio` is a Poisson's ratio [dimensionless]
- `von_mises_radius` is the radius of von Mises yield surface in (deviatoric) stress space [stress]
- `isotropic_hardening_rate` is the rate of isotropic hardening
- `initial_confining_stress` is the initial confining stress $p = -1/3\sigma_{ii}$ and it is positive in compressions (since there is that – (minus) sign in front of sum of normal stresses (σ_{ii} indicial notation summation convention applies) that are positive in tension [stress].
- `algorithm` can be explicit or implicit.
- `number_of_subincrements` number of subincrements in constitutive simulation
- `maximum_number_of_iterations` maximum number of iterations
- `tolerance_1` Explicit: tolerance for intersection point (distance between two consecutive points) Implicit: yield function tolerance

- `tolerance_2` Implicit: residual tolerance

Material Model: von_mises_isotropic_hardening_accelerated,

for which a full command is:

```
1  add material # <.> type ←
    vonmises_isotropic_hardening_accelerated
2  mass_density = <M/L^3>
3  elastic_modulus = <F/L^2>
4  poisson_ratio = <.>
5  von_mises_radius = <F/L^2>
6  isotropic_hardening_rate = <.>
7  initial_confining_stress = <F/L^2>
8      maximum_number_of_iterations = <.>
9      tolerance_1 = <.>
10     tolerance_2 = <.>;
```

where:

- `mass_density` is the mass density of material [M/L^3]
- `elastic_modulus` is an isotropic modulus of elasticity of a material [stress]
- `poissons_ratio` is a Poisson's ratio [dimensionless]
- `von_mises_radius` is the radius of von Mises yield surface in (deviatoric) stress space [stress]
- `isotropic_hardening_rate` is the rate of isotropic hardening
- `initial_confining_stress` is the initial confining stress $p = -1/3\sigma_{ii}$ and it is positive in compressions (since there is that – (minus) sign in front of sum of normal stresses (σ_{ii} indicial notation summation convention applies) that are positive in tension [stress].
- `number_of_subincrements` number of subincrements in constitutive simulation
- `maximum_number_of_iterations` maximum number of iterations
- `tolerance_1` Explicit: tolerance for intersection point (distance between two consecutive points) Implicit: yield function tolerance
- `tolerance_2` Implicit: residual tolerance

Material Model: von_mises_kinematic_hardening,

```
1 add material # <.> type vonmises_kinematic_hardening
2   mass_density = <M/L^3>
3   elastic_modulus = <F/L^2>
4   poisson_ratio = <.>
5   von_mises_radius = <F/L^2>
6   armstrong_frederick_ha = <.>
7   armstrong_frederick_cr = <.>
8   initial_confining_stress = <F/L^2>
9   algorithm = explicit (or) implicit
10  number_of_subincrements = <.>
11  maximum_number_of_iterations = <.>
12  tolerance_1 = <.>
13  tolerance_2 = <.>;
```

where:

- `von_mises_radius` is the radius of von Mises yield surface in (deviatoric) stress space [stress]
- `initial_confining_stress` is the initial confining stress $p = -1/3\sigma_{ii}$ and it is positive in compressions (since there is that – (minus) sign in from of sum of normal stresses that are positive in tension).
- `number_of_subincrements` number of subincrements in constitutive simulation
- `maximum_number_of_iterations` maximum number of iterations
- `tolerance_1` Explicit: tolerance for intersection point (distance between two consecutive points) Implicit: yield function tolerance
- `tolerance_2` Implicit: residual tolerance

Material Model: `vonmises_linear_kinematic_hardening`,

```
1  add material # <.> type vonmises_linear_kinematic_hardening
2      mass_density = <M/L^3>
3      elastic_modulus = <F/L^2>
4      poisson_ratio = <.>
5      von_mises_radius = <F/L^2>
6      kinematic_hardening_rate = <.>
7      initial_confining_stress = <F/L^2>
8      algorithm = explicit (or) implicit
9      number_of_subincrements = <.>
10     maximum_number_of_iterations = <.>
11     tolerance_1 = <.>
12     tolerance_2 = <.>;
```

where:

- `von_mises_radius` is the radius of von Mises yield surface in (deviatoric) stress space [stress]
- `initial_confining_stress` is the initial confining stress $p = -1/3\sigma_{ii}$ and it is positive in compressions (since there is that – (minus) sign in from of sum of normal stresses that are positive in tension).
- `number_of_subincrements` number of subincrements in constitutive simulation
- `maximum_number_of_iterations` maximum number of iterations
- `tolerance_1` Explicit: tolerance for intersection point (distance between two consecutive points) Implicit: yield function tolerance
- `tolerance_2` Implicit: residual tolerance

Material Model: von_mises_kinematic_hardening_accelerated,

```
1  add material # <.> type ←
    vonmises_kinematic_hardening_accelerated
2      mass_density = <M/L^3>
3      elastic_modulus = <F/L^2>
4      poisson_ratio = <.>
5      von_mises_radius = <F/L^2>
6      armstrong_frederick_ha = <.>
7      armstrong_frederick_cr = <.>
8      initial_confining_stress = <F/L^2>
9      algorithm = explicit (or) implicit
10     number_of_subincrements = <.>
11     maximum_number_of_iterations = <.>
12     tolerance_1 = <.>
13     tolerance_2 = <.>;
```

where:

- **von_mises_radius** is the radius of von Mises yield surface in (deviatoric) stress space [stress]
- **initial_confining_stress** is the initial confining stress $p = -1/3\sigma_{ii}$ and it is positive in compressions (since there is that – (minus) sign in from of sum of normal stresses that are positive in tension).
- **number_of_subincrements** number of subincrements in constitutive simulation
- **maximum_number_of_iterations** maximum number of iterations
- **tolerance_1** Explicit: tolerance for intersection point (distance between two consecutive points) Implicit: yield function tolerance
- **tolerance_2** Implicit: residual tolerance

Material Model: `vonmises_linear_kinematic_hardening_accelerated`,

```
1  add material # <.> type ←
    vonmises_linear_kinematic_hardening_accelerated
2      mass_density = <M/L^3>
3      elastic_modulus = <F/L^2>
4      poisson_ratio = <.>
5      von_mises_radius = <F/L^2>
6      kinematic_hardening_rate = <.>
7      initial_confining_stress = <F/L^2>
8      algorithm = explicit (or) implicit
9      number_of_subincrements = <.>
10     maximum_number_of_iterations = <.>
11     tolerance_1 = <.>
12     tolerance_2 = <.>;
```

where:

- `von_mises_radius` is the radius of von Mises yield surface in (deviatoric) stress space [stress]
- `initial_confining_stress` is the initial confining stress $p = -1/3\sigma_{ii}$ and it is positive in compressions (since there is that – (minus) sign in from of sum of normal stresses that are positive in tension).
- `number_of_subincrements` number of subincrements in constitutive simulation
- `maximum_number_of_iterations` maximum number of iterations
- `tolerance_1` Explicit: tolerance for intersection point (distance between two consecutive points) Implicit: yield function tolerance
- `tolerance_2` Implicit: residual tolerance

Material Model: `druckerprager_perfectly_plastic`, material with Drucker-Prager yield surface with no hardening or softening. A full command for this material model is:

```
1  add material # <.> type druckerprager_perfectly_plastic
2      mass_density = <M/L^3>
3      elastic_modulus = <F/L^2>
4      poisson_ratio = <.>
5      druckerprager_angle = <.>
6      initial_confining_stress = <F/L^2>
7      algorithm = explicit or implicit
8      number_of_subincrements = <.>
9      maximum_number_of_iterations = <.>
10     tolerance_1 = <.>
11     tolerance_2 = <.>;
```

where

- `druckerprager_angle` coefficient related to the soil friction angle.

$$M = \frac{6 \sin \phi}{3 - \sin \phi} \quad (\text{B.1})$$

- `initial_confining_stress` Initial confining stress [F/L^2]
- `number_of_subincrements` number of subincrements in constitutive simulation
- `maximum_number_of_iterations` maximum number of iterations
- `tolerance_1` Explicit: tolerance for intersection point (distance between two consecutive points) Implicit: yield function tolerance
- `tolerance_2` Implicit: residual tolerance

Material Model: `druckerprager_perfectly_plastic_accelerated`, accelerated material with Drucker-Prager yield surface with no hardening or softening. Full command is:

```
1 add material # <.> type ←
   druckerprager_perfectly_plastic_accelerated
2   mass_density = <M/L^3>
3   elastic_modulus = <F/L^2>
4   poisson_ratio = <.>
5   druckerprager_angle = <.>
6   initial_confining_stress = <F/L^2>
7   number_of_subincrements = <.>
8   maximum_number_of_iterations = <.>
9   tolerance_1 = <.>
10  tolerance_2 = <.>;
```

where

- `druckerprager_angle` coefficient related to the soil friction angle.

$$M = \frac{6 \sin \phi}{3 - \sin \phi} \quad (\text{B.2})$$

- `initial_confining_stress` Initial confining stress [F/L^2]
- `number_of_subincrements` number of subincrements in constitutive simulation
- `maximum_number_of_iterations` maximum number of iterations
- `tolerance_1` Explicit: tolerance for intersection point (distance between two consecutive points) Implicit: yield function tolerance
- `tolerance_2` Implicit: residual tolerance

Material Model: drucker_prager_isotropic_hardening, material with Drucker-Prager yield surface with isotropic hardening of the yield surface. Full command is:

```
1 add material # <.> type druckerprager_isotropic_hardening
2   mass_density = <M/L^3>
3   elastic_modulus = <F/L^2>
4   poisson_ratio = <.>
5   druckerprager_angle = <.>
6   isotropic_hardening_rate = <.>
7   initial_confining_stress = <F/L^2>
8   algorithm = explicit (or) implicit
9     number_of_subincrements = <.>
10    maximum_number_of_iterations = <.>
11    tolerance_1 = <.>
12    tolerance_2 = <.>;
```

where:

- `mass_density` is the mass density of material [M/L^3]
- `elastic_modulus` is an isotropic modulus of elasticity of a material [stress]
- `poissons_ratio` is a Poisson's ratio [dimensionless]
- `druckerprager_angle` coefficient related to the soil friction angle.

$$M = \frac{6 \sin \phi}{3 - \sin \phi} \quad (\text{B.3})$$

- `isotropic_hardening_rate` is the rate of isotropic hardening
- `initial_confining_stress` is the initial confining stress $p = -1/3\sigma_{ii}$ and it is positive in compressions (since there is that – (minus) sign in front of sum of normal stresses (σ_{ii} indicial notation summation convention applies) that are positive in tension [stress].
- `algorithm` can be explicit or implicit.
- `number_of_subincrements` number of subincrements in constitutive simulation
- `maximum_number_of_iterations` maximum number of iterations

- `tolerance_1` Explicit: tolerance for intersection point (distance between two consecutive points) Implicit: yield function tolerance
- `tolerance_2` Implicit: residual tolerance

Material Model: drucker_prager_isotropic_hardening_accelerated, accelerated material with Drucker-Prager yield surface with isotropic hardening of the yield surface. Full command is:

```

1  add material # <.> type druckerprager_isotropic_hardening
2  mass_density = <M/L^3>
3  elastic_modulus = <F/L^2>
4  poisson_ratio = <.>
5  druckerprager_angle = <.>
6  isotropic_hardening_rate = <.>
7  initial_confining_stress = <F/L^2>
8  number_of_subincrements = <.>
9  maximum_number_of_iterations = <.>
10 tolerance_1 = <.>
11 tolerance_2 = <.>;

```

where:

- `mass_density` is the mass density of material [M/L^3]
- `elastic_modulus` is an isotropic modulus of elasticity of a material [stress]
- `poissons_ration` is a Poisson's ratio [dimensionless]
- `druckerprager_angle` coefficient related to the soil friction angle.

$$M = \frac{6 \sin \phi}{3 - \sin \phi} \quad (\text{B.4})$$

- `isotropic_hardening_rate` is the rate of isotropic hardening
- `initial_confining_stress` is the initial confining stress $p = -1/3\sigma_{ii}$ and it is positive in compressions (since there is that – (minus) sign in front of sum of normal stresses (σ_{ii} indicial notation summation convention applies) that are positive in tension [stress]).
- `number_of_subincrements` number of subincrements in constitutive simulation
- `maximum_number_of_iterations` maximum number of iterations

- `tolerance_1` Explicit: tolerance for intersection point (distance between two consecutive points) Implicit: yield function tolerance
- `tolerance_2` Implicit: residual tolerance

Material Model: `druckerprager_kinematic_hardening`, material with Drucker-Prager yield surface with kinematic hardening of the yield surface. Full command is:

```
1 add material # <.> type druckerprager_kinematic_hardening
2   mass_density = <M/L^3>
3   elastic_modulus = <F/L^2>
4   poisson_ratio = <.>
5   druckerprager_angle = <.>
6   armstrong_frederick_ha = <.>
7   armstrong_frederick_cr = <.>
8   initial_confining_stress = <F/L^2>
9   algorithm = explicit or implicit
10  number_of_subincrements = <.>
11  maximum_number_of_iterations = <.>
12  tolerance_1 = <.>
13  tolerance_2 = <.>;
```

where

- `mass_density` is the mass density of material [M/L^3]
- `druckerprager_angle` coefficient related to the soil friction angle.

$$M = \frac{6 \sin \phi}{3 - \sin \phi} \quad (\text{B.5})$$

- `armstrong_frederick_ha` [F/L^2]
- `armstrong_frederick_cr` [F/L^2]
- `initial_confining_stress` Initial confining stress [F/L^2]
- `number_of_subincrements` number of subincrements in constitutive simulation
- `maximum_number_of_iterations` maximum number of iterations
- `tolerance_1` Explicit: tolerance for intersection point (distance between two consecutive points) Implicit: yield function tolerance
- `tolerance_2` Implicit: residual tolerance

Material Model: `druckerprager_kinematic_hardening_accelerated`, accelerated material with Drucker-Prager yield surface with kinematic hardening of the yield surface. Full command is:

```

1 add material # <.> type ↔
   druckerprager_kinematic_hardening_accelerated
2   mass_density = <M/L^3>
3   elastic_modulus = <F/L^2>
4   poisson_ratio = <.>
5   druckerprager_angle = <.>
6   armstrong_frederick_ha = <F/L^2>
7   armstrong_frederick_cr = <F/L^2>
8   initial_confining_stress = <F/L^2>
9   number_of_subincrements = <.>
10  maximum_number_of_iterations = <.>
11  tolerance_1 = <.>
12  tolerance_2 = <.>;

```

where

- `mass_density` is the mass density of material [M/L^3]
- `druckerprager_angle` coefficient related to the soil friction angle.

$$M = \frac{6 \sin \phi}{3 - \sin \phi} \quad (\text{B.6})$$

- `armstrong_frederick_ha` [F/L^2]
- `armstrong_frederick_cr` [F/L^2]
- `initial_confining_stress` Initial confining stress [F/L^2]
- `number_of_subincrements` number of subincrements in constitutive simulation
- `maximum_number_of_iterations` maximum number of iterations
- `tolerance_1` Explicit: tolerance for intersection point (distance between two consecutive points) Implicit: yield function tolerance
- `tolerance_2` Implicit: residual tolerance

Material Model: rounded_mohr_coulomb, (command syntax is in development)

. . .

Material Model: cam_clay Full command is

```
1 add material # <.> type camclay
2   mass_density = <M/L^3>
3   reference_void_ratio = <.>
4   critical_stress_ratio_M = <.>
5   lambda = <.>
6   kappa = <.>
7   poisson_ratio = <.>
8   minimum_bulk_modulus = <F/L^2>
9   pressure_reference_p0 = <F/L^2>
10  initial_confining_stress = <F/L^2>
11  algorithm = explicit or implicit
12  number_of_subincrements = <.>
13  maximum_number_of_iterations = <.>
14  tolerance_1 = <.>
15  tolerance_2 = <.>;
```

where

- `mass_density` is the mass density of material [M/L^3]
- `reference_void_ratio` e_0 void ratio at the reference pressure, [dimensionless]
- `critical_stress_ratio_M` Cam-Clay slope of the critical state line in stress space, [dimensionless]
- `lambda` Cam-Clay normal consolidation line slope, (unit: dimensionless)
- `kappa` Cam-Clay unload-reload line slope, (unit: dimensionless)
- `minimum_bulk_modulus`
- `pressure_reference_p0` p_0 Cam-Clay parameter. Tip of the yield surface in q - p space. [F/L^2]
- `initial_confining_stress` initial confining (mean) pressure
- `algorithm` use explicit or implicit constitutive integration.
- `number_of_subincrements` number of subincrements in constitutive simulation
- `maximum_number_of_iterations` maximum number of iterations

- `tolerance_1` Explicit: tolerance for intersection point (distance between two consecutive points) Implicit: yield function tolerance
- `tolerance_2` Implicit: residual tolerance

Material Model: cam_clay_accelerated

A full command is

```
1 add material # <.> type camclay_accelerated
2   mass_density = <M/L^3>
3   reference_void_ratio = <.>
4   critical_stress_ratio_M = <.>
5   lambda = <.>
6   kappa = <.>
7   poisson_ratio = <.>
8   minimum_bulk_modulus = <F/L^2>
9   pressure_reference_p0 = <F/L^2>
10  initial_confining_stress = <F/L^2>
11  number_of_subincrements = <.>
12  maximum_number_of_iterations = <.>
13  tolerance_1 = <.>
14  tolerance_2 = <.>;
```

where

- `mass_density` is the mass density of material [M/L^3]
- `reference_void_ratio` e_0 void ratio at the reference pressure, [dimensionless]
- `critical_stress_ratio_M` Cam-Clay slope of the critical state line in stress space, [dimensionless]
- `lambda` Cam-Clay normal consolidation line slope, (unit: dimensionless)
- `kappa` Cam-Clay unload-reload line slope, (unit: dimensionless)
- `minimum_bulk_modulus`
- `pressure_reference_p0` p_0 Cam-Clay parameter. Tip of the yield surface in q - p space. [F/L^2]
- `initial_confining_stress` initial confining (mean) pressure
- `number_of_subincrements` number of subincrements in constitutive simulation
- `maximum_number_of_iterations` maximum number of iterations

- `tolerance_1` Explicit: tolerance for intersection point (distance between two consecutive points) Implicit: yield function tolerance
- `tolerance_2` Implicit: residual tolerance

Material Model: `sanisand2004`, Full command is:

```
1 add material # <.> type sanisand2004
2   mass_density = <M/L^3>
3   e0 = <.>
4   sanisand2004_G0 = <.>
5   poisson_ratio = <.>
6   sanisand2004_Pat = <.>
7   sanisand2004_p_cut = <.>
8   sanisand2004_Mc = <.>
9   sanisand2004_c = <.>
10  sanisand2004_lambda_c = <.>
11  sanisand2004_xi = <.>
12  sanisand2004_ec_ref = <.>
13  sanisand2004_m = <.>
14  sanisand2004_h0 = <.>
15  sanisand2004_ch = <.>
16  sanisand2004_nb = <.>
17  sanisand2004_A0 = <.>
18  sanisand2004_nd = <.>
19  sanisand2004_z_max = <.>
20  sanisand2004_cz = <.>
21  initial_confining_stress = <F/L^2>
22  algorithm = explicit (or) implicit
23    number_of_subincrements = <.>
24    maximum_number_of_iterations = <.>
25    tolerance_1 = <.>
26    tolerance_2 = <.>;
```

where

- MaterialNumber: Number of the ND material to be used ;
- `mass_density` is the mass density of material [M/L^3]
- `sanisand2004_e0` initial void ratio
- `sanisand2004_G0` elastic shear modulus
- `poisson_ratio` Poisson's ratio
- `sanisand2004_Pat` atmospheric pressure
- `sanisand2004_p_cut` pressure cut-off ratio

- `sanisand2004_Mc`
- `sanisand2004_c` tension-compression strength ratio
- `sanisand2004_lambda_c` parameter for critical state line
- `sanisand2004_xi` parameter for critical state line
- `sanisand2004_ec_ref` reference void for critical state line
- `sanisand2004_m` opening of the yield surface
- `sanisand2004_h0` bounding surface parameter
- `sanisand2004_ch` bounding surface parameter
- `sanisand2004_nb` bounding surface parameter
- `sanisand2004_A0` dilatancy parameter
- `sanisand2004_nd` dilatancy parameter
- `sanisand2004_z_max` fabric parameter
- `sanisand2004_cz` fabric parameter
- `initial_confining_stress` is the initial confining stress $p = -1/3\sigma_{ii}$ and it is positive in compressions (since there is that – (minus) sign in front of sum of normal stresses (σ_{ii} indicial notation summation convention applies) that are positive in tension [stress]).
- `algorithm` can be explicit or implicit.
- `number_of_subincrements` number of subincrements in constitutive simulation
- `maximum_number_of_iterations` maximum number of iterations
- `tolerance_1` Explicit: tolerance for intersection point (distance between two consecutive points) Implicit: yield function tolerance
- `tolerance_2` Implicit: residual tolerance

Material Model: sanisand2008

Full command is

```
1 add material # <.> type sanisand2008
2   mass_density = <M/L^3>
3   e0 = <.>
4   sanisand2008_G0 = <.>
5   sanisand2008_K0 = <.>
6   sanisand2008_Pat = <.>
7   sanisand2008_k_c = <.>
8   sanisand2008_alpha_cc = <.>
9   sanisand2008_c = <.>
10  sanisand2008_lambda = <.>
11  sanisand2008_ec_ref = <.>
12  sanisand2008_m = <.>
13  sanisand2008_h0 = <.>
14  sanisand2008_ch = <.>
15  sanisand2008_nb = <.>
16  sanisand2008_A0 = <.>
17  sanisand2008_nd = <.>
18  sanisand2008_p_r = <.>
19  sanisand2008_rho_c = <.>
20  sanisand2008_theta_c = <.>
21  sanisand2008_X = <.>
22  sanisand2008_z_max = <.>
23  sanisand2008_cz = <.>
24  sanisand2008_p0 = <F/L^3>
25  sanisand2008_p_in = <F/L^3>
26  algorithm = explicit (or) implicit
27  number_of_subincrements = <.>
28  maximum_number_of_iterations = <.>
29  tolerance_1 = <.>
30  tolerance_2 = <.>;
```

where

- MaterialNumber: Number of the ND material to be used ;
- Algorithm: Explicit (=0) or Implicit (=1) ;
- rho: density ;
- e0: initial void ratio at zero strain ;

- G0: Reference elastic shear modulus [stress];
- K0: Reference elastic bulk modulus [stress];
- [sanisand2008_Pat](#): atmospheric pressure for critical state line ;
- [sanisand2008_k_c](#): cut-off factor; for $p < k_c P_{at}$, use $p = k_c P_{at}$ for calculation of G ; (a default value of $k_c = 0.01$ should work fine) ;
- [sanisand2008_alpha_cc](#): critical state stress ratio ;
- [sanisand2008_c](#): tension-compression strength ratio ;
- [sanisand2008_lambda](#): parameter for critical state line ;
- [sanisand2008_xi](#): parameter for critical state line ;
- [sanisand2008_ec_ref](#): reference void for critical state line, ; $e_c = e_r \lambda (p_c / P_{at})^{\xi}$;
- [sanisand2008_m](#): opening of the yield surface ;
- [sanisand2008_h0](#): bounding surface parameter ;
- [sanisand2008_ch](#): bounding surface parameter ;
- [sanisand2008_nb](#): bounding surface parameter ;
- [sanisand2008_A0](#): dilatancy parameter ;
- [sanisand2008_nd](#): dilatancy parameter ;
- [sanisand2008_p_r](#): LCC parameter ;
- [sanisand2008_rho_c](#): LCC parameter ;
- [sanisand2008_theta_c](#): LCC parameter ;
- [sanisand2008_X](#): LCC parameter ;
- [sanisand2008_z_max](#): fabric parameter ;

- `sanisand2008_cz`: fabric parameter ;
- `sanisand2008_p0`: yield surface size ;
- `sanisand2008_p_in` ;
- `number_of_subincrements` number of subincrements in constitutive simulation
- `maximum_number_of_iterations` maximum number of iterations
- `tolerance_1` Explicit: tolerance for intersection point (distance between two consecutive points) Implicit: yield function tolerance
- `tolerance_2` Implicit: residual tolerance

Material Model: saniclay (command syntax is in development) ,

. . .

Material Model: `pisano`,

Full command is

```
1 add material # <.> type pisano
2   elastic_modulus = <F/L^2>
3   poisson_ratio = <.>
4   M_in = <F/L^2>
5   kd_in = <.>
6   xi_in = <.>
7   h_in = <.>
8   m_in = <.>
9   mass_density = <M/L^2>
10  initial_confining_stress = <F/L^2>
11  beta_min = <.>;
```

where

...

Material Model: uniaxial_fiber_elastic for which a full command is:

```
1 add material # <.> type uniaxial_elastic
2   elastic_modulus = <F/L^2>
3   viscoelastic_modulus = <mass / length / time> ;
```

Material Model: uniaxial_fiber_concrete02 for which a full command is:

```
1 add material # <.> type uniaxial_concrete02
2   compressive_strength = <F/L^2>
3   strain_at_compressive_strength = <.>
4   crushing_strength = <F/L^2>
5   strain_at_crushing_strength = <.>
6   lambda = <.>
7   tensile_strength = <F/L^2>
8   tension_softening_stiffness = <F/L^2>;
```

Material Model: uniaxial_fiber_steel01 for which a full command is:

```
1 add material # <.> type uniaxial_steel01
2   yield_strength = <F/L^2>
3   elastic_modulus = <F/L^2>
4   strain_hardening_ratio = <.>
5   a1 = <.>
6   a2 = <.>
7   a3 = <>
8   a4 = <.> ;
```

Material Model: uniaxial_fiber_steel02 for which a full command is:

```
1 add material # <.> type uniaxial_steel02
2   yield_strength = <F/L^2>
3   elastic_modulus = <F/L^2>
4   strain_hardening_ratio = <.>
5   R0 = <.>
6   cR1 = <.>
7   cR2 = <.>
8   a1 = <.>
9   a2 = <.>
10  a3 = <>
11  a4 = <.> ;
```

Modeling: Nodes

Nodes can be added to the finite element model:

```
1 add node # <.> at (<L>,<L>,<L>) with <.> dofs;
```

For example:

```
1 add node No 1 at (1.0*m, 2.5*m, 3.33*m) with 3 dofs;
```

adds a node number 1 at coordinates $x = 1.0m$, $y = 2.5m$ and $z = 3.33m$, with 3 dofs.

Nodes can also be removed from the finite element model (for example during excavation):

```
1 remove node No (or #) <.>;
```

Nodal masses can be added using:

```
1 add mass to node # <.>
2 mx = <M>
3 my = <M>
4 mz = <M>
5 Imx = <M*L^2>
6 Imy = <M*L^2>
7 Imz = <M*L^2>;
```

or

```
1 add mass to node # <.>
2 mx = <M>
3 my = <M>
4 mz = <M>;
```

Modeling: Finite Elements

The basic structure of all element commands is

```
1 add element No (or #)
2   type <finite_element_type>
3   with nodes (<.>, ..., <.>)|
4   {element dependent parameters};
```

Elements can be removed using:

```
1 remove element # <.>;
```

Choices for `finite_element_type` are listed below

Finite Element: Finite Element: `truss`,

for which a full command is:

```
1 add element No (or #) <element_number> type truss  
2 with nodes (n1, n2)  
3 use material No (or #) <material_number>  
4 section_area <section_area> [unit];  
5 mass_density <mass_density> [unit];
```

where

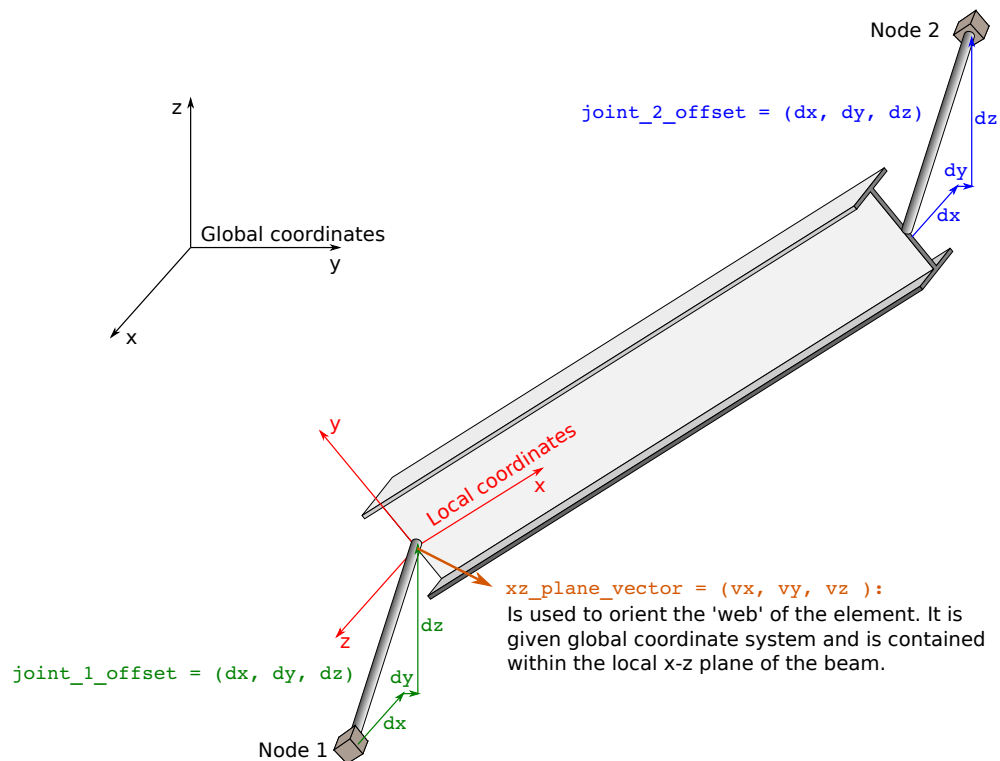
- No (or #) <element_number> is a unique element integer number (does not have to be sequential, any unique positive integer number can be used)
- `type truss` is the element type
- `with nodes` (n1, n2) are the 2 nodes (node numbers) defining this element
- `use material` No (or #) is the material number which makes up the element. Material has to be a uniaxial material, and it can be either elastic or one of the elastic-plastic materials defined for uniaxial behavior.
- `section_area` is the cross section area [L^2]

Finite Element: `beam_elastic`, linear elastic Euler-Bernoulli 3D beam element with end offsets and consistent mass matrix. The full command is:

```

1  add element # <.> type beam_elastic with nodes (<.>, <.>)
2      cross_section = <L^2>
3      elastic_modulus = <F/L^2>
4      shear_modulus = <F/L^2>
5      torsion_Jx = <length^4>
6      bending_Iy = <length^4>
7      bending_Iz = <length^4>
8      mass_density = <M/L^3>
9      xz_plane_vector = (<.>, <.>, <.> )
10     joint_1_offset = (<L>, <L>, <L> )
11     joint_2_offset = (<L>, <L>, <L> );

```



where

- No (or #) `<element_number>` is a unique element integer number (does not have to be sequential, any unique positive integer number can be used)
- `type beam_elastic` is the element type

- `with nodes` (`n1`, `n2`) are the 2 nodes (node numbers) defining this element
- `cross_section` is the cross section area, $[L^2]$
- `elastic_modulus` elastic modulus of the material which makes up the beam, $[F/L^2]$
- `shear_modulus` shear modulus of the material which makes up the beam, $[F/L^2]$
- `torsion_Jx` cross section polar (torsional) moment of inertia, $[L^4]$
- `bending_Iy` cross section moment of inertia about local y axis, $[L^4]$
- `bending_Iz` cross section moment of inertia about local z axis, $[L^4]$
- `mass_density` mass per unit volume of the material, $[M/L^3]$
- `xz_plane_vector` a vector which defines the orientation of the local (beam coordinate system) xz plane in global coordinates.
- `joint_1_offset` vector defining the rigid offset between end of beam and connection node 1, $[L]$
- `joint_2_offset` vector defining the rigid offset between end of beam and connection node 2, $[L]$

Finite Element: `beam_elastic_lumped_mass`,

linear elastic Euler-Bernoulli 3D beam element with end offsets and lumped mass matrix.

The full command is:

```
1 add element # <.> type beam_elastic_lumped_mass with nodes ↔
  (<.>, <.>)
2   cross_section = <L^2>
3   elastic_modulus = <F/L^2>
4   shear_modulus = <F/L^2>
5   torsion_Jx = <length^4>
6   bending_Iy = <length^4>
7   bending_Iz = <length^4>
8   mass_density = <M/L^3>
9   xz_plane_vector = (<.>, <.>, <.> )
10  joint_1_offset = (<L>, <L>, <L> )
11  joint_2_offset = (<L>, <L>, <L> );
```

where

- No (or #) `<element_number>` is the unique element integer number (does not have to be sequential, any unique positive integer number can be used)
- `type beam_elastic_lumped_mass` is the element type
- `with nodes` (`n1`, `n2`) are the 2 nodes defining this element
- `cross_section` is the cross section area, $[L^2]$
- `elastic_modulus` elastic modulus of the material which makes up the beam, $[F/L^2]$
- `shear_modulus` shear modulus of the material which makes up the beam, $[F/L^2]$
- `torsion_Jx` cross section polar (torsional) moment of inertia, $[L^4]$
- `bending_Iy` cross section moment of inertia about local y axis, $[L^4]$
- `bending_Iz` cross section moment of inertia about local z axis, $[L^4]$
- `mass_density` mass per unit volume of the material, $[M/L^3]$
- `xz_plane_vector` unit vector which defines the orientation of the web of the beam in global coordinates.

- `joint_1_offset` vector defining the rigid offset between end of beam and connection node 1, $[L]$
- `joint_2_offset` vector defining the rigid offset between end of beam and connection node 2, $[L]$

Finite Element: `beam_displacement_based`

```
1 add element # <.> type beam_displacement_based with nodes ↔  
  (<.>, <.>)  
2   number_of_integration_points = <.>  
3   section_number = <.>  
4   mass_density = <M/L^3>  
5   integration_rule = Lobatto | Legendre | Radau | ↔  
     NewtonCotes  
6   xz_plane_vector = (<.>, <.>, <.> )  
7   joint_1_offset = (<L>, <L>, <L> )  
8   joint_2_offset = (<L>, <L>, <L> );
```

where

- No (or #) `<element_number>` is the unique element integer number (does not have to be sequential, any unique positive integer number can be used)
- `type beam_displacement_based` is the element type
- `with nodes` (`n1`, `n2`) are the 2 nodes defining this element
- `number_of_integration_points` is number of integration points to be used along the beam element
- `section_number` is the number of predefined section
- `mass_density` mass per unit volume of the material, $[M/L^3]$
- `integration_rule` integration rule to be used among Lobatto, Legendre, Radau, or NewtonCotes.
- `xz_plane_vector` unit vector which defines the orientation of the web of the beam in global coordinates.
- `joint_1_offset` vector defining the rigid offset between end of beam and connection node 1, $[L]$
- `joint_2_offset` vector defining the rigid offset between end of beam and connection node 2, $[L]$

Finite Element: `beam_9dof_elastic`

```
1 add element # <.> type beam_9dof_elastic
2   with nodes (<.>, <.>)
3   cross_section = <L^2>
4   elastic_modulus = <F/L^2>
5   shear_modulus = <F/L^2>
6   torsion_Jx = <length^4>
7   bending_Iy = <length^4>
8   bending_Iz = <length^4>
9   mass_density = <M/L^3>
10  xz_plane_vector = (<.>, <.>, <.> )
11  joint_1_offset = (<L>, <L>, <L> )
12  joint_2_offset = (<L>, <L>, <L> );
```

where

- No (or #) `<element_number>` is the unique element integer number (does not have to be sequential, any unique positive integer number can be used)
- `type beam_9dof_elastic` is the element type
- `with nodes` (`n1`, `n2`) are the 2 nodes defining this element, where the first node (`n1`) is the one with 3 DOFs and the second (`n2`) is the one with 6 DOFs
- `cross_section` is the cross section area, $[L^2]$
- `elastic_modulus` elastic modulus of the material which makes up the beam, $[F/L^2]$
- `shear_modulus` shear modulus of the material which makes up the beam, $[F/L^2]$
- `torsion_Jx` cross section polar (torsional) moment of inertia, $[L^4]$
- `bending_Iy` cross section moment of inertia about local y axis, $[L^4]$
- `bending_Iz` cross section moment of inertia about local z axis, $[L^4]$
- `mass_density` mass per unit volume of the material, $[M/L^3]$
- `xz_plane_vector` unit vector which defines the orientation of the web of the beam in global coordinates.

- `joint_1_offset` vector defining the rigid offset between end of beam and connection node 1, $[L]$
- `joint_2_offset` vector defining the rigid offset between end of beam and connection node 2, $[L]$

This beam has zero stiffness components for torsion. It should be used either as a connection of solid and another beam element or in case of being used on its own, the corresponding dof for torsion (dof 7) Should be fixed!

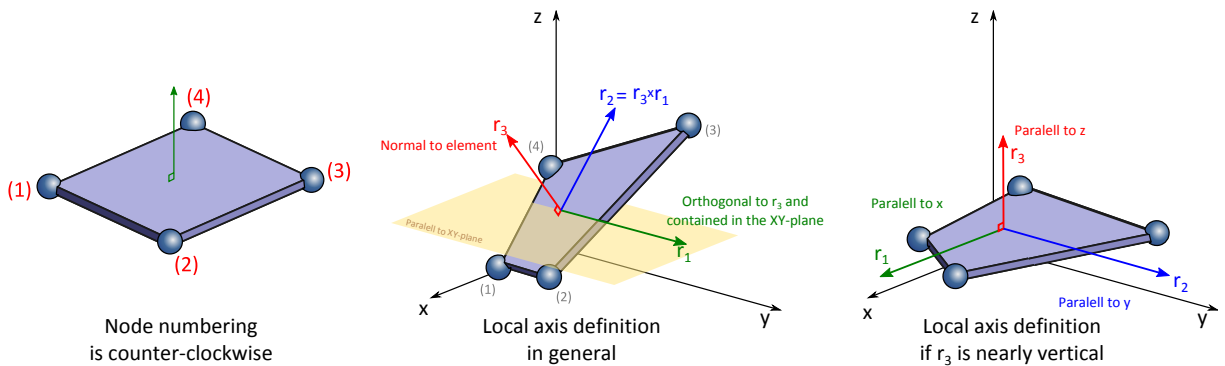
Node 1 should have 3 dofs while node 2 should have 6 dofs.

Finite Element: 4NodeShell_ANDES, ANDES based 3D shell element including drilling degrees of freedom. Made up by patching together 4 ANDES shell triangle elements (and then averaging two and two squares made up two and two triangles). The full command is:

```

1 add element # <.> type 4NodeShell_ANDES
2   with nodes (<.>, <.>, <.>)
3   use material # <.>
4   and acceleration field # <.>
5   thickness = <L> ;

```



- No (or #) <element_number> is the unique element integer number (does not have to be sequential, any unique positive integer number can be used)
- `material # <.>` number of a previously defined material. (see `add material ...`)
- `acceleration field # <.>` number of a previously defined acceleration field to use for self weight (see `add acceleration field ...`)
- `thickness` shell thickness, $[L]$

Finite Element: 3NodeShell_ANDES

```
1 add element # <.> type 3NodeShell_ANDES
2   with nodes (<.>, <.>, <.>)
3   use material # <.>
4   and acceleration field # <.>
5   thickness = <L> ;
```

- No (or #) <element_number> is the unique element integer number (does not have to be sequential, any unique positive integer number can be used)

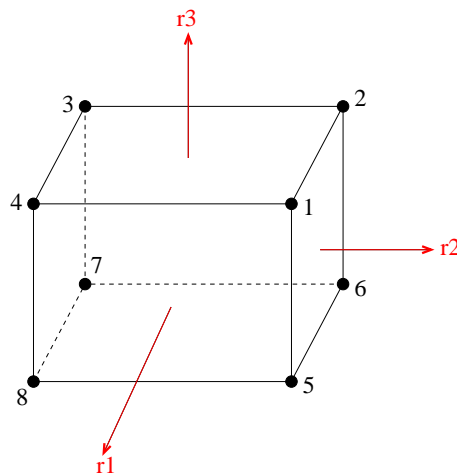
Finite Element: 8_node_brick, for which a full command is:

```
1 add element No (or #) <element_number> type 8NodeBrick
2   with nodes (n1, n2, n3, n4, n5, n6, n7, n8)
3   use material No (or #) <material_number>
4   and
5   acceleration field No (or #) <acceleration_field_number> ←
   >;
```

(This acceleration field part of element command is bound to be moved to loading)

where:

- No (or #) <element_number> is the unique element integer number (does not have to be sequential, any unique positive integer number can be used)
- type 8NodeBrick is the element type.
- with nodes (n1, n2, n3, n4, n5, n6, n7, n8) are the 8 nodes for this element, in the order as per figure below



- use material No (or #) is the material number which makes up the element (nonlinear elastic or elastic-plastic material properties for each integration (Gauss) point will evolve independently as the element deforms).

- `and acceleration field` No (or #) is the acceleration field used to develop body forces for the element (gravity for example). This command will be extracted from element command and will be moved to a different location (loading section).

Example add eight node brick, number 1 with nodes 1, 2, 3, 4, 5, 6, 7, 8, made up of material number 1 and loaded with body force field number 1

```
add element No 1 type 8NodeBrick
    with nodes (1, 2, 3, 4, 5, 6, 7, 8)
    use material No 1 and
    acceleration field 1;
```

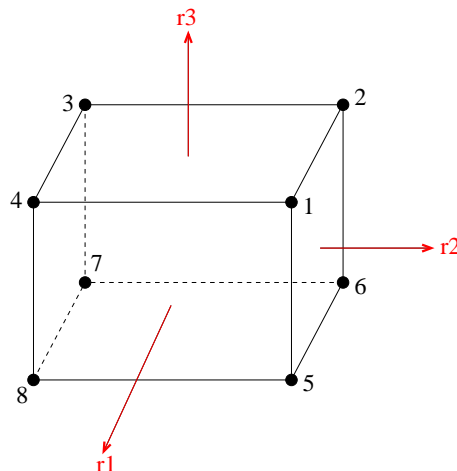
Finite Element: 8_node_brick_elastic, for which a full command is:

```
1 add element No (or #) <element_number> type 8↵  
  NodeBrick_elastic  
2   with nodes (n1, n2, n3, n4, n5, n6, n7, n8)  
3   use material No (or #) <material_number>  
4   and  
5   acceleration field No (or #) <acceleration_field_number↵  
    >;
```

(This acceleration field part of element command is bound to be moved to loading)

where:

- No (or #) <element_number> is the unique element integer number (does not have to be sequential, any unique positive integer number can be used)
- type 8NodeBrick_elastic is the element type. It is used if linear elastic material is used (stiffness creation is much faster). In this case, the stiffness and mass matrices will not be updated at each step.
- with nodes (n1, n2, n3, n4, n5, n6, n7, n8) are the 8 nodes for this element, in the order as per figure below



- use material No (or #) is the material number which makes up the element. This element will work with linear elastic material only.

- `and acceleration field` No (or #) is the acceleration field used to develop body forces for the element (gravity for example). This command will be extracted from element command and will be moved to a different location (loading section).

Example add eight node brick, number 1 with nodes 1, 2, 3, 4, 5, 6, 7, 8, made up of material number 1 and loaded with body force field number 1

```
add element No 1 type 8NodeBrick_elastic
    with nodes (1, 2, 3, 4, 5, 6, 7, 8)
    use material No 1 and
    acceleration field 1;
```

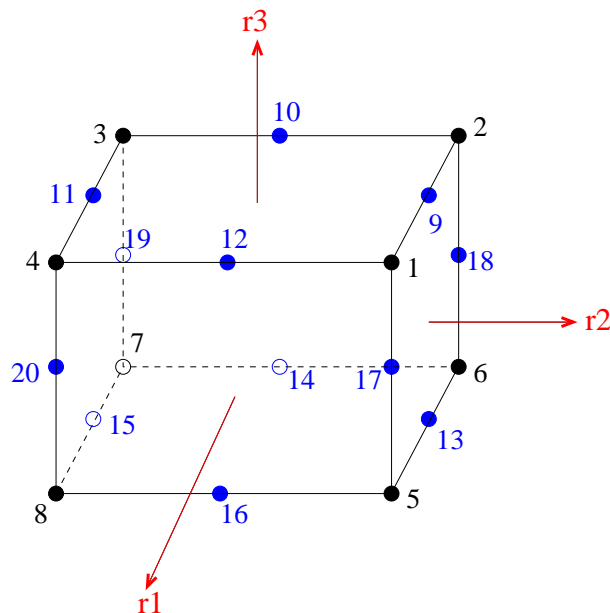
Finite Element: 20_node_brick, for which a full command is:

```
1 add element No (or #) <element_number> type 20NodeBrick
2   with nodes (n1, n2, n3, n4, n5, n6, n7, n8,
3               n9, n10, n11, n12, n13, n14, n15, n16,
4               n17, n18, n19, n20 )
5   use material No (or #) <material_number>
6   and
7   acceleration field No (or #) <acceleration_field_number↔
   >;
```

(This acceleration field part of element command is bound to be moved to loading)

where:

- No (or #) <element_number> is the unique element integer number (does not have to be sequential, any unique positive integer number can be used)
- type 20NodeBrick is the element type. 20NodeBrick_elastic can be used if elastic material is used. In this case, the stiffness and mass matrices will not be updated at each step.
- with nodes (n1, n2, n3, n4, n5, n6, n7, n8, n9, n10, n11, n12, n13, n14, n15, n16, n17, n18, n19, n20) are the 20 nodes for this element, written in the order defined as per figure below



- `use material` No (or #) is the material number which makes up the element (nonlinear elastic or elastic-plastic material properties for each integration (Gauss) point will evolve independently as the element deforms)
- `and acceleration field` No (or #) is the acceleration field used to develop body forces for the element (gravity for example). This command will be extracted from element command and will be moved to a different location (loading section).

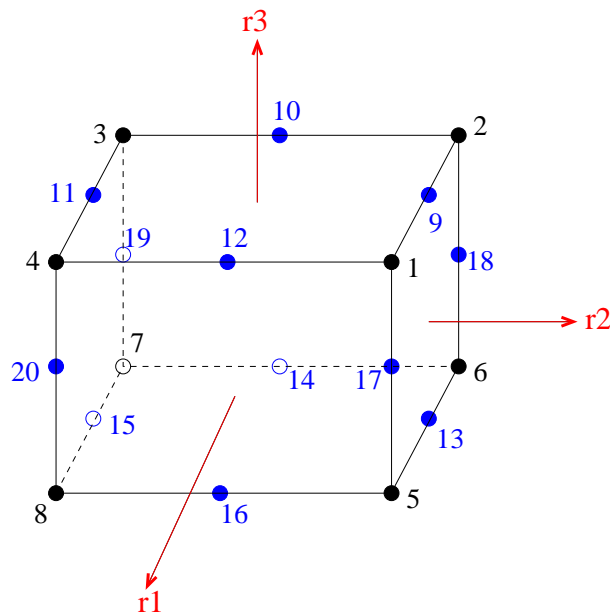
Finite Element: 20_node_brick_elastic, for which a full command is:

```
1 add element No (or #) <element_number> type 20↵
  NodeBrick_elastic
2   with nodes (n1, n2, n3, n4, n5, n6, n7, n8,
3               n9, n10, n11, n12, n13, n14, n15, n16,
4               n17, n18, n19, n20 )
5   use material No (or #) <material_number>
6   and
7   acceleration field No (or #) <acceleration_field_number↵
   >;
```

(This acceleration field part of element command is bound to be moved to loading)

where:

- No (or #) <element_number> is the unique element integer number (does not have to be sequential, any unique positive integer number can be used)
- type 20NodeBrick_elastic is the element type, and is used if linear elastic material is used. In this case, the stiffness and mass matrices will not be updated at each step.
- with nodes (n1, n2, n3, n4, n5, n6, n7, n8, n9, n10, n11, n12, n13, n14, n15, n16, n17, n18, n19, n20) are the 20 nodes for this element, written in the order defined as per figure below



- `use material` No (or #) is the linear elastic material number which makes up the element.
- `and acceleration field` No (or #) is the acceleration field used to develop body forces for the element (gravity for example). This command will be extracted from element command and will be moved to a different location (loading section).

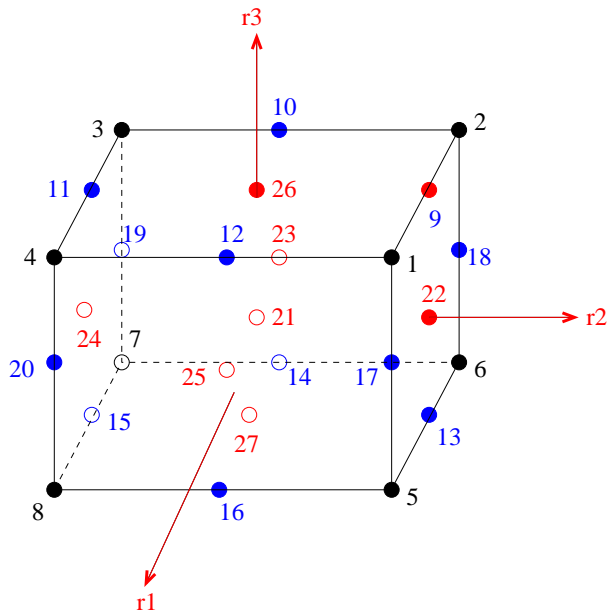
Finite Element: 27_node_brick, for which a full command is:

```
1 add element No (or #) <element_number>
2     type 27NodeBrick
3     with nodes (n1, n2, n3, n4, n5, n6, n7, n8,
4                 n9, n10, n11, n12, n13, n14, n15, n16↵
5                 ,
6                 n17, n18, n19, n20, n21, n22, n23,
7                 n124, n25, n26, n27 )
8     use material No (or #) <material_number>
9     and
    acceleration field No (or #) <↵
        acceleration_field_number>;
```

(This acceleration field part of element command is bound to be moved to loading)

where:

- No (or #) <element_number> is the unique element integer number (does not have to be sequential, any unique positive integer number can be used)
- `type 27NodeBrick` is the element type.
- `with nodes` (n1, n2, n3, n4, n5, n6, n7, n8, n9, n10, n11, n12, n13, n14, n15, n16, n17, n18, n19, n20, n21, n22, n23, n24, n25, n26, n27) are the 27 nodes for this element, written in the order defined as per this figure
- `use material` No (or #) is the material number which makes up the element (nonlinear elastic and/or elastic-plastic material properties for each integration (Gauss) point will evolve independently as the element deforms)
- `and acceleration field` No (or #) is the acceleration field used to develop body forces for the element (gravity for example). This command will be extracted from element command and will be moved to a different location (loading section).



Finite Element: 27_node_brick_elastic, for which a full command is:

```

1 add element No (or #) <element_number>
2   type 27NodeBrick_elastic
3   with nodes (n1, n2, n3, n4, n5, n6, n7, n8,
4             n9, n10, n11, n12, n13, n14, n15, n16↵
5             ,
6             n17, n18, n19, n20, n21, n22, n23,
7             n24, n25, n26, n27 )
8   use material No (or #) <material_number>
9   and
   acceleration field No (or #) <↵
   acceleration_field_number>;

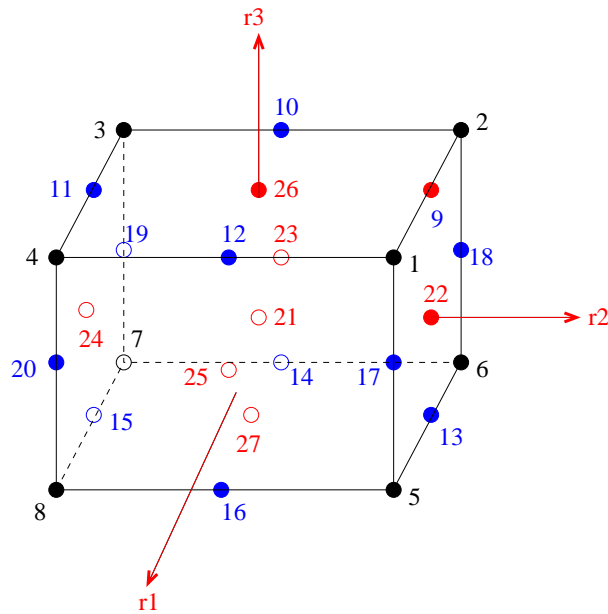
```

(This acceleration field part of element command is bound to be moved to loading)

where:

- No (or #) <element_number> is the unique element integer number (does not have to be sequential, any unique positive integer number can be used)
- type 27NodeBrick_elastic is the element type and is used if elastic material is used. In this case, the stiffness and mass matrices will not be updated at each step.
- with nodes (n1, n2, n3, n4, n5, n6, n7, n8, n9, n10, n11, n12, n13, n14, n15, n16, n17, n18, n19, n20)

n21, n22, n23, n24, n25, n26, n27) are the 27 nodes for this element, written in the order defined as per this figure



- `use material` No (or #) is the linear elastic material number which makes up the element .
- `and` `acceleration field` No (or #) is the acceleration field used to develop body forces for the element (gravity for example). This command will be extracted from element command and will be moved to a different location (loading section).

Finite Element: variable_node_brick_8_to_20, for which a full command is:

```

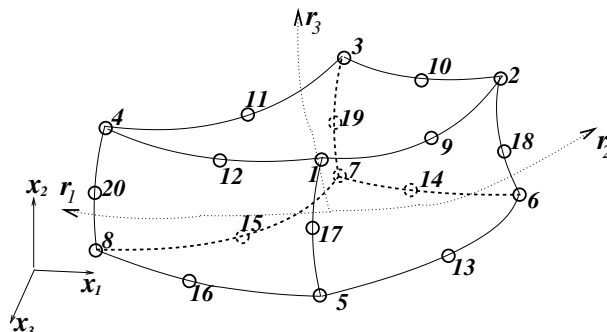
1 add element No (or #) <element_number> type ←
   variable_node_brick_8_to_20
2     with nodes (n1, n2, n3, n4, n5, n6, n7, n8,
3                 n9, n10, n11, n12, n13, n14, n15, n16 ←
4                 ,
5                 n17, n18, n19, n20)
6     use material No (or #) <material_number>
7     and
   acceleration field No (or #) <←
   acceleration_field_number>;

```

(This acceleration field part of element command is bound to be moved to loading)

where:

- No (or #) <element_number> is the unique element integer number (does not have to be sequential, any unique positive integer number can be used)
- **type** variable_node_brick_8_to_20 is the element type
- **with nodes** (n1, n2, n3, n4, n5, n6, n7, n8, n9, n10, n11, n12, n13, n14, n15, n16, n17, n18, n19, n20) are the 8 to 20 nodes for this element, written in the order defined as per this figure. Nodes 1-8 are obligatory, while any other nodes can be used but do not have to, the element will automatically pick proper shape functions. This element is good for transitions in meshing.



- **material** No (or #) is the material number which makes up the element (nonlinear elastic and/or elastic-plastic material properties for each integration (Gauss) point will

evolve independently as the element deforms)

- **acceleration field** No (or #) is the acceleration field used to develop body forces for the element (gravity for example). This command will be extracted from element command and will be moved to a different location (loading section).

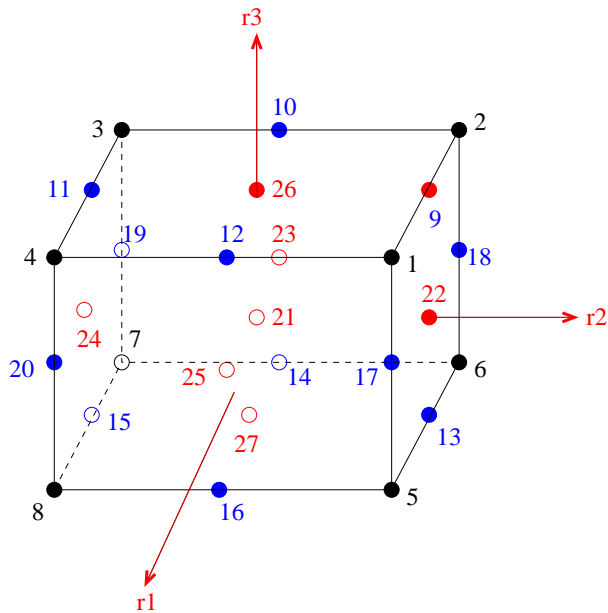
Finite Element: `variable_node_brick_8_to_27`, for which a full command is:

```
1 add element No (or #) <element_number> type ↔  
   variable_node_brick_8_to_27  
2     using <.> Gauss points each direction  
3     with nodes (n1, n2, n3, n4, n5, n6, n7, n8,  
4                 n9, n10, n11, n12, n13, n14, n15, n16 ↔  
5                 ,  
                 n17, n18, n19, n20, n21, n22, n23, ↔  
                 n24, n25, n26, n27)  
6     use material No (or #) <material_number>  
7     and  
8     acceleration field No (or #) <↔  
       acceleration_field_number>;
```

(This acceleration field part of element command is bound to be moved to loading)

where:

- No (or #) <element_number> is the unique element integer number (does not have to be sequential, any unique positive integer number can be used)
- `type variable_node_brick_8_to_27` is the element type
- `with nodes` (n1, n2, n3, n4, n5, n6, n7, n8, n9, n10, n11, n12, n13, n14, n15, n16, n17, n18, n19, n20, n21, n22, n23, n24, n25, n26, n27) are the 8 to 27 nodes for this element, written in the order defined as per this figure. Nodes 1-8 are obligatory, while any other nodes can be used but do not have to, the element will automatically pick proper shape functions. This element is good for transitions in meshing.
- `material` No (or #) is the material number which makes up the element (nonlinear elastic and/or elastic-plastic material properties for each integration (Gauss) point will evolve independently as the element deforms)
- `acceleration field` No (or #) is the acceleration field used to develop body forces for the element (gravity for example). This command will be extracted from element command and will be moved to a different location (loading section).



Finite Element: `penalty_element_for_applying_generalized_displacement`

for which a full command is:

```

1  add element # <.>
2      type penalty_for_applying_generalized_displacement
3      with node (<.>)
4      stiffness = <corresponding unit to dof>;
5      dof [DOFTYPE];

```

where

- No (or #) `<element_number>` is a unique element integer number (does not have to be sequential, any unique positive integer number can be used)
- `type` `penalty_for_applying_displacement` is the element type
- `with node` (`n1`) is the number of pre-existing node
- `stiffness` penalty stiffness to be used for the element. If the dof is `ux`, `uy`, `uz`, `Ux`, `Uy`, or `Uz`, the corresponding stiffness unit is $[M/T^2]$. If the dof is `rx`, `ry`, or `rz`, the corresponding stiffness has the unit of moment $[ML^2/T^2]$. If the dof is `p`, the corresponding stiffness has the unit of stress $[M/LT^2]$.

- **DOFTYPE** is the dof to be constrained from the existing node ($u_x, u_y, u_z, r_x, r_y, r_z, U_x, U_y, U_z, p$)

Finite Element: `penalty` element

A full command is:

```
1 add element # <.> type penalty
2   with nodes (<.> , <.>)
3   stiffness = <corresponding unit to dof>;
4   dof to constrain [DOFTYPE]
```

where

- No (or #) `<element_number>` is a unique element integer number (does not have to be sequential, any unique positive integer number can be used)
- `type penalty` is the element type
- `with node` (`n1` , `n2`) is the number of pre-existing nodes
- `stiffness` penalty stiffness to be used for the element. If the dof is `ux`, `uy`, `uz`, `Ux`, `Uy`, or `Uz`, the corresponding stiffness unit is $[M/T^2]$. If the dof is `rx`, `ry`, or `rz`, the corresponding stiffness has the unit of moment $[ML^2/T^2]$. If the dof is `p`, the corresponding stiffness has the unit of stress $[M/LT^2]$.
- `DOFTYPE` is the dof to be constrained between nodes (`ux`, `uy`, `uz`, `rx`, `ry`, `rz`, `Ux`, `Uy`, `Uz`, `p`)

Finite Element: 8NodeBrick_up

A full command is:

```
1 add element # <.> type 8NodeBrick_up
2   with nodes (<.>, <.>, <.>, <.>, <.>, <.>, <.>, <.>)
3   use material # <.> and acceleration field No (or #) <.>
4   porosity = <.>
5   alpha = <.>
6   rho_s = <M/L^3>
7   rho_f = <M/L^3>
8   k_x = <L^3*T/M>
9   k_y = <L^3*T/M>
10  k_z = <L^3*T/M>
11  K_s = <F/L^2>
12  K_f = <F/L^2>;
```

Note that, the permeability k is used with dimensions of $[length]^3[time]/[mass]$, which is different from the usual soil mechanics convention, where the permeability has the dimension of velocity, i.e. $[length]/[time]$. Their values are related by $k = K/\rho_f g$, where g is the gravitational acceleration at which the permeability is measured.

Finite Element: 8NodeBrick_upU

for which a full command is:

```
1 add element # <.> type 8NodeBrick_upU
2   with nodes (n1, n2, n3, n4, n5, n6, n7, n8)
3   use material # <.> and acceleration field No (or #) <.>
4   porosity = <.>
5   alpha = <.>
6   rho_s = <M/L^2>
7   rho_f = <M/L^2>
8   k_x = <L^3*T/M>
9   k_y = <L^3*T/M>
10  k_z = <L^3*T/M>
11  K_s = <F/L^2>
12  K_f = <F/L^2>;
```

Finite Element: 20NodeBrick_upU

for which a full command is:

```
1 add element # <.> type 20NodeBrick_upU
2   with nodes (n1, n2, n3, n4, n5, n6, n7, n8,
3             n9, n10, n11, n12, n13, n14, n15, n16,
4             n17, n18, n19, n20)
5   use material # <.> and acceleration field No (or #) <.>
6   porosity = <.>
7   alpha = <.>
8   rho_s = <M/L^3>
9   rho_f = <M/L^3>
10  k_x = <L^3*T/M>
11  k_y = <L^3*T/M>
12  k_z = <L^3*T/M>
13  K_s = <F/L^2>
14  K_f = <F/L^2>;
```

Note that, the permeability k is used with dimensions of $[length]^3[time]/[mass]$, which is different from the usual soil mechanics convention, where the permeability has the dimension of velocity, i.e. $[length]/[time]$. Their values are related by $k = K/\rho_f g$, where g is the gravitational acceleration at which the permeability is measured.

Finite Element: 27NodeBrick_upU (command syntax is in development) ,

...

Finite Element: `contact`

A full command is:

```
1 add element # <.> type contact
2   with nodes (<.>, <.>)
3   normal_stiffness = <F/L^2>
4   tangential_stiffness = <F/L^2>
5   friction_ratio = <.>
6   contact_plane_vector = (<.>, <.>, <.> );
```

Finite Element: neoprene_rubber_isolator_element (command syntax is in development) ,

...

Finite Element: `led_core_rubber_isolator_element` (command syntax is in development) ,

...

Finite Element: frictional_pendulum_isolator_element_01

(command syntax is in development) ,

...

Finite Element: frictional_pendulum_isolator_element_03
(command syntax is in development) ,

...

Modeling: Damping

Two types of damping are available

First, define the damping.

```
1 add damping # <.> type Rayleigh with a0 = <1/time> a1 = <↔  
   time> stiffness_to_use  
2 = Initial_Stiffness -or- Current_Stiffness -or- ↔  
   Last_Committed_Stiffness;
```

```
1 add damping # <.> type Caughey3rd  
2 with a0 = <T> a1 = <1/time> a2 = <.> stiffness_to_use = [↔  
   Initial_Stiffness][Current_Stiffness][↔  
   Last_Committed_Stiffness];
```

```
1 add damping # <.> type Caughey4th  
2 with a0 = <T> a1 = <1/time> a2 = <.> a3 = <.> ↔  
   stiffness_to_use = [Initial_Stiffness][Current_Stiffness][↔  
   Last_Committed_Stiffness];
```

then apply it to the element or node.

```
1 add damping # <.> to element # <.>;
```

```
1 add damping # <.> to node # <.>;
```

Modeling: Constraints, Supports, Master-Slave Connections, etc.

```
1 fix node # <node_number> dofs [ux uy uz p Ux Uy Uz rx ry rz ←  
  all];
```

where at least one of the DOF fixity codes (`ux uy uz p Ux Uy Uz rx ry rz all`) has to be invoked. These codes are

- `ux`, translation in x direction (for solid phase only in $u - p - U$ and $u - p$ elements)
- `uy`, translation in y direction (for solid phase only in $u - p - U$ and $u - p$ elements)
- `uz`, translation in z direction (for solid phase only in $u - p - U$ and $u - p$ elements)
- `Ux`, translation of pore fluid phase in x direction (for $u - p - U$ elements)
- `Uy`, translation of pore fluid phase in y direction (for $u - p - U$ elements)
- `Uz`, translation of pore fluid phase in z direction (for $u - p - U$ elements)
- `rx`, rotation around x axes (for structural elements)
- `ry`, rotation around y axes (for structural elements)
- `rz`, rotation around z axes (for structural elements)
- `all`, all applicable DOFs for a given node

Example fix translation x and y for node #3 `fix node # 3 dofs ux uy;`

Example fix all appropriate DOFs for node #7. `fix node # 7 dofs all;`

```
1 free node # <.> dofs [ux uy uz p Ux Uy Uz rx ry rz]
```

```
1 add constraint equaldof with  
2 master node # <.> and  
3 slave node # <.>  
4 dof to constrain <.>;
```

```
1 remove constraint equaldof node # <.>
```

```
1 add single point constraint to node # <.>  
2 dof to constrain <dof_type>  
3 constraint value of <.>
```

Modeling: Static Loads, Self Weight and other Acceleration/Inertia Related Forces

```
1 add acceleration field No <acceleration field number>
2   ax = <acceleration in x direction>*[L/T^2]
3   ay = <acceleration in y direction>*[L/T^2]
4   az = <acceleration in z direction>*[L/T^2];
```

Example adding acceleration induced loading field for (some) elements `add acceleration`↵

`field` No 1

`ax = 0*m/s^2`

`ay = 0*m/s^2`

`az = -9.81*m/s^2;`

Modeling: Nodal Loads

The general signature to add loads is

```
1 add load # <.> to node # <.>
2   type <load type> <direction> = <force_amplitude>
3   {more parameters};
```

The load # is a unique number assigned to each load. The node # is the number of a node which has already been defined. The load type refers to the functional form in time or pseudotime (for static analysis) and can be any of the list

- **linear** Constant rate time dependence.
- **path** Use an arbitrary function defined in an external file.

Each force type except linear have additional parameters which will be explained later.

The force direction refers to the degree of freedom the force will be added to. These force directions are the conjugate in energy of the DOFs defined earlier. These are,

- **Fx**, force in x direction ¹
- **Fy**, force in y direction ¹
- **Fz**, force in z direction ¹
- **F_fluid_x**, force to the pore fluid phase in x direction ²
- **F_fluid_y**, force to the pore fluid phase in y direction ²
- **F_fluid_z**, force to the pore fluid phase in z direction ²
- **Mx**, moment about x axes ³
- **My**, moment about y axes ³
- **Mz**, moment about z axes ³

¹Applies to solid phase only when connected to coupled elements

¹Applies to fluid phase when connected to coupled elements

⁰For elements with rotational DOFs, i.e. beams, shells

Example command for adding three linear forces ($f_x = -10 * kN$, $f_y = -10 * kN$, $f_z = -10 * kN$) to node # 1:

```
1 add load # 1 to node 1 type linear Fx = -10*kN;  
2 add load # 2 to node 1 type linear Fy = -10*kN;  
3 add load # 3 to node 1 type linear Fz = -10*kN;
```

The force `type` refers to the functional dependence in time (or pseudotime) that the force will have. The possible functional forms have been listed before. Listed are additional parameters which define these forces.

1. `linear` Receives no extra parameters. In this case the magnitude of the force is interpreted as the magnitude of the force after one second of time (or pseudotime) has passed.

2. `path`

```
1 add load # <.> to node # <.> type path_series FORCETYPE = <↔  
  force or moment scale factor> series_file = "STRING";
```

```
1 add load # <.> to node # <.> type path_time_series FORCETYPE ↔  
  = <force or moment scale factor> time_step = <T> ↔  
  series_file = "STRING";
```

Modeling Loads: Selfweight

```
1 add load # <.>  
2 to element # <.>  
3 type self_weight;
```

Modeling: Brick Surface Load

Surface of 8 node brick element with same pressure magnitudes at all nodes:

```
1 add load # <.> to element # <.> type surface at nodes (<.> , ←  
  <.> , <.> , <.>) with magnitude <.>;
```

Surface of 8 node brick element with different pressure magnitudes at all nodes:

```
1 add load # <.> to element # <.> type surface at nodes (<.> , ←  
  <.> , <.> , <.>) with magnitudes (<.> , <.> , <.> , <.>);
```

Surface of 20 node brick element with same pressure magnitudes at all nodes:

```
1 add load # <.> to element # <.> type surface at nodes (<.> , ←  
  <.> , <.> , <.>, <.>, <.>, <.>, <.>) with magnitude <.>;
```

Surface of 20 node brick element with different pressure magnitudes at all nodes:

```
1 add load # <.> to element # <.> type surface at nodes (<.> , ←  
  <.> , <.> , <.>, <.>, <.>, <.>, <.>) with magnitudes (<.> ←  
  , <.> , <.> , <.>, <.>, <.>, <.>);
```

Surface of 27 node brick element with same pressure magnitudes at all nodes:

```
1 add load # <.> to element # <.> type surface at nodes (<.> , ←  
  <.> , <.> , <.>, <.>, <.>, <.>, <.>, <.>) with magnitude ←  
  <.>;
```

Surface of 27 node brick element with different pressure magnitudes at all nodes:

```
1 add load # <.> to element # <.> type surface at nodes (<.> , ←  
  <.> , <.> , <.>, <.>, <.>, <.>, <.>, <.>) with magnitudes ←  
  (<.> , <.> , <.> , <.>, <.>, <.>, <.>, <.>, <.>);
```

Modeling: Motion Time Histories

If the time increment is constant during the analysis, the following command can be used (the input files will have only one column corresponding to displacement, velocity, or acceleration):

```
1 add imposed motion # <.> to node # <.> dof DOFTYPE
2 time_step = <T>
3 displacement_scale_unit = <L>
4 displacement_file = "filename"
5 velocity_scale_unit = <L/T>
6 velocity_file = "filename"
7 acceleration_scale_unit = <L/L^2>
8 acceleration_file = "filename";
```

If the time increment is defined in the files or it might not be changed with constant increment during the analysis, the following command can be used (the input files will have two columns. The first column is the time while the second column will have corresponding displacement, velocity, or acceleration):

```
1 add imposed motion # <.> to node # <.> dof DOFTYPE
2 displacement_scale_unit = <displacement>
3 displacement_file = "filename"
4 velocity_scale_unit = <velocity>
5 velocity_file = "filename"
6 acceleration_scale_unit = <acceleration>
7 acceleration_file = "filename";
```

Modeling: Domain Reduction Method

```
1 add domain reduction method loading # <.>
2 time_step = <T>
3 scale_factor = <.>
4 number_of_steps = <.>
5 number_of_drm_nodes = <.>
6 number_of_drm_elements = <.>
7 x_max = <L>
8 x_min = <L>
9 y_max = <L>
10 y_min = <L>
11 z_max = <L>
12 z_min = <L>
13 element_file = "filename"
14 nodes_file = "filename"
15 displacement_file = "filename"
16 acceleration_file = "filename";
```

Modeling: Penalty Displacements

First the penalty element should be defined and the displacement time history should be added to the penalty element using the following commands depending on the type of the displacement input:

```
1 add penalty displacement # <.> to element # <.> DOFTYPE = <L↵  
  > type linear;
```

```
1 add penalty displacement # <.> to element # <.> dof DOFTYPE ↵  
  type path_series time_step = <T> scale_factor = <.> ↵  
  series_file = "STRING";
```

```
1 add penalty displacement # <.> to element # <.> dof DOFTYPE ↵  
  type path_time_series scale_factor = <.> series_file = "↵  
  STRING";
```

Modeling: Removing loads and motions

Loads and motions can be removed using:

```
1 remove load # <.>
```

```
1 remove imposed motion # <.>
```

B.2.4 Simulation

Simulation: Solvers

```
1 define solver ProfileSPD (or) profilespd | UMFpack (or) ←  
  umfpack;
```

Simulation: Static Solution Advancement

```
1 simulate <.> steps using static algorithm;
```

Simulation: Dynamic Solution Advancement

```
1 simulate <.> steps using transient algorithm time_step = <T↵  
   >;
```

```
1 simulate <.> steps using variable transient algorithm  
2 time_step = <T>  
3 minimum_time_step = <.>  
4 maximum_time_step = <.>  
5 number_of_iterations = <.>
```

Simulation: Generalized Eigenvalue Analysis

At any given point in an analysis a generalized eigenvalue of the system can be performed, based on the current mass and tangent stiffness matrices. The command to do this is.

```
1 simulate using eigen algorithm number_of_modes = <.>;
```

The first `number_of_modes` eigenvalues are displayed on screen after the analysis is performed. If more eigenvalues are requested than degrees-of-freedom the system has, the excess reported values are set to NaN (not a number).

Simulation: Solution Integrators

```
1 define static integrator displacement_control  
2   using node # <.> dof DOFTYPE increment <L>;
```

```
1 define load factor increment <.>;
```

```
1 define dynamic integrator Newmark  
2   with gamma = <.> beta = <.>;
```

```
1 define dynamic integrator Hilber_Hughes_Taylor  
2   with alpha = <.>;
```

Simulation: Solution Algorithms

```
1 define algorithm With_no_convergence_check (or) ↔  
  with_no_convergence_check | Newton (or) newton | ↔  
  Modified_Newton (or) modified_newton;
```

Simulation: Convergence Criteria

```
1 define convergence test
2 Norm_Displacement_Increment | Energy_Increment | Norm_Unbalance ←
   tolerance = <L>
3 verbose_level = <0>|<1>|<2>;
```

Simulating: Response and State

For saving the response of the model including nodal displacements, element forces, and element stresses in mysql format, the following command can be used:

```
1 save response of model type mysql
2     databasename <.>
3     host <.>
4     username <.>
5     password <.>
6     port <.>
7     socket <.>
```

For saving the state of the analysis in mysql format, the following command can be used:

```
1 save state of model type mysql
2     commit # <.>
3     databasename <.>
4     host <.>
5     username <.>
6     password <.>
7     port <.>
8     socket <.>
9     clientFlag <.>;
```

Restoring the state of the analysis from mysql format, can be done using the following command:

```
1 restore state of model type mysql
2     commit # <.>
3     databasename <.>
4     host <.>
5     username <.>
6     password <.>
7     port <.>
8     socket <.>
9     clientFlag <.>;
```

The input arguments are:

- `commit #`
- `databasename`: Name of the database to be created/used in mysql
- `host`: Name/IP of the computer which the database will be created/used (for the local

computer "localhost" can be used)

- `username`: Username on the mysql server
- `password`: Password corresponding to the username to be used on mysql server (if no password is setup up leave it empty)
- `port`: mysql port (default is 3306)
- `socket`: path to mysql.sock file
- `clientFlag`

B.2.5 Checking the Mesh

```
1 check mesh filename;
```